Modeling and Simulation in Science, Engineering and Technology

Complex Flows in Industrial Processes

Antonio Fasano
Editor

With 102 Figures

Springer-Science+Business Media, LLC

Antonio Fasano
University of Florence
Dipartimento di Matematica "U. Dini"
Viale Morgagni 67/a 50134
Firenze, Italy

Library of Congress Cataloging-in-Publication Data
Fasano, A. (Antonio)
Complex flows in industrial processes / Antonio Fasano.
p. cm.—(Modeling and simulation in science, engineering and technology)
Includes bibliographical references and index.
ISBN 978-1-4612-7106-2 ISBN 978-1-4612-1348-2 (eBook)
DOI 10.1007/978-1-4612-1348-2

1. Manufacturing processes—Mathematical models. 2. Fluid dynamics—Mathematical models. I. Title. II. Series: Modeling in science, engineering & technology.
TS183. F37 1999
658.5'001'5118—dc21 99-33030
CIP

AMS Subject Classifications: 76A, 76B, 76C, 76S, 80A

Printed on acid-free paper.

Originally published by Birkhauser Boston in 2000
Softcover reprint of the hardcover 1st edition 2000

ISBN 978-1-4612-7106-2
SPIN 10682919

Typeset by TechBooks, Fairfax, VA.

9 8 7 6 5 4 3 2 1

Contents

Preface

Despite the fact that fluid dynamics and filtration through porous media are classical research areas in engineering, physics, and mathematics, there are still many industrial processes that require the study of new mathematical models for flows of particular complexity, due to the peculiar properties of the systems involved.

The aim of this book is to provide a number of examples showing how frequently such situations arise in various branches of industrial technology. The selection of the subjects was motivated not only by their industrial relevance and mathematical interest. What I had in mind was a collection of problems having a really distinctive character, thus bringing some fresh air into one of the oldest and most revered domains of applied mathematics. The incredible richness of nonstandard flow problems in industrial applications has always been, and still is, a constant surprise to me. Therefore I tried to offer a very large spectrum of subjects, with special attention devoted to those problems in which the modeling phase is far from being obvious, and the mathematical content is absolutely nontrivial. With such a view to diversity, topics have been selected from a variety of sources (such as glass industry, polymers science, coffee brewing, fuels pipelining), and contributors from different backgrounds (mathematics, physics, chemical engineering) have been included. Consequently, the mathematical nature of the problems formulated spans over a large range, so that their theoretical investigation and numerical computation require a variety of different techniques.

Chapters have been grouped in three classes:

i) "Flows of nonlinear materials" is a generic title emphasizing peculiar rheological properties (polymeric flows, stability problems in extrusion, and coal-water slurries).

ii) "Flows accompained by thermal processes" is a large class in which we have included specific problems such as phase change in polymers,

where the flow is thermally induced, various flow problems in the glass industry, and the flow fields that accompany mass and heat transfer in polymerization processes.

iii) "Nonlinear flows in porous media" is another broad title we have chosen for a group of very peculiar processes which are in reality quite loosely related to one another, namely: espresso coffee brewing, the manufacturing of composite materials, and the flow of liquid through porous media with hydrophile granules. However, they do have a common denominator, which is the interaction of the flow with the solid components of the system.

Because of space constraints, we have chosen only a few illustrative examples. Many more problems of great relevance can be found in different areas. A remarkable case is the one of oil reservoir technology, a very rich source of important (and probably more widely known) mathematical problems, so large and fast developing that today we can consider it as a classical research field, for which an extensive literature exists, and that is in turn an inexhaustible collection of complex flow problems, whose size is out of the conceivable range of the present book.

Thus we are not pursuing any idea of completeness, which would certainly be a hopeless goal. The material gathered here is just a sampling from a big boiling pot, which I hope can be stimulating to those who like real world applications of fluid dynamics treated with mathematical rigor. For this reason quite a few open problems deserving further investigation have been included in each presentation.

I would like to thank Prof. Nicola Bellomo who encouraged me to be the editor of this book. Of course I am deeply grateful to all the authors who made the nontrivial effort to contribute a chapter on problems with such special characteristics.

Firenze, Italy ANTONIO FASANO

Contributors

DANIELE ANDREUCCI
Dipartimento Metodi e Modelli Matematici
Universitá di Roma "La Sapienza"
Roma, Italy

E. CARNIANI
Snamprogetti S.p.A.
Fano 61032
Italy

E. DONATI
Snamprogetti S.p.A
Fano 61032
Italy

D. ERCOLANI
Snamprogetti S.p.A.
Fano 61032
Italy

ANGIOLO FARINA
Dipartimento Ingegneria Aeronautica e Spaziale
Politecnico di Torino
Torino 10129
Italy

ANTONIO FASANO
Dipartimento di Matematica "U. Dini"
Universitá di Firenze
Firenze 50134
Italy

G. IANNIRUBERTO
Dipartimento di Ingegneria Chimica
Universitá Federico II
Napoli 80125
Italy

K. LAEVSKY
Department of Mathematics and Computer Science
Eindhoven University of Technology
Eindhoven 5600 MB
The Netherlands

A. MANCINI
Dipartimento di Matematica "U. Dini"
Universitá di Firenze
Firenze 50134
Italy

G. Marrucci
Dipartimento di Ingegneria Chimica
Universitá Federico II
Napoli 80125
Italy

R.M.M. Mattheij
Department of Mathematics and Computer Science
Eindhoven University of Technology
Eindhoven 5600 MB
The Netherlands

S. Mazzullo
Dipartimento di Matematica "U. Dini"
Universitá di Firenze
Firenze 50134
Italy

M. Petracco
illycaffè s.p.a.
Via Flavia 110
Trieste 34147
Italy

Luigi Preziosi
Dipartimento di Matematica
Politecnico di Torino
Torino 10129
Italy

Riccardo Ricci
Dipartimento di Matematica "F. Enriques"
Universitá di Milano
Milano, Italy

Fabio Rosso
Dipartimento di Matematica "U. Dini"
Universitá di Firenze
Firenze 50134
Italy

F. Talamucci
Dipartimento di Matematica "U. Dini"
Universitá di Firenze
Firenze 50134
Italy

Alessandro Terenzi
Snamprogetti S.p.A.
Fano 61032
Italy

A.A.F. van de Ven
Eindhoven University of Technology
Eindhoven 5600 MB
The Netherlands

Part I

Flows of Nonlinear Materials

1

Molecular Theories of Polymer Viscosity

G. MARRUCCI AND G. IANNIRUBERTO

Dipartimento di Ingegneria Chimica
Università Federico II
Napoli, Italy

ABSTRACT. The viscosity of polymeric liquids crucially depends on polymer concentration c and molar mass M. These dependencies can generally be predicted from relatively simple theories, because what really matters is the chain-like structure of the polymer molecule rather than its detailed chemistry. In this chapter we summarize the main concepts leading to these predictions throughout the concentration range, i.e., from dilute solutions up to polymer melts. However, only the so-called zero-shear viscosity will be considered because the nonlinear effects arising from the coupling between flow and molecular "structure" are more complex and fall outside the scope of this chapter. In dilute solutions the important concept is that of "intrinsic" viscosity which, through dependence on M, reveals structural features of the polymer (flexible chain vs. rigid rodlike, for example) as well as the solvent quality. In semidilute solutions of long polymers, the overall structure of the system becomes that of an impermanent network of entangled chains. The viscosity is then related to the elasticity of the network and to the kinetics of chain disengagement. Typically, the viscosity scaling takes the form of power laws in both M and c. The M dependencies remain the same in the particularly relevant case of polymer melts. The chapter ends with a brief description of systems with localized interactions (or sticky points) in which the viscosity is particularly sensitive to the strength of such interactions.

A. Fasano (ed.), *Complex Flows in Industrial Processes*

1.1 Introduction

Viscosity is a property of liquids that, unlike other important properties like density, easily varies by many orders of magnitude. It is a common experience that some liquids are very mobile (water, alcohol, most solvents) while others are extremely viscous (thick oils, molten asphalt, glycerine, etc.). These differences are ultimately related to the different molecular structures of the various substances, and it would be nice if the viscosity of a liquid could be predicted by knowing the structure of the constituent molecules. For relatively "small" molecules, such as those just mentioned, a prediction of their viscosity in the liquid state does not seem possible, however; there are probably too many relevant structural features of the constituent molecules and their influence is too subtle. On the other hand, our inability to predict the viscosity of those substances is mostly irrelevant, as it can easily be measured once and for all.

Polymeric substances are a different story. As we shall discuss in the following, the viscosity of polymeric liquids, both solutions and melts, is better understood. Also, understanding the viscosity of polymers can be much more useful. There are several reasons why the latter statement is true. One of them is that all synthetic polymers, and many natural polymers as well, come in a range of molecular masses. For example, polystyrene can be produced with M ranging from a few thousand to several million, corresponding to proportionally different lengths of the molecule (most polymers are linear chains). Measuring the viscosity for each possible M value would clearly be cumbersome; however, the M-dependence of the viscosity of polymeric liquids can be very strong. It is useful, therefore, to understand why and how the M-dependence of viscosity comes about; even more so because polymers tend to show a "universal" behavior. Such universality is due to the chain-like structure of the polymer molecule, a feature that often dominates over other details of the chemical structure. As a consequence, so-called "scaling laws" can often be found that apply to a whole class of polymeric substances.

Another aspect that makes the viscosity of polymers worth studying is their behavior in solution. When a polymeric substance is progressively added to a solvent, the viscosity of the solution soon becomes dominated by the polymer, sometimes even at very low concentrations. (Some polymeric additives are effective "viscosizers.") Thus it is important to understand why this is so and which are the scaling laws of viscosity with concentration. For the case of polyelectrolytes, i.e., polymers carrying ionizable groups all along the chain, the viscosity will also depend on other variables like the ionic strength of the solution and, possibly, pH. For some polymers, the role

played by local interactions can be particularly important. In most cases, these polymers are "block copolymers," made up by chemically different sequences linked in the same chain. Then it may happen that sequences that do not like the solvent tend to stick together, forming temporary bonds. The same can also occur in the melt, just because the different sequences do not like each other. The effect of these bonds on viscosity can be dramatic.

In this chapter we briefly discuss some of these effects. We will start with dilute solutions, where the concept of "intrinsic" viscosity is encountered. The behavior of the viscosity in such a limit, though showing some intricacies, can be understood on the basis of classical hydrodynamics. Next we consider semidilute solutions, then concentrated solutions and melts. Here, in order to understand the viscosity, we need to first touch upon rubber-like elasticity and polymer viscoelasticity. The digression will be very brief, however; we will soon return to focus on viscosity. We will conclude by discussing one example of localized interactions.

An important aspect of polymer viscosity will not be considered here however, because the corresponding theory would require too long a presentation. We refer to the nonlinear behavior, i.e., to the fact that the viscosity of polymeric liquids (defined, as for all other substances, by the ratio of the shear stress to the velocity gradient) itself depends on the velocity gradient (or shear rate) in fast flows. In very general terms, the nonlinear behavior is brought about by the influence of flow on the "structure" of the polymeric liquid; for example, the material loses isotropy as the molecules align in the flow direction. The theory of the nonlinear behavior of polymeric liquids is an active research topic.

1.2 Dilute Solutions and Intrinsic Viscosity

In the limit of dilute solutions interpolymer contacts are infrequent so that we can consider only the interactions of the polymer molecules with the solvent. Let us first examine ordinary flexible polymers, the molecule of which is a "random coil" in solution, i.e., the chain resembles the path of a random walk in 3D space (see Fig. 1.1). The overall appearance of the random coil is that of a soft ball which, because of thermal motion, fluctuates in shape. On average, however, the shape can be taken as spherical, because no directions of space are preferred.

We will then calculate the viscosity η of the polymer solution as if it were a dilute suspension of spherical particles, for which we can rely on

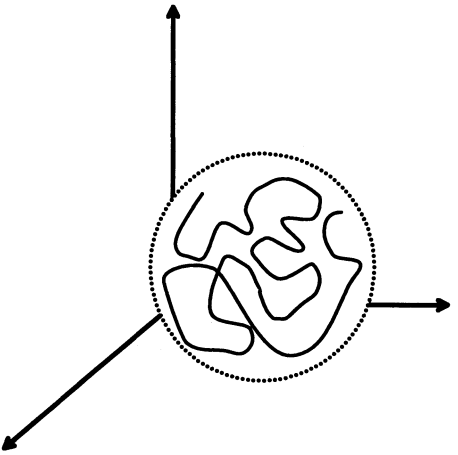

Figure 1.1 — In the liquid state the polymer chain is coiled up; the shape is spherical on average.

Einstein's formula

$$\frac{\eta - \eta_s}{\eta_s} = 2.5\phi \tag{1.1}$$

where η_s is the viscosity of the solvent and ϕ is the volume fraction occupied by the spherical particles. The latter can be written as the product νV of the number ν of polymer molecules per unit volume of solution times the "effective" or "hydrodynamic" volume V of the polymer coil. Because ν can itself be expressed through c (mass of polymer per unit volume of solution) and M (molar mass of the polymer) as $\nu = \aleph c/M$, (where $\aleph$ is Avogadro number), Eq. (1.1) can be rewritten in terms of the so-called "intrinsic viscosity" $[\eta]$ of the polymer as

$$[\eta] = \lim_{c \to 0} \frac{1}{c} \frac{\eta - \eta_s}{\eta_s} = K \frac{V}{M} \tag{1.2}$$

where the numerical constant K incorporates both 2.5 and Avogadro number.

The intrinsic viscosity is readily obtained from the experimental determination of η versus concentration, the limit in the definition of $[\eta]$ emphasizing the concept of dilute solutions (no interactions among polymer molecules). Once $[\eta]$ has been measured, the rightmost part in Eq. (1.2) can be used to obtain useful information on the polymer, provided we can estimate V, itself determined by the "size" of the random coil. Though perhaps deserving a whole chapter of its own, the problem of the coil size can be summarized as follows.

A measure of the coil size is obtained from the end-to-end vector $\mathbf{R}$ through the ensemble average $\langle R^2 \rangle$. The simplest model for the coil is the "ideal" chain, which ignores the excluded volume repulsion between chain segments as well as any energetic effect arising from the quality of the solvent (see below). The chain then becomes entirely equivalent to a random walk, and the result is [9]

$$\langle R^2 \rangle = nb^2; \qquad n \propto M \tag{1.3}$$

where b is the length of the statistical "monomer" (or Kuhn segment), and n is the number of steps in the random walk, i.e., the number of monomers in the chain. Although b depends on the chemical details of the polymer chain, being smaller for more flexible chains, Eq. (1.3) is "universal." As long as this simple model is applicable, it predicts that the size of the random coil of whatever polymer "scales" with the square root of its molecular mass M.

When the excluded volume interaction is accounted for, the coil is predicted to swell up somewhat. The calculations become much more complex because the statistics are those of a self-avoiding walk (SAW). However, to a very good approximation, the following result holds true:

$$\langle R^2 \rangle \approx n^{1.2} b^2 \propto M^{1.2} \tag{1.4}$$

Eq. (1.4) applies to the case of *good* solvents, i.e., to the case where polymer-solvent contacts have the same energy as contacts between two polymer segments. Conversely, if polymer-solvent contacts are energetically less favored, i.e., the solvent quality is poorer, then the coil size decreases and the prediction of Eq. (1.3) may be approached.

A situation may arise where, by compensation of effects, Eq. (1.3) is obeyed exactly. This will occur in suitably poor solvents (called θ solvents) at a temperature (called θ, or Flory, temperature) at which the excluded volume effect and the energetic interactions (Van der Waals or otherwise) cancel one another. At the θ condition, the statistics are virtually the same as the ideal chain.

Eq. (1.3) is also exactly obeyed in a completely different, yet very important, situation: in polymer melts. Indeed, although a melt of identical chains is obviously a "good solvent" for any one of them, excluded volume interactions are *screened* in the melt. The latter effect can be understood by considering that, in the melt, the self-uncrossability condition (which swells up the chain in a good solvent of small molecules) is indistinguishable from the condition that segments of different chains cannot cross each other either. A polymer segment hitting another polymer segment in the melt does not "know" if that segment belongs to the same chain. We will come back to this important property of the melt state later in this chapter.

Going back to the viscosity problem, we can in any event estimate the volume V in Eq. (1.2) as $V \approx \langle R^2 \rangle^{3/2}$. Hence, the expression for the intrinsic viscosity becomes

$$[\eta] = K \frac{\langle R^2 \rangle^{3/2}}{M} \tag{1.5}$$

Eq. (1.5) is fully consistent with the experiments. These show that $[\eta] = KM^a$, where the exponent a, which depends on the polymer-solvent pair, always falls in the interval $0.5 \leq a \leq 0.8$. The limiting values correspond to θ solvent and good solvents, respectively, in full agreement with the predictions of Eqs. (1.3) and (1.4). The θ condition effectively represents a lower limit for the coil size in solution. Indeed, by further reducing the temperature below the θ-temperature, the coil shrinks to a globule and precipitates from the solution. For practical purposes, the intrinsic viscosity of a polymer is used to determine in a simple way its molar mass M. For such a use, a suitable solvent is chosen (and a suitable temperature), and the parameters K and a are empirically determined once and for all by using polymer samples of known M value.

The intrinsic viscosity, however, is also a basic ingredient of the theory of polymers. Among other things, it shows the "effectiveness" of polymers in generating large viscosities. To prove this point we start by considering that Eq. (1.2), just like Eq. (1.1), applies in general to a suspension of spherical particles. However, if the particles are solid (e.g., glass beads), both equations show that the size of the beads is irrelevant. In Eq. (1.1), the volumetric fraction ϕ is clearly insensitive to bead size; the same applies to the ratio volume/mass in Eq. (1.2). Conversely, for the case of polymers, the intrinsic viscosity becomes sensitive to the molecular size M, and it grows with increasing M. Where does the difference originate? The answer is found in the concept of volume *spanned* by the molecule as opposed to that literally *occupied.* The former is the volume of the sphere containing the coil in Fig. 1.1 and is obviously much larger than the latter. On the other hand, it is the former that constitutes the relevant volume in hydrodynamics, hence appropriately entering Eq. (1.2) as V. In its motion, the solvent interacts hydrodynamically with the coil as a whole, almost as if it were a solid sphere of volume V.

To better understand the interplay of these factors, let us perform the following "thought" experiment. A Maxwell demon enters the solution and cuts all polymer molecules in half. Obviously the polymeric mass concentration has not been changed, and yet the polymer contribution to viscosity drops (by a factor $\sqrt{2}$ in a θ solvent). Indeed, although the particles have doubled in number, their individual hydrodynamic volume has been more than halved (in θ solvents it is reduced by the factor $2^{3/2}$).

The "viscosizing" efficiency of polymers (large viscosities with little mass) is further amplified if the polymer molecules are rigid and rod-like

rather than flexible and coil-like. Indeed the hydrodynamic volume here becomes that of the sphere spanned by the rod-like molecule in its Brownian rotation, hence growing with M^3. The ratio V/M, i.e., the intrinsic viscosity $[\eta]$ (see Eq. (1.2) or (1.5)), then grows with as much as the second power of M. The same conclusion is reached, in fact with better precision, by arguing as follows. The friction coefficient of a rod (in the Stokes regime) is given by [10]

$$\zeta_{\text{rod}} \approx \eta_s \frac{L}{\ln(L/d)} \tag{1.6}$$

where L and d are rod length and diameter, respectively, and the omitted numerical front factor is of order unity. (In fact that factor depends on the rod orientation with respect to fluid velocity; yet the difference between the extreme cases of orthogonal and parallel orientation is only by a factor of 2.) The friction coefficient times the square of the rod-solvent relative velocity gives the energy dissipated by the rod per unit time. Now, because the relative velocity (for any assigned velocity gradient) scales with L, we deduce that the dissipation per rod scales with the rod geometry as $L^3/\ln(L/d)$. The last quantity is the equivalent of the hydrodynamic volume of the rod. Indeed, multiplying the dissipation per rod by the number of rods per unit volume gives the dissipation per volume, hence the viscosity. As the number of rods decreases inversely with increasing L (at fixed rod concentration by weight c), the intrinsic viscosity scales as

$$[\eta]_{\text{rod}} \propto \frac{L^2}{\ln(L/d)} \propto M^a \tag{1.7}$$

where we mean that for L large enough the power law with $a = 2$ represents just a slight overestimation. Experimental values of the exponent for rigid polymers confirm this prediction. Of course, a value of the exponent less than 2 can also come from a partial flexibility of the chain.

The concept of hydrodynamic volume for a polymer chain can be profitably used to understand, for example, the viscous behavior of polyelectrolytes. The viscosity of these polymers is observed to increase significantly with decreasing ionic strength. The explanation is that, at low ionic strengths, the counter-ions of the polyelectrolyte are dispersed in the solvent and far away from the chains; hence, like charges of the same chain are no longer electrically screened by the counter-ions and will repel each other. The chains become longer and more rigid (see Fig. 1.2), and the viscosity correspondingly increases.

It may be instructive to conclude this section by comparing the friction coefficient of an extended chain to that of the same chain when coiled up. Let us then consider a chain of n monomers of length b. When the chain is coiled up its friction coefficient is that of a sphere of size $\langle R^2 \rangle^{1/2}$; hence,

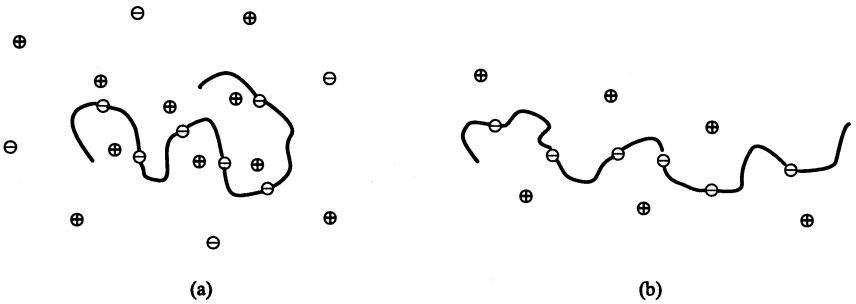

Figure 1.2 — A polyelectrolyte carrying negative charges along the chain: (a) at high ionic strength (obtained by adding NaCl, for example) the chain is coiled up; (b) at low ionic strength the chain extends because of repulsion of the negative charges bound to the chain.

depending on the solvent, we may write (see Eqs. (1.3) and (1.4))

$$\zeta_{\text{coil}} \approx \eta_s n^{\nu} b \qquad \begin{array}{ll} \nu = 0.5 & \theta \text{ solvents} \\ \nu = 0.6 & \text{good solvents} \end{array} \tag{1.8}$$

On the other hand, when the chain is fully extended, Eq. (1.6) holds true with $L = nb$. Hence

$$\zeta_{\text{extended}} \approx \eta_s \frac{nb}{\ln n + \ln(b/d)} \approx \eta_s \frac{nb}{\ln n} \tag{1.9}$$

Notice finally that the isolated monomer would have a friction coefficient of order $\eta_s b$. Therefore, under no circumstances the friction is additive along the chain, i.e., we never obtain that the chain friction is equal to n times $\eta_s b$. However, Eq. (1.9) shows that in the extended conformation the correction with respect to simple additivity is only given by $\ln n$. This occurs because the *hydrodynamic interactions* among the monomers of the chain are rather weak in the extended chain. In the general case, the friction coefficient becomes much smaller in the coiled state because the monomers get closer to one another and, correspondingly, the hydrodynamic interactions become stronger. In the coiled state, the monomers in the inside of the coil are "shielded" by those on the outside.

In some cases, however, the difference in friction between the coiled and the extended chain is minor. This will occur for wormlike persistent chains ($b/d \gg 1$) in good solvents if n is not too large. For example, for $n = 100$ and $b/d = 10$, Eq. (1.8) gives $100^{0.6} = 16$, which is even slightly larger than the prediction of Eq. (1.9), i.e., $100/\ln 1000 = 14.5$. It seems that some recent data by Chu and coworkers on DNA [12] can be interpreted in this way, i.e., by properly accounting for hydrodynamic interactions.

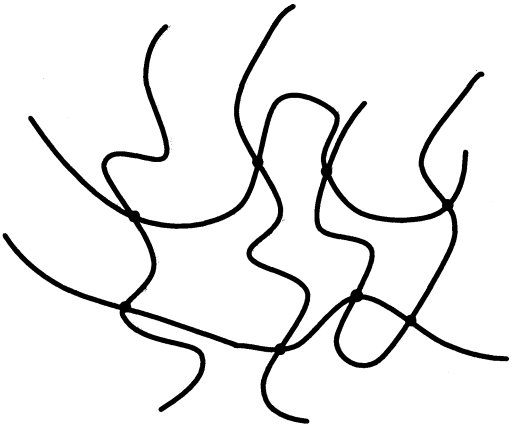

Figure 1.3 — A permanent network; the cross-links are represented as black dots.

1.3 Polymeric Networks

In the previous section we only invoked concepts of classical hydrodynamics. Here, jumping to a sort of opposite extreme, we focus on rubber networks where the polymer behavior is purely elastic. The network (see Fig. 1.3) consists of polymer chains permanently linked at junction points (called cross-links) so that the whole rubber sample consists of a single giant molecule. Rubber cannot flow but can deform to a considerable extent.

The large deformability is due to the fact that rubber elasticity is *entropic* in nature, i.e., it is due to the thermal motion of the polymer chains. As a consequence, the shear modulus G is given by [15]

$$G \approx \nu kT \tag{1.10}$$

where ν is the number of chains (a chain goes from a cross-link to the next) per unit volume and kT is thermal energy. One should notice the analogy with the volume elasticity of gases, which is also entropic in nature and generates the well-known law for the pressure $p = \nu kT$, with ν the number of molecules per unit volume. In the case of gases, the thermal motion of the molecules is translational, and the pressure arises from the force exerted by the molecules hitting the wall of the container. In the rubber case the thermal motion is *conformational*: chains continuously explore different conformations. Because all conformations are energetically equivalent, the most probable state of the chain is that obtained with the largest number of conformations (the coiled state). When deforming a piece of rubber, we extend chains, pulling them toward less favorable conditions (in terms of

available conformations). A reaction force will then arise (proportional to thermal energy kT) that attempts to restore the previous shape.

The concept of rubber-like elasticity is fundamental in polymer physics. It can readily be extended to polymer *viscoelasticity*. Indeed, consider again the network depicted in Fig. 1.3, and assume that the cross-links are not permanent; rather, assume that they have a finite lifetime τ. With a mean frequency $1/\tau$, all chains of the network detach from it, relax their deformation (if any is present), and then re-attach to the network.

Such a temporary, or impermanent, network describes a *liquid* rather than a solid. Indeed, because the chains periodically relax the deformation by detaching from the network, the material can be macroscopically deformed without limit, i.e., it can flow. The crucial parameters of the impermanent network are the relaxation time τ and the instantaneous elastic modulus G, which is still given by Eq. (1.10). (Although in this case chains detach and re-attach continuously, ν in Eq. (1.10) is the number of chains per unit volume which, at any instant, are attached to the network.) We shall soon prove that the viscosity is given by the product of these two constitutive parameters, i.e., that

$$\eta = G\tau \tag{1.11}$$

To obtain Eq. (1.11) let us first recall that, by definition of elastic modulus, we may write

$$\sigma = G\gamma \tag{1.12}$$

where σ is the shear stress and γ is the shear deformation. Eq. (1.12) applies as such to the permanent network of a rubber. For the temporary network subjected to a shear flow, the macroscopic deformation is obviously undefined, but an internal microscopic deformation can still be recognized. Indeed, the chains deform progressively while remaining attached to the network for a time τ. Hence, if $\dot{\gamma}$ is the shear rate, we can estimate the average deformation stored in the network at any instant as $\gamma = \dot{\gamma}\tau$. The shear stress in the flowing system is then obtained from Eq. (1.12) as:

$$\sigma = G\tau\dot{\gamma} \tag{1.13}$$

On the other hand, because from the macroscopic viewpoint we define the viscosity η through the ratio $\sigma/\dot{\gamma}$, Eq. (1.11) remains (heuristically) proved.

To be precise, we should point out that Eq. (1.11) strictly applies to the case of a single relaxation time. Polymeric systems often show a set (or a continuous spectrum) of relaxation times, in which case Eq. (1.11) is replaced by a summation (or an integral) [7]. In many significant cases, however, one of the relaxation times is dominant, so that Eq. (1.11) can be used with good approximation. In the following sections, our estimates for the viscosity will invariably be based on Eq. (1.11).

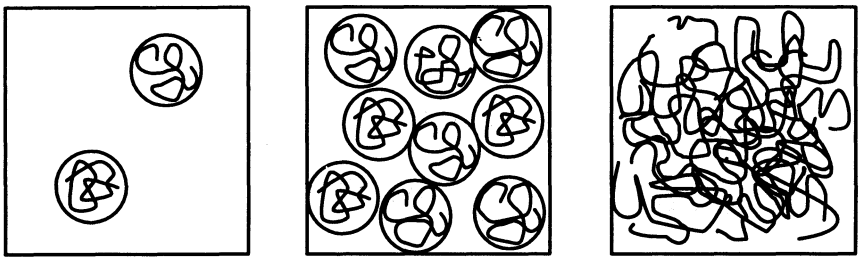

(a) (b) (c)

Figure 1.4 — A (a) dilute solution ($c < c^*$); (b) solution at the overlap concentration ($c \approx c^*$); (c) semidilute entangled solution ($c \gg c^*$).

1.4 Semidilute Solutions in Good Solvents

In the section on intrinsic viscosity we examined the case where the polymer molecules are so far apart in the solution that the interactions among them can be ignored. With increasing concentration, polymer–polymer encounters become more and more frequent. In good solvents these interactions are repulsive in nature, due to excluded volume, implying that the coil-containing spheres avoid overlapping (see Fig. 1.4a). A concentration is reached, however, at which overlapping cannot be avoided (see Fig. 1.4b). Such a critical concentration c^* is readily calculated from the condition that the spheres just touch, i.e. (in terms of hydrodynamic volume fraction ϕ) from the condition $\phi^* \approx 1$. Then, using Eqs. (1.1) and (1.2), we estimate $c^* \approx [\eta]^{-1}$. At concentrations $c > c^*$ the coils interpenetrate considerably (see Fig. 1.4c), but because the critical concentration c^* is very small (for large M), there exists a concentration range in which the solution can still be considered dilute, in the sense that the polymer segments are still in contact mostly with the solvent. In such a range, the solution is therefore called *semidilute.*

As first suggested by de Gennes [3], semidilute solutions in good solvents enjoy simple "scaling laws." The reason for the (relative) simplicity is that the whole behavior of semidilute solutions can be described through the concept of *screening length* ξ. The meaning of this quantity is illustrated in Fig. 1.5. Because the chains interpenetrate, there are many contacts between them. The screening length ξ defines the average distance between consecutive contacts, and the chain segments spanning consecutive contacts are called "blobs" because the shape of the space they span is spherical on average. Within a blob, the excluded volume interaction remains important because, at that scale, the chain only interacts with the

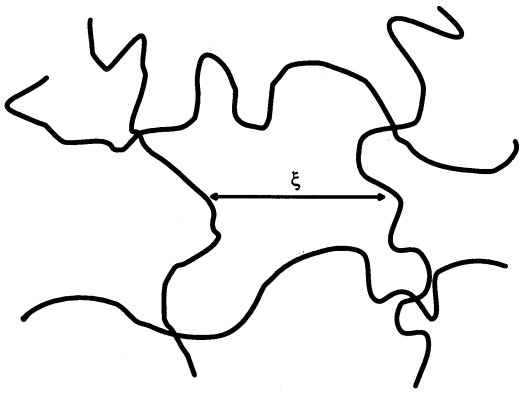

Figure 1.5 — The mesh size (or blob size) ξ for interpenetrating coils.

solvent (and with itself), not with other chains. Conversely, for distances larger than ξ, the excluded volume interaction is effectively screened because interacting blobs cannot distinguish whether they belong to the same chain or to different ones.

The length ξ as a function of the concentration c can be estimated as follows. From pure dimensional analysis we may write:

$$\xi = R_0 f(c/c^*) \tag{1.14}$$

The reference length R_0 is the mean size of the isolated coil, i.e., $R_0 = \sqrt{\langle R_0^2 \rangle}$, where the average under the square root is given by Eq. (1.4). The unspecified function f in Eq. (1.14) is then required to become unity for $c \leq c^*$, i.e., in dilute solutions. In the semidilute range, i.e., for $c > c^*$, the unknown function is determined by the requirement that ξ becomes independent of chain length (or molar mass M). Now, because R_0 is proportional to $M^{0.6}$ (see Eq. 1.4), there follows that $f(c/c^*)$ must be a power law of appropriate exponent, such that the M-dependence of c^* cancels the M-dependence of R_0. From $c^* \approx [\eta]^{-1} \propto M^{-0.8}$, the following *scaling law* for semidilute solutions in good solvents is therefore obtained:

$$\xi = R_0 \left(\frac{c}{c^*} \right)^{-0.75} \tag{1.15}$$

As mentioned earlier, all relevant quantities in semidilute solutions with good solvents will soon be obtained from the screening length. Also, all functional dependencies take the form of power laws, i.e., they obey scaling rules similar to that just derived for ξ. In particular the concentration dependence will always appear through the nondimensional ratio c/c^* or, equivalently, through the product $c[\eta]$.

The first quantity we now consider, which is relevant for estimating the viscosity, is the modulus G of the impermanent network that the semidilute

solution forms at values of c somewhat larger than c^*. Indeed, when each chain is in contact with many other chains all along its contour length (as it certainly does for $c \gg c^*$), the chains become *entangled* to one another. The bundle of entangled chains permeates space and is equivalent to one of the networks considered in the previous section. The network is temporary in nature because the chains are not permanently attached to one another and can slide one past another. Such sliding motions will in fact determine the relaxation time τ, which is to be calculated. For the moment, however, let us concentrate on the elastic modulus of this impermanent network.

Following Eq. (1.10), in order to calculate G we need to know the number ν of elastically active chains per unit volume of the network (i.e., of the semidilute solution in our case). We expect that each polymer chain, insofar as it experiences many contacts with other chains, will generally contain more than one elastically active chain segment. In fact, it is sensible to assume that one elastically active segment corresponds to some definite number of contacts. Hence, because there is one contact per blob, the number of active segments per unit volume is proportional to the number of blobs per unit volume $1/\xi^3$. The following scaling for G is then immediately obtained:

$$G \approx \frac{kT}{\xi^3} \propto c^{2.25} \tag{1.16}$$

The concentration dependence of the elastic modulus predicted by Eq. (1.16), i.e., a power law with an exponent slightly larger than 2, is well confirmed experimentally [13]. Also, because (for any given c) ξ is M-independent, G is predicted to be independent of M as well. The M-independent G value is called the "plateau" modulus and is observed by plotting either $G(t)$ vs. $\log t$ or $G'(\omega)$ vs. $\log \omega$, where $G(t)$ and $G'(\omega)$ are typical material functions of linear viscoelasticity [7]. They are obtained from experiments of stress relaxation following step deformations or from the frequency response of the material, respectively. In both cases (see Fig. 1.6), there is a "window" of either time or frequency in which G stays constant, and such a plateau value is molecular weight–independent.

To proceed with the other factor that (together with G) determines the viscosity, i.e., with the relaxation time τ, we first need to consider the diffusive motion of an entangled chain. Because chains cannot cross one another, the diffusive motion can only take place along the chain itself. Except for this longitudinal motion, the entangled chain can explore the surroundings only over a very limited distance. Conversely, by a sequence of diffusive steps along its own contour length, it can eventually move over long distances. The diffusive motion along the contour length was called *reptation* by de Gennes, as it reminds of the motion of the snakes [2]. The restriction in lateral motion owing to chain uncrossability was represented by Edwards [6] in terms of a *tube* constraining the chain all along its contour

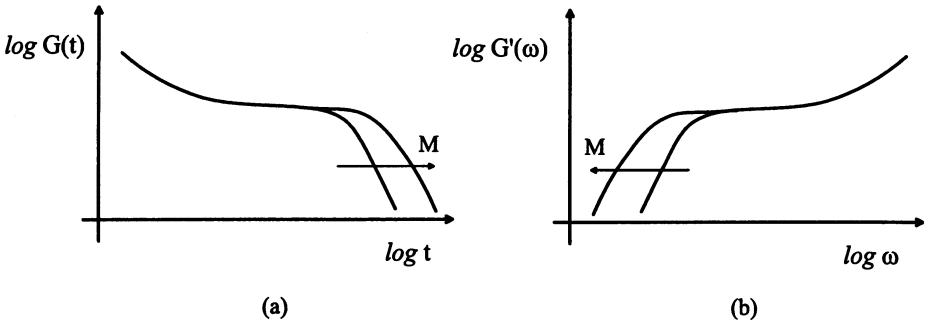

Figure 1.6 — (a) Shear modulus relaxation after a step deformation and (b) storage modulus G' as a function of frequency ω. In both cases there is a "plateau" region extending in length with increasing M; the plateau value itself is independent of M.

(see Fig. 1.7). The tube diameter is a measure of the short distance that the chain is able to explore in its lateral motion. In our semidilute solutions, the diameter of this constraining tube is expected to be somewhat larger, but not much larger, than ξ itself.

In order to estimate the diffusion coefficient D of the chain in its motion along the contour length we can resort to another famous Einstein formula, namely,

$$D = \frac{kT}{\zeta} \tag{1.17}$$

which links D to the friction coefficient. In our case, we must consider the friction coefficient of the whole chain ζ_{chain}. In its turn, ζ_{chain} can be

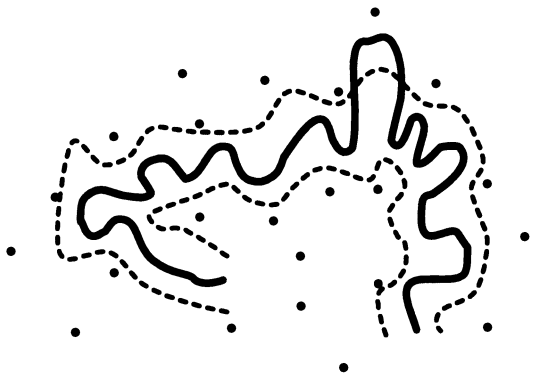

Figure 1.7 — A polymeric chain in a grid of topological obstacles made of other chains (the dots in the figure); each chain is then effectively confined in a tubelike region.

estimated as follows. The chain segment forming a single blob, taken by itself, would have a friction coefficient ζ_{blob} given by the Stokes expression (the blob behaves hydrodynamically as a sphere of size ξ)

$$\zeta_{\text{blob}} \approx \eta_s \xi \tag{1.18}$$

where η_s is, we recall, the solvent viscosity. On the other hand, the friction of the whole chain is obtained by summing up the contribution of the blobs forming that chain. Indeed, because of the polymer–polymer contacts, the hydrodynamic interactions are screened for distances larger than ξ. Hence the friction becomes *additive* over the blobs of the same chain. We may then write

$$\zeta_{\text{chain}} \approx N \eta_s \xi, \qquad D = kT/(N \eta_s \xi) \tag{1.19}$$

where N is the number of blobs per chain.

From D, which describes the diffusion of the chain along its own tube of constraints, the relaxation time τ of the impermanent network is obtained through the following argument. Consider a step deformation of the network. As a consequence of the deformation, the system becomes anisotropic and a stress arises. In order for the elastically active segments of a chain to relax the anisotropy, it is required that the chain diffuse along its tube of constraints. Indeed, in so doing, it will abandon the anisotropic tube and create a new isotropic one. This occurs because, in the longitudinal diffusion process (reptation), the advancing chain end is free to choose its direction randomly. If we call L the curvilinear length of the tube, we can estimate τ as the time required for the chain to diffuse longitudinally a distance L. Indeed, when such a time has elapsed, the whole chain (hence all its segments) will have renewed orientation and regained isotropy. We then obtain

$$\tau \approx \frac{L^2}{D} \approx \frac{\eta_s}{kT}(N\xi)^3 \tag{1.20}$$

where the last (approximate) equality makes use of Eq. (1.19) for D, as well as of $L \approx N\xi$.

To be precise, we should account for the fact that not all segments of the chain have the same relaxation time. Clearly, segments closer to chain ends will renew their orientation sooner than segments deeper inside. The exact treatment of reptation dynamics [2] shows, however, that Eq. (1.20) provides the dominant relaxation time. Up to 80% of the stress will relax according to τ, while the other 20% only will relax with faster modes. Further refinements of the basic theory are also required due to fluctuation in tube length L, as well as to account for constraint release (with regard to the test chain) brought about by reptation of the surrounding chains (so-called "double reptation"). Some of these refinements marginally alter the scaling laws (see below). Here we shall continue, however, with the basic simple treatment.

Let us combine the two factors that make up the viscosity. From Eq. (1.16) for G and Eq. (1.20) for τ, the formally simple result is obtained:

$$\eta = G\tau = \eta_s N^3 \tag{1.21}$$

The problem now becomes that of determining how N, the number of blobs per chain, scales with either M or c. Regarding the first scaling, the answer is immediate. At fixed c, the blob size ξ is fixed also; hence N must be proportional to M, and from Eq. (21) the following scaling for η is obtained:

$$\eta \propto M^3 \tag{1.22}$$

The dependence of η on c requires a little more work. We first need to calculate the number of chain monomers contained in a blob, called n_{blob}. Within a blob, the excluded volume interaction typical of good solvents is active; hence we may write (see Eq. (1.4)):

$$\xi \approx n_{\text{blob}}^{0.6} b \;\Rightarrow\; n_{\text{blob}} \approx (\xi/b)^{5/3} \tag{1.23}$$

Then, because the total number of monomers is n, we find

$$N = n/n_{\text{blob}} \approx n b^{5/3} \xi^{-5/3} \approx n b^{5/3} R_0^{-5/3} (c/c^*)^{5/4} \approx (c/c^*)^{5/4} \tag{1.24}$$

where we have used Eq. (1.23) for n_{blob}, then Eq. (1.15) for ξ, and finally Eq. (1.4) for R_0. In conclusion, Eq. (1.21) becomes

$$\eta \approx \eta_s (c/c^*)^{3.75} \tag{1.25}$$

Needles to say, Eq. (1.25) also contains the proportionality expressed by Eq. (1.22) because $c^* \approx [\eta]^{-1} \propto M^{-0.8}$.

Experiments show a dependence of η on M and c somewhat stronger than that predicted by Eq. (1.25). In particular the typical dependence of η on M is with a power somewhere between 3.3 and 3.5 instead of 3. We shall comment on this discrepancy soon. However, the experiments fully confirm the basic scaling insofar as data obtained for different values of c and M fall on a single curve if plotted vs. $c[\eta]$, i.e., vs. c/c^* [11].

The explanation for the discrepancy on the M^3 prediction was provided by Doi [4] and is based on the role played by fluctuations of the tube length, which were neglected in the basic theory. The argument is that the power of 3 would be reached asymptotically for very large M, i.e., when fluctuation becomes negligible. For all M values of practical interest, fluctuations are important, more so when M is smaller. They determine that the chain renews orientation at a faster rate than is predicted by reptation at fixed tube length L. The dependence on M is then more complex but essentially equivalent to a power law with an exponent of about 3.3.

With increasing polymer concentrations further complications arise because the friction is no longer only between polymer and solvent. Friction

between polymer segments becomes increasingly important as we go from semidilute solutions to concentrated solutions, all the way up to the neat polymer, i.e., to the polymer melt. For their importance in applications, in the following section we will briefly discuss polymer melts.

1.5 Polymer Melts

In polymer melts the only relevant variable (for a given chemistry of the chain) is, of course, the chain length or chain mass M. Polymer melts behave differently depending on M. At low M-values the molecules do not form a network. They behave "individually," and the viscosity grows moderately with increasing M. Above a critical value M_c, the behavior becomes that of an entangled network, and the viscosity starts growing with M much more steeply [7].

For $M > M_c$ the entangled network exhibits, as expected, a plateau modulus G independent of M. The plateau modulus of molten polymers typically falls in the range $0.1 \div 1.0\,\mathrm{MPa}$, depending on the "chemistry" of the chain. However, because the local interactions among chains should not directly contribute to the rubber-like modulus of the network, the "chemistry" should influence the modulus only indirectly through some basic chain properties. One of these basic properties is related to the chain statistics. In the section on the intrinsic viscosity we already mentioned that the statistics of the chain in the melt are ideal because the excluded volume interaction is screened. This implies (cf. Eq. (1.3)) that $\langle R^2 \rangle$ is proportional to M. Hence, the "chemistry" enters the chain statistics through the characteristic ratio $\langle R^2 \rangle / M$, which is independent of M. The other important parameter of a polymer melt influenced by the chain chemistry but independent of M is the mass density ρ, which specifies how much chain length can be packed in the unit volume. The "structure" of the temporary network formed by the entangled chains should therefore be determined only by these two parameters, ρ and $\langle R^2 \rangle / M$.

For what was said earlier, the plateau modulus G of a molten polymer is expected to depend on ρ and $\langle R^2 \rangle / M$. More specifically, because a rubber-like modulus is in any way proportional to kT (cf. Eq. (1.10)), we expect that

$$\frac{G}{kT} = f(\rho, \langle R^2 \rangle / M) \tag{1.26}$$

where f is some function. From here on, simple dimensional analysis provides the desired scaling law for the plateau modulus. Indeed, because G/kT is dimensionally a reciprocal volume, the mass should disappear from the relationship. Hence ρ and $\langle R^2 \rangle / M$ cannot appear separately

but only through their product $\rho\langle R^2\rangle/M$. Moreover, because the latter grouping defines a reciprocal length, we must have

$$\frac{G}{kT} \propto \left(\rho\frac{\langle R^2\rangle}{M}\right)^3 \tag{1.27}$$

which, to within a constant numerical factor, completely specifies the function f, i.e., the scaling of the plateau modulus of a polymer melt.

The scaling of Eq. (1.27) is well confirmed by experiments [8]. Minor deviations are probably due to energetic factors that were ignored in the preceding argument. From the same scaling, we also obtain the critical molecular mass M_c, which marks the onset of the entangled behavior. Indeed, because from Eq. (1.10) $G = \nu kT$, where ν is the number of elastically active chains per unit volume, we may also write Eq. (1.10) for our case as

$$G = \aleph\frac{\rho kT}{M_e} \tag{1.28}$$

where M_e is the molecular mass of the elastically active chain, i.e., of the chain segment between consecutive entanglements. Comparison of Eqs. (1.27) and (1.28) shows that

$$M_e \propto \rho^{-2}\left(\langle R^2\rangle/M\right)^{-3} \tag{1.29}$$

The scaling defined by Eq. (1.29) for M_e obviously applies to M_c as well. This concludes the scaling laws of the M-independent quantities.

Regarding the other factor that determines the viscosity, i.e., the relaxation time τ, the situation for $M > M_c$ is similar to that already discussed for the entangled semidilute solutions. The chains must reptate to relax the stress. Hence, τ, and consequently the viscosity η, is predicted to scale with M^3 (see Eq. (1.22)) or, accounting for fluctuations, approximately with $M^{3.4}$. Fig. 1.8 shows a typical log–log plot of melt viscosity vs. M. Above M_c the slope is about 3.4, while below M_c the slope is 1. For $M < M_c$ the network of entangled chains no longer exists, and the observed behavior is well described by the classical Rouse model [5, 14]. In such a model the chain dynamics is simply that of a chain in a viscous solvent *without* hydrodynamic interactions between chain segments. Indeed, in the melt, hydrodynamic interactions (just as excluded volume interactions) are screened at all length scales. Because of this screening effect the friction is additive along the chain. Hence the melt viscosity comes out proportional to M in the Rouse regime. This behavior should be contrasted with that in dilute solutions where the intrinsic viscosity of a flexible polymer always comes out *less* than proportional to M because of the hydrodynamic interactions.

The diagram in Fig. 1.8 is "universal," i.e., it remains the same for all flexible polymers independent of their specific chemistry. The horizontal scaling in Fig. 1.8 is dictated by M_c, i.e., by Eq. (1.29). The vertical scaling

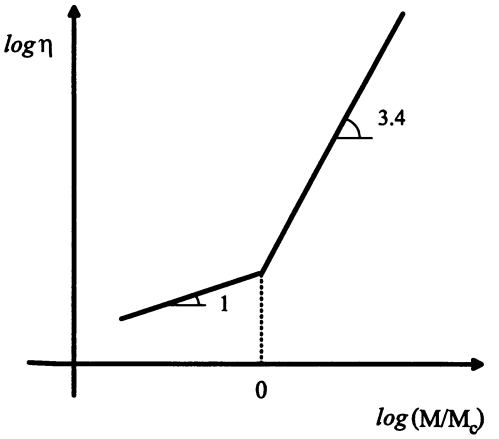

Figure 1.8 — Typical plot of melt viscosity as a function of molecular mass.

cannot be anticipated from theory because it involves a basic friction coefficient (between monomers of the polymeric chains) that is determined by the chemistry in a complex way (cf. the discussion in the Introduction for the case of small molecules). However, a single experimental value of the viscosity (either in the Rouse regime at low M or in the entangled regime at high M) is sufficient to set the vertical scale for any specific chain chemistry.

1.6 Localized Interactions

In this last section we will briefly examine some special effects due to localized interactions. A typical example of such interactions is provided by polymeric chains to which segments have been added (two or more segments per chain) having a "different" chemistry. These segments are called *sticky points* because for energetic reasons they like to stick together to form aggregates. Examples are essentially of two types. In one case, the polymer is water soluble (hydrophilic) and the special segments are hydrophobic. Thus in an aqueous solution the hydrophobic segments want to segregate from water, forming clusters. The other case is somehow opposite: The polymer is insoluble in water and sticky points are strongly polar or even ionic (like in the "ionomers"). In either case, above the critical concentration c^*, the polymeric chains will form a network in which the junctions are aggregates of the sticky points (see Fig. 1.9).

The "stickiness" is related to the energy by which the segments are held together in the aggregates. This energy E must be larger than thermal

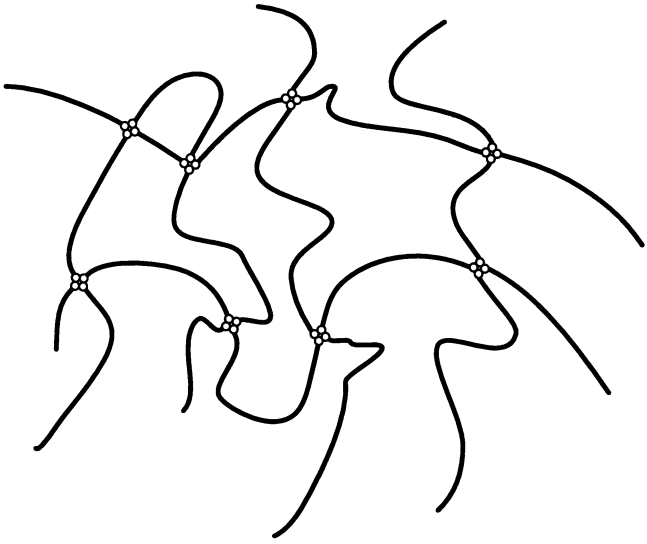

Figure 1.9 — A network of "telechelic" chains; the chains carry sticky points at the ends only (the empty circles). The sticky points cluster together to form the nodes of the network.

energy kT, but not much larger. Indeed, if E is of order kT, thermal motions do not allow aggregates to be stable; the points are not sticky enough, and the chains interact in the normal way, i.e., by friction only. At the opposite extreme, if $E \gg kT$, the aggregation process becomes irreversible; the junctions, once formed, are permanent, and the system becomes a solid (a gel). In a suitable window of E/kT values the stickiness is such that the network is impermanent (the chains can detach by thermal motion, if not too frequently) and the behavior remains liquid-like.

As always, the viscosity of the system can be calculated through Eq. (1.11). The new aspect here is that the relaxation time τ is no longer related to a friction process; rather, it is determined by the stickiness of the junction, i.e., by E/kT. More specifically, calling ω_0 the basic frequency (of order 10^8 s^{-1}) of Brownian motion (which "attempts" to detach the sticky point from the aggregate), the frequency ω of successful detachments is related to ω_0, through the Boltzmann factor:

$$\omega = \omega_0 \exp(-E/kT) \tag{1.30}$$

Clearly ω is much less than ω_0 if E/kT is of order 10 or more.

If the relaxation time of the chain due to friction is much less than $1/\omega$, i.e., if the chain without sticky points would relax faster than $1/\omega$, then detachment becomes the controlling mechanism for relaxation. The relaxation time τ of the impermanent network is then just equal to $1/\omega$ and

is entirely determined by the energy E of the sticky points. In some cases the energy E can itself be easily tuned. For example, during preparation of the polymer, E can be modified by changing the length of the special segment which provides the localized interaction [1]. Alternatively, for a fixed chemistry, E can be altered by adding to the solution trace amounts of a solvent that selectively goes inside the aggregates.

The possible changes in the relaxation time mentioned earlier can be used to modify the viscosity even by orders of magnitude. In particular, we can obtain a very large viscosity with a very small mass of polymer. To this end, it is sufficient that the network is made up of very few chains ($c \approx c^*$) of large M (c^* small) carrying at their extremities sticky points with a large E value (τ large). Thus, although the elastic modulus ($\approx c^* kT/M$) will be very small, the viscosity will remain as large as we wish. This example shows again the enormous efficiency of polymers as viscosizers. It also shows the possibility of gaining good control over the viscosity and more generally over the rheology, of polymeric liquids.

References

1. Annable, T., Buscall, R., Ettelaie, R., and Whittlestone, D., The rheology of solutions of associating polymers: Comparison of experimental behavior with transient network theory, *J. Rheol.*, **37**, 695 (1993).
2. de Gennes, P.G., Reptation of a polymer chain in the presence of fixed obstacles, *J. Chem. Phys.*, **55**, 572 (1971).
3. de Gennes, P.G., *Scaling Concepts in Polymer Physics*, Cornell University Press, Ithaca, New York (1979).
4. Doi, M., Explanation for the 3.4-power law for viscosity of polymeric liquids on the basis of the tube model, *J. Polym. Sci.: Polym. Phys. Ed.*, **21**, 667 (1983).
5. Doi, M., and Edwards, S.F., *The Theory of Polymer Dynamics*, Clarendon Press, Oxford (1986).
6. Edwards, S.F., The statistical mechanics of polymerised materials, *Proc. Phys. Soc. (London)*, **92**, 9 (1967).
7. Ferry, J.D., *Viscoelastic Properties of Polymers*, Wiley, New York (1980).
8. Fetters, L.J., Lohse, D.J., Richter, D., Witten, T.A., and Zirkel, A., Connection between polymer molecular weight, density, chain dimensions, and melt viscoelastic properties, *Macromolecules*, **27**, 4639 (1994).

9. Flory, P.J., *Principles of Polymer Chemistry*, Cornell University Press, Ithaca, New York (1953).
10. Happel, J., and Brenner, H., *Low Reynolds Number Hydrodynamics*, Prentice Hall, Englewood Cliffs, New Jersey (1965).
11. Kulicke, W.M., and Kniewske, R., The shear viscosity dependence on concentration, molecular weight, and shear rate of polystyrene, *Rheol. Acta*, **23**, 75 (1984).
12. Larson, R., Perkins, T., Smith, D., and Chu, S., Hydrodynamics of a DNA molecule in a flow field, *Phys. Rev. E*, **55**, 1794 (1997).
13. Pearson, D.S., Recent advances in the molecular aspects of polymer viscoelasticity, *Rubber Chem. Technol.*, **60**, 439 (1987).
14. Rouse, P.E., A theory of the linear viscoelastic properties of dilute solutions of coiling polymers, *J. Chem. Phys.*, **21**, 1272 (1953).
15. Treloar, L.R.G., *The Physics of Rubber Elasticity*, Clarendon Press, Oxford (1975).

2

Sedimentation in Coal-Water Slurry Pipelining

FABIO ROSSO

Universitá di Firenze
Dipartimento di Matematica "U. Dini"
Firenze, Italy

ABSTRACT. In this chapter we present an overview of recent investigations on the problem of sedimentation related to the pipelining of a coal-water slurry. The two main aspects of the problem are the determination of the sedimentation velocity and the understanding and modeling of the dynamics of the sedimentation bed that accumulates on the bottom of the pipe. The analysis is carried out using a combination of suggestions dictated by experimental evidence and suitable mathematical techniques. The result is a model that appears to be both easily manageable and flexible. Predictions of the model are compared with experiments finding a remarkable agreement with the available data.

2.1 Slurry Handling and Pipeline Transport: A Brief Outlook on Hydrotransport

The idea of transporting solids using a carrier fluid is rather old and intuitive. Indeed according to Apollodorus and Pausanias (first century B.C.) this transportation technique, now known as *hydrotransport*, was first used by Herakles, who in one day cleaned up thirty years' worth of accumulated filth left by thousands of cattle in King Augeas's stables by diverting two rivers to form an open-channel hydrotransport system [42]. Despite the mythological nature of this tale, known as Herakles' fifth task, any kind of

A. Fasano (ed.), *Complex Flows in Industrial Processes*

solid can in principle be moved from one place to another that is hundreds of miles away using a liquid as the transportation tool.

The modern stage of slurry pipeline technology began, more or less, forty years ago. A *slurry* is essentially a suspension of solid particles in a carrier fluid; we are interested in these suspensions because by using an appropriate technology, they can be pipelined very far from their production site. Generally the required technology depends on the chemical and physical nature of the suspended particles. This area of investigation is so important that scientists and industries involved in this field meet almost every year at highly specialized international meetings such as the Hydrotransport Conferences (there have been thirteen through 1999) or the International Conferences on Slurry Technology. The underlying idea is that hydrotransport may, in many cases, be an attractive alternative to other modes of transport (rail, ships, etc.). It also has several advantages, such as a moderate environmental impact, relatively little infrastructure work needed, and possible low operation and maintenance costs.

For a long time, especially in the early stage of the development of this technology, it was generally thought that the only operational regime to prevent particle settling was the turbulent one; indeed the primary duty when designing a slurry pipeline is to ensure that it will not be blocked because of sediment accumulation on the pipe lower wall. However, the cost of maintaining a turbulent regime must also be considered. For this reason recent studies on slurries have addressed the possibility of controling settling within the laminar regime (which requires less pumping power and is therefore less expensive). If the sediment buildup process could be modeled accurately, then designers would be able to predict the conditions that lead to blockage, and thereby design systems so that the possibility of a blockage is avoided.

The engineering approach to the problem of designing a slurry pipeline is a remarkable combination of basic fluid mechanics and chemical concepts, phenomenological laws, empirical laws, and intuitions guided by specific pilot plant data. The blockage problem is certainly the most focused but many others are related to it; the interested reader may look at the papers published on this subject in the proceedings of the last hydrotransport conferences (see the References). However, it is not easy for people not specifically trained in this area to read those contributions and find, when looking at a specific problem, a common point of view among different writers. For these reasons, we try to present an approach to the problem of sediment buildup and evolution of the growing bed that is, to a reasonable extent, as self-consistent and readable as possible, even for people not expert in this area.

In this chapter we report the main results of a research work on the problem of sedimentation in the pipelining of *concentrated* coal-water slurry (CWS). This subject has involved our group in industrial mathematics at

the University of Florence for several years. The problem was researched in cooperation with the engineering team of Snamprogetti, an Italian company that is well-known among those designing and selling technology for fuel energy production and transportation. Snamprogetti has fully investigated all problems related to CWS technology (see Terenzi et al. [36]) both at their pilot plant in Fano (Italy) and in the field, using an industrially operating pipeline.[1] The pilot plant is equipped with sophisticated measuring devices (for example, a gamma-densimeter) that provide direct evidence and sufficiently clear data on the growth of the bed with time.

Although the model and the approach presented here are dependent on the particular type of slurry under investigation, we believe that the basic ideas can be easily adapted to other similar physical systems.

The CWS mixture considered here enters into the category of *concentrated* slurries because it consists of about 70% (by weight) ground coal such that the size distribution has two peaks around 10 μm and 100 μm. The remaining 30% is water with a small percentage (0.5%) of chemical additive needed to fluidize the suspension. This fluid is perfectly stable *at rest* even after years, i.e., particle concentration remains constant in time everywhere. This stability is completely ascribed to the action of the chemical agent; indeed, additive molecules, being highly polar, coat the coal particles with positive charges so that mutual repulsive forces prevent natural sedimentation.

The rheological behavior of concentrated CWS at low shear rates can be reasonably described by the Bingham model, that is (in laminar flows with simple geometry),

$$(\tau - \tau_0)_+ = \eta_B \dot{\gamma}, \tag{2.1}$$

where τ, τ_0, η_B, and $\dot{\gamma}$ denote the shear stress, yield stress, plastic viscosity and shear rate, respectively, and $(\bullet)_+$ means the positive part of $(\bullet)$. Of course, more complicated models can be used but (2.1) is sufficient for our purposes.

When a CWS is stirred in a vessel or pumped through a pipeline, the action of shear dramatically modifies this picture through a phenomenon called *rheological degradation*, which has also been deeply investigated and fully explained (see, for example, ([9], [10], [11], [15], [21], [22], [23], [24], [26], [32]). However, the time scale of this phenomenon is many orders of magnitude larger than that of sedimentation, so that if we focus on the latter problem, the time dependency of rheological parameters can be neglected. Therefore we can consider a CWS as a time-independent Bingham fluid.

[1] Snamprogetti built a 250-Km-long operating pipeline connecting Belovo to Novosibinsk (Siberia).

The solid fraction does not generally consist only of *pure* coal; even after a suitable treatment (*beneficiation*), ground coal from the mill hardly contains less than about 6% of other micronized minerals and steel residues due to beneficiation itself.

Impurities generally have a size comparable to or higher than that of the top size of coal particles; the inner structure of a CWS provided by the residual adhesion forces among the coal particles (which is responsible for the yield stress) is sufficient to prevent settling at rest. This is no longer true when a CWS experiences a shear rate, as if it is stirred in a viscometer or pumped in a pipeline. Indeed while the tendency of the pure coal particles to settle is prevented by the action of the chemical stabilizer, this is not true for impurities that, having a different chemical structure, do not react with the additive. Therefore the settling of these particles cannot be controlled, leading to a sediment buildup at the bottom of the pipe when the CWS is pipelined at long distances. This phenomenon can also be observed if the CWS is placed in a rotating bob-cup viscometer. In the pipe flow the reduction of the hydraulic diameter due to the sediment buildup leads either to increase the pressure gradient (assuming that we can) to maintain the discharge or to decrease the latter if we cannot. Both cases are either unsafe or economically disadvantageous. Therefore what is needed is a model to predict the evolution of the growing bed in order to choose the optimal discharge and plan the periodical (unavoidable) shutdown of the pumps and cleaning of the first portion of the pipeline (the only one interesting to the settling phenomenon).

The aim of this chapter is to describe the investigative work and results about the described problem conducted at the facilities of Snamprogetti.

2.2 Some General Facts about Sedimentation

Consider a single spherical rigid particle settling with constant velocity $\mathbf{v}_s$ in a Newtonian viscous liquid at rest that extends to infinity in all directions. The uniform motion of the falling particle results from the equilibrium of three forces: the particle's own weight $\frac{4}{3}\pi\delta^3\rho_s\mathbf{g}$, Archimedes' lifting force $-\frac{4}{3}\pi\delta^3\rho_l\mathbf{g}$, and the viscous force exerted by the fluid on the sphere. For small Reynolds numbers (say $\mathcal{R}e \ll 1$) Stokes [35] proved that the viscous force exerted by the fluid (*drag* force) is parallel (and opposite in direction) to $\mathbf{v}_s$ and of magnitude $6\pi\delta\eta v_s$. Then a force balance immediately yields the well-known formula

$$v_s = \frac{2g(\rho_s - \rho_l)}{9\eta}\delta^2 \tag{2.2}$$

It is common practice to express the forces exerted on moving bodies by the fluid in terms of a dimensionless parameter C_D called *drag coefficient*

obtained by dividing the drag force $6\pi\delta\eta v_s$ by $(1/2)\rho_s v_s^2$ and by the area of the body projected on a plane normal to $\mathbf{v}_s$; thus the drag coefficient is here

$$C_D = \frac{24}{\mathcal{R}e}, \quad \text{with } \mathcal{R}e = \frac{2\delta v_s \rho_s}{\eta} \tag{2.3}$$

For a particle of sand falling through water at room temperature, the hypothesis $\mathcal{R}e \ll 1$ is satisfied provided that $\delta \ll 0.006$ cm. From the mathematical point of view, the Stokes hypothesis ($\mathcal{R}e \ll 1$) is equivalent to a suitable linear approximation of the *nonlinear* Navier-Stokes equation. This approximation (and thus the Stokes solution) contains various drawbacks and physical inconsistencies (the most famous one is probably the so-called Stokes paradox (see, for example, [25]). Oseen ([30],[31]) proposed a different linearization that yields, instead of (2.3), the following expression

$$C_D = \frac{24}{\mathcal{R}e}\left(1 + \frac{3}{16}\mathcal{R}e\right) \tag{2.4}$$

However, in many cases of practical interest, neither (2.3) nor (2.4) is in agreement with measured values. Based on experimental evidence, a variety of ad hoc formulas for the terminal velocity of the particle have been suggested; a relatively recent state of the art can be found in [13] and [14]. Research in this field, based almost exclusively on sophisticated experiments and numerical simulations, is still very active.

In a typical sedimentation problem we have a situation rather different from that considered theoretically; the host fluid may be *non-Newtonian* and sheared, particle's may settle within a dense population of similar particles, particles' shape and volume may be irregular and randomly distributed, the particle surface may change its electrical charge distribution interacting with chemical additives in the host fluid, wall effects on falling particles may not be negligible, and so on.

Cases in which the host fluid is non-Newtonian have been extensively studied in recent years. Several theoretical and/or experimental approaches have been used, and suggestions have been made to correct the correlation (2.3) for the different rheological behaviors. For fluids without yield stress (in particular, the power law fluids), one can refer to Acharya et al. [1], Leal [27], and the review papers of Chhabra ([12], [13]), where a rather complete bibliography can be found.

For Bingham fluids the situation is more complicated; here we give a short account of the previous investigation, referring to [13] for further information and details.

First the yield stress τ_0 can prevent settling of particles up to a critical radius which, if $\Delta\rho := \rho_s - \rho_l$, is given by

$$\delta_0 = \alpha\frac{\tau_0}{g\Delta\rho} \tag{2.5}$$

as can be seen, simply assuming that the force due to the yield stress is proportional to it and to the area of the spherical particle.

Concerning the numerical value of the proportionality constant α, there is no agreement among authors; α ranges from 1.5 to 10. These differences, however, can be mainly ascribed to possible different (experimentally very delicate) determinations of τ_0.

The study of the motion of a spherical particle in a Bingham plastic fluid has also been investigated from both a theoretical and an experimental point of view; we recall the papers by Tyabin [38] and Andres [3], where the drag force is expressed as

$$F_D = \alpha\delta^2\tau_0 + \beta\eta_B v_s\delta \tag{2.6}$$

where the coefficients α and β are either experimentally fitted or theoretically calculated in terms of the quantity $k := (3\tau_0/(\delta g\Delta\rho))^{1/2}$. In subsequent chapters a correlation between C_D and a modified Reynolds number was outlined (the interested reader may consult the papers of Ansley and Smith [4] and Dedegil [19]). Other interesting contributions on this subject are due to [39], [40], and [41].

A very good fit with these experimental results was obtained by Beris et al. [6] integrating the equation of motion by finite elements, thus also recovering the lower and upper estimates previously obtained by Yoshioka et al. [43].

In all the papers listed here, the motion of a single sphere with a sufficiently large radius in an unsheared environment was considered. In the paper by Thomas [37], an experiment of sedimentation in a sheared fluid was described.

As we have seen, the general picture concerning sedimentation is rather involved, and there is no conclusive theory flexible enough to be adapted to a variety of settling phenomena in pipeline flows.

In [15] and [17] we presented some new ideas about the problem of determining v_s in a *sheared* fluid (not necessarily Newtonian), when the particle belongs to a large settling population. Of course in a sheared environment, the particle velocity is now expected to depend on the local value of the shear rate. The novelty of our approach consists mainly in looking at the problem of finding the *effective viscosity* experienced by a population $\mathcal{P}$ of particles as an *inverse* problem.

A possible alternative approach to the problem of finding the correct form of v_s could be the following: to collect data (generally a discrete set) from some suitably designed experiment on the base of some formula of type

$$data = \mathcal{F}(v_s) \tag{2.7}$$

where $\mathcal{F}$ is determined by geometry and type of experiment. If we don't make any a priori assumptions about the form of v_s, (2.7) is an *inverse problem with discrete data* to which we could apply the technique

developed by Bertero, De Mol, and Pike some years ago (see [7] and [8]). In the appendix, we give a short presentation of this functional method. We tested this approach against available experimental data and found encouraging conclusions. However, the method is specifically designed for laboratory tests and cannot be directly applied to a Bingham flow in a pipeline. Nevertheless, we can derive useful indications to deduce the settling velocity of a particle as a function of the radial coordinate of the pipe, if the flow is stationary.

In the next section we present the derivation of v_s with particular reference to CWS.

2.3 Sedimentation in a CWS Sheared in a Rotating Viscometer

The CWS used in the experiments considered to collect our data was prepared with a Polish coal according to the SP REOCARB process (a Snamprogetti patent).[2]

The geometry we considered is that of a rotational bob-cup viscometer (designed on purpose with a widened gap), where the settling of particles is transverse to the direction of shearing (exactly as in the pipeline flow). The viscometer was filled up with CWS in which a population $\mathcal{P}$ of sand particles with density $\rho_s > \rho_{CWS}$ has been initially homogeneously dispersed.

Then we pointed our attention to a cross-sectional cell C_z of the viscometer of thickness h, with top and bottom bases placed, respectively, at $z-h$ and z, the z-axis being directed as the gravity vector $\mathbf{g}$. The quantity to be measured is the net mass variation in C_z due to the settling of $\mathcal{P}$.

Let us first notice that there may be a fraction of $\mathcal{P}$ that does not settle, depending on the steady laminar shearing motion generated by a uniform rotation of the inner cylinder. This circumstance has to be ascribed to the internal structure of the CWS (responsible for the yield stress), which is partially or totally modified by the shearing conditions. Indeed in Bingham fluids at rest the yield stress may be able to sustain suspended particles (see, for example, [36]).

For a fluid in laminar motion in a rotational viscometer, $\dot{\gamma}$ denotes the absolute value of the only significant component $\frac{du}{dr}$ (with $\mathbf{u} = (0, u(r), 0)$) of the strain rate tensor.

We *do not postulate* the existence of a relationship of the type (2.5) nor do we enter the debate about the dimension and shape of the *unsheared envelope* surrounding the particles hypothized by some authors (see [2],[4],[6],[14] for a review of this topic).

[2] All laboratory experiments concerning the settling of particles in a rotating viscometer were performed and monitored by Snamprogetti.

Better references for experimental details concerning the theory we are going to illustrate are [15] and [36]. We confine ourselves to reporting only the main conclusions.

In a Bingham plastic there can be, in principle, a fraction of $\mathcal{P}$ that does not settle, depending on the particle size, τ_0, and $\dot{\gamma}$. If we call δ_0 the critical value of δ below which particles do not settle, the *critical radius–shear rate* curve can be evaluated from experimental data by measuring the fraction of $\mathcal{P}$ that remains in the upper cell of observation at the latest shearing time. The function $\delta_0(\dot{\gamma})$ can be determined using the law

$$\mathcal{M}_\infty = \mathcal{M}_0 \frac{\displaystyle\int_0^{\delta_0(\dot{\gamma})} \Omega(\delta)\, d\delta}{\displaystyle\int_0^{\infty} \Omega(\delta)\, d\delta} \tag{2.8}$$

where $\mathcal{M}_\infty$ is the mass of particles retained in C_1 (the highest observation cell) for $t \to \infty$, $\Omega(\delta)$ is the particle radius distribution function per unit mass of $\mathcal{P}$, and $\mathcal{M}_0$ is the mass of particles present in C_1 at $t = 0$.

Dimensional analysis shows that particles starting with zero velocity reach the stationary settling regime almost instantaneously. Thus each cell C_z will experience an emptying wave starting from the moment in which the heaviest particle, which left the level $z = 0$ at $t = 0$, has reached the level $z - h$.

The settling velocity of a particle of radius δ is assumed to be of the form

$$v_s(\alpha; \delta, \delta_0) = \alpha f(\delta, \delta_0)$$

where $f(\delta, \delta_0)$ is an increasing function of δ $(\delta \geq \delta_0)$, such that $f(\delta_0, \delta_0) = 0$, and the parameter α has to be determined as a function of $\dot{\gamma}$.

In the spirit of Stokes' formula (2.2), we can introduce an effective viscosity for sedimentation:

$$\eta_{eff} := \frac{1}{\alpha}$$

In the classical Newtonian case we would have $\delta_0 = 0$, $f(\delta) = \delta^2$, and η_{eff} is just, up to a proportionality constant, the fluid bulk viscosity η.

As far as the choice of the function f is concerned, we follow Dedegil [19], who proposed

$$f(\delta, \delta_0) = \delta(\delta - \delta_0)_+ \tag{2.9}$$

however we think of δ_0 as given by the experimental formula (2.8), better than (2.5).

Via an elementary mass balance it is easy to see that the mass variation experienced by C_z is given explicitly by

$$\mathcal{M}(\alpha; t, \dot{\gamma}) = \mathcal{M}_0 + \rho_s \Sigma \mathcal{K} \int_{\delta_0}^{\infty} \Omega(\delta) \Phi[v_s(\delta); t] \, d\delta \tag{2.10}$$

where Σ is the cross-sectional area of C_z, $\mathcal{K}$ is the volume fraction of $\mathcal{P}$ to the mixture (CWS plus $\mathcal{P}$)[3], and

$$\Phi[v_s(\delta); t] = \min\{v_s(\delta)t, z - h\} - \min\{v_s(\delta)t, z\} \tag{2.11}$$

For every cell C and every fixed pair *shear rate* $\dot{\gamma}$ – *shearing time* t, the left-hand side of (2.10) is a number given by the experimental data, and the right-hand side of (2.10) is just an implicit function of α. Solving such equations numerically we obtain the corresponding values of the parameter α. We expect, within the limits of the experimental errors, that such a parameter α does not depend on the cell of observation or on the shearing time t. Therefore we can define a function $\eta_{eff} = \eta(\dot{\gamma})$. Using equation (2.9), we can compare the experimental data with the emptying wave (2.10), and we obtain the corresponding values of α as a function of $\dot{\gamma}$ (see Figure 2.1). In all experiments done at the Snamprogetti

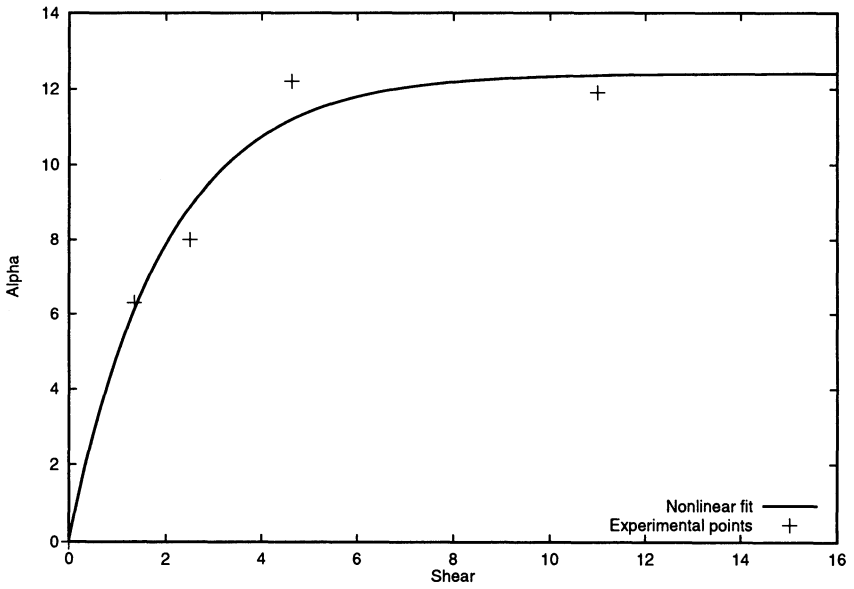

Figure 2.1 — Experimentally determined values of $\alpha(\dot{\gamma})$ for $\dot{\gamma} = \{0.001, 1.35, 2.51, 4.64, 11.64\}$ in S^{-1}; the solid line is the graph of $12.4103 - 12.3487e^{-x/2}$, a nonlinear fit of these data via the least square method.

[3] By definition $\mathcal{K} = \frac{4\pi}{3} \int_0^{\infty} \delta^3 N(\delta) \, d\delta$ where N denotes the size distribution function of $\mathcal{P}$ per unit volume of mixture ($\mathcal{P} + CWS$). Therefore $N(\delta) = \rho_s \mathcal{K} \Omega(\delta)$.

laboratories, $\delta_0(\dot{\gamma})$ turned out to be practically zero. Therefore we definitely set $f(\delta) = \delta^2$, and consequently

$$v_s(\dot{\gamma}, \delta) = \alpha(\dot{\gamma})\delta^2 \tag{2.12}$$

The knowledge of the function $\alpha(\dot{\gamma})$ is crucial to develop the model for the evolution of the sedimentation bed in a pipeline, which will be presented in the next section.

2.4 Buildup and Evolution of the Sedimentation Bed in a Pipeline

The argument of this section is largely based on the ideas presented in [16], [20], [28], and [29]. Let us first specify the geometry (see Figure 2.2) and symbols.

If $\frac{dp}{dx}$ denotes the constant pressure gradient (< 0) and $V_x(r)$ the velocity profile of the main flow, $\dot{\gamma} = \dot{\gamma}(r) = |\frac{dV_x}{dr}|$ is the shear rate; as we said in Section 2.1 the CWS behaves as a Bingham fluid, so we still assume $(\tau - \tau_0)_+ = \eta_B \dot{\gamma}$. Then, by coupling the Navier-Stokes equations with boundary conditions, one easily gets

$$V_x(r) = \begin{cases} -\dfrac{R^2}{4\eta_B}\dfrac{dp}{dx}\left(1 - \dfrac{r^2}{R^2}\right) - \dfrac{\tau_0 R}{\eta_B}\left(1 - \dfrac{r}{R}\right), & \text{for } r \geq \hat{R} \\ -\dfrac{1}{4\eta_B}\dfrac{dp}{dx}(R - \hat{R}), & \text{for } r \leq \hat{R} \end{cases} \tag{2.13}$$

where $r = \hat{R}$ is the interface bounding the rigid core. The momentum balance equation implies $\tau = \frac{r}{2}|\frac{dp}{dx}|$, so that

$$\hat{R} = \frac{2\tau_0}{|dp/dx|} \tag{2.14}$$

Moreover,

$$\dot{\gamma}(r) = \frac{1}{2\eta_B}|\frac{dp}{dx}|(r - \hat{R})_+ \tag{2.15}$$

A key assumption of the current model is that the sediment thickness h is sufficiently small compared to the pipe radius R so that the flow geometry will never be significantly affected by the sedimentation bed growing at the bottom of the pipe. Bearing in mind that for values of h close to 2% of the pipe diameter a precautional shutdown and cleaning operation is mandatory, the above assumption does not sound as a limitation.

The trajectory of a particle $P = P(\delta, \rho_s, [0, y_0, z_0])$ of radius δ and density ρ_s entering the pipe at the initial position $(0, y_0, z_0)$ is fully described

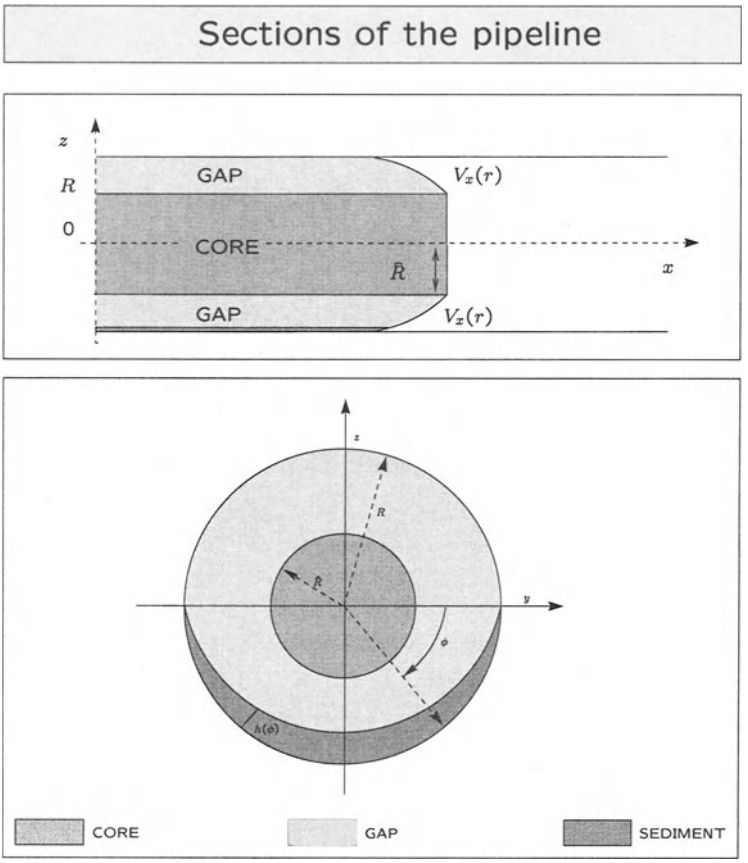

Figure 2.2 — Longitudinal (top) and transversal (bottom) cross sections of the pipe; the function $h(x,t,\phi)$ describes the bed profile (the indicated profile is only for illustration purposes).

by the system

$$\begin{cases} \dot{x} = V_x(r) \\ \dot{z} = -v_s(\delta, r) \\ r = \sqrt{z^2 + y_0^2} \end{cases} \tag{2.16}$$

Recalling the analysis of Section 3, we *assume* the settling velocity v_s to be $v_s(\delta, r) = \alpha(\dot{\gamma}(r))\delta^2$. The function $\alpha(\dot{\gamma})$, determined experimentally,[4] is that shown in Figure 2.1.

[4] We have a numerical code that gives $\alpha(\dot{\gamma})$ on the basis of laboratory tests in which the settling phenomenon is suitably monitored in a bob-cup viscometer, as described in Section 2.3.

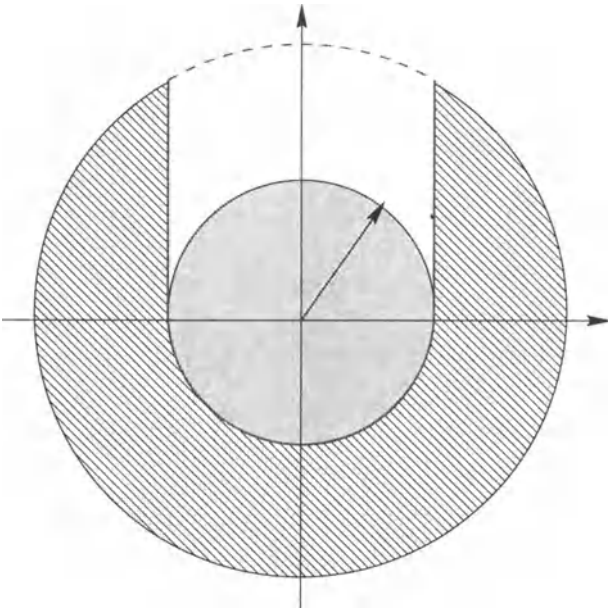

Figure 2.3 — Transverse cross section of the pipe with contributing and noncontributing regions to the dynamics of the bed. In the darker central region particles do not settle since $\dot{\gamma} = 0$, while in the white region above they settle but never reach the bed; only particles settling in the shaded region contribute to the growing of the bed.

It is evident from the system just described that particle motion remains confined in the vertical plane $y = y_0$. Moreover experiments definitely show that $\alpha(0) = 0$ and $\dot{\alpha} \geq 0$. As a consequence, only particles coming into the pipe through the gray-shaded region shown in Figure 2.3 contribute to the growing sediment.

Any particle P coming in through the gray-shaded region of the initial cross section $\{x = 0\}$ ends its trajectory at the point $(x^\star, y_0, z^\star)$ defined via

$$\begin{cases} z^\star = -\sqrt{R^2 - y_0^2} \\ x^\star = \displaystyle\int_z^{z_0} \frac{V_x(\tilde{r})}{v_s(\tilde{r}, \delta)}\, d\tilde{z} \\ \qquad \text{with } \tilde{r} = \sqrt{\tilde{z}^2 + y_0^2} \end{cases} \tag{2.17}$$

From (2.17) it can easily be proved that, for any fixed $x^\star$, the locus $\Gamma(x^\star, \delta)$ of points on $\{x = 0\}$ formed by those particles with radius δ, ending their

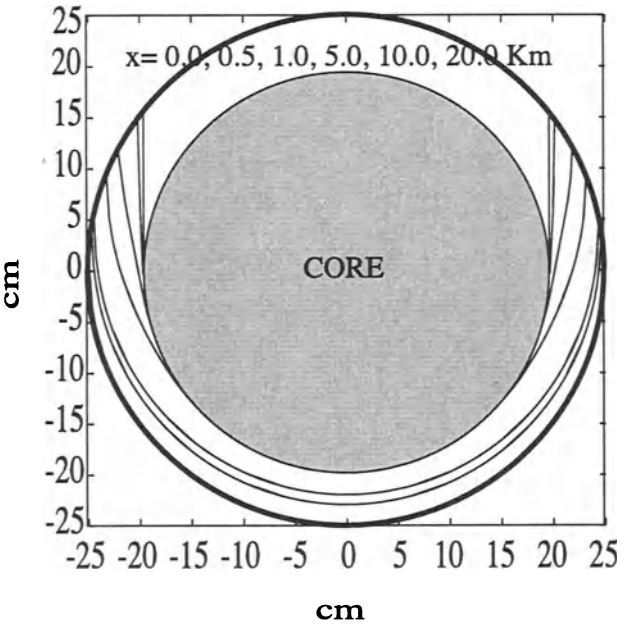

Figure 2.4 — Some $\Gamma(x^\star, \delta)$ graphs for $Q = 250$ m^3/h, $\delta = 0.0067$ cm; the slopes of the U-shaped curves increase with $x^\star$. The steepest U-shaped curve corresponds to $x^\star = +\infty$.

trajectories on the pipe wall at $x = x^\star$, is actually *a graph* (see Fig. 2.4), which we denote by

$$z_0 = \mathcal{Z}(y_0; x^\star, \delta)$$

The settling rate per unit length at distance x from the initial cross section due to particles with radii between δ and $\delta + d\delta$ is given by

$$S(x;\delta)\,d\delta = \frac{4}{3}\pi\delta^3\rho_s N(\delta)\,d\delta \int_{-y_M}^{+y_M} v_s(\sqrt{y_0^2 + (\mathcal{Z})^2}, \delta)\,dy_0 \qquad (2.18)$$

where $\mathcal{Z} = \mathcal{Z}(y_0; x, \delta)$, $N(\delta)\,d\delta$ is the number of settling particles with radii between δ and $\delta + d\delta$ per unit volume of mixture $(\mathcal{P} + CWS)$, and the endpoints $\pm y_M$ of $\Gamma(x, \delta)$ are implicitly defined by

$$y_M^2(x,\delta) + \mathcal{Z}^2(x^\star, y_M(x,\delta)) = R^2$$

Because N vanishes outside $[\delta_{\min}, \delta_{\max}]$, the overall settling rate (per unit length of the pipeline) will be given by

$$S_T(x) = \int_{\delta_m}^{\delta_M} S(x;\delta)\,d\delta. \qquad (2.19)$$

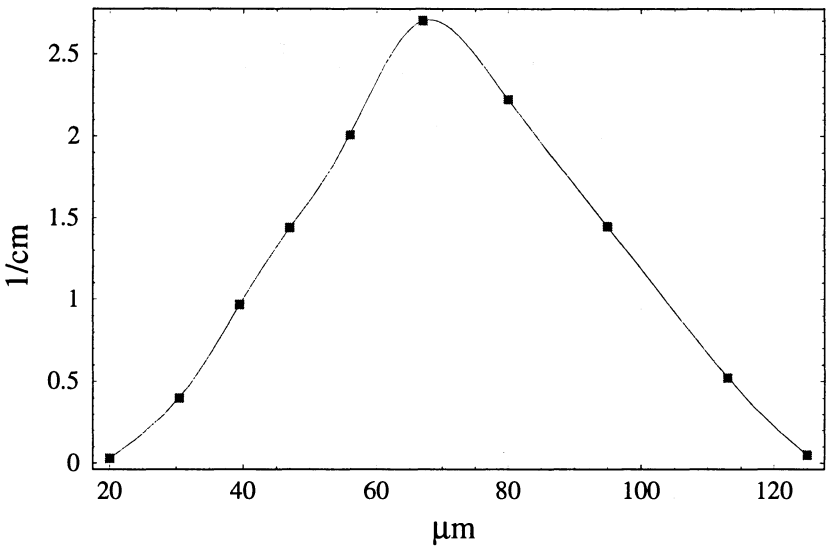

Figure 2.5 — Size distribution of sand particles used for experiments; the continuous line is a spline fit of data points $(\delta, \delta^3 N(\delta))$.

Analysis shows that S_T is a rapidly decreasing function of x and is practically zero if x is sufficiently large.[5]

Equation (2.19) provides the source term balancing the rate of change of the cross-sectional area $a(x,t)$ of the bed. However, a precise and complete description of the actual dynamics of the bed appears to be rather complex. Indeed there are infinitely many different profiles $h(\phi, x, t)$ that correspond to the same function $a(x,t)$ and there is no "natural" equation to describe the evolution of h. However, such a level of sophistication is absolutely not needed in our case, because for the particular nature of the problem, experimental observations cannot be that accurate. Indeed the best equipment available (a gamma-densimeter) provides only a reasonable measure of the average thickness of the bed as a function of time where the monitoring device is placed. The only clear experimental indication is that *pure settling* cannot be the only driving mechanism in the dynamics of the bed. Indeed, were this the case, the bed would grow continuously, filling the pipe in a finite time. Therefore pure settling (fully described by $S_T(x)$) needs to be coupled with a *transport* action, which consists of a

[5] In our simulations with a known population of sand particles ($\delta_{\min} = 0.0035$ cm, $\delta_{\max} = 0.0113$ cm; see Figure 2.5), $\rho_s = 2.67$ g/cm^3 and with a CWS with known rheological characteristic parameters ($\tau_0 = 8.89$ P, $\eta_B = 0.16$ Ps), we found $S_T \simeq 0$ at $x = 10$ Km for a flow rate Q of $\simeq 100$ m^{3}h^{-1} and at $x = 60$ Km for a flow rate Q of $\simeq 450$ m^{3}h^{-1} (pipe radius $R = 25$ cm).

partial mass removal in the horizontal direction due to the action of the main flow. The idea is that, during a first stage, the whole bed flows in the pipe; then, when the bed has reached a critical thickness Δ, a *static* layer begins to grow just below the dynamic one (see Fig. 2.6). The value of Δ depends on the main volumetric flow rate Q.

To be more precise, the model is based on the following hypotheses:

(i) the radial thickness $h(\phi, x, t)$ of the bed (see Fig. 2.7) is proportional to its cross-sectional area $a(x, t)$ via

$$h(\phi, x, t) = C(\phi)a(x, t)$$

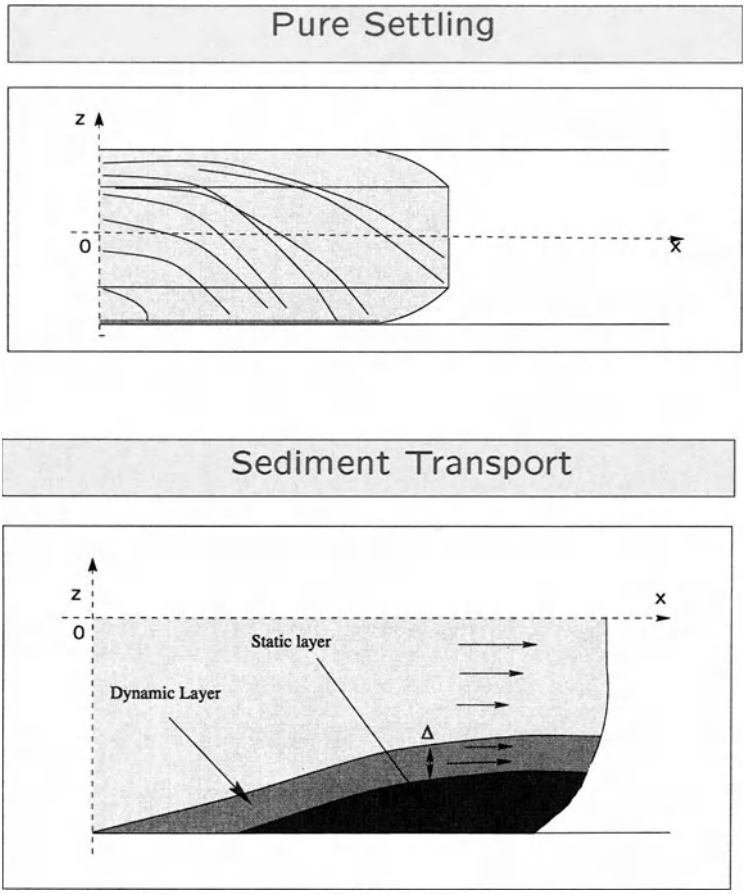

Figure 2.6 — The settling (top) and transport (bottom) actions driving the dynamics of the bed; when the dynamic layer has reached the critical thickness Δ, the static sublayer begins to develop below it.

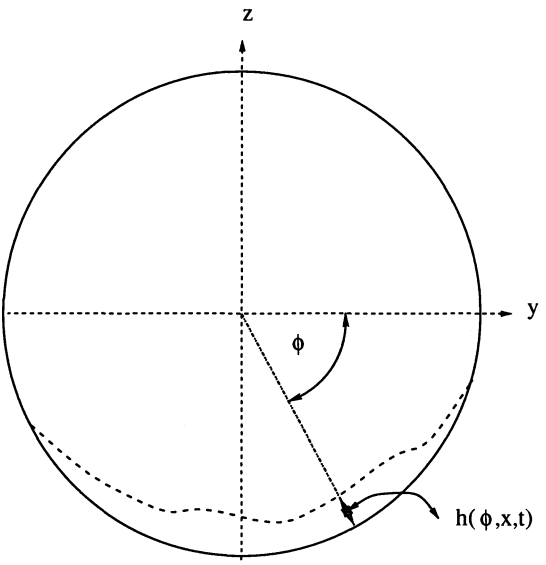

Figure 2.7 — Function $h(\phi, x, t)$ describes the radial thickness of the bed; ϕ is the azimuthal coordinate.

(ii) The cross-sectional area of the bed always remains small enough so that the flow geometry of the main flow is not significantly modified (in [33], it is partially relaxed); in other words

$$a(x,t) \ll \pi R^2$$

(iii) The cross-sectional profile is *sufficiently regular* and *physically consistent* in the sense that $C(\phi)$ must satisfy the following constraints:

1. $C(0) = C(\pi) = 0$,
2. $C'(\phi) > 0$, for all $\phi \in [0, \pi/2)$,
3. $C(\phi) = C(\pi - \phi)$, for all $\phi \in [0, \pi/2)$, and
4. $C'(\phi) \leq \left[\frac{R}{a(x,t)} - C(\phi)\right] \cot(\phi)$, for all $\phi \in (0, \pi/2)$.

(iv) The volumetric flow rate in the x direction *due to the moving layer of the bed* is described by the function

$$q(x,t) = 2\int_0^{\frac{\pi}{2}} \tilde{q}(x,t,\phi)\, d\phi \tag{2.20}$$

where

$$\tilde{q}(x,t,\phi) = \begin{cases} \lambda_1 R h(x,t,\phi), & \text{for } h(x,t,\phi) < \Delta \\ \lambda_2(a(x,t))R\Delta, & \text{for } h(x,t,\phi) \geq \Delta \end{cases} \tag{2.21}$$

in such a way that $\tilde{q}(x,t,\phi)\,d\phi$ is just the volume of sediment passing through a section of width $d\phi$ per unit time consistently with the hypotheses $h \ll R$ and $\Delta \ll R$. The parameter λ_1 and the function $\lambda_2(a)$ have to be chosen so that $\tilde{q}(x,t,\phi)$ is continuous.

Obviously $C(\phi)$ takes its maximum at $\phi = \pi/2$; therefore (2.4) is satisfied if, for example, $C'(\phi) \leq [\frac{R}{a(x,t)} - C(\pi/2)]\cot(\phi)$ provided that $a(x,t) < R/C(\pi/2)$. Condition 4 can be easily interpreted: the z-coordinate of a point on the bed profile is given by

$$z(\phi,x,t) = -(R - C(\phi)a(x,t))\sin\phi$$

Provided that $a(x,t)$ is sufficiently small, condition 4 is equivalent to saying that $\partial z/\partial\phi < 0$ for all $\phi \in [0,\pi/2)$.

Assumptions on h are justified by the fact that in the absence of experimental information it is convenient to choose working hypotheses that are simple and meaningful.

Let us define $g(2\phi/\pi) = C(\phi)/C(\pi/2)$ with $\phi \in [0,\pi/2]$. Because of the hypotheses made on C, g is invertible on $[0,1]$; let us also set $G(s) = \int_0^s g(u)\,du$. The cross-sectional area $a(x,t)$ is described by $\int\int_{\mathcal{A}} r\,dr d\phi$, where

$$\mathcal{A} = \{(r,\phi)/\phi \in [0,\pi], \quad R - C(\phi)a(x,t) \leq r \leq R\}$$

neglecting higher-order terms (recall (ii)), this yields $C(\pi/2) = 1/[\pi RG(1)]$. Moreover, for given $a(x,t)$, we have $0 \leq h(\phi,x,t) \leq C(\pi/2)a(x,t)$; thus if $a \leq a_o := \Delta/C(\pi/2)$ then $h(\phi,x,t) \leq \Delta$ for all $\phi \in [0,\pi/2]$. In this case, by recalling the definition of $q(x,t)$ in hypothesis (iv), we immediately obtain $q(x,t) = 2\lambda_1 R\int_0^{\pi/2} h(\phi,x,t)\,d\phi = \lambda_1 a(x,t)$, being $2R\int_0^{\pi/2} C(\phi)\,d\phi = 1$. If, instead, $a(x,t) > a_0$, then there exists $\widehat{\phi}(a) \in [0,\pi/2]$ such that $h(\widehat{\phi},x,t) = \Delta$. Notice that $\widehat{\phi}(a) = (\pi/2)g^{-1}(a/a_0)$ and that $\widehat{\phi}' < 0$. Therefore, for all cross sections x and instants t for which $a(x,t) > a_0$, we have

$$q(x,t) = 2\left[\int_0^{\widehat{\phi}(a)} \lambda_1 Rh(\phi,x,t)\,d\phi + \int_{\widehat{\phi}(a)}^{\pi/2} \lambda_2(a)R\Delta\,d\phi\right]$$

$$= \pi R\Delta\left[\lambda_1\frac{a}{a_0}G(\frac{2}{\pi}\widehat{\phi}(a)) + \lambda_2(a)(1 - \frac{2}{\pi}\widehat{\phi}(a))\right]$$

Notice that $q(a_0^+) = q(a_0^-)$; indeed $\widehat{\phi}(a_0) = \pi/2$ and

$$q(a_0^+) = \pi R\Delta\lambda_1 G(1) = (\pi RG(1)C(\pi/2))\lambda_1 a_0 = \lambda_1 a_0.$$

The simplest choice for $\lambda_2(a)$ is the linear one: $\lambda_2(a) = \lambda_1 + \widehat{\lambda}_1(a - a_0)$, with $\widehat{\lambda}_1 > 0$.

The preceding analysis shows that we can write $q(x,t)$ as an explicit function of $a(x,t)$; in particular we have

$$q'(a) = \begin{cases} \lambda_1, & \text{for } a < a_0 \\ \pi R\Delta\{\frac{\lambda_1}{a_0} G(\frac{2}{\pi}\widehat{\phi}(a)) \\ \quad + \widehat{\lambda}_1(1 - \frac{2}{\pi}\widehat{\phi}(a)) - (\frac{2}{\pi}\widehat{\lambda}_1(a - a_0)\widehat{\phi}'(a)\}, & \text{for } a \geq a_0 \end{cases} \tag{2.22}$$

It is not difficult to check that $q'(a) > 0$; thus $q(a)$ is invertible in $[0, q_\infty)$ being $q_\infty = \lim_{a\to\infty} q$. If $\lim_{a\to a_0^+}(a - a_0)\frac{d}{da}g^{-1}(a_0/a) = 0$, then $q'(a)$ is also continuous for all $a > 0$. For future purposes it is also useful to notice that

$$q''(a) = \begin{cases} 0, & \text{for } a < a_0 \\ \pi R\Delta[(\frac{\lambda_1}{a} - 2\widehat{\lambda}_1)\widehat{\phi}'(a) - \widehat{\lambda}_1(a - a_0)\widehat{\phi}''(a)], & \text{for } a \geq a_0 \end{cases} \tag{2.23}$$

We are now ready to write the dynamic equation for the evolution of the bed; a simple mass balance over a portion of the pipe of unit length yields

$$\frac{\partial a}{\partial t} + q'(a)\frac{\partial a}{\partial x} = \tilde{S}_T(x) \tag{2.24}$$

where we set $\tilde{S}_T(x) := \frac{1}{\rho_s(1-\varepsilon)} S_T(x)$, ρ_s and ε being the density of the settled material and the porosity of the bed, respectively. The conversion factor $(1 - \varepsilon)$ is needed because the rate of change of the cross-sectional area due to the settled material depends on its degree of porosity.

We complete equation (2.24) with the following initial-boundary conditions

$$a(x,0) = a(0,t) = 0 \tag{2.25}$$

System (2.24)–(2.25) can be solved by the method of characteristics. Within the class of regular solutions, condition (2.25) implies that $a(x,t) \leq a_0$ in a neighborhood $A = A_1 \cup A_2$ of the initial lines $x = 0$ and $t = 0$. If

$$\frac{1}{\lambda_1}\int_0^\infty \tilde{S}_T(u)\,du < a_0 \tag{2.26}$$

then this neighborhood covers the whole region $A = \{(x,t)/x \geq 0, t \geq 0\}$, equation (2.24) is linear everywhere in A, and the solution is

$$a(x,t) = \begin{cases} \frac{1}{\lambda_1}\int_0^x \tilde{S}_T(u)\,du, & \text{for } (x,t) \in A_1 := \{(x,t)/0 < x < \lambda_1 t\} \\ \frac{1}{\lambda_1}\int_{x-\lambda_1 t}^x \tilde{S}_T(u)\,du, & \text{for } (x,t) \in A_2 := \{(x,t)/0 < \lambda_1 t < x\} \end{cases} \tag{2.27}$$

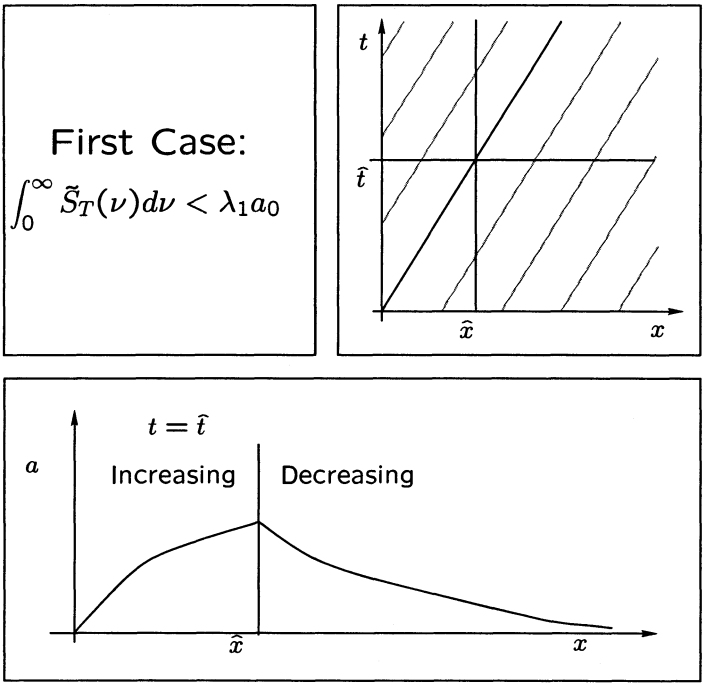

Figure 2.8 — The region $A_1 \cup A_2$ in the simplest case; the balance equation is linear and the characteristics are straight lines. At any instant $\hat{t}$, $a(x,t)$ takes its maximum at $\hat{x} = \lambda_1 \hat{t}$.

Thus the solution is globally defined, grows below the line $t = \frac{1}{\lambda_1}x$, takes its maximum along $t = \frac{1}{\lambda_1}x$, and remains stationary for $t > \frac{1}{\lambda_1}x$ (see Fig. 2.8).

If (2.26) does not hold, the situation is much more complicated: Besides regions A_1 and A_2 we have two further regions, A_3 and A_4, to consider. Indeed let us define $x_0 > 0$ such that

$$\frac{1}{\lambda_1}\int_0^{x_0} \tilde{S}_T(u)\,du = a_0 \tag{2.28}$$

We now have

$$A_1 = \{(x,t)/0 \le x \le x_0,\ t \ge \tfrac{x}{\lambda_1}\}$$
$$A_2 = \{(x,t)/0 \le x,\ 0 \le t \le t_\gamma(\xi),\ \xi \ge 0\}$$

where the line $\gamma(\xi) := (x_\gamma(\xi), t_\gamma(\xi))$ is defined by

$$\begin{cases} a_0 = \frac{1}{\lambda_1}\int_\xi^{x_\gamma(\xi)} \tilde{S}_T(u)\,du \\ t_\gamma(\xi) = \frac{1}{\lambda_1}\left(x_\gamma(\xi) - \xi\right) \\ \xi \ge 0, \quad x_\gamma(0) = x_0, \quad t_\gamma(0) = \frac{1}{\lambda_1}x_0 \end{cases} \tag{2.29}$$

Region A_3 is covered by all characteristics coming out from the line $\{x = x_0, \quad t \geq \frac{x_0}{\lambda_1}\}$. These characteristics never intersect each other; the line

$$t_\sigma(x) = \frac{x_0}{\lambda_1} + \int_{x_0}^{x} \frac{du}{q'\left(q^{-1}\left(\int_0^\eta \tilde{S}_T(u)\,du\right)\right)}, \quad x \geq x_0 \tag{2.30}$$

bounds region A_3 from below. Region A_4 is finally defined as follows

$$A_4 := \{(x,t)/x \geq x_0, \quad t_\gamma(\xi) \leq t \leq t_\sigma(x), \quad \xi \geq 0\}$$

In region $A_1 \cup A_2$ system (2.24) is still linear, and the solution is as before. In region $A_3 \cup A_4$ system (2.24) is fully nonlinear. In A_3 the solution is stationary (as in A_1); it is

$$a(x) = q^{-1}\left(\int_0^x \tilde{S}_T(u)\,du\right)$$

$\frac{\partial a}{\partial x} > 0$, $a(x,t)$ is increasing in $A_1 \cup A_3$. In region A_4 the analysis is more complicated because characteristics may intersect each other (see Fig. 2.9). Global existence of a solution in this case is guaranteed only if $q''(a) < 0$ and $q_\infty > \int_0^\infty \tilde{S}_T(u)\,du$. If $q''(a) > 0$ the existence is guaranteed only for $t < \hat{t}$, where $\hat{t}$ can be explicitly determined as a function of $\tilde{S}_T$ and Δ (see [28] for details).

For $q_\infty \leq \int_0^\infty \tilde{S}_T(u)\,du$ this conclusion continues to be true but the definition of $q(a)$ needs to be slightly modified; indeed the model is physically significant only as long as $a(x,t)$ remains small. Therefore we can always think of $q(a)$ as defined by (2.20) until a exceeds some upper bound and extend $q(a)$ (for example, linearly) to get $q_\infty = +\infty$. After that, condition $q_\infty > \int_0^\infty \tilde{S}_T(u)\,du$ is always satisfied.

Actually $q''(a) > 0$ means that the transport mechanism is rather efficient; this could lead to the formation of a shock front along the bed profile. Thus a classical solution no longer exists and weak solutions should be considered, although it seems unrealistic that the moving bed can really exhibit any jump, due to its incoherence. In region A_4 we have $\frac{\partial a}{\partial x} < 0$; moreover $\frac{\partial a}{\partial x}$ is continuous except along the curve $t = t_\sigma(x)$ where $a(x,t)$ takes its maximum for each t. For a given $\bar{t} > 0$, let $\bar{x}(\bar{t})$ be defined by $t_\sigma(\bar{x}(\bar{t})) = \bar{t}$. Then we can write

$$\max_{t<\bar{t}} a(x,t) = a(\bar{x}(\bar{t}),\bar{t})$$

and prove that the estimate

$$a(x,t) \leq q^{-1}\left(\int_0^\infty \tilde{S}_T(u)\,du\right)$$

holds everywhere in the existence domain of $a(x,t)$.

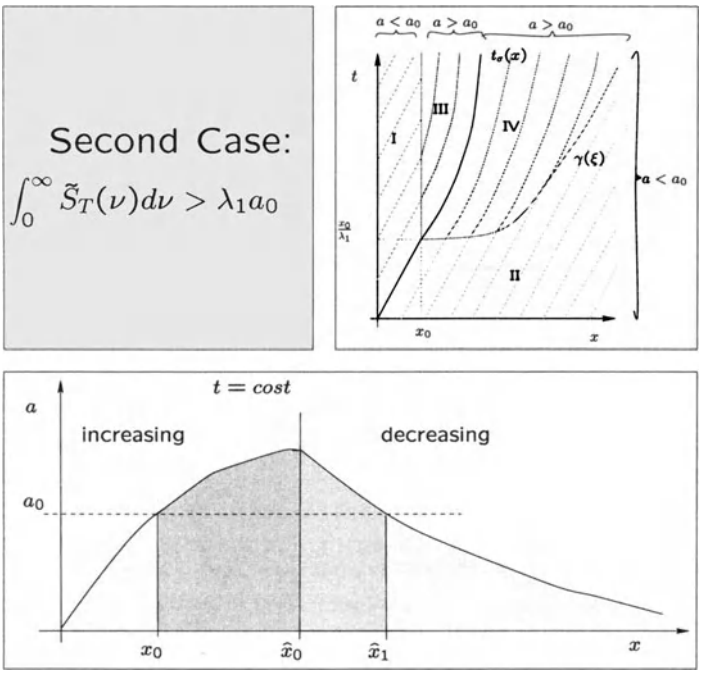

Figure 2.9 — The region $A_1 \cup A_2 \cup A_3 \cup A_4$ when the balance equation is nonlinear. In this case the characteristic lines may intersect in region A_4; as long as $t \leq x_0/\lambda_1$ the picture is the same as in Figure 2.8. For $t > x_0/\lambda_1$, $a(x,t)$ takes its maximum along $t_\sigma(x)$; at x_1, $a(x,t)$ decreases below the value a_0 again.

2.5 Numerical Simulations

The function $g(\psi)$ assigns a predefined geometry to the cross-sectional profile of the bed. We choose $g(u) = u(2-u)$ but more general choices are possible such as $g(u) = u^k(2-u)^k$; for $k > 1$ the bed shows thinner edges (see Fig. 2.10).

For $k = 1$ we get $\widehat{\phi}(a) = \frac{\pi}{2}(1 - \sqrt{1 - \frac{a_0}{a}})$, and so

$$q''(a) = \omega(\phi) := \frac{\pi R^2 a_0 (3\hat{\lambda}_1 a_0 - 2\lambda_1)}{8a^3\sqrt{1 - \frac{a_0}{a}}} \tag{2.31}$$

Moreover condition (iii,4) reads

$$a(x,t) \leq \frac{\pi^3 R^2}{6(\pi - 2\phi)\tan\phi + \phi(\pi - \phi)}$$

which is satisfied for any $\phi \in [0,\pi]$ if $a(x,t) \leq \min_{\phi\in[0,\pi]} \omega(\phi) = \frac{2\pi^2}{24+3\pi^2}\pi R^2$.

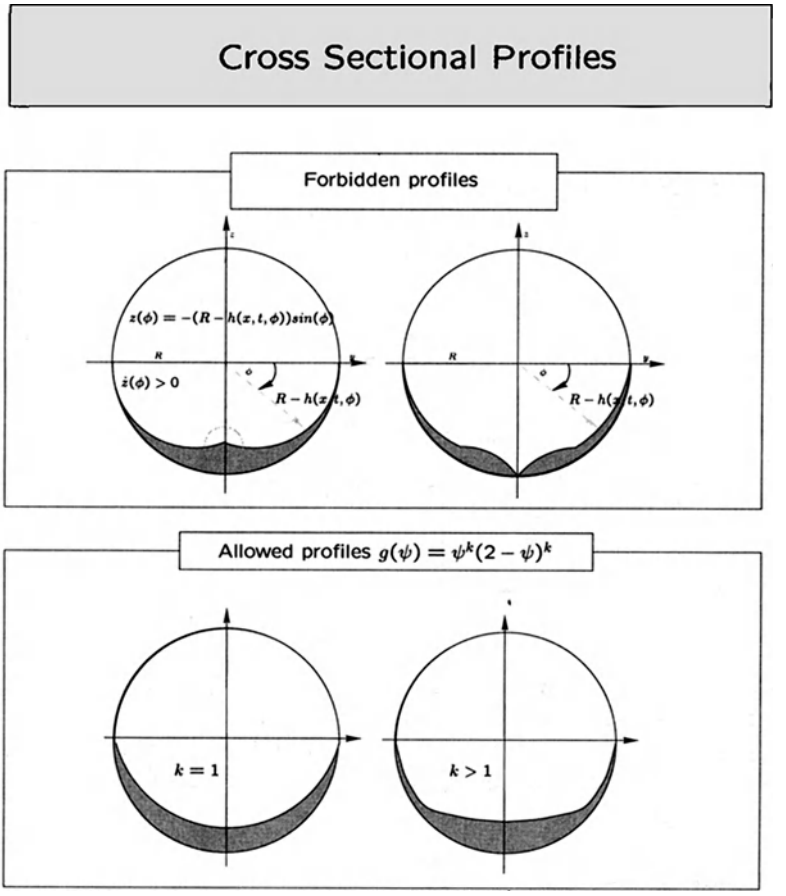

Figure 2.10 — Nonadmissible (top) and admissible (bottom) cross-sectional bed profiles; the forbidden profiles violate the hypotheses (iii,4) we made on function $C(\phi)$.

The parameter λ_1 has the physical meaning of a "velocity,"namely the mean velocity of the dynamic layer of sediment. We decided to set $\lambda_1 = V_x(R - \frac{\Delta}{2})$ (though other choices are possible) so identifying the velocity of the moving layer with that of the main flow of CWS $\frac{\Delta}{2}$ units away from the bottom pipe wall.

If we choose $\widehat{\lambda}_1 = 0$, then $\lambda_2(a) = \lambda_1$ and (2.20) yields a finite value of q_∞; thus we need to modify the definition of $q(a)$ as explained before in order to avoid critical conditions in the existence proof. Because of (2.31), $\widehat{\lambda}_1 = 0$ implies $q'' < 0$ and the solution is globally defined.

In the case $\widehat{\lambda}_1 \neq 0$, the dynamic layer moves with mean velocity λ_1 for $h < \Delta$ and grows linearly as $a - a_0$ for $h > \Delta$. This case is more

Table 2.1

Q (m^3/h)	100	150	250	450
Δ (cm)	0.7	1.0	1.8	3.2

complicated because, as we said before, the existence of a classical solution cannot be guaranteed for all times. All simulations to be shown next have been carried out (for simplicity) for $\widehat{\lambda}_1 = 0$. Therefore, from now on, we definitely assume $\lambda_2(a) = \lambda_1$.

The analysis developed in Section 2.4 shows that the value of the quantity $S_\infty = \int_0^\infty \widetilde{S}_T(u)\,du$ (which we assume to be finite, consistent with the real situation) plays a central role in discriminating two distinct situations. If $S_\infty < \lambda_1 a_0$ then the bed never reaches the level Δ; therefore it remains fully dynamic and never develops a static sublayer. If, on the contrary, $S_\infty > \lambda_1 a_0$, a static layer definitely develops, which keeps growing below the dynamic one as shown in Figure 2.6.

Given a point a distance x from the origin, $a(x,t)$ reaches its maximum value $a_{\max}(x)$ at that point, at time $t_\sigma(x)$; it turns out that

$$a_{\max}(x) = a(x, t_\sigma(x)) = q^{-1}\Big(\int_0^x \widetilde{S}_T(u)\,du\Big) \tag{2.32}$$

Once $a(x,t)$ has reached its maximum value at a given point, the graph of a for $\hat{x} < x$ remains stationary, i.e., independent of t, for all $t \geq t_\sigma(x)$; in other words the bed "crest" moves ahead toward infinity just like a wave, leaving a stationary "frozen" profile behind.

The choice of Δ is a very delicate matter. This is truly the key parameter of the model (as is evident from the choice of λ_1). On the other hand, direct experimental indications about Δ seem actually inaccessible for several reasons. First of all Δ is essentially a dynamical parameter, i.e., it cannot be measured at rest. Secondly, accurate dynamical measurements are not actually available, even with sophisticated instruments. Last but not least, CWS is an opaque substance and direct optical measurements are out of discussion.

For all these reasons we were forced to identify Δ indirectly as follows: We focused on the richest set of experimental data available, namely, those obtained at the flow rate $Q^\star = 250\ m^3/h^{-1}$. Once these are fixed as "reference"data, we select Δ in such a way that numerical simulation based on our model, must fit the experimentally observed behavior. Then we assume that Δ depends linearly on Q with $\Delta(0) = 0$. This approach led us to set $\Delta = 1.8\frac{Q}{Q^\star}$ cm and so to the values in Table 2.1 for the other flow rates used in our simulations.

Let us now define t_{cr} as the time instant at which the thickness h of the bed reaches a given critical level h_{cr}. We know that $t = t_\sigma(x)$ is the steady

Table 2.2

Q (m^3/h)	Δ (cm)	Gap (cm)	t_{cr}(days)	x_{cr} (Km)
100	0.7	3.5	0.4	0.48
150	1.0	4.2	0.5	1.24
250	1.8	5.4	∞	≥ 100
450	3.2	7.1	∞	≥ 100

curve "drawn" by the maxima of $a(x,t)$ as long as time elapses and the bed keeps growing. If $(x, t_\sigma(x))$ is a point on this curve in the (x,t)-plane then, bearing in mind (i) in Section 2.4, (2.32), and the fact that $t_\sigma(x)$ is invertible (see [28]), we get

$$h_{cr} = q^{-1}\Big(\int_0^{t_\sigma^{-1}(t_{cr})} \widetilde{S}_T(u)\,du\Big) \max_{\phi\in[0,\pi/2]} C(\phi)$$

Let us come now to numerical simulations. The rheological parameters of CWS are those mentioned at the end of Section 2.2. The size distribution of the settling material is described in [15] and [18].

The pipe radius R and length L are set equal to 25 cm and 100 km, respectively. Figure 2.11 shows the curves $\widetilde{S}_T(x)$ at all flow rates we considered.

Table 2.2 shows critical times and distances needed by the *static* sediment to reach 2% (= 1 cm) of the pipe diameter.

For $Q = 250$ and 450 m^3/h, t_{cr} and x_{cr} are out of the computational range. Table 2.3 shows, just for these flow rates, both time and distances for which the *dynamic* layer rises up to 1.5 cm (no *static* layer develops in these cases).

However 100 m^3/h is generally considered a very low regime (for $R = 25$ cm) from the point of view of economical convenience, because industrial pumps actually allow much higher regimes. For high values of Q the gap between the rigid core and the pipe wall is large enough for $h_{cr} = 2R/100$ to continue to be a very significant parameter. A more interesting choice might be the time T_{cr} needed by the whole system to reach a state in which the thickness of the static layer is above $h_{cr} = 2R/100$ *over*

Table 2.3

Q (m^3/h)	Δ (cm)	t (days)	x (Km)
250	1.8	0.39	4.3
450	3.2	0.38	10.1

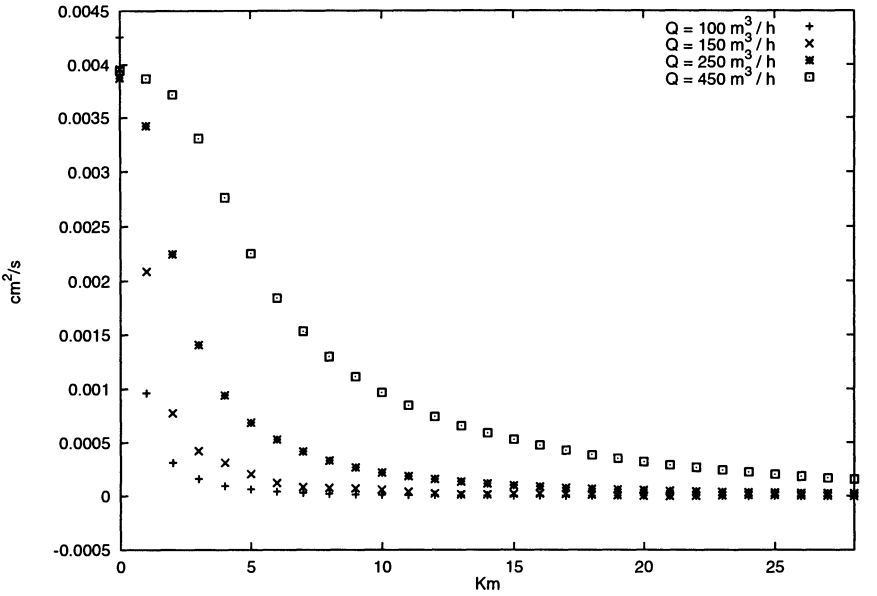

Figure 2.11 — Function $S_T(x)$ at various flow rates.

a longitudinal section of the pipe with length $L_{cr} \simeq L/100$ *(*$= 1\,\mathrm{Km}$*)* (L = total length of the pipeline). From the industrial point of view (at flow rates ≥ 250 m^3/h) this may be just the time after which a pipe shutdown and cleaning for sediment removal is highly recommended. Table 2.4 shows t_{cr}, x_{cr}, and T_{cr} for $Q = 250$ m^3/h and $L = 100$ Km for various values of Δ. It was just this analysis to suggest the value 1.8 cm as the one for which our simulations fit better available data.

Table 2.4

Δ (cm)	t_{cr} (days)	x_{cr} (Km)	T_{cr} (days)
1.4	0.71	3.57	1.01
1.5	0.97	4.99	1.35
1.6	1.51	7.5	2.08
1.7	3.20	14.2	3.85
1.8	∞	∞	∞
1.9	∞	∞	∞
2.0	∞	∞	∞

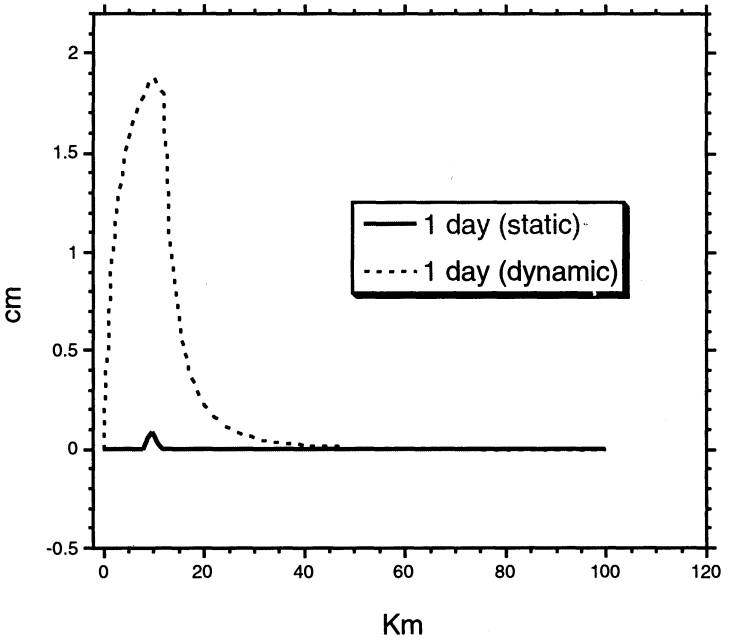

Figure 2.12 — Static (solid line) and mobile (dotted line) sediment profile after one day at 250 m^3/h.

Figures 2.12, 2.13, and 2.14 show the static and dynamic bed profiles for $Q = 250$ m^3/h and $\Delta = 1.8$ cm when $t = 1$ day, $t = 5$ days, and $t = 10$ days. As can be seen, the static sediment is still below the critical level of 1 cm even after 10 days.

2.6 Conclusions and Open Problems

In this review chapter we tried to report some of the results obtained in modeling the problem of particle sedimentation in a sheared slurry. Among other things, we developed a functional method to determine v_s (described in the appendix). However, this approach has been applied only to the simple Newtonian case. For a Bingham fluid this method appears rather complicated and has not yet been developed. This forced us to follow the more traditional approach based on the assumption that v_s has some preassigned dependence on the radius of the particle.

As far as we know, the model for evolution of the bed is totally new and, despite its simplicity, seems capable of predicting the critical values to operate an industrial pipeline under safe conditions. The numerical code developed by A. Mancini is the property of Snamprogetti.

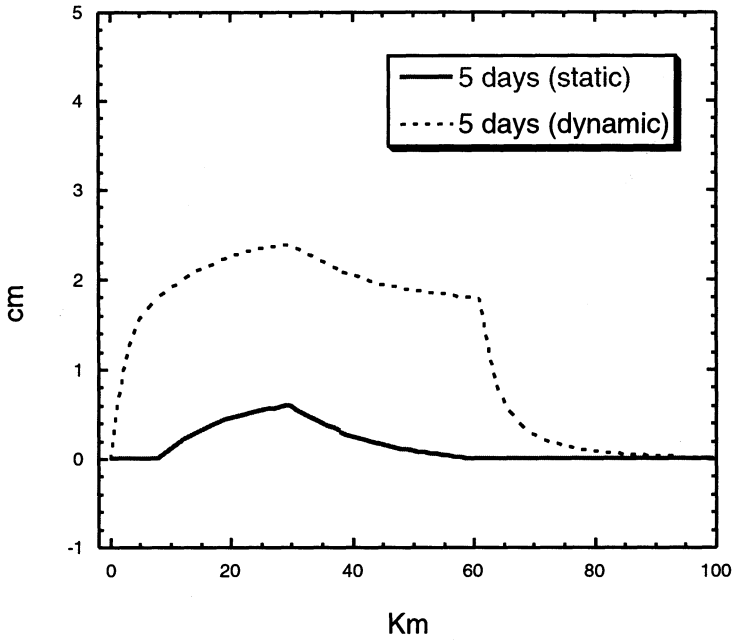

Figure 2.13 — Static (solid line) and mobile (dotted line) sediment profile after five days at 250 m^3/h.

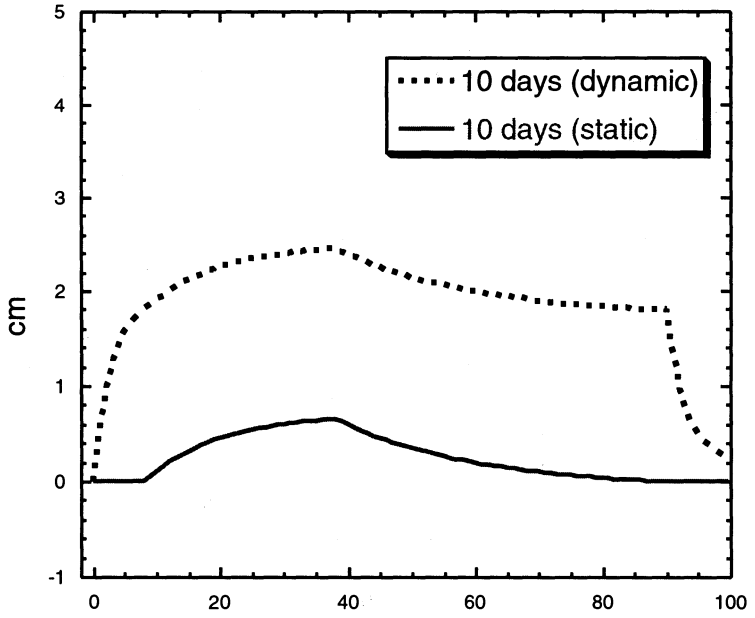

Figure 2.14 — Static (solid line) and mobile (dotted line) sediment profile after ten days at 250 m^3/h.

Although the assumptions we made for industrial designers are rather reasonable and make the model easy to handle, there are still some side questions that deserve further investigation. We list some of them here.

The model presented here does not consider the sliding motion of particles once they have touched the wall. This would add better information about the cross-sectional profile of the bed, which in the model is assigned a priori. This is certainly a very difficult problem because very little experimental information is available.

The existence proof for equation (2.24) guarantees global existence in time if $q'' < 0$. If this condition is not fulfilled, a shock develops and it seems more reasonable to switch to a different transport model. This analysis is not expected to be very hard but is still missing.

2.7 Appendix: A Functional Approach to Settling Velocity of Particles in a Finite Container

We considered a liquid container V that can be either a cylinder or a rotational viscometer. The container is filled with a liquid $\mathcal{L}$ whose constitutive law we do not need to specify now. Therefore V is characterized by its height l and the radii $R_1 \geq 0$ and $R_2 > R_1$ of the inner and outer cylinders, respectively. Indeed our approach bypasses not only the rheological nature of $\mathcal{L}$ but also a detailed description of some intricate aspects of sedimentation such as fluid–particle and/or particle–particle interactions, wall effects, particle shape effects, and so on (see [12],[15],[34]). Let us suppose that a population $\mathcal{P}$ of particles is uniformly distributed in $\mathcal{L}$ at time $t = 0$. If the particle density $\rho_{\mathcal{P}}$ is greater than the liquid density $\rho_{\mathcal{L}}$, $\mathcal{P}$ is expected to settle toward the bottom of V. If $\mathcal{L}$ has a yield stress there may be a fraction of $\mathcal{P}$ that never settles, although the unsettled fraction generally changes according to the shearing condition.

The family $\mathcal{P}$ is supposed to be represented by a rather large number $\mathcal{N}$ (say $\geq 10^5$) of particles with random shape and very small size.

Let us direct our attention over a cross-sectional cell C of the container V of thickness h with the top and bottom bases placed, respectively, at $z - h$ ($z > h$) and $z \geq 0$, the z-axis being directed as the gravity vector ($z = 0$ denotes the top of V). The quantity to be measured is the net mass variation in C due to the settling of $\mathcal{P}$.

As we already said in Section 2.2, the stationary settling regime is generally reached almost instantaneously, and the observation cell C will experience an emptying wave starting from the moment the heaviest particle that left $z = 0$ at $t = 0$ reaches the level $z - h$.

Let us recall equation (2.10): For given $\dot{\gamma}$, $\mathcal{M}$ measures the mass due to $\mathcal{P}$ present in C at time t.

It is more convenient to write (2.10) as follows

$$\mathcal{M}^\star(v;t,\dot\gamma) = \lambda \int_U \Omega(\delta)\Phi[v(\delta);t]\,d\delta \tag{2.33}$$

where

$$\mathcal{M}^\star = 1 - \mathcal{M}/\mathcal{M}_o,\ \ \lambda = -\rho_p \Sigma K/\mathcal{M}_o,\ \ U = \text{supp}\ \Omega \cap [\delta_o(\dot\gamma),\infty)$$

and δ_o is a possible critical radius defined by (2.8).

For $\{z,h,\dot\gamma\}$ given,[6] the right-hand side of (2.33) defines a (formal) nonlinear operator N that maps $v(\delta)$ into the function

$$Nv(t) = \lambda \int_U \Omega(\delta)\Phi[v(\delta);t]\,d\delta \tag{2.34}$$

The function $1 - \mathcal{M}^\star(t)$ measures the percentage of $\mathcal{P}$ present in C at time t. Because $\mathcal{M}^\star(t)$ is a measurable data, the functional equation

$$Nv = \mathcal{M}^\star \tag{2.35}$$

can be used, in principle, to determine v.

As emphasized in [34] the fully nonlinear problem is rather complicated. In this case it is possible and reasonable, on the basis of a suitable physical approximation, to linearize the problem. This leads to the functional equation

$$Aw = g \tag{2.36}$$

where A is a linear operator. In particular, (2.36) turns out to be a Fredholm equation of the first kind, which, as is well known, is ill-posed in the sense of Hadamard.

The choice of solution (which will be called "reference" solution) to be used as the zeroth order approximation of (2.35) depends mainly on the physical situation. For example, if the fluid $\mathcal{L}$ is *almost* Newtonian it may be reasonable to linearize (2.35) around (2.2), while for a Bingham plastic other choices are more suitable.

Let us decompose the unknown u into the reference solution v plus a "perturbation" w due to all effects mentioned at the beginning of Section 2.2. Then

$$Nu \approx (N'[v],w) + Nv \tag{2.37}$$

where $N'[v]$ is the Frechét derivative of N calculated in v and $(.,.)$ is a scalar product to be specified. To calculate $N'[v]$ explicitly we shall make some assumptions on the class of reference solutions v. It is quite natural to

[6] From the experimental point of view, this means to have definitely fixed C and the shearing condition for $\mathcal{L}$.

ask that $v > 0$ in $(\delta_o, +\infty)$, $v = 0$ in $[0, \delta_o]$, and that $dv/d\delta > 0$ in $(\delta_o, +\infty)$. Here $\delta_o \geq 0$ as a function of $\dot{\gamma}$ is supposed to be known. Consequently there exists the inverse $\tilde{v}$ of v defined over $[0, +\infty)$, and we can write

$$\Phi = \begin{cases} 0, & \delta \leq \tilde{v}(c_1(t)) \\ z - h - v(\delta)t, & \tilde{v}(c_1(t)) \leq \delta \leq \tilde{v}(c_2(t)) \\ -h, & \delta \geq \tilde{v}(c_2(t)) \end{cases} \tag{2.38}$$

where $c_1(t) = \frac{z-h}{t}$ and $c_2(t) = \frac{z}{t}$. Then an elementary calculation shows that

$$(N'[v], w) = -\lambda \int_A t\Omega(\delta)\mathcal{X}_{I(t)}(\delta)w(\delta)\, d\delta \tag{2.39}$$

where $\mathcal{X}_{I(t)}(\delta)$ is the characteristic function of $I(t) = [\delta_1(t), \delta_2(t)]$ and $\delta_i(t) = \tilde{v}(c_i(t))$. The formal structure of our problem is thus the following

$$Aw := (N'[v], w) = \mathcal{M}^\star - \lambda N v \tag{2.40}$$

In other words, the right-hand side of (2.39) denotes the difference between the effective emptying wave $\mathcal{S}$ (observable) and a reference emptying wave corresponding to v. If v is assigned, equation (2.40) is the explicit form of equation (2.36) in the unknown w we were looking for. However, in a typical experiment $\mathcal{S}$ is available only over a finite set of time values $t_{i=1,\ldots,n}$. Thus $\mathbf{g} := \mathcal{M}^\star - \lambda N v$ is a vector in R^n rather than a function of t and so equation (2.40) is actually a Fredholm equation of first kind *with discrete data.* It is quite natural therefore to discretize the kernel $k(\delta, t) := \lambda t\Omega(\delta)\mathcal{X}_{I(t)}(\delta)w(\delta)$ by putting $k_i(\delta) := k(\delta, t_i)$, the operator A by putting $A_i w := \int_U k_i(\delta)w(\delta)\, d\delta$, and to consider just the discretized problem

$$A_i w = \mathbf{g}_i, \quad (i = 1, \ldots, n) \tag{2.41}$$

It is easy to see that each A_i is bounded in $L^2(U)$ being

$$|A_i w_2 - A_i w_1| \leq C_i ||w_2 - w_1|| \tag{2.42}$$

where $C_i = \lambda t_i (\max_U \Omega)\sqrt{(\text{meas}\, U)}$, and $||\cdot|| = \sqrt{(.,.)}$ denotes the usual L^2-norm. By the Riesz theorem there exists a set of functions $\{\phi_i\}_{i=,\ldots,n}$ in $L^2(U)$ such that

$$A_i w = (w, \phi_i), \quad i = 1, \ldots, n \tag{2.43}$$

The precise formulation of the problem is thus the following: *Given the set* $\{\phi_i\}_{i=1,\ldots,n}$ *in* $L^2(U)$ *and the data* $\mathbf{g} \in R^n$, *find a function* $w \in L^2(U)$ *such that*

$$(\phi_i, w) = \mathbf{g}_i, \quad i = 1, \ldots, n \tag{2.44}$$

Problems like these have been deeply investigated by Bertero et al. in [7] and [8], where the concept of solution is generalized in such a way as to overcome the following intrinsic difficulty of (2.44); this equation provides information only about a *finite* number of components of w, which in turn implies a lack of uniqueness and, if n is large, also that of numerical stability. These unpleasant features have to be related to the ill-posedness of the original infinite-dimensional problem (2.40) as is known from the theory of Fredholm equations of the first kind.

To proceed further let us denote by $\mathcal{A} : w \in L^2(U) \rightarrow \mathbf{g} \in R^n$ the mapping defined according to the rule

$$(\mathcal{A}w)_i = (w, \phi_i), \quad i = 1, \ldots, n \tag{2.45}$$

where $(\mathcal{A}w)_i$ denotes the ith component of $\mathcal{A}w$; of course $(\mathcal{A}w)_i = A_i w$. The mapping $\mathcal{A}$ is onto when the ϕ_i are linearly independent (a circumstance that is hard—if not impossible—to check in practice); otherwise the range of $\mathcal{A}$ has dimension $n' < n$. Let us denote by X the subspace of $L^2(U)$ spanned by the ϕ_i. Regardless of whether the ϕ_i is independent, the orthogonal complement $X_\perp$ of X is just the null space $\mathcal{N}(\mathcal{A})$ of $\mathcal{A}$. The adjoint $\mathcal{A}^*$ of $\mathcal{A}$, defined by $(\mathcal{A}w, \mathbf{g})_{R^n} = (w, \mathcal{A}^*\mathbf{g})_{L^2(U)}$ transforms $\mathbf{g}$ into an element of X because if $w \in X_\perp$ then $(w, \mathcal{A}^*\mathbf{g})_{L^2(U)} = 0$. Evidently $\mathcal{A}^*\mathbf{g} = \sum_{i=1}^n g_i \phi_i$. Therefore it is clear that, given $\mathbf{g} \in R^n$, the problem of finding a $w \in L^2(U)$ such that

$$\mathcal{A}w = \mathbf{g} \tag{2.46}$$

when the ϕ_i are not linearly independent, has a solution if and only if $\mathbf{g} \in X$. If $\mathbf{g} \notin X$ one defines a *pseudo-solution* of equation (2.46) as any $\widetilde{w} \in X$ such that

$$||\mathcal{A}\widetilde{w} - \mathbf{g}||_{R^n} = \text{minimum} \tag{2.47}$$

This definition is well-motivated from the physical point of view; the minimum (2.47) is just the norm of the component of $\mathbf{g}$ orthogonal to $R^{n'}$, and this component is purely an effect of the experimental errors (see [7]). Because the set of pseudo-solutions is closed and convex, there exists a unique pseudo-solution of minimal norm called the *generalized* solution and denoted by $w^\dagger$. This solution always depends continuously on the data.

To obtain an explicit representation of $w^\dagger \in X$ we need to construct the set $\{\lambda_i, \epsilon_i, \mathbf{e}_i\}$ (called the *singular system of* $\mathcal{A}$) by solving the problem

$\mathcal{A}\epsilon_i = \lambda_i \mathbf{e}_i$, $\mathcal{A}^*\mathbf{e}_i = \lambda_i \epsilon_i$. This set can be computed with standard techniques (see [7] for more details); in particular it turns out that the numbers λ_i^2 are the eigenvalues of the Gram matrix associated with the functions ϕ_i, which are all positive, and their number is equal to the number $n' \leq n$ of linearly independent ϕ_i. Bearing this in mind, the representation formula for $w^\dagger$ is the following:

$$w^\dagger = \sum_{i=1}^{n} \frac{1}{\lambda_i} (\mathbf{g}, \mathbf{e}_i) \epsilon_i \tag{2.48}$$

Clearly, if there are only $n' < n$ linearly independent ϕ_i, we have only n' terms in equation (2.48).

The maximum eigenvalue λ_M and the minimum eigenvalue λ_m have an important meaning; the ratio $c(\mathcal{A}) = \lambda_M/\lambda_m$ is called the "condition number" of $\mathcal{A}$. If $c(\mathcal{A}) \gg 1$, the problem of computing $w^\dagger$, although well-posed, is "ill-conditioned." This circumstance is due to the ill-posedness of the related infinite-dimensional problem and could lead to large numerical errors. The situation does not improve by increasing the number n of available data g_i, because in this case the finite-dimensional problem becomes "closer" to the infinite-dimensional one.

The preceding method was applied to a population of sand particles uniformly dispersed in glycerine:[7] sand is 12% by weight and 9% by volume, with a density of 2.67 g/cm^3 and diameter distribution between 100 and 150 μm. The container is just a static cylinder with diameter 2.64 cm and height 14 cm held at a temperature of 4°C. At this temperature the glycerine viscosity is $\approx 6.13\,\text{Pa} \times \text{s}$, and the calculated coefficient $\frac{2g(\rho_s - \rho_l)}{9\eta}$ in (2.2) turns out to be $\approx 5.0\ \text{cm}^{-1} \times \text{s}^{-1}$. The chosen observation cell lies between $z = 4.5$ cm and $z + h = 5.88$ cm. Measures are taken every hour starting at time $T_1 = 6\,h$ seven times. We found

$$\mathbf{g} = -(.524, .429, .345, .264, .195, .181, .168) \tag{2.49}$$

We solved the singular system and found in particular that $c(\mathcal{A}) = \lambda_M/\lambda_m \approx 4.932$, which is quite acceptable. The generalized solution $w^\dagger$ of the inverse problem (the solid line in Figure 2.15 looks rather irregular, being essentially a linear combination of characteristic functions. The dashed curve is obtained by "smoothing" $w^\dagger$ around a $\beta\delta^2$-type curve with $\beta \approx 2.2\text{cm}^{-1} \times \text{s}^{-1}$; a comparison between the latter and (2.2) (the dotted line) reveals the presence of *retarding* effects (due, for example to the nonspherical shape of particles and mutual interactions).

[7] All experiments to collect the necessary data were conducted at the Snamprogetti research facility in Fano (Italy).

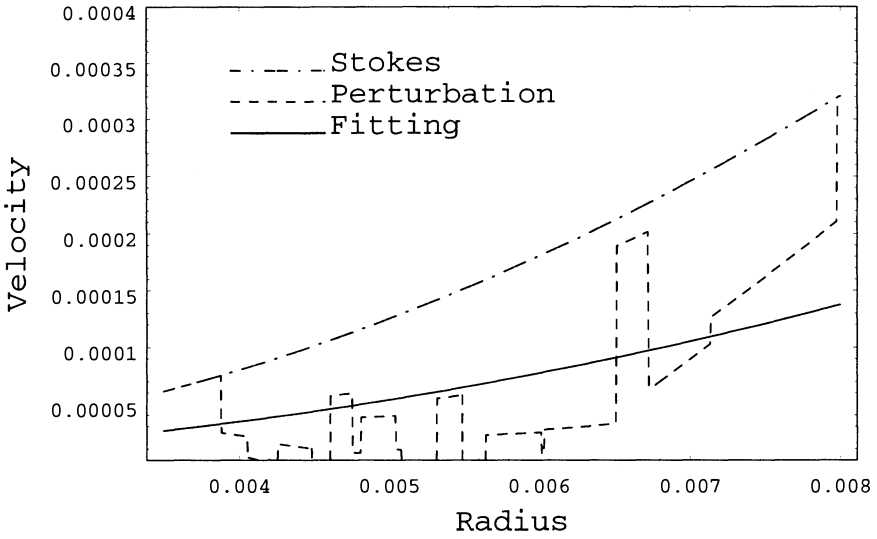

Figure 2.15 — The generalized solution of the inverse problem compared with the Stokes solution and a δ^2-type curve fitting the available data points.

List of Symbols

$\mathbf{v}_s$: sedimentation velocity
δ: particle radius
δ_0: particle critical settling radius
$\mathbf{g}$: gravity acceleration
ρ_s: particle density
ρ_l: liquid density
$\mathbf{T}$: Cauchy stress tensor
$\mathbf{n}$: outward unit normal to a regular surface
η: Newtonian fluid viscosity
$\mathcal{R}e$: Reynolds number
τ: shear stress
$\dot{\gamma}$: shear rate
τ_0: yield stress (Bingham model)
η_B: plastic viscosity (Bingham model)
$\mathcal{S}$: the mass of settling particles present (at given time) in an observation cell of a rotational viscometer
$\frac{dp}{dx}$: the constant pressure gradient (<0) in a pipeline
$V_x(r)$: fluid velocity profile in a pipeline
R: pipeline inner radius

Acknowledgments

This work was partially supported by the C.N.R. – G.N.F.M. Strategic Project "Metodi Matematici in Fluidodinamica e Dinamica Molecolare" and by C.N.R. contract #98.01027.*CT*01.

References

1. Acharya, A., Mashelkar, R.A., and Ulbrecht, J., Flow of inelastic and viscoelastic fluids past a sphere I. Drag coefficient in creeping and boundaty-layer flows, *Rheol. Acta*, **15**, 454–470 (1976).
2. Adachi, K., and Yoshioka, N., On creeping flow of a viscoplastic fluid past a circular cylinder, *Chem. Eng. Sci.*, **28**, 215–26 (1973).
3. Andres, V.T., Equilibrium and motion of a sphere in a viscoplastic fluid, *Soviet Phis. Doklady*, **5**, 723–26 (1960).
4. Ansley, R.,W., and Smith, T.,N., Motion of spherical particles in a Bingham plastic, *AIChE J.*, **13**, 1193–6 (1967).
5. Astarita, G., The engineering reality of yield stress, *J. Rheol.*, **34**, 275–7 (1990).
6. Beris, A. N., Tsamopoulos, J.A., Armstrong, R.C., and Brown, R.A., Creeping motion of a sphere through a Bingham plastic, *J. Fluid Mech.*, **158**, 219–44 (1985).
7. Bertero, M., De Mol, C., and Pike, E.R., Linear inverse problems with discrete data. 1: General formulation and singular system analysis, *Inverse Problems*, **1**, 301–30 (1985).
8. Bertero, M., De Mol, C., and Pike, E.R., Linear inverse problems with discrete data. 2: Stability and regularization, *Inverse Problems* **14**, 573–94 (1988).
9. Brenner, H., Dynamics of particles in a viscous fluid, *Chem. Eng. Sci.*, **17**, 435–9 (1962).
10. Brookes, G.F., and Whitmore, R.L., Drag forces in Bingham plastics, *Rheol. Acta*, **8**, 472–80 (1969).
11. Carniani, E., Ercolani, D., Meli, S., Pellegrini, L., and Primicerio, M., Shear degradation of concentrated CWS in pipeline flow, *Proc.13th Int. Conf. Slurry Technology*, Denver (1988).
12. Chhabra, R.P., Steady non-Newtonian flow about a rigid sphere, *Encyclopedia of Fluid Mechanics*, **1**, 983–1033 (1986).

13. Chhabra, R.P., Bubbles, Drops and Particles in Non-Newtonian Fluids, CRC Press, London (1992).

14. De Angelis, E., Modelli stazionari e non per fluidi di Bingham in viscosimetro e in condotta Ph.D. Thesis, University of Florence (1996).

15. De Angelis, E., Fasano, A., Primicerio, M., Rosso, F., Carniani, E., and Ercolani, D., Modelling sedimentation in CWS, in *Hydrotransport 12: Proc. of the 12th Int'l Conf. on Slurries Handling and Pipeline Transport*, edited by C.A. Shook, MEP Publ. (1993), 399–414.

16. De Angelis, E., and Mancini, A., A model for the dynamics of sediments in a pipe, *Mathematical and Computer Modelling*, **25**, 65–78 (1997).

17. De Angelis, E., and Rosso, F., A functional approach to the problem of evaluating the velocity for a population of particles settling in a liquid, *Proc. of the 6th European Consortium for Mathematics in Industry(1993)*, edited by A. Fasano and M. Primicerio, B.G. Teubner (1994), 191–8.

18. De Angelis, E., Fasano, A., Primicerio, M., Rosso, F., Carniani, E., and Ercolani, D., Sedimentation bed dynamics for fluids with yield stress in a pipe, *Proc. of the 4th Int. Conf. "Fluidodinamica Multifase nell'Impiantistica Industriale"* (1994), 85–93.

19. Dedegil, M.Y., Drag coefficient and settilng velocity of particles in non-Newtonian suspensions, *Trans. ASME*, **109**, 319–23 (1987).

20. Fasano, A., A mathematical model for the dynamics of sediments in a pipeline, in *Progress in Industrial Mathematics at ECMI 94*, edited by H. Neunzert, Weley and Teubner Publ. (1996), 241–9.

21. Fasano, A., and Primicerio, M. Modelling the rheology of a coal-water slurry, *Proc. of the 4th Europ. Consortium on Mathematics in Industry*, edited by H.J. Wacker and W. Zulhener, B.G. Teubner and Kluwer Academic Publ. (1991), 269–74.

22. Fasano, A., and Primicerio, M., New results on some classical parabolic free boundary problems, *Quart. Appl. Math.*, **38**, 439–60 (1990).

23. Fasano, A., Manni, E., and Primicerio, M., Modelling the dynamics of fluidizing agents in coal–water slurries, *Proc. of the International Symposium on Nonlinear Problems in Engineering and Science*, edited by S. Xiao and X. Hu, Science Press, Beijing (1992), 64–71.

24. Fasano, A., Primicerio, M., and Rosso, F., On quasi-steady axisymmetric flows of Bingham type with stress-induced degradation, *Computing*, **49**, 213–37 (1992).

25. Galdi, G. P. *An Introduction to the Mathematical Theory of the Navier-Stokes Equations, Vol I: Linearized Stationary Problems*, Springer Tracts in Natural Philosophy, **38**, Springer Verlag (1994).

26. Gianni, R., Pezza, L., and Rosso, F., The constant flow rate problem for fluids with increasing yield stress in a pipe, *Theoretical and Computational Fluid Mechanics*, **7**, 6, 477–93 (1995).

27. Leal, L.G., Particle motions in a viscous fluid, *Ann. Rev. Fluid Mech.*, **12**, 435–76 (1980).

28. Mancini, A., Evoluzione di profili di sedimentazione nel trasporto di sospensioni concentrate in condotta, Thesis Dept. Math. "U.Dini," University of Florence (1995).

29. Mancini, A., Evolution of sediment profiles in the transport of coal water slurries through a pipeline, in *Progress in Industrial Mathematics at ECMI 96*, edited by M. Brøns, M. Bendsøe, and M.P. Sørensen, Teubner, Stuttgart (1997), 441–9.

30. Oseen, C.W., Über die Stokessche Formel und über eine Verwandte Aufgabe in der Hydrodynamik, *Ark. Mat. Astron. Fys.*, **6**, 1–20 (1910).

31. Oseen, C.W. *Neuene Methoden und Ergebnisse in der Hydrodynamik*, Akademische Verlagsgesellshalt, Leipzig (1927).

32. Primicerio, M., Dynamics of slurries, *Proc. of the 2nd European Consortium on Mathematics in Industry 1987*, edited by H. Neunzert, B.G. Teubner (1988), 121–34.

33. Parrini, S., Moto stazionario di un fluido di Bingham in una condotta con sezione trasversale non circolare Thesis Dept. Math. "U. Dini,"University of Florence (1995).

34. Rosso, F., On two inverse problems in hydrodynamics of non-Newtonian fluids, in *Recent Advances in Mechanics of Structured Continua—1993*, edited by M. Massoudi and K.R. Rajagopal, **160**, ASME Publ., New York (1993) 95–103.

35. Stokes, G.G., On the effect of the internal friction of fluids on the motion of pendulums, *Trans. Cam. Phil. Soc.*, **9**, 8–27 (1851).

36. Terenzi, A., Carniani, E., Donati, E., and Ercolani, D., Problems on nonlinear fluid dynamics in industrial plants, this volume.

37. Thomas, A.D., Settling of particles in a horizontally sheared Bingham plastic, *1st Nat. Conf. on Rheology*, Melbourne, 89–92 (1979).

38. Tyabin, N.V. Some questions on the theory of viscoplastic flow of disperse systems, *Colloid J. U.S.S.R.*, **15**, 153-9 (1953).

39. Turian, R.M., Hsu, F.L., Avramidis, K.S., Sung, D.J., and Allendorfer, R.K., Settling and rheology of suspensions of narrow-sized coal particles, *AIChE J.*, **38**, 969–87 (1992).

40. Valentik, L., and Whitmore, R.L., The terminal velocity of spheres in Bingham plastics, *Brit. J. Appl. Phys.*, **16**, 1197–1203 (1965).

41. Wildemuth, C.R., and Williams, M.C., Viscosity of suspensions modeled with a shear-dependent maximum packing fraction, *Rheol. Acta*, **23**, 627–35 (1984).

42. Wilson, K.C., Hydrotransport 1 to 12, better by the dozen, opening address, *Hydrotransport 12, Int. Conf. on Slurry Handling and Pipeline Transport*, edited by C.A. Shook, BHR Group Conference Series, Publication No. 6, Mechanical Engineering Publication Ltd., London (1993).

43. Yoshioka, N., Adachi, K., and Ishimura, H., On creeping flow of a viscoplastic fluid past a sphere, *Kagaku Kogaku*, **10**, 1144–52 (1971) (in Japanese).

3

Problems of Nonlinear Fluid Dynamics in Industrial Plants

ALESSANDRO TERENZI, E. CARNIANI, E. DONATI, AND D. ERCOLANI

Snamprogetti S.p.A.
Fano, Italy

ABSTRACT. Pipeline transportation of complex fluids generally involves an analysis of nonlinear fluid dynamic phenomena, especially during transient phases. Snamprogetti has developed some models for predictions of pipeline flow characteristics relevant to both non-Newtonian solid-liquid suspensions and compressible fluid transport. This chapter is divided into two parts:

- **CWS Pipeline Flow: Homogeneous and Heterogeneous Conditions**, describing the properties of coal-water slurries considered both in their homogeneous flow conditions (transient motion influenced by complex rheological behavior) and with respect to prediction of unstable flow caused by settling processes.
- **Transient Compressible Flow at High Mach Numbers: A Conservative Method for Pipeline Flow**, describing the development of a code for simulation of transient phenomena associated with gas pipeline flow at high Mach numbers.

Part A: CWS Pipeline Flow: Homogeneous and Heterogeneous Conditions

ABSTRACT. *Fluid mechanical properties of high concentrated coal-water slurries (CWS) are quite complex and involve different kinds of scientific*

A. Fasano (ed.), *Complex Flows in Industrial Processes*

branches. Depending on chemical additives used and the industrial preparation process, these mixtures may or may not be stable with respect to settling phenomena. Often they exhibit non-Newtonian thixotropic rheological properties producing special behavior during pipeline flow, even if they can be considered homogeneous. Snamprogetti developed computer programs to simulate steady-state and transient flow conditions (startup, shutdown) of stable suspensions, based on Cheng–Evans rheological theory. Owing to the presence of impurities inside the coal (ash content, iron fragment, etc.) in certain fluid mechanical conditions, heterogeneous flow occurs and the settling process must be analyzed.

The movement of each solid particle is affected by interactions with other particles, with the fluid, and with the pipe wall. Snamprogetti developed computer codes that allow the prediction of critical settling conditions both in static columns and during pipe flow. By using experimental data of settling velocity vs. shear rate, the dynamic program calculates the growth rate and final evolution of a bed composed by heavier particles at the pipe bottom, through integration of continuity equations for the fluid and for the bed.

By using these codes, Snamprogetti can lead the industrial preparation selecting suitable CWS properties and preventing unstable conditions. Experimental data obtained in Snamprogetti facilities are also presented.

3.A.1 Introduction

A coal-water fuel (CWF) is a dense suspension of coal particles in water (also called CWS, coal-water slurry). Suitable optimization of the coal particle size distribution and the use of appropriate fluidizing and stabilizing additives allow us to produce highly concentrated suspensions (up to 70% by weight) that are pumpable in long pipelines and burnable directly in power plants without previous dewatering.

The technology of coal-water fuels has received a great deal of attention, especially after the oil crisis of the 1970s. At the end of the 1970s, Snamprogetti, the engineering company of ENI Group, developed a proprietary technology, named REOCARB, for production, pipeline transportation, and combustion of CWF.

To obtain the maximum allowable slurry concentration, the Snamprogetti REOCARB technology is based on a bimodal particle size distribution of the coal particles obtained by two milling stages: the first in a micronizing ball mill (especially developed and designed by SP) to produce the fine fraction and the second in a finishing rod mill to produce the coarse one.

Specific low-cost stabilizing and fluidizing additives patented by Snamprogetti are used to obtain fluid and stable suspensions that satisfy the

specifications requested for pipeline transportation, handling, storage, and combustion.

The first integrated CWF transportation and combustion system was designed and constructed by Snamprogetti in Siberia (Russia) from 1986 to 1989. The system consists of one production plant located in the Belovo district, near the coal mines, with a design capacity of 3 MTA of slurry as dry coal and a 262-km 20″ pipeline to transport CWF to the Novosibirsk power plant.

A second important industrial CWF plant was realized by Snamprogetti in Porto Torres, Sardinia (Italy). This plant, with a capacity of 500,000 t/y of CWF, represents the first application of the complete technological cycle including coal beneficiation, preparation, and combustion of cleaned coal-water fuels.

In Section 3.A.2 we will present a description of slurry rheological behavior and its influence on pipe flow, more evident during transient operations (startup, shutdown), developed under the assumption of homogeneous fluid (see also [17], [20], [21]).

In Section 3.A.3 the microscopic model of rheological degradation will be presented. In Section 3.A.4 a general discussion about settling of solid particles in fluids, with special attention to suspensions of solids in non-Newtonian liquids, will be presented.

In Section 3.A.5 computer codes developed at Snamprogetti representing heterogeneous fluid behavior in both static and dynamic conditions will be described, considering the flow pattern modification caused by the growing of a bed of heavier particles at the pipe bottom.

3.A.2 Homogeneous CWS Model: Rheology and Fluid Mechanics

The rheological behavior of CWS can be described by the Cheng–Evans model (see [4], [5], [6]), taking care of their non-Newtonian and thixotropic properties:

$$\tau = \tau_{00} + \lambda(\tau_{01} - \tau_{00}) + [K_0 + \lambda(K_1 - K_0)]\dot{\gamma}^N \tag{3.A.1}$$

All symbols are explained at the end of this part. This is a Herschel–Bulkley model, in which the parameters depend on a structure factor λ in a linear way.

This factor λ represents the internal state of CWS; it can vary between 0 and 1, where $\lambda = 0$ means minimum structuration state (minimum viscosity, low interaction forces between particles), while $\lambda = 1$ means maximum structuration state (maximum viscosity, strong interaction forces).

A kinetic equation describes the λ time evolution, allowing the determination of CWS state during transient phases:

$$\frac{d\lambda}{dt} = a(1-\lambda) - b\dot{\gamma}\lambda \tag{3.A.2}$$

where a represents the velocity of the structure construction process, while $b\dot{\gamma}$ is the velocity of the destruction process, depending on the flow conditions. The flow of CWS in pipelines can be studied by coupling the rheological equations (3.A.1), (3.A.2) to the momentum and flow balance equations:

$$\rho\frac{dU}{dt} = -\frac{\partial p}{\partial x} - \frac{2}{r}\tau \tag{3.A.3}$$

$$\frac{\partial u}{\partial r} - \dot{\gamma} \tag{3.A.4}$$

$$Q(t) = \int_0^R u(r,t)2\pi r\, dr. \tag{3.A.5}$$

In Figures 3.A.1 and 3.A.2 the inlet pressure and flow rate time evolutions are shown, referring to transient tests carried out in the Snamprogetti test-loop (170 m long, branch with 4″ internal diameter). The rheological parameters of tested slurries A and B are reported in Table 3.A.1.

In these transient tests, a startup followed by a steady-state condition and a shutdown are represented. The pressure curve shows all the various aspects of CWS fluid mechanics.

In fact, during startup the initial pressure rise is necessary to overcome the yield stress, which has its maximum value due to CWS static permanence for a long time; the flow rate begins to increase only after the pressure threshold has been exeeded. When the steady-state flow rate value is reached, the pressure achieves a peak value (inertial effects are present in this phase) and then it decreases in time for CWS thixotropy.

During the shutdown phase, the inertial term appearing in the motion equation (3.A.3) provides a negative contribution to total pressure, due to decelerating conditions; in this case negative relative pressures could be

Table 3.A.1. Slurry Rheological Parameters

Slurry	τ_{00} (Pa)	τ_{01} (Pa)	K_0 (Pa·s^N)	K_1 (Pa·s^N)	N	a (min^{-1})	b (s/min)
CWS A	0.51	1.05	0.73	0.85	0.85	0.36	0.2
CWS B	3.53	6.89	4.42	4.54	0.5	1.65	0.17
CWS C	3.55	8.55	1.08	1.48	0.58	0.53	0.29

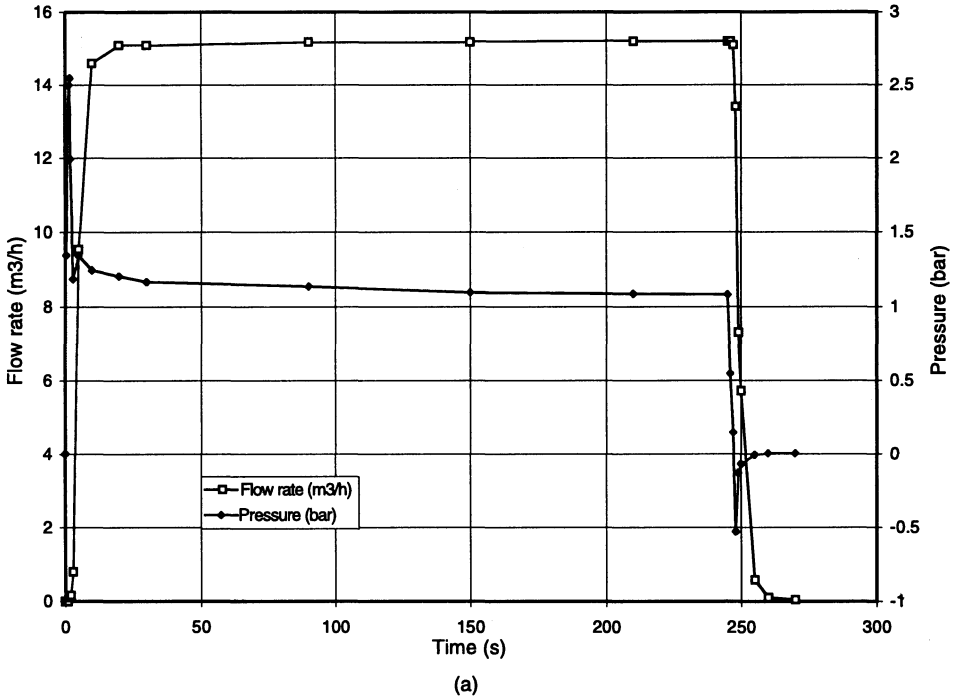

(a)

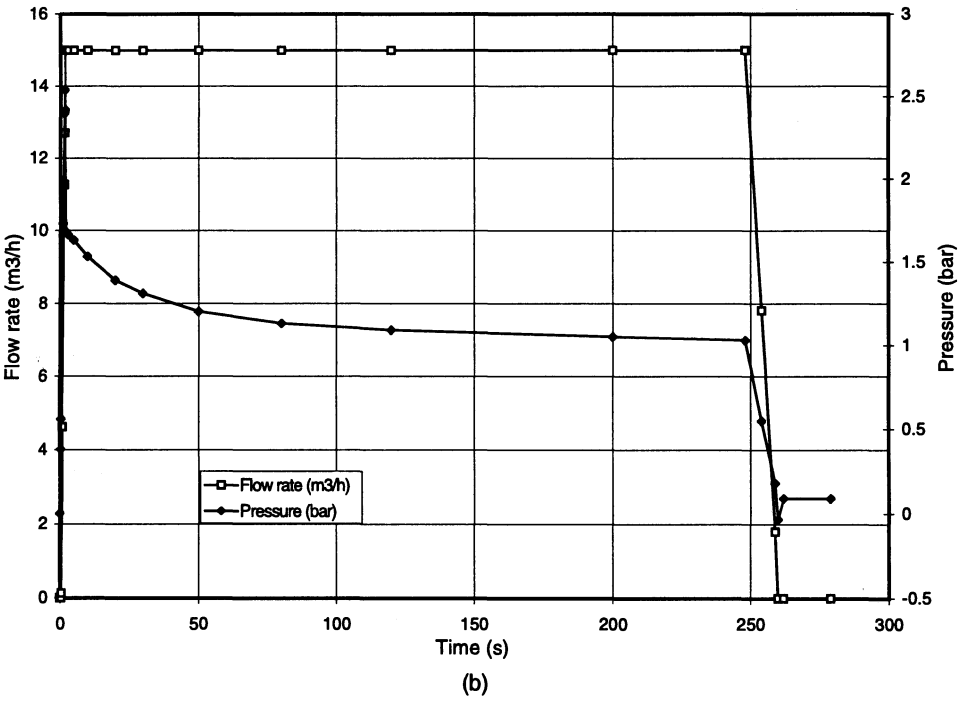

(b)

Figure 3.A.1 — Slurry A, transient test at 15 m^3/h: (a) experimental curve; (b) theoretical curve.

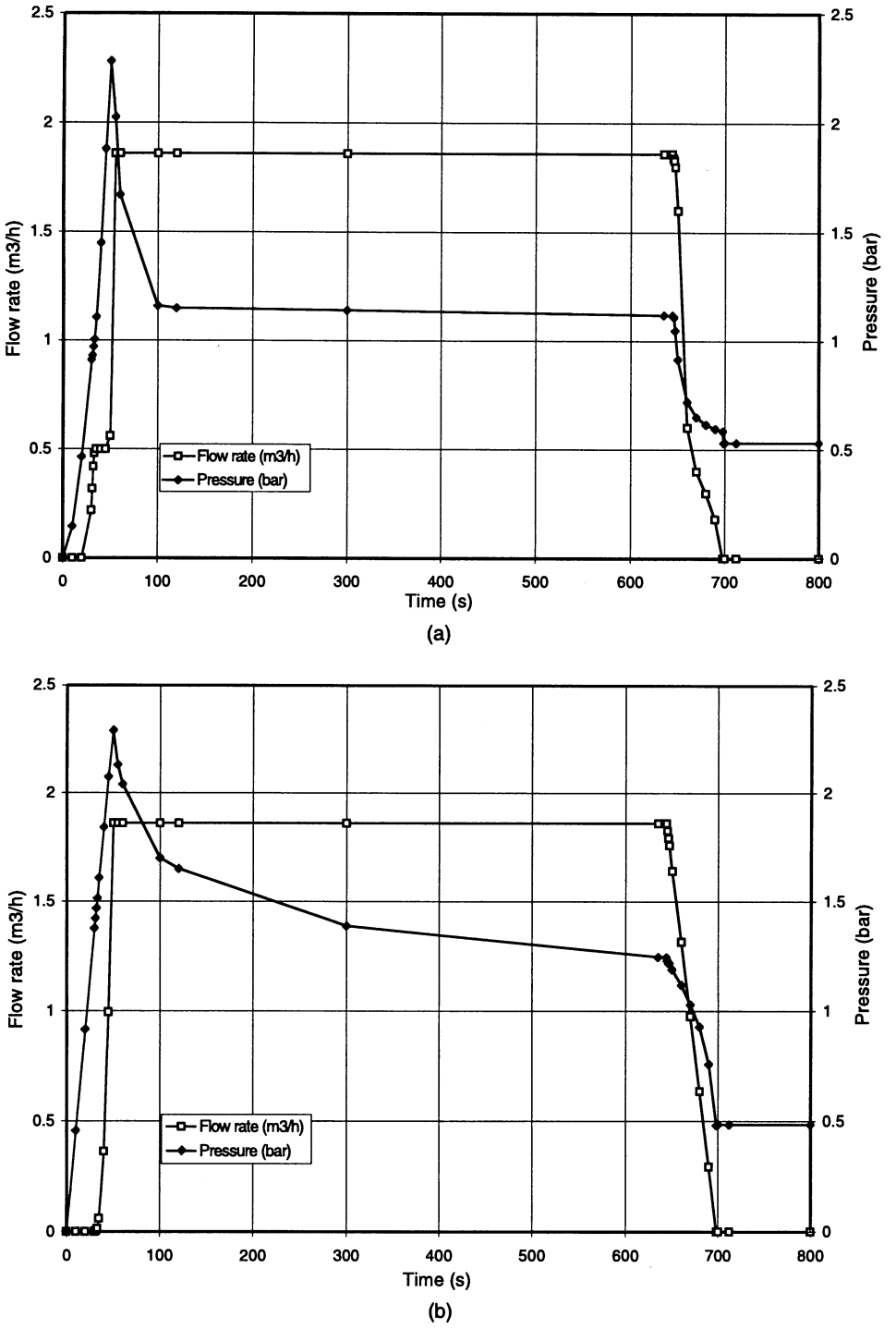

Figure 3.A.2 — Slurry B, transient test at 2 m^3/h: (a) experimental curve; (b) theoretical curve.

achieved. At the end of shutdown a residual pressure can occur, due to plastic fluid behavior. The situation is symmetrical to the restart phase: When the flow rate decreases, the pressure gradient also decreases, causing a progressive increase in central plug dimensions; when the flow rate vanishes, the pressure does not become null, but it assumes a value balancing the yield stress the fluid has at that moment. Successively, the pressure holds this value, because a static condition is realized.

Following [6], we introduce this notation, valid for describing startup:

IF = incoming fluid, that is fresh fluid coming from the tank.

OF = outgoing fluid, that is, fluid that has been in static conditions in the pipe, for a certain time.

The shutdown can be accomplished in two ways:

- it could occur before OF has completely left the pipe; in this case, the whole yield stress in the duct is defined by structural conditions of both fluids (OF and IF) present;
- it could occur after OF has left the pipe; the yield stress is determined by IF only.

In the first situation, the total pressure drop at a given moment shall be the summation of the losses for the two regions:

$$\Delta p_{\text{tot}} = \Delta p(IF) + \Delta p(OF) + \text{inertial term} \tag{3.A.6}$$

in the second situation, (3.A.6) becomes:

$$\Delta p_{\text{tot}} = \Delta p(IF) + \text{inertial term} \tag{3.A.7}$$

The residual pressure is determined by (3.A.6) or (3.A.7) at the moment in which the flow rate vanishes. Concerning steady-state conditions, in Figures 3.A.3 and 3.A.4 comparisons between experimental volume-averaged velocities measured on pipe section transverse chords by a magnetic velocity meter and theoretical values obtained by a steady-state computer code are presented (see [18]).

The rheological parameters of tested slurry C are shown in Table 3.A.1. Steady-state tests have been carried out on a 6″ branch of the test-loop, in which the velocity meter is installed. Both transient and steady-state comparisons show good agreement between theory and experiments.

3.A.3 Microscopic Model of Rheological Degradation

One of the most important problems, encountered in developing the CWF technology was the degradation of the rheological properties of the slurries,

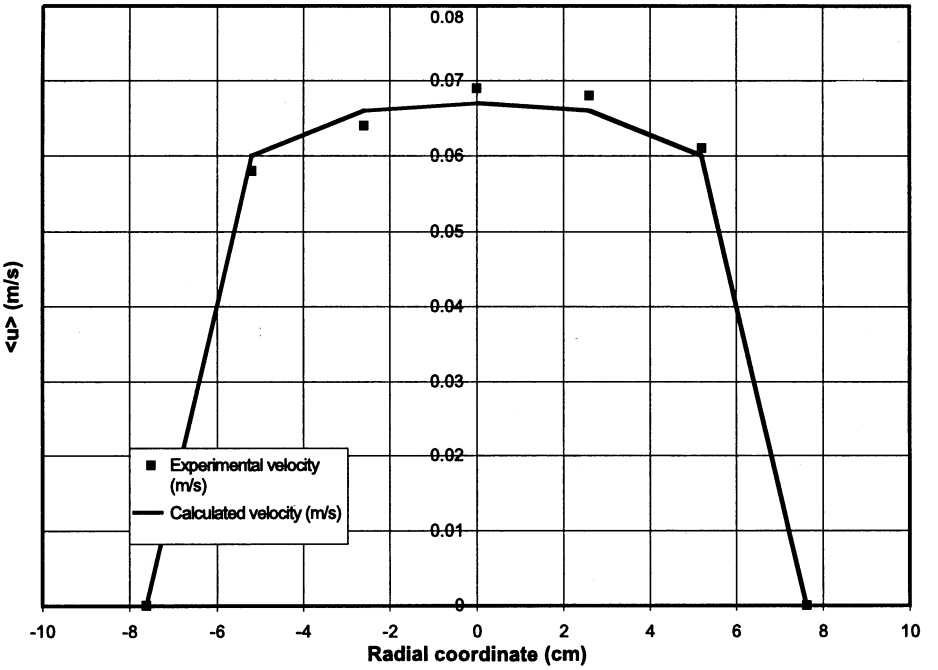

Figure 3.A.3 — Comparision between calculated and experimental volume-averaged velocity values at $Q = 4$ m^3/h.

with a dramatic increase of their viscosity, when subjected to intense stirring in batch or recirculated through a pump in a test loop.

The basic idea to explain this phenomenon was to link the rate of change of rheological parameters to the power supplied to the fluid by the stirring systems or the pump (see [13]).

Such a conjecture was confirmed by experiments. Indeed, plotting rheological parameters vs. the total supplied energy (i.e., assuming energy as a new time scale) the curves related to different experiments are basically coincident, as shown in Figure 3.A.5.

A mathematical model was developed to describe the influence of microscopic dynamics on the evolution of the macroscopic rheological parameters.

This model was developed in cooperation with Eniricerche, the research company of the ENI Group, and the Departments of Chemistry and Mathematics of the University of Florence. A crucial point is to model the dynamics of the fluidizing agent. Basically we can say that it can exist in two states:

- dissolved in water (with concentration A);
- adsorbed on coal particles.

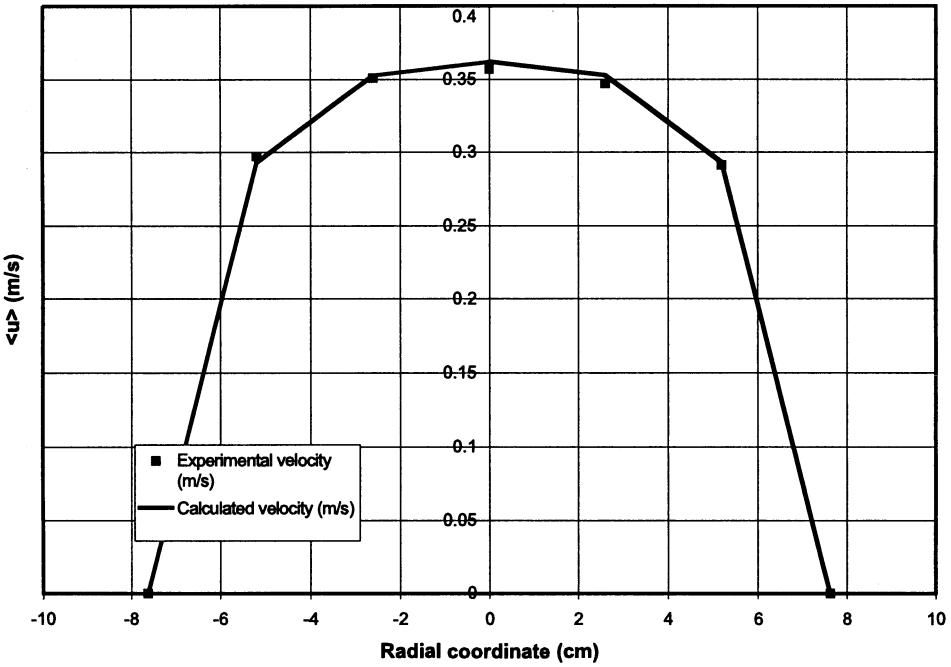

Figure 3.A.4 — Comparision between calculated and experimental volume-averaged velocity values at $Q = 20$ m^3/h.

However, not all the substance adsorbed exerts a fluidizing action. There can be a fraction of it that is not efficient, depending on how it is linked to the particle.

We shall denote by B the concentration of the dispersant adsorbed in the active way and by C the concentration of the inert fraction. Apparently, for reasons not yet completely understood, internal friction can cause the transition $B \to C$. Also a temperature increase seems to produce a similar effect (or the direct transition $A \to C$), but we will not consider this point for the sake of simplicity.

On the other hand, a transition $A \to B$ can occur to replace the dispersant becoming inert. The dynamics of the three "populations" can be described by the system:

$$A' = -\omega A(B_0 - B) \tag{3.A.8}$$

$$B' = \omega A(B_0 - B) - f(P_0)B \tag{3.A.9}$$

$$C' = f(P_0)B \tag{3.A.10}$$

where $f(P_0)$ is a function of the power dissipated P_0, B_0 is an initial condition, and $'$ means time derivative. The solution of this system is described in [13] for different rheological models.

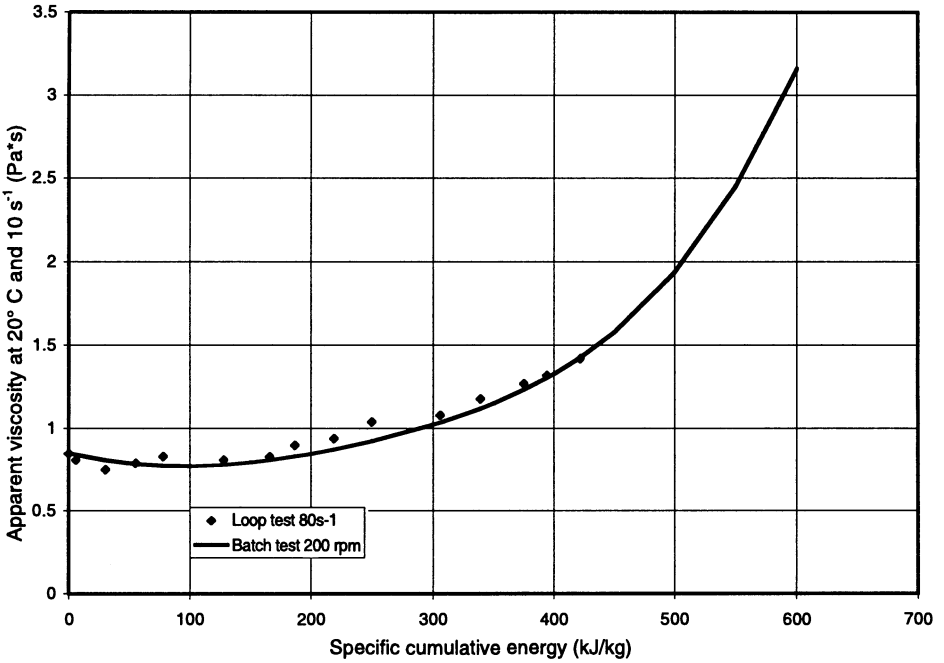

Figure 3.A.5 — Batch and loop CWS rheological degradation tests.

3.A.4 Suspensions Settling

As specified in Section 3.A.1, several parameters can affect the stability of a solid-liquid mixture, namely, chemical additives, coal concentration, grain size distribution, percentage and composition of mineral matter, rheological behavior, and flow configuration (see also [19]).

Settling is more likely to occur in slurries with high mineral matter content because these materials are noticeably denser than coal and coal-water mixtures; a suitable industrial process should provide a beneficiation for withdrawing these heavier particles from the coal matrix as much as possible. In any case a certain amount of mineral matter is still present, even if beneficiation has been effected, and other parameters must be assessed to ensure stability.

Chemical additives, coal concentration, grain size distribution, and amorphous mineral matter all influence the rheological properties, which are very important in defining one of the main interactions at which solid particles are submitted, i.e., the fluid-particle interaction.

It is assumed that only the crystalline mineral matter characterized by high density and large diameter are interesting in sedimentation. In fact, as shown by previous studies [2], amorphous mineral matter acts in the opposite direction as a CWS stabilizer by swelling and adhering to the coal particles.

The thixotropic fluid behavior is responsible for the different value of the drag force exerted by the fluid in static and dynamic conditions because of the viscosity variations (especially the yield stress). Thus a slurry can be stable when stationary in a vessel and can become unstable during pipe flow. The vessel and the pipe are also different with respect to another fundamental interaction, i.e., wall-particle interaction.

Experimental evidence shows an original phenomenon concerning high concentrated CWS: It is more stable in big tanks than in small containers; this means the wall effect increases the settling velocity, unlike Newtonian suspension where the wall influence acts in the opposite way.

The third interaction concerning the particle settling motions is with the other particles, producing the so-called "hindered settling."

Let us consider the particle-fluid interaction in more detail. The motion equation of a solid particle moving through a fluid, in "creeping flow" conditions ($Re_p < 0.1$) is:

$$\nabla \cdot \hat{\tau} = \vec{\nabla} p. \tag{3.A.11}$$

By solving the motion equation (3.A.11), with appropriate boundary conditions, the velocity and pressure fields are obtained. The drag force exerted by the fluid on the particle is:

$$\vec{F}_p = \iint_{S_p} \hat{\tau} \cdot \vec{n}\, dS \tag{3.A.12}$$

where the surface integral is calculated on the particle surface. For Newtonian fluids, the constitutive equation in tensor form is:

$$\hat{\tau} = \mu_f \hat{\Delta}. \tag{3.A.13}$$

In this case an analytical solution of (3.A.11) exists (see [14]), and the drag force for a spherical particle is given by:

$$\vec{F}_p = -3\pi\mu_f D \vec{U}_p \tag{3.A.14}$$

For non-Newtonian fluids, usually an analytical solution for the motion equation does not exist, and it is necessary to resort to numerical methods. Few attempts at numerical resolution are reported in the literature, and then for Bingham fluids only (see [1], [3]). As reported in Section 3.A.2, CWS is often described by a time-dependent Herschel–Bulkley model,

which in its time-independent tensor form is expressed by:

$$\hat{\tau} = \left\{ K \left| \sqrt{\frac{1}{2}(\hat{\Delta} : \tilde{\Delta})} \right|^{N-1} + \frac{\tau_0}{\left| \sqrt{\frac{1}{2}(\hat{\Delta} : \hat{\Delta})} \right|} \right\} \hat{\Delta} \quad \text{when } \frac{1}{2}(\hat{\tau} : \hat{\tau}) > \tau_0^2 \tag{3.A.15}$$

$$\hat{\Delta} = 0 \quad \text{when } \frac{1}{2}(\hat{\tau} : \hat{\tau}) < \tau_0^2 \tag{3.A.16}$$

For this kind of fluid, the yield stress provides a force that can sustain suspended solid particles, even in static conditions; settling can occur only if the resulting gravity force is greater than the yield stress force, constituting a threshold value:

$$\frac{\pi D^3}{6}(\rho_s - \rho_f)g > \left(\frac{\pi D}{2}\right)^2 \tau_0. \tag{3.A.17}$$

The yield stress force explains the static stability of CWS (Newtonian suspensions cannot be stable in this condition); it gives account also of stability during flow because the CWS pipe motion is laminar and the turbulent suspending force is absent. Referring to the other fundamental interactions, they can be treated analytically with the "reflection method" (see [14]):

$$\vec{V} = \vec{V}_0 + \vec{V}_1 + \vec{V}_2 + \vec{V}_3 + \cdots \tag{3.A.18}$$

$$\vec{V}_0 = \vec{U}_p \quad \text{on } P$$

$$\vec{V}_1 = -\vec{V}_0 \quad \text{on } S$$

$$\vec{V}_2 = -\vec{V}_1 \quad \text{on } P$$

$$\vec{V}_3 = -\vec{V}_2 \quad \text{on } S$$

where P represents the particle surface and S the boundary surface. By applying the reflection method, the perturbed velocity field for a Newtonian suspension due to particle-particle interaction is (hindered settling):

$$V = U_p \left(1 - \frac{\phi}{\phi_{\max}}\right)^{\alpha} \tag{3.A.19}$$

where $\alpha = 2$ for highly concentrated suspensions.
The drag force acting on a spherical particle settling in a Newtonian fluid in the presence of a wall is:

$$\vec{F}_p = -3\pi\mu_f D\vec{U}_p\beta \tag{3.A.20}$$

where β = constant (>1).

3.A.5 Heterogeneous CWS Model: Static and Dynamic Stability

Calculation of the settling velocity in unstable solid-liquid suspensions is complicated by the simultaneous action of several factors, as outlined in Section 3.A.4.

A first step in the study of this phenomenon in highly concentrated CWS was the elaboration of a computer program simulating the sedimentation in a static vessel, developed in cooperation with the University of Karlsruhe (Germany) (see [10]).

Given a CWS with solid volume concentration ϕ and a certain grain size distribution (but constant solid density ρ_s) filling a static sedimentation column of height H, this code assumes a discretization procedure shown in Figure 3.A.6. The continuous grain size curve is divided in n groups (with average particle diameter d_i, $i = 1, \ldots, n$) and the vessel is subdivided in m elements.

In unstable suspensions, the mixture will have a uniform concentration at the initial time and will develop a concentration profile as a function of height at successive instants. For continuity reasons, if a certain amount of solid settles down, a corresponding quantity of liquid rises up.

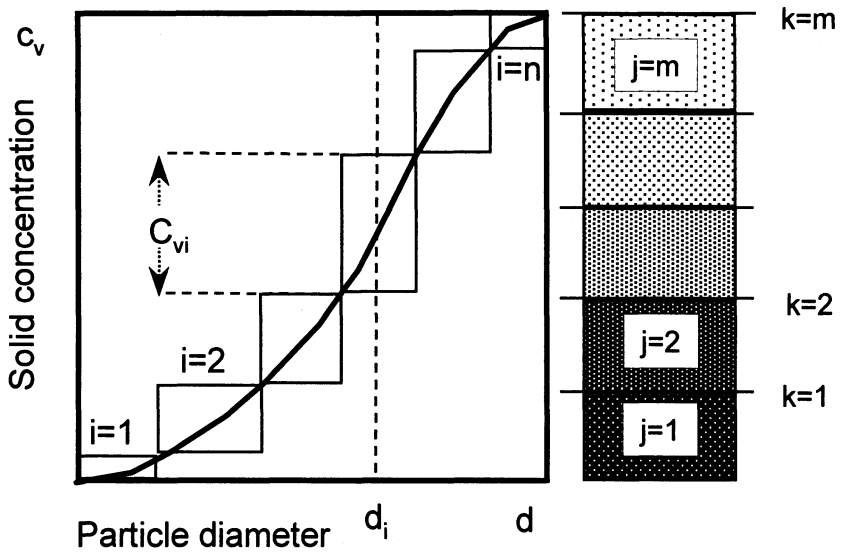

Figure 3.A.6 — Consideration of suspended grain material in $n = 6$ groups of diameter d_i and division of the vessel into $m = 5$ elements.

The absolute velocities of the solid particles and the fluid are connected according to the following equation

$$V_i = V_f + W_i \tag{3.A.21}$$

The relative settling velocity of particles with diameter d_i, taking care of the hindered settling effect, is given by:

$$W_i = W_{0i}\left(1 - \frac{\phi}{\phi_{\max}}\right)^2 \tag{3.A.22}$$

where the settling velocity of a single spherical particle with diameter d_i in a still Newtonian unbounded fluid is:

$$W_{0i} = \frac{d_i^2}{18\mu_f}(\rho_s - \rho_f)g. \tag{3.A.23}$$

In Figures 3.A.7, 3.A.8, and 3.A.9 some comparisons between volume concentration profiles calculated and measured in experiments are shown. Tests were carried out on Newtonian suspensions with mass concentration in the range 14.5%–32%. Their properties are reported in Table 3.A.2.

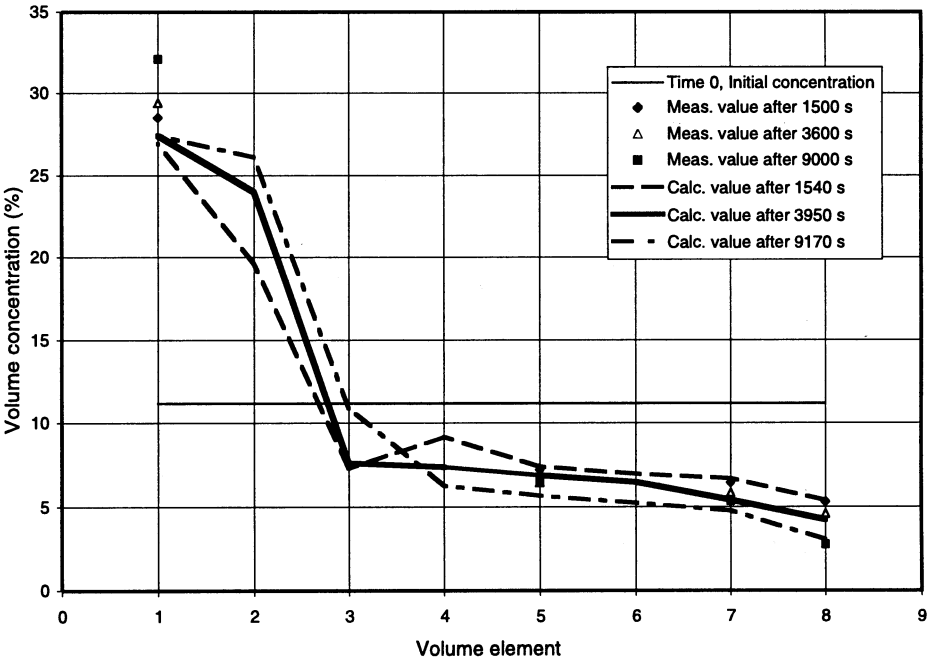

Figure 3.A.7 — Static settling test 1: initial coal mass concentration = 14.5%.

Table 3.A.2. Slurry Properties for Static Settling Tests

Stating Settling Test 1	Stating Settling Test 2	Stating Settling Test 3
$\mu_f = 0.001$ Pa·s	$\mu_f = 0.001$ Pa·s	$\mu_f = 0.001$ Pa·s
$\rho_f = 1000$ kg/m^3	$\rho_f = 1000$ kg/m^3	$\rho_f = 1000$ kg/m^3
$\rho_s = 1350$ kg/m^3	$\rho_s = 1350$ kg/m^3	$\rho_s = 1350$ kg/m^3
Initial mass concentration of coal = 14.5%	Initial mass concentration of coal = 30.0%	Initial mass concentration of coal = 32.0%
Initial volume concentration of coal = 11.2%	Initial volume concentration of coal = 24.1%	Initial volume concentration of coal = 25.8%

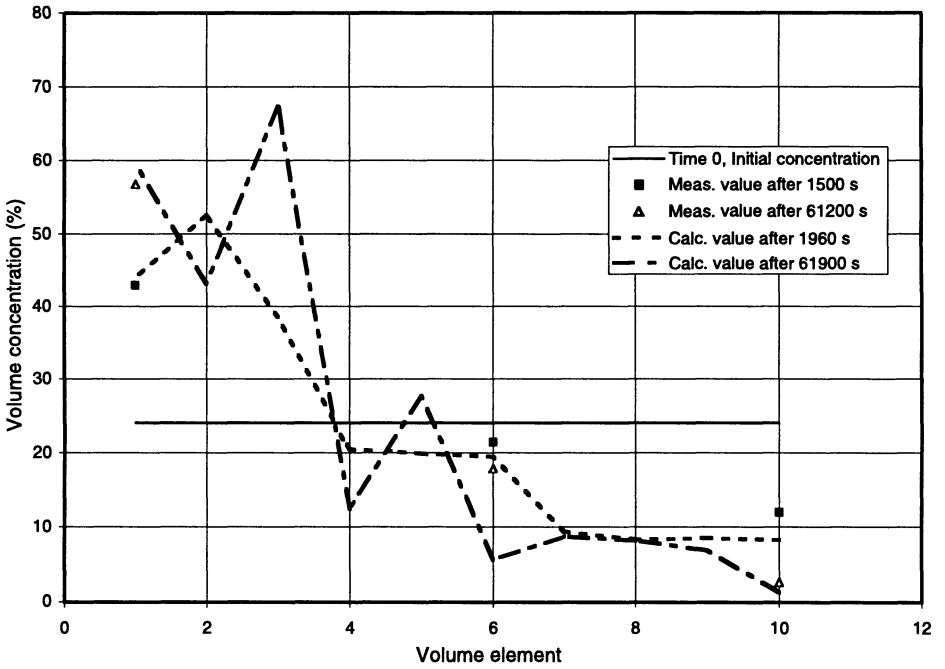

Figure 3.A.8 — Static settling test 2: initial coal mass concentration = 30%.

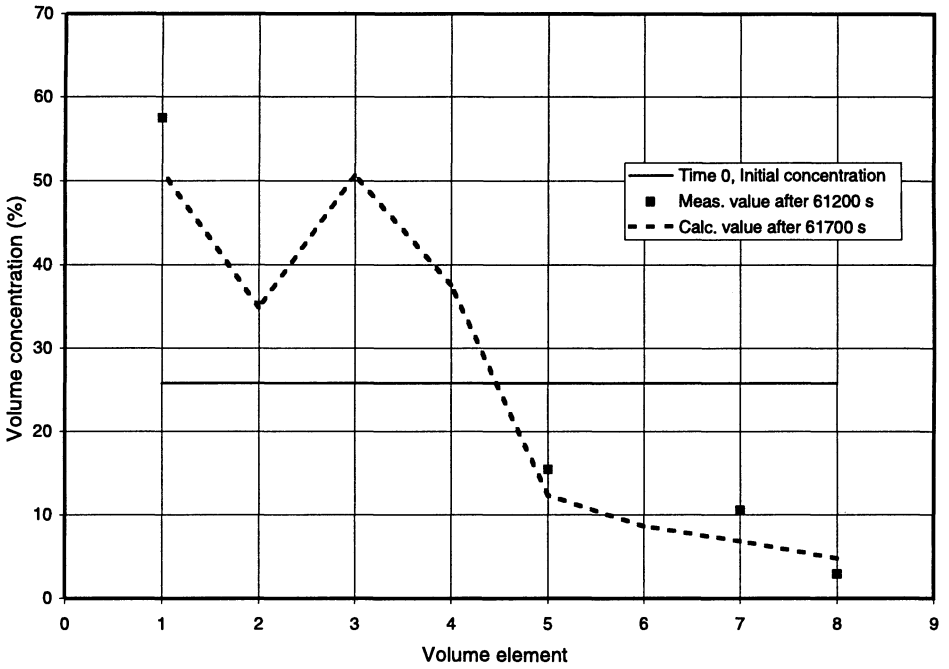

Figure 3.A.9 — Static settling test 3: initial coal mass concentration = 32%.

The sedimentation column was of height $H = 68$ cm and 27 cm internal diameter (see [10]). The program also contains a correlation for Bingham suspensions, developed according to Dedegil theory (see [9]). On the basis of this option, the program correctly predicts the static stability of highly concentrated CWS having high values of yield stress. The simplified approach used for the static settling model cannot be used for the dynamic program that simulates settling during pipe flow. In fact it does not take account of wall effects or solid density distribution (remember, ash particles are the most subject to settling).

But the main problem is the correct definition of the settling velocity as a function of rheological parameters because during pipe flow each fluid thread has a proper structuration state, i.e., a proper rheology with non-Newtonian thixotropic properties. The analytical calculation of the settling velocity is a difficult task for this kind of mixture; Snamprogetti developed an experimental method for measuring this quantity in cooperation with a research group at the math department U. Dini of the University of Florence. The experiments were carried out on suspensions of sand particles with fixed density (of the same order of ash) and particle size distribution (100–150 mm) in clean CWS, filling a rotational viscometer working at different values of shear rate.

The settling velocity of a particle with diameter D was determined in this form [7], [15]:

$$\nu(\alpha, D) = \alpha(\dot{\gamma}) \cdot f(D) \tag{3.A.24}$$

where the function $\alpha(\dot{\gamma})$ is the reciprocal of the effective viscosity perceived by the particle:

$$\eta_{\text{eff}} = \frac{1}{\alpha(\dot{\gamma})} \tag{3.A.25}$$

and the function $f(D)$ is given by:

$$f(D) = D(D - D^*(\dot{\gamma})) \tag{3.A.26}$$

and $D^*(\dot{\gamma})$ is the critical diameter for the mixture in the structuration state corresponding to the shear rate $\dot{\gamma}$, i.e., particles with diameter less than this value do not settle because they are sustained by the mixture structure.

The heterogeneous pipe flow has also been developed in cooperation with the University of Florence; it is described in [8], [11], [12], [15] and [16]. We can conclude from these papers that the high flow rate conditions only ensure the absence of a static bed, and the worst situation occurs at low flow rates. Different opposite factors work at different flow rates, causing the resulting behavior of CWS with respect to dynamic stability; they are summarized in Table 3.A.3.

Usually the increasing stability factors tend to be more efficient at high flow rates. To be sure of stability at low rates one should use a quasi-static condition, which is not convenient for practical applications.

Table 3.A.3. CWS Dynamic Stability

	Low Flow Rate	High Flow Rate
Increasing stability	High structuration state	High horizontal momentum High efficiency of sediment transport
Decreasing stability	Low horizontal momentum Low efficiency of sediment transport	Low structuration state

3.A.6 Conclusions

Computer codes developed by Snamprogetti can describe all the possible pipeline flow configurations relevant to high concentrated CWS transportation. The homogeneous flow model can handle the complex rheological behavior, allowing the prediction of high inlet pressures realized during different startup phases.

The heterogeneous dynamic flow model can follow the formation of a sediment bed on the pipe bottom, describing the time evolution at different pipe locations. It can define the stability flow condition range for a certain suspension, and it can drive the pigging operations in case of unstable flow regime occurrence.

Notation

τ: shear stress (Pa)
τ_{00}, τ_{01}: Cheng–Evans shear stress parameters (Pa)
K_0, K_1: Cheng–Evans consistency parameters (Pa·s^N)
N: Cheng–Evans exponent
$\dot{\gamma}$: shear rate (s^{-1})
ρ: CWS density (kg/m^3)
p: pressure (Pa)
u: fluid thread velocity (m/s)
U: mean flow velocity (m/s)
r: radial coordinate (m)
x: longitudinal coordinate (m)
Q: volume flow rate (m^3/s)
R: pipe radius (m)
A: concentration fluidizing agent dissolved in water
B: concentration of the dispersant adsorbed in the active way
C: concentration of the inert fraction
P_0: dissipated power in the degradation model
B_0, ω: microscopic degradation model's constants
Re_p: settling particle Reynolds number $= \frac{\rho_p U_p D}{\mu_f}$
ρ_p: settling particle density (kg/m^3)
U_p: settling particle velocity (m/s)
D: settling particle diameter (m)
μ_f: fluid dynamic viscosity (Pa·s)
$\hat{\tau}$: viscous stress tensor (Pa)
$\vec{F}_p$: drag force on settling particle (N)
$\vec{n}$: unit vector normal to surface S
dS: surface integration element (m^2)

S_p: settling particle surface (m^2)
$\widehat{\Delta}$: shear rate tensor (s^{-1})
$\widehat{\Delta} : \widehat{\Delta}$: shear rate double tensor product (s^{-2})
K: time-independent Herschel–Bulkley consistency index ($Pa \cdot s^N$)
τ_0: time-independent Herschel–Bulkley yield stress (Pa)
N: time-independent Herschel–Bulkley exponent
$\vec{V}, V$: perturbed velocity field (m/s)
ϕ: solid volume concentration
ϕ_{max}: maximum packing solid volume concentration
ρ_s: solid density (kg/m^3)
ρ_f: fluid density (kg/m^3)
V_i: absolute settling velocity of particles belonging to grain size group with mean diameter d_i (static settling program) (m/s)
V_f: fluid velocity (stating settling program) (m/s)
W_i: relative settling velocity of particles belonging to grain size group with mean diameter d_i (static settling program) (m/s)
d_i: mean diameter of ith grain size group (static settling program)
W_{0i}: relative settling velocity of a single particle with diameter d_i in a still unbounded fluid (static settling program) (m/s)

References

1. Beris, A.N., Tsamopoulos, J.A., and Armstrong, R.C., Creeping motion of a sphere through a Bingham plastic, *J. Fluid Mech.*, **158**, 219–44 (1985).
2. Carniani, E., Donati, E., Ercolani, D., and Ferroni, E., and Gabrielli, G., Influence of mineral matter on CWS characteristics, *14th Int. Tech. Conf. on Coal & Slurry Technology,* Clearwater, Fl., USA, 553–64 (1989).
3. Chabra, R.P., *Bubbles, Drops and Particles in Non-Newtonian Fluids*, CRC Press, Boca Raton, Fl., (1993).
4. Cheng, D.C.H., Yield stress: A time dependent property and how to measure it, *Stevenage: Warren Spring Laboratory*, Report n. LR 540 (MH) (1985).
5. Cheng, D.C.H., and Evans, F., Phenomenological characterization of the rheological behaviour of inelastic reversible thixotropic and antithixotropic fluids, *Br. J. Appl. Phys.* **16**, 1599 (1965).
6. Cheng, D.C.H., and Whittaker, W., The start-up flow of thixotropic fluids in pipelines, *Stevenage: Warren Spring Laboratory*, Report n. LR 155 (MH) (1972).

7. De Angelis, E., Modelli stazionari e non stazionari per fluidi di Bingham in viscosimetro e in condotta, *Ph.D. Thesis*, Univ. of Florence (1996).
8. De Angelis, E., Fasano, A., Primicerio, M., Rosso, F., and Carniani, E., Sedimentation bed dynamics for fluids with yield stress in a pipe, *Quarto Convegno Internazionale di Fluidodinamica Multifase nell'Impiantistica Industriale*, Ancona-Italy, 85–93 (1994).
9. Dedegil, M.Y., Drag Coefficient and Settling Velocity of Particles in Non-Newtonian Suspensions, *International Symposium on Slurry Flows* **38**, *107th American Mechanical Engineering*, Anaheim, Calif., USA, 9–15 (1986).
10. Ercolani, D., Terenzi, A., Weber, M., and Dedegil, M.Y., Mathematical simulation of the sedimentation of heterogeneous particles in a highly concentrated suspension, *The Second Italian Conference on Chemical and Process Engineering*, Firenze-Italy (1995).
11. Fasano, A., A mathematical model for the dynamics of sediments in pipeline, *Proceedings of the 7th ECMI Conference* 1994, edited by H. Neunzert, Wiley & Teubner, 241–9 (1996).
12. Fasano, A., Pipeline of liquid fuels with peculiar rheological properties, *2nd Alan Tyler Memorial Lecture*, ECMI 98, edited by S. Bergh et al., Teubner, (1998).
13. Fasano, A., Manni, C., and Primicerio, M., Modelling the dynamics of fluidizing agents in coal-water slurries, *Proceedings of the International Symposium on Nonlinear Problems in Engineering and Science*, edited by Shutie Xiao and Xiang-Cheng Hu, Science Press, Beijing, 64–71 (1991).
14. Happel, J., and Brenner, H., *Low Reynolds Number Hydrodynamics*, Kluwer Academic Publishers, Boston (1983).
15. Mancini, A., Evolution of sedimentation profiles in the transport of CWS through a pipeline, *Progress in Ind. Math.* (ECMI 96), edited by M. Brons et al., Teubner 1997, 442–9.
16. Rosso, F., Sedimentation of impurities during the pipelining of coal-water slurries, *Complex Flows in Industrial Processes*, MSSET series, Birkhauser (1999).
17. Terenzi, A., Carniani, D., and Ercolani, D., CWS fluid dynamics experimental activity in pilot plant, *Quarto Convegno Internazionale di Fluidodinamica Multifase nell'Impiantistica Industriale*, Ancona, Italy, 94–108 (1994).
18. Terenzi, A., Ercolani, D., and Carniani, D., Determinazione teorico-sperimentale di profili di velocità nel moto in condotta di sospensioni solido-liquido non-newtoniane, *Impiantistica Italiana, Anno VII n.* **3**, 159–68 (1995).

19. Terenzi, A., Ercolani, D., and Carniani, E., Rheological properties and settling behaviour influences in CWS pipeline flow, *21th Int. Tech. Conf. on Coal Utilization & Fuel Systems*, Clearwater, Fl., USA, 645–56 (1996).

20. Terenzi, A., Ercolani, D., Lapasin, R., and Alessandrini, A., Modelli di flusso in condotta di miscele acqua-carbone, *Terzo Convegno internazionale di Fluidodinamica Multifase nell'Impiantistica Industriale*, Castelnuovo di Garfagnana (LU)-Italy, 135–52 (1992).

21. Terenzi, A., Ercolani, D., Lapasin, R., and Alessandrini, A., Pipeline flow models of coal-water slurries, *18th International Technical Conference on Coal Utilization & Fuel Systems*, Clearwater, Florida, USA, 703–19 (1993).

Part B: Transient Compressible Flow at High Mach Numbers: A Conservative Method for Pipeline Flow

ABSTRACT. *A computer code called Machnet has been developed to predict phenomena occurring during transient phases associated with gas pipeline flow at high Mach numbers. Rapid depressurization of vessels and pipelines is a representative example of this fluid mechanical condition. The code is based on a one-dimensional conservative approach derived from the Godunov scheme, with a first-order explicit time integration. It includes a treatment of friction and heat exchange effects and a description of valves and orifices installed in the pipes. Section changes are also analyzed, and the boundaries are simulated considering their real shape within the numerical method used for the interior cells, without resort to characteristics. The adopted thermodynamic model refers to the perfect gas scheme with correction factors taking care of real behavior.*

Comparisons are shown between Machnet simulations and analogous calculations from other programs or with available experimental data.

3.B.1 Introduction

A design procedure for gas transporting systems should include an analysis of transient phenomena occurring during blowdown operations, which could generate critical flow conditions at high Mach numbers (>0.2). The

designer should be able to predict the pressure of shock waves traveling in the pipeline and to evaluate their strength and effect on the entire system and on devices and fittings installed in the tube. Furthermore, very low temperatures can be reached in downstream valves and orifices, due to gas expansion, and pipe wall material may overcome the brittle-fracture point. Three-dimensional codes integrating the full set of motion equations can simulate such kinds of flow problems, but they should require a dense calculation grid to handle complex piping systems with size typical of gas compression stations, causing very large calculation times and difficulty with input operations. Therefore the codes are suitable for representing small parts of plants, provided appropriate closure relationships are selected (e.g., realistic turbulence models). Thus the need for a one-dimensional "user-friendly" code becomes apparent; nevertheless in this case information relevant to multidimensional flow configurations must be added to this simpler calculation scheme.

A computer program of this kind called Machnet has been developed (see [19]), and the three-dimensional code FLUENT version 4.4 has been used to supply complex motion definitions in fitting and boundary areas. This code was used to simulate several transient flow conditions referring to the schematic system reported in Figure 3.B.1; the vessel can be considered either as a static region where total and static quantities coincide or as a pipe with a larger size than the venting downstream tube where gas motion occurs.

A discharge process can be divided in two parts: First a "strong wave period," during which large-amplitude waves propagate across the piping system, is followed by a "quasi-steady period" when quasi-steady configurations are generated after the mutual interaction and boundary reflection of traveling waves, which eventually achieve a final equilibrium state. Because possible shock waves and contact discontinuities can be present in the flow field, a conservative form of the equations has been considered.

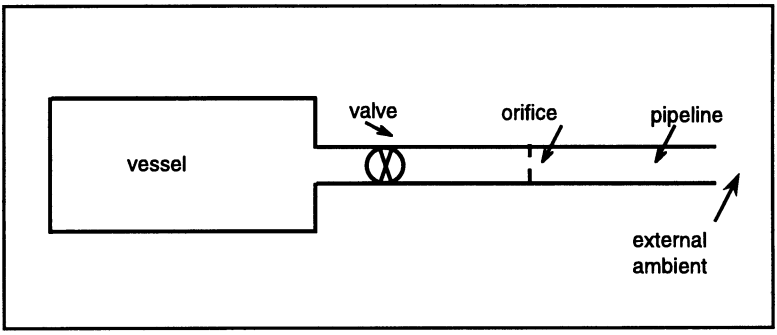

Figure 3.B.1 — Schematic system simulable by Machnet.

In fact, the discretization of the nonconservative form gives rise to internal sources; for continuous flows, these numerical source terms are of the same order as the truncation error and hence can be neglected. However, numerical experiments and comparisons consistently show that nonconservative formulations are generally less accurate than conservative ones, particularly in the presence of strong gradients.

For discontinuous flows, such as transonic flows with shock waves, these numerical source terms can become important across the discontinuity and they give rise to large errors. This is indeed the case, and the discretization of the nonconservative form will not lead to the correct shock intensities. Therefore in order to obtain, in the numerical computation, the correct discontinuities (such as the Rankine–Hugoniot relations for the Euler equation) it has been shown by Lax [12] that it is necessary to discretize the conservative form of the flow equations.

The numerical reference scheme selected is the Godunov method, based on the introduction of physical properties in the discretization process. In Godunov's method, the solution is considered a piecewise constant over each mesh cell at a fixed time, and the evolution of the flow to the next time step results from the wave interactions originating at the boundaries between adjacent cells. The cell interfaces separate two different fluid states, U_L on the left side and U_R on the right side, and the resulting local interaction can be exactly resolved because the initial conditions at time $t = n\Delta t$ corresponds to the Riemann or shock tube problem.

This problem has an exact solution that is generally composed of a shock wave, a contact discontinuity, and an expansion fan separating regions of uniform flow conditions. The solutions to the Riemann problem at each cell interface produce a perturbation of the piecewise constant fluid state, resulting from the propagating waves over the time interval Δt.

Each wave carries information in an upwind manner; hence the resulting state will only depend on the local physical properties. In order to define completely the interaction between adjacent cells, the time interval over which the waves are allowed to propagate should be limited by the condition that the adjacent Riemann problems do not interfere. This leads to a form of CFL condition. This fundamental stability condition of most explicit schemes for wave and convection equations expresses that the distance covered during the time interval Δt by the disturbances propagating with speed c, should be lower than the minimum distance between two mesh points.

This means that the mesh ratio $\Delta t/\Delta x$ has to be chosen in such a way that the domain of dependence of the differential equation should be contained in the domain of dependence of the discretized equation. In other words, the numerical scheme defining the approximation in each mesh point must be able to include all the physical information that influences the behavior of the system at the same point.

The new piecewise constant approximation at time $t = (n+1)\Delta t$ is then obtained by averaging, over each cell, the fluid states resulting from the perturbation waves. This produces an explicit conservative scheme, which is, however, of first-order accuracy as will be shown next. Actually Godunov's scheme was the first successful conservative upwind scheme.

Because the exact solution of the Riemann problem requires the resolution of a nonlinear algebraic equation, which can be quite time-consuming, approximate Riemann solutions could be considered, reducing the computation work at each interface. The approximate solver selected in this work is Roe's method.

3.B.2 Governing Equations

The most general flow conditions representing compressible flow are described by the Navier–Stokes equations, including spatial area change, friction, and thermal exchange terms, which in their one-dimensional form are [8]:

$$\frac{\partial \rho}{\partial t} + \frac{\partial(\rho u)}{\partial x} = -\frac{1}{S}\frac{dS}{dx}\rho u \tag{3.B.1}$$

$$\frac{\partial(\rho u)}{\partial t} + \frac{\partial(\rho u^2 + p)}{\partial x} = -\frac{1}{S}\frac{dS}{dx}\rho u^2 + \tau \tag{3.B.2}$$

$$\frac{\partial(\rho E)}{\partial t} + \frac{\partial(\rho u H)}{\partial x} = -\frac{1}{S}\frac{dS}{dx}\rho u H + q_H \tag{3.B.3}$$

where ρ is the density, u the velocity, p the pressure, S the pipe internal cross section, and E and H the total energy and enthalpy per unit mass, respectively, given by the following:

$$E = e + \frac{u^2}{2} \tag{3.B.4}$$

$$H = e + \frac{p}{\rho} + \frac{u^2}{2} \tag{3.B.5}$$

where e is the internal energy per unit mass.

τ and q_H are the source terms due to friction and thermal exchange between gas and pipe wall, given by:

$$\tau = -\frac{f}{R_p}\rho u^2 \tag{3.B.6}$$

$$q_H = -\widehat{h}_i(T_{\text{aw}} - T_{\text{wall}}) \tag{3.B.7}$$

where f is the Fanning friction factor, R_p the pipe internal radius, $\widehat{h}_i$

the surface corrected internal heat transfer coefficient, and T_{aw} and T_{wall} the adiabatic wall and internal pipe wall temperatures, respectively. The adiabatic wall temperature (cfr. [13], [18]) is defined on the basis of the recovery factor $\mathcal{R}$, which is a measure of the fraction of the local free stream dynamic temperature rise recovered at the wall; as a function of the bulk gas temperature T and its specific heat at constant pressure C_p it is:

$$T_{\text{aw}} = T + \frac{\mathcal{R}}{2}\frac{u^2}{C_p} \tag{3.B.8}$$

In this work the Colebrook–White correlation for the friction factor covering both smooth and rough pipes is assumed ([1], [9]):

$$\frac{1}{\sqrt{4f}} = -2\log\left[\frac{\epsilon}{3.7D_p} + \frac{2.51}{\text{Re}\sqrt{4f}}\right] \tag{3.B.9}$$

where Re is the pipe Reynolds number based on diameter D_p and ϵ is the pipe roughness.

Friction and heat exchange effect, in a negligible way, the flow field during the "strong wave period," thus the Euler system of equations should be a reasonable approximation in this condition. The Navier-Stokes equations in conservative form result in:

$$\frac{\partial \mathbf{U}}{\partial t} + \frac{\partial \mathbf{F}}{\partial x} = \mathbf{Q} \tag{3.B.10}$$

where the conservative variables vector $\mathbf{U}$ is:

$$\mathbf{U} = \begin{bmatrix} U_1 \\ U_2 \\ U_3 \end{bmatrix} = \begin{bmatrix} \rho \\ \rho u \\ \rho E \end{bmatrix} \tag{3.B.11}$$

and the flux vector $\mathbf{F}$ is:

$$\mathbf{F} = \begin{bmatrix} F_1 \\ F_2 \\ F_3 \end{bmatrix} = \begin{bmatrix} \rho u \\ \rho u^2 + p \\ \rho u H \end{bmatrix}. \tag{3.B.12}$$

The source vector $\mathbf{Q}$ is the summation of the area change plus friction and thermal exchange terms:

$$\mathbf{Q} = \mathbf{Q}_S + \mathbf{Q}_{fq} \tag{3.B.13}$$

$$\mathbf{Q}_S = \begin{bmatrix} -\chi F_1 \\ -\chi(F_2 - p) \\ -\chi F_3 \end{bmatrix} \tag{3.B.14}$$

$$\mathbf{Q}_{fq} = \begin{bmatrix} 0 \\ -\dfrac{f}{R_p}\dfrac{U_2^2}{U_1} \\ -\widehat{h}_i\left[\dfrac{(\gamma-1)}{RU_1}\left(U_3 - \dfrac{1}{2}\dfrac{U_2^2}{U_1}\right)\left(1 + \dfrac{\mathcal{R}}{2}\dfrac{u^2}{C_p}\right) - T_{\text{wall}}\right] \end{bmatrix} \tag{3.B.15}$$

where χ is the area change term $\frac{1}{S}\frac{dS}{dx}$ and the gas temperature in the thermal convective flux has been expressed using the perfect gas assumption

$$T = \frac{p}{R\rho} \tag{3.B.16}$$

$$p = (\gamma - 1)\rho e = (\gamma - 1)\left[U_3 - \frac{1}{2}\frac{U_2^2}{U_1}\right] \tag{3.B.17}$$

where R is the gas constant and γ the isentropic coefficient given by the specific heat ratio.

3.B.3 Heat Transfer

Concerning the heat transfer process for the gas flowing along the pipe, the Sieder–Tate correlation has been assumed to define the internal heat transfer coefficient by forced convection ([2], [17], [20]):

$$Nu = 0.026(\text{Pr})^{1/3}(\text{Re}^{0.8}) \tag{3.B.18}$$

where the symbols are Nusselt, Reynolds, and Prandtl numbers, respectively. In case of internal convection for still gas the heat transfer coefficient is defined according to Ford approach (see [4]). The radial conduction process through the pipe layers is described by solving the Fourier equation in cylindrical geometry:

$$\rho_l C_{pl}\frac{\partial T}{\partial t} = \frac{1}{r}\frac{\partial}{\partial r}\left(rk_l\frac{\partial T}{\partial r}\right) \tag{3.B.19}$$

where ρ_l, C_{pl}, and k_l are the layer density, specific heat at constant pressure, and thermal conductivity, and r is the radial coordinate. The external heat transfer coefficient is calculated by using referenced correlations for different environments (see [10]).

3.B.4 Numerical Method

In order to define the solution at time $t = (n+1)\Delta t$ of the system (3.B.10) from the known solution at $t = n\Delta t$, the Godunov method builds up a piecewise constant approximation of the last one. Because the piecewise constant approximation is an average of the solution over the cell of size Δx, the spatial error is of the order Δx, and hence the resulting scheme will be first-order accurate in space. Note that the approximation corresponds to a finite volume representation whereby the discrete values represent the average of the state variables over the cells.

Exact relations for the average cell values can be obtained from the integral conservation laws. Integrating the scalar conservation equation $\partial U/\partial t + \partial F/\partial x = Q$ over x in the domain $(\overline{a}, \overline{b})$ gives the general relation:

$$\frac{d}{dt}\int_{\overline{a}}^{\overline{b}} U(x,t)\,dx = F(\overline{a},t) - F(\overline{b},t) + \int_{\overline{a}}^{\overline{b}} Q\,dx \tag{3.B.20}$$

and if further integrated in time, from $t = n\Delta t$ to $t = (n+1)\Delta t$, we obtain the exact relation:

$$\int_{\overline{a}}^{\overline{b}} U^{n+1}(x)\,dx - \int_{\overline{a}}^{\overline{b}} U^{n}(x)\,dx = -\Delta t\left[\widehat{F}(U(\overline{b})) - \widehat{F}(U(\overline{a}))\right] + \int_{n\Delta t}^{(n+1)\Delta t} dt \int_{\overline{a}}^{\overline{b}} Q\,dx \tag{3.B.21}$$

where $\widehat{F}$ is the time average of the physical flux between $n\Delta t$ and $(n+1)\Delta t$. Defining the average state variable over the cell $(i-\frac{1}{2}, i+\frac{1}{2})$ as:

$$\overline{U}_i = \frac{1}{\Delta x}\int_{i-1/2}^{i+1/2} U(x,t)\,dx \tag{3.B.22}$$

the integral conservation relation (3.B.21) becomes

$$\overline{U_i^{n+1}} - \overline{U_i^{n}} = -\frac{\Delta t}{\Delta x}\left[\widehat{F}(U_{i+1/2}) - \widehat{F}(U_{i-1/2})\right] + \frac{1}{\Delta x}\int_{n\Delta t}^{(n+1)\Delta t} dt \int_{\overline{a}}^{\overline{b}} Q\,dx \tag{3.B.23}$$

This is an exact relation in conservation form. It expresses the variation,

over the time interval Δt, of the cell-averaged state variables as resulting from the balance of time-averaged fluxes at the boundaries of the cell. The numerical flux of the scheme is to be considered as an approximation to the time average of the physical flux at the cell interfaces and the mesh point variables U_i^n as a representation of the cell averages.

For the friction and heat transfer source terms the following statement can be written:

$$Q = Q(U). \tag{3.B.24}$$

The spatial average over the calculation cell can be made in a way that is similar to state variable averaging:

$$\overline{Q} = \frac{1}{\Delta x} \int_{i-1/2}^{i+1/2} Q(\overline{U}_i)\, dx = Q(\overline{U}_i) \tag{3.B.25}$$

considering $U = \overline{U}_i$ over the cell. The time average can be carried out considering the friction and heat transfer contributions become noticeable during the quasi-steady period only:

$$\int_{n\Delta t}^{(n+1)\Delta t} Q(\overline{U}_i)\, dt = \Delta t \cdot Q(\overline{U_i^n}). \tag{3.B.26}$$

That is, the source term is evaluated on the basis of the state variable at time $n\Delta t$. For the area change source term concerning the mass and energy conservation equations, the spatial average is

$$-\int_{\overline{a}}^{\overline{b}} F(U) \cdot \chi\, dx = -F_i(U)\chi \Delta x \tag{3.B.27}$$

with

$$F_i(U) = \frac{1}{2}\left[F(\overline{a}, t) + F(\overline{b}, t)\right]. \tag{3.B.28}$$

The time average of (3.B.27) can be carried out on the basis of (3.B.28), considering the time average of physical flux:

$$-\int_{n\Delta t}^{(n+1)\Delta t} F_i(U)\chi\, dt = -\chi \frac{\Delta t}{2}\left[\widehat{F}(U_{i+1/2}) + \widehat{F}(U_{i-1/2})\right]. \tag{3.B.29}$$

This is the final expression for the area change source term appearing in the integrated conservation equations. For the momentum equation the flux term F must be replaced by:

$$\Phi = F - p. \tag{3.B.30}$$

Following the procedure outlined by (3.B.27) to (3.B.29) the corresponding integrated source term is:

$$-\chi\frac{\Delta t}{2}\left[\widehat{\Phi}(U_{i+1/2})+\widehat{\Phi}(U_{i-1/2})\right] \tag{3.B.31}$$

The following assumption on the area change spatial rate has been made:

$$\chi = \text{constant.} \tag{3.B.32}$$

This means the area changes in an exponential way inside each cell. The solution for the local Riemann problem at cell interfaces represents the physical step of the whole procedure. The discontinuities at the interfaces are resolved in a superposition of waves satisfying locally the conservation equations. A description of different configurations giving the complete solution of the Riemann problem is reported in Appendix A.

Because the exact solution of the Riemann problem requires resolution of a nonlinear algebraic equation, which can be quite time-consuming, approximate Riemann solutions have been considered, and Roe's method has been selected. The approximate Riemann solver developed by Roe [16] is based on a characteristic decomposition of the flux differences. While ensuring the conservation properties of the scheme, Roe's approach is an ingenious way of extending the linear wave decomposition, which is the exact linear solution to Riemann's problem, to nonlinear equations.

In this method the following expressions for the interface fluxes referred to cell i results:

$$F^*_{i+1/2} = F_i + \widetilde{A}^-(U_{i+1} - U_i) \tag{3.B.33}$$

$$F^*_{i-1/2} = F_i - \widetilde{A}^+(U_i - U_{i-1}) \tag{3.B.34}$$

The matrix $\widetilde{A}$ represents the local Jacobian expressed as a function of the variables ρ, u, H replaced by an average weighted by the square root of densities; $\widetilde{A}^+$ and $\widetilde{A}^-$ are built by negative and positive eigenvalues contributions.

The resulting expression of the first-order explicit upwind Roe method for the Navier-Stokes equations is:

$$U_i^{n+1} - U_i^n = -\frac{\Delta t}{\Delta x}\left[F^*_{i+1/2} - F^*_{1-1/2}\right] + (\textit{source term}) \tag{3.B.35}$$

where the interface flux difference based on (3.B.33) to (3.B.34) is:

$$\widetilde{A}^-_{i+1/2}(U_{i+1} - U_i) + \widetilde{A}^+_{i-1/2}(U_i - U_{i-1}) \tag{3.B.36}$$

The source term definition developed for the basic Godunov scheme remains valid with this approach.

Table 3.B.1

	Subsonic	Supersonic
Inlet	p, ρ	p, ρ, u
Outlet	p	—

3.B.5 Boundary Conditions

The classical treatment of boundaries in one-dimensional flows is based on the characteristic boundary method, which adds the Riemann invariants for the outgoing characteristics to the imposed physical boundary conditions. Referring to the primitive variables p, ρ, u the physical boundary conditions are imposed depending on the type of boundary flow, on the basis of Table 3.B.1.

A first application of the characteristic method was based on the space extrapolation of the characteristic variables within the actual scheme founded on conservative variables and boundary conditions imposed on the primitive variables; this method was adopted by Yee et al. [21].

However, the interaction of propagating shock waves with this kind of boundary was found to generate a nonphysical solution with spurious excess energy generation in the boundary cells; this numerical error has been explained by the wrong extrapolation of characteristic variables across a shock because in this case they should not remain constant.

Therefore a new treatment of boundary conditions has been used, on the basis of the complete physical definition of corresponding flow regions. If a pipe connecting a vessel to atmosphere is considered, the pipe inlet can be outlined through a convergent variable area region from the cell having the static vessel state to the first cell of the pipe where flow with a velocity relevant to its cross section occurs. At the pipe outlet an exit jet is located, with a generally divergent cross section passing from the last cell of the pipe to external ambient conditions. In this way the use of characteristics is avoided, and all flow regions are calculated by the same numerical method. In the following the modeling of the exit jet is described.

3.B.6 Exit Jet

If the model of pipe connecting a vessel to atmosphere is analyzed with the assumption of isentropic flow, its fluid mechanical configuration can

be referred to as the isentropic nozzle scheme, which narrows continually toward its end, so that the minimum cross-sectional area is at that end. If we indicate with p_V and p_e pressure values relevant to vessel static conditions and external ambient, respectively, the flow inside the tube is subsonic only if the following condition is verified:

$$\frac{p_e}{p_V} > \left(\frac{2}{\gamma+1}\right)^{\gamma/(\gamma-1)} \tag{3.B.37}$$

In this case, in steady flow, the pressure in the pipe is equal to p_e, and the whole of the pressure drop p_V to p_e occurs in the inlet convergent section. If $p_e = p^*$, that is, if

$$p_e = p^* = \left(\frac{2}{\gamma+1}\right)^{\gamma/(\gamma-1)} p_V \tag{3.B.38}$$

the pipe flow velocity becomes equal to the local velocity of sound, and the discharge reaches its maximum. When the external pressure decreases further, the pipe pressure remains constant at p^*, and the fall of pressure from p^* to p_e occurs outside the tube, in the surrounding medium. In other words, the pressure drop along the tube cannot be greater than from p_V to p^*, whatever the external pressure.

The exit jet definition introduced in Machnet has been carried out in order to reproduce the correct sonic/subsonic flow configurations and to generate the correct boundary behavior concerning wave reflection. Referring to the exit jet shape, direct observation of jets of pipes discharging to atmosphere suggests this flow region can be divided in two parts:

- a first regular conical jet with a fixed span angle;
- a second irregular section where gas passes from the flow conditions to the infinite ambient state.

The last transition has been defined through a large area change, and a friction factor is calculated in a such a way that the gas loses all its kinetic energy. The first jet section must be described more accurately in order to satisfy the above requirements. For the span angle the Schlieren photographs of flow from a supersonic nozzle at different back pressures reported by Liepmann and Roshko [14] have been used to fix its dependence on the flow parameters.

Machnet can run using an outlet characteristic method when shock waves are absent, as an alternative to the jet model. While the jet model is built in such a way as to reproduce all flow configurations, with the characteristic method the sonic/subsonic transition must be determined

performing the following test:

$$\frac{p_e}{p_{\text{out}}} > \left(\frac{2}{\gamma+1}\right)^{\gamma/(\gamma-1)} \Rightarrow \begin{array}{ll} \text{IF YES:} & \text{use subsonic characteristics} \\ \text{IF NO:} & \text{use sonic characteristics} \end{array} \tag{3.B.39}$$

where p_{out} is the total pressure of the fluid element leaving the end of the tube.

3.B.7 Orifices and Valves

The presence of an intermediate orifice has been provided in Machnet. The streamlines trend near this fitting consists in a convergent region before it that is followed by a divergent jet extending for a certain length until the full section flow is reached. In this way it assumes the shape of a nozzle. The total length of the orifice divergent region L_D has been identified as the length of the steady shock wave region downstream a nozzle as defined by Shapiro [18].

The following correlation of Shapiro's experimental data results:

$$\frac{L_D}{D_p} = 5.3015 \ln(M_U) + 5.2925 \tag{3.B.40}$$

where M_U represents the Mach number preceding shock.

The orifice friction factor is defined according to the correlation between mass flow rate and pressure drop, relevant to compressible steady flow through orifices, reported by Crane [3]:

$$W = 0.0003512(YC)d_1^2\sqrt{\Delta p_{UD}\rho_U} \tag{3.B.41}$$

where Y and C are the net expansion factor and the flow coefficient for square edge orifices, d_1 is the orifice diameter, ρ_U the gas density 1 diameter upstream of the orifice, and Δp_{UD} the pressure drop between points 1 diameter upstream and 0.5 diameter downstream of the orifice.

The presence of large variations of physical quantities near the orifice location involves the use of an irregular grid with narrowing spatial steps near high gradient regions. Machnet can simulate the opening process of a valve in a finite time, in addition to the instantaneous opening of an ideal valve or a rupture diaphragm. In the region surrounding the valve a time area changing term is present in the equations of motion; the energy and mass conservation equations, when expressed with the flow cross section

factor S yield

$$\frac{\partial U}{\partial t} + \frac{\partial F}{\partial x} + \frac{U}{S}\frac{\partial S}{\partial t} + F\chi = Q \tag{3.B.42}$$

By putting

$$\widehat{Q} = Q - F\chi \tag{3.B.43}$$

the discretized expression for the equation of motion (3.B.42) in the conservative variable $U = \overline{U}_i$, is:

$$U^{n+1} = \frac{[1 + \ln S^n - < \ln S >]}{[1 + \ln S^{n+1} - < \ln S >]} U^n - \frac{\Delta t}{\Delta x} \frac{[\widehat{F}(U_{i+1/2}) - \widehat{F}(U_{i-1/2})]}{[1 + \ln S^{n+1} - < \ln S >]}$$
$$+ \frac{1}{\Delta x} \frac{\iint \widehat{Q}\, dx\, dt}{[1 + \ln S^{n+1} - < \ln S >]}. \tag{3.B.44}$$

where $< \ln S >$ means time averaged value. For the momentum equation the only variation to this analysis is in the formulation of the source term $\widehat{Q}$:

$$\widehat{Q} = Q - \Phi\chi. \tag{3.B.45}$$

3.B.8 Different Boundaries and Gas Models

Machnet can simulate other kinds of boundaries not included in the simplified scheme reported in Figure 3.B.1, namely, a closed wall and a second pipe instead of a static vessel. The closed wall boundary is treated using the symmetry model, relating the conservative variables of the "hidden" cell behind the wall (subscript h) to the variables of the cell interior to the pipe adjacent to the wall (subscript a):

$$\begin{aligned} (U_1)_h &= (U_1)_a \\ (U_2)_h &= -(U_2)_a \\ (U_3)_h &= (U_3)_a \end{aligned} \tag{3.B.46}$$

The pipe replacing the vessel in Figure 3.B.1 can be used when the approximation of static gas in the depressurizing ambient is not more valid; the flow is treated like the venting pipe, considering a variable area region connecting the two pipes. Furthermore a second pipe with a different diameter can be added downstream of the venting pipe; it can be closed end or discharging full bore to the exterior.

Referring to the gas thermodynamic model, a perfect gas scheme with correction factors has been used; these factors are the compressibility Z and the isentropic coefficients γ_V, γ_T (s means constant entropy) defined

in this way (cfr. [15]):

$$\gamma_V = -\left(\frac{V}{p}\right)\left(\frac{\partial p}{\partial V}\right)_s \tag{3.B.47}$$

$$\gamma_T = \frac{m_T}{m_T - 1} \tag{3.B.48}$$

with $m_T = \frac{T}{p}(\frac{\partial p}{\partial T})_s$. Averaged values of these factors in the range of pressures and temperatures considered are used.

3.B.9 Results and Discussion

A complete procedure to validate Machnet should require the availability of experimental profiles relevant to physical quantities measured during transient flow in gas pipelines, and these are very difficult to obtain. Therefore only one test case is presented in conjunction with experimental data; it concerns the blowdown of a vessel containing nitrogen initially at 150 bar (a) and 17°C (cfr. [7]). Other test cases have been simulated with FLUENT 4.4 and PRO II 3.32, providing a comparison with referenced calculation schemes. In the following, a full description of examined test cases is presented. Steady tests calculated by Machnet are limiting results of transient calculations.

Test Case No. 1: Riemann Problem

This test case is the simulation of a Riemann problem for which the analytical solution can be obtained by applying the theory exposed in Appendix A. It refers to a perfect gas with the following properties:

Molecular mass = 18 kg/kmol

Isentropic coefficient = 1.4

and to an initial discontinuity given by (cfr. Appendix A for notation):

$$p_1 = 20.26 \cdot 10^5 \text{ Pa}$$

$$p_4 = 101.3 \cdot 10^5 \text{ Pa}$$

$$T_1 = T_4 = 300 \text{ K}$$

$$u_1 = -400 \text{ m/s}$$

$$u_4 = -200 \text{ m/s}.$$

The solution is composed of a rarefaction wave propagating in the high-pressure side and a shock wave in the low pressure region. The flow direction in the intermediate region is negative, i.e., the gas moves toward the

high-pressure side. From the iterative solution of (3.B.53) the intermediate pressure is about $58.4 \cdot 10^5$ Pa.

In Figure 3.B.2 pressure and density trends relevant to a 10-m-long tube with the initial discontinuity at 5 m are shown; in the density profile the contact wave is manifest. Due to first-order spatial approximation, waves are more smeared in the numerical solution with respect to the analytical one, but the magnitude of pressures, densities, and other physical properties are predicted in the intermediate regions.

Test Case No. 2: Shock Reflection from a Closed End

This test case concerns the interaction of a shock wave with a boundary, namely, a rigid wall. This situation could occur during pipeline flow if a propagating shock is incident on a closed valve.

Let us consider a semi-infinite pipe with an initial discontinuity at 5 m from the wall, located on the low-pressure side. The gas is perfect with the same properties of test case no. 1.

The initial conditions are:

$$\begin{aligned} p_1 &= 20 \cdot 10^5 \text{ Pa} \\ p_4 &= 100 \cdot 10^5 \text{ Pa} \\ T_1 &= T_4 = 300 \text{ K} \\ u_1 &= u_4 = 0 \text{ m/s}. \end{aligned}$$

The solution of this Riemann problem consists of a shock wave propagating in the low pressure region, with the following properties upstream its front:

$$\begin{aligned} p_2 &= 42.5 \cdot 10^5 \text{ Pa} \\ T_2 &= 375 \text{ K} \\ u_2 &= 250 \text{ m/s}. \end{aligned}$$

Shock velocity $= \sqrt{\frac{\gamma+1}{2}\frac{p_2}{\rho_1}} = 595\,\text{m/s}$.

Following Shapiro [18] the ratio of reflected wave pressure p_{ref} to the incident pressure p_2 is given by:

$$\frac{p_{\text{ref}}}{p_2} = \frac{\left(1 + 2\dfrac{\gamma-1}{\gamma+1}\right)\dfrac{p_2}{p_1} - \dfrac{\gamma-1}{\gamma+1}}{\dfrac{\gamma-1}{\gamma+1}\dfrac{p_2}{p_1} + 1} \approx 1.97. \qquad \text{(3.B.49)}$$

Formula (3.B.49) implies $p_{\text{ref}} = 83.7 \cdot 10^5$ Pa.

Figure 3.B.3 represents pressure profiles at different times; the reflected wave has a pressure in perfect agreement with the prescribed value. At successive instants, this pressure level is modified by interaction with the contact wave.

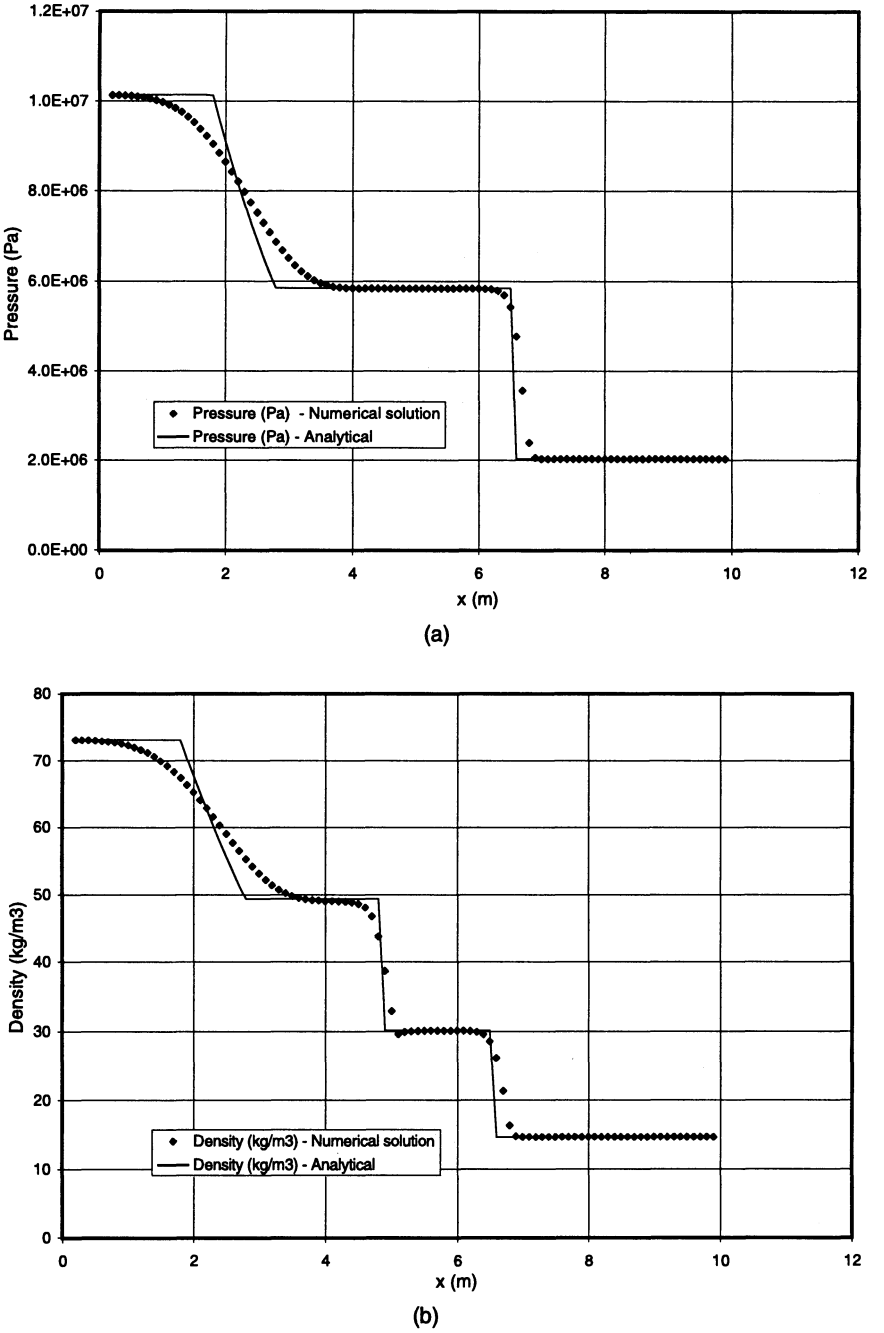

Figure 3.B.2 — Comparison between Machnet numerical solution and analytical solution for a Riemann problem. (a) Pressure waves propagation. (b) Density waves propagation.

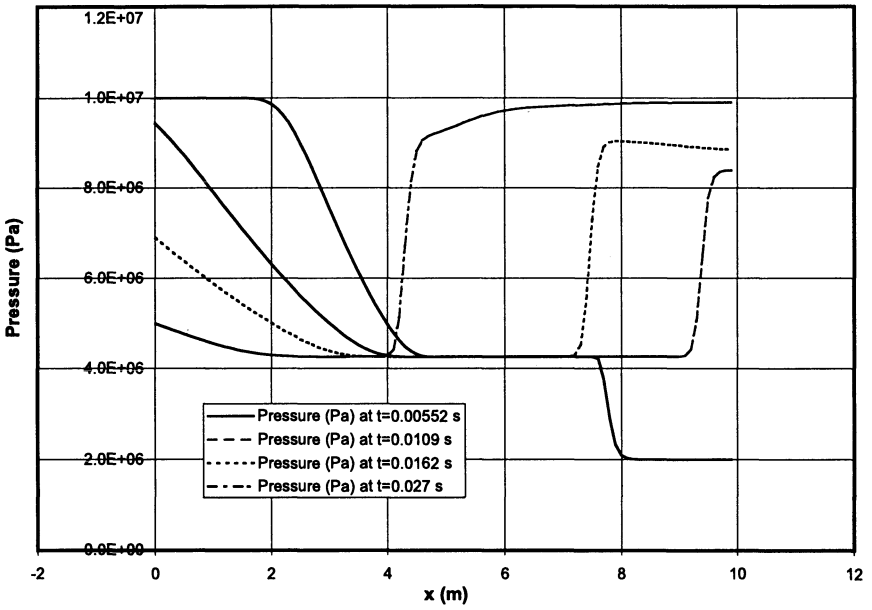

Figure 3.B.3 — Pressure pattern at different times caused by the shock wave reflection process from a closed end.

Test Case No. 3: Pipe with Intermediate Orifice and Large Pressure Jump

In this test case a pipe with an orifice having area ratio 0.25 in an intermediate position has been analyzed. Boundaries are represented by infinite vessels at fixed pressures, and the flow is assumed adiabatic. The fluid considered is natural gas treated as perfect gas with:

Molecular mass = 18 kg/kmol

Isentropic coefficient = 1.3

Geometrical and physical conditions are:

Pipe diameter = 0.2 m

Pipe length = 10 m

Pipe roughness = 25 μm

Orifice position = 4.5 m

Orifice diameter = 0.1 m (area ratio = 0.25)

Upstream vessel pressure = $200 \cdot 10^5$ Pa

Downstream vessel pressure = $1.013 \cdot 10^5$ Pa

Upstream vessel temperature = 273 K

Downstream vessel temperature = 273 K

Gas viscosity = 0.0109 m Pa·s

In Figure 3.B.4 the steady pressure and temperature profiles as calculated by Machnet and FLUENT are shown, providing good agreement between the two codes, considering the different flow description (one or three dimensions).

Test Case No. 4: Double Orifice

In Figure 3.B.5 steady profiles of pressure, temperature, and Mach number relevant to a pipe with two orifices installed along it are shown. The gas is a perfect "corrected" gas with:

Molecular mass = 19.4 kg/kmol

$\gamma_V = 1.3$

$\gamma_T = 1.3$

Viscosity = 0.012 m Pa·s

$Z = 0.8$

The boundary conditions, referring to infinite vessels, are:

Upstream vessel pressure = $66 \cdot 10^5$ Pa

Downstream vessel pressure = $1.013 \cdot 10^5$ Pa

Upstream vessel temperature = 293 K

Downstream vessel temperature = 293 K

The pipe characteristics are:

Pipe diameter = 0.2086 m

Pipe length = 58.5 m

Pipe roughness = 40 μm

The orifice diameters are:

First orifice diameter = 0.062 m

Second orifice diameter = 0.1 m.

A second pipe with a larger diameter is connected to the principal pipe downstream of the second orifice. Its properties are:

Pipe diameter = 0.34 m

Pipe length = 4 m

Pipe roughness = 40 μm.

Diagrams show that sonic conditions occur in four points: the first orifice, second orifice, the section change between two pipes, and the pipe outlet.

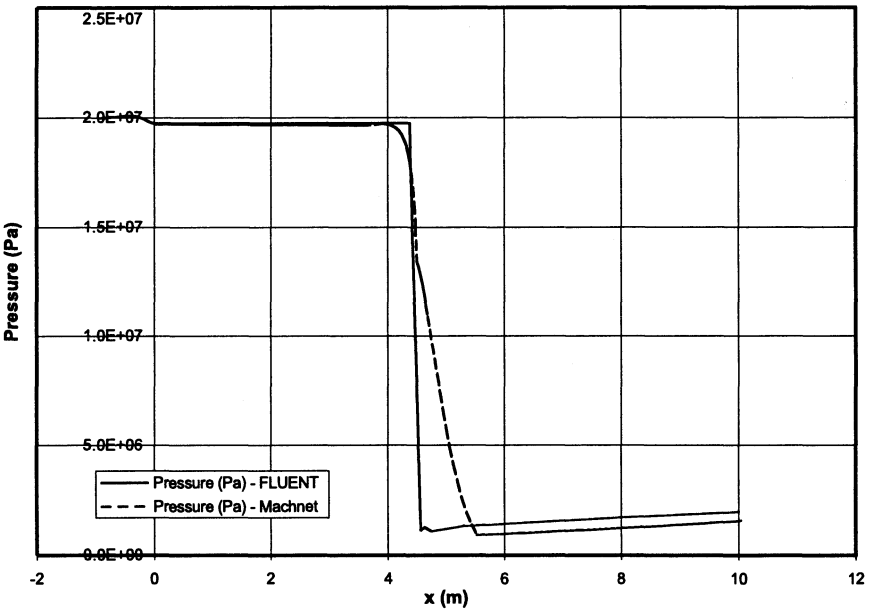

(a)

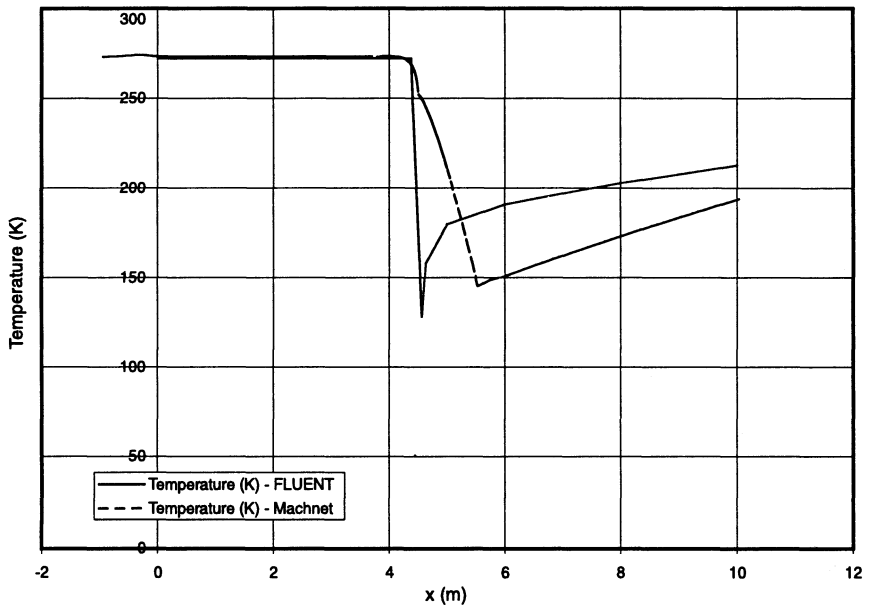

(b)

Figure 3.B.4 — Steady flow in a pipeline with intermediate orifice and high pressure jump. Comparison Machnet vs. FLUENT. (a) Pressure profile. (b) Temperature profile.

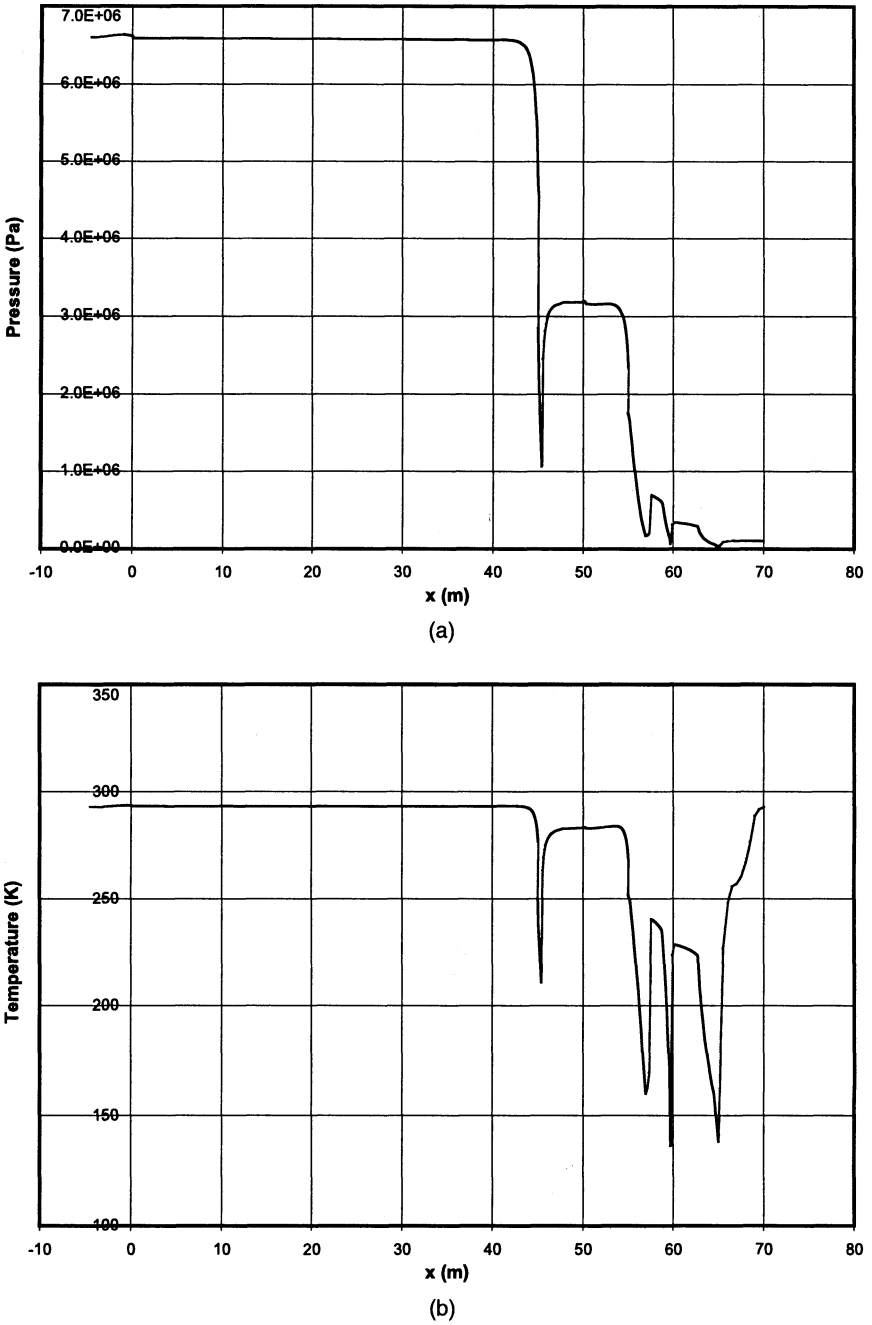

Figure 3.B.5 — Steady flow in a pipeline with two intermediate orifices and a second downstream pipe with a different cross section. (a) Pressure profile. (b) Temperature profile.

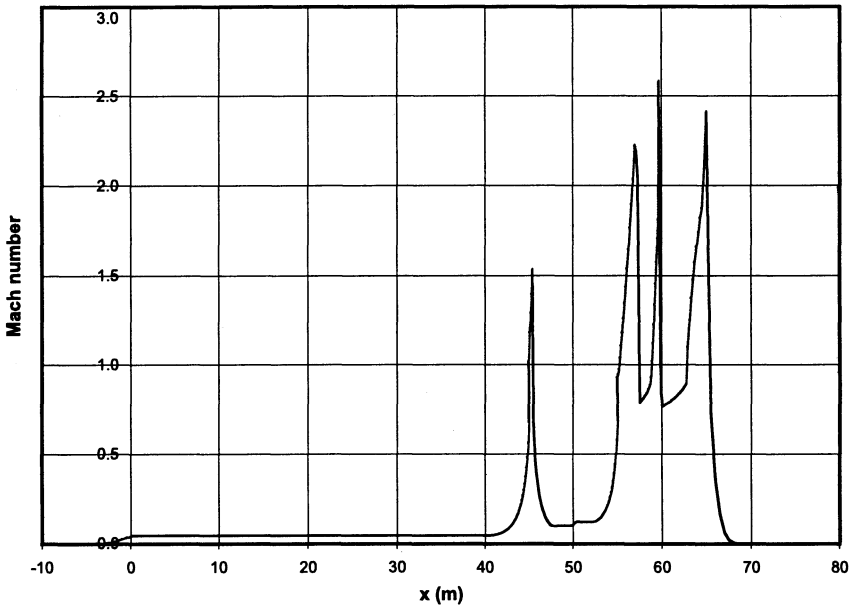

Figure 3.B.5 — (*Continued*) (c) Mach number profile.

The steady mass flow rate value calculated by Machnet is 35.9 kg/s, in good agreement with the mass flow rate calculated on the basis of Crane [3] methods.

Test Case No. 5: Opening of a Valve in a Finite Time

An actual blowdown process occurs through the opening of a valve in a finite time; the associated Riemann problem corresponding to a sudden opening is obviously idealized. A typical opening velocity is 1 inch/s, which is a very long time compared to the time scale of wave propagation in a Riemann problem.

Figure 3.B.6 represents pressure profiles realized during the complete opening of a valve installed in a pipe with the same characteristics of test case no. 3, containing the same gas and with the following boundary conditions:

Upstream vessel pressure $= 1.93 \cdot 10^5$ Pa

Downstream vessel pressure $= 1.013 \cdot 10^5$ Pa

Upstream vessel temperature $= 300$ K

Downstream vessel temperature $= 300$ K

The valve position corresponds to orifice location. The system evolution is determined by the propagation of small amplitude waves; at each instant

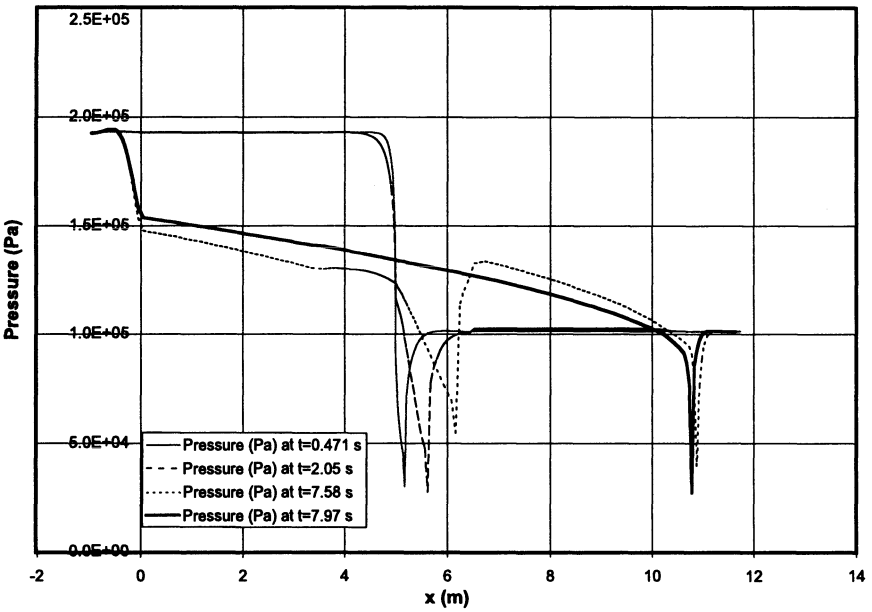

Figure 3.B.6 — Complete opening of a valve with velocity 1″/s. Pressure profiles at different times calculated by Machnet.

the pressure profile seems quasi-steady. In this case the complete opening time is 7.87 s and the pressure profile at 7.97 s is almost the final result of the transient phase. During the opening process the quasi-steady shock wave downstream of the orifice extends in length because of the progressive increase in flow rate.

Test Case No. 6: Adiabatic Blowdown of Vessels

Three calculations are presented here concerning the adiabatic depressurization of vessels, simulated with PRO II to obtain reference results.

Case 6.1: Helium Vessel Venting at 40 Bar

This test is relevant to a vessel of 10 m^3, discharging to the atmosphere through an orifice with a 0.26-m diameter, containing helium initially at $40 \cdot 10^5$ Pa and 473 K. In Figure 3.B.7 pressure, temperature, and mass flow rate time trends are shown. Helium is represented by a perfect gas model with:

Molecular mass = 4 kg/kmol

Isentropic coefficient = 1.66

A good agreement between Machnet and PRO II is observed.

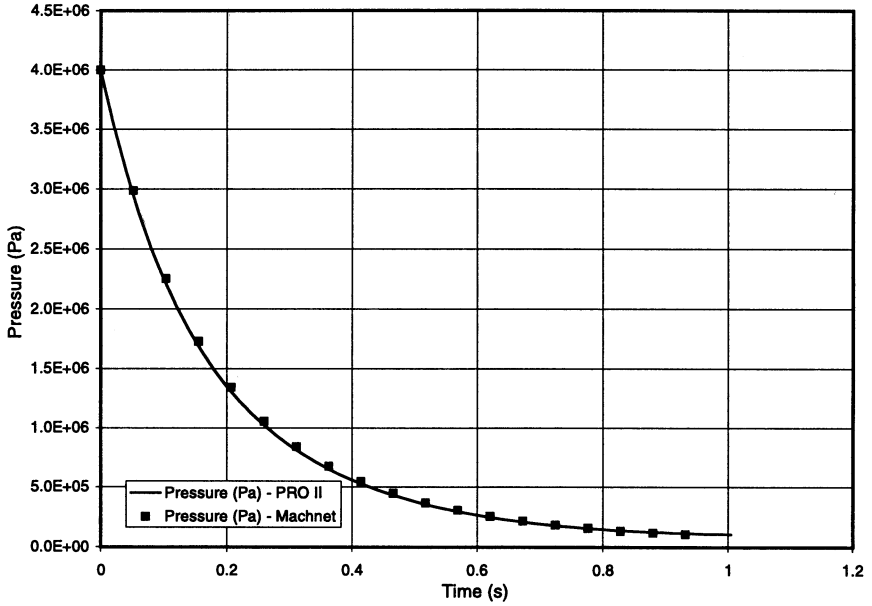

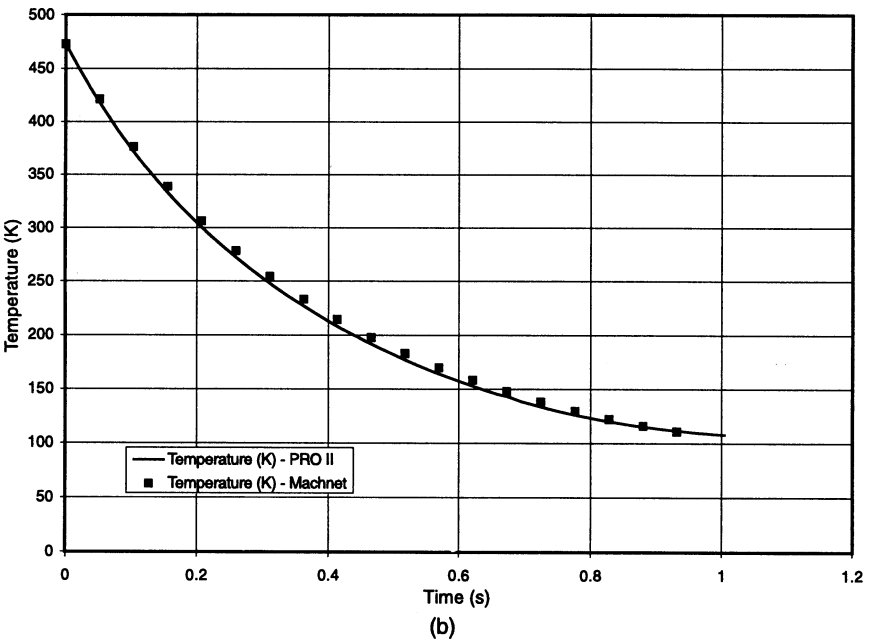

Figure 3.B.7 — Adiabatic vessel venting with helium initially at 40 bar. (a) Pressure time evolution. (b) Temperature time evolution.

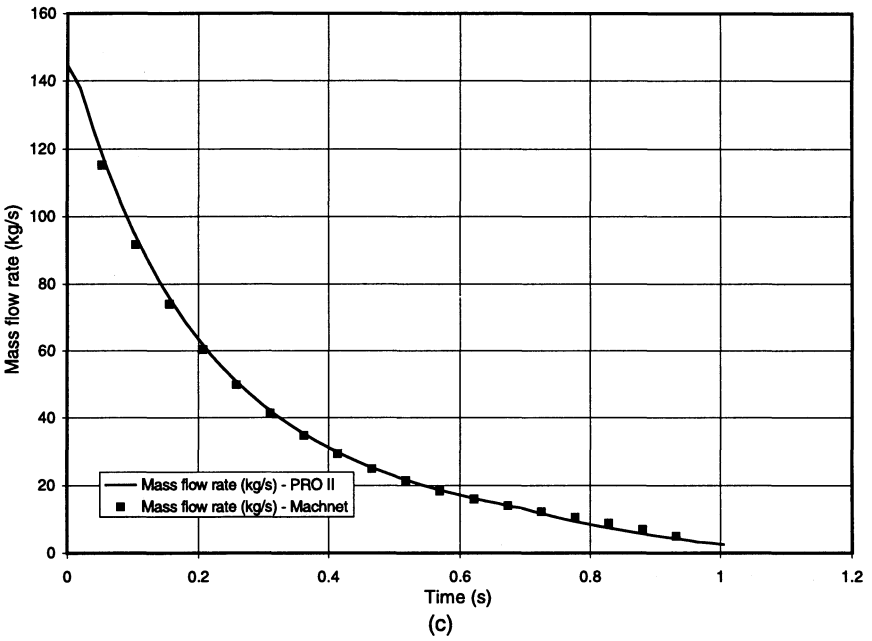

Figure 3.B.7 — (*Continued*) (c) Mass flow rate time evolution.

Case 6.2: Methane Vessel Venting at 65 Bar

This test is relevant to a vessel of 10 m^3, discharging to the atmosphere through an orifice with a 0.26-m diameter, containing methane initially at $65 \cdot 10^5$ Pa and 500 K. In Figure 3.B.8 pressure, temperature, and mass flow rate time trends are shown. Methane is represented by a corrected perfect gas model with

Molecular mass = 16 kg/kmol

$\gamma_V = 1.26$

$\gamma_T = 1.2475$

$Z = 1$

A good agreement between Machnet and PRO II is observed, apart from a deviation of temperature prediction at the end of blowdown, probably caused by an incomplete reproduction of real gas effects by the corrected perfect gas model.

Case 6.3: Methane Vessel Venting at 150 Bar

In this test the blowdown of a vessel of 50 m^3, discharging to an external medium at 20 bar through an orifice with a 0.3-m diameter, containing

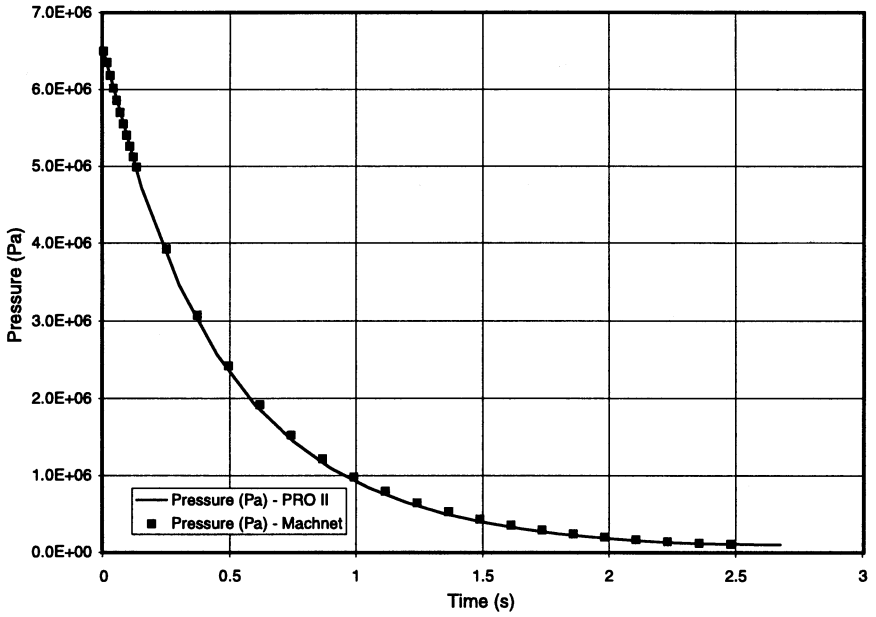

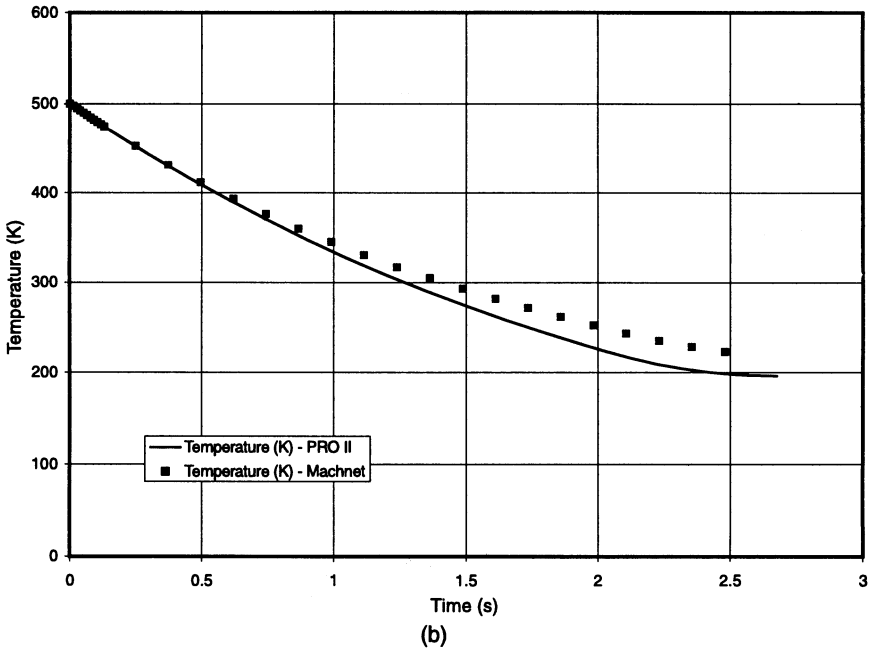

Figure 3.B.8 — Adiabatic vessel venting with methane initially at 65 bar. (a) Pressure time evolution. (b) Temperature time evolution.

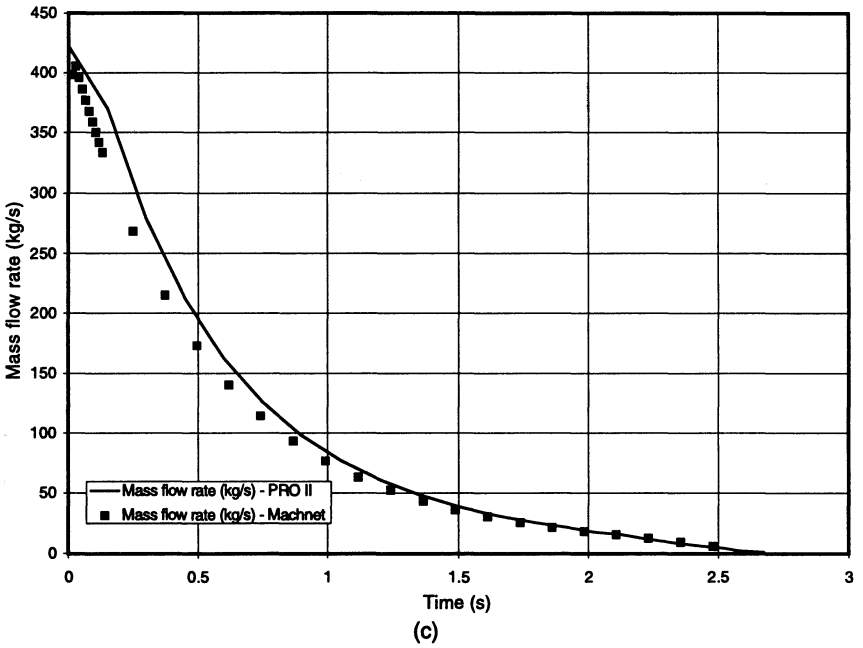

Figure 3.B.8 — (*Continued*) (c) Mass flow rate time evolution.

methane initially at $150 \cdot 10^5$ Pa and 273 K is analyzed. In Figure 3.B.9 pressure, temperature, and mass flow rate time trends are shown. Methane is represented by a corrected perfect gas model with

Molecular mass = 16 kg/kmol

$\gamma_V = 1.74$

$\gamma_T = 1.39$

$Z = 0.76$

Pressure and mass flow rate time trends are in good agreement with PRO II predictions; temperature deviations at the end of the blowdown are caused mainly by liquid formation.

Test Case No. 7: Nitrogen Vessel Venting

This test case refers to a blowdown experiment described in [7]. A vertical vessel with length 1.524 m, inside diameter 0.273 m, and wall thickness 0.025 m, discharging through an orifice with a diameter of 0.00635 m, containing nitrogen initially at $150 \cdot 10^5$ Pa, 290 K, was used for testing. Surrounding medium was still air at 290 K.

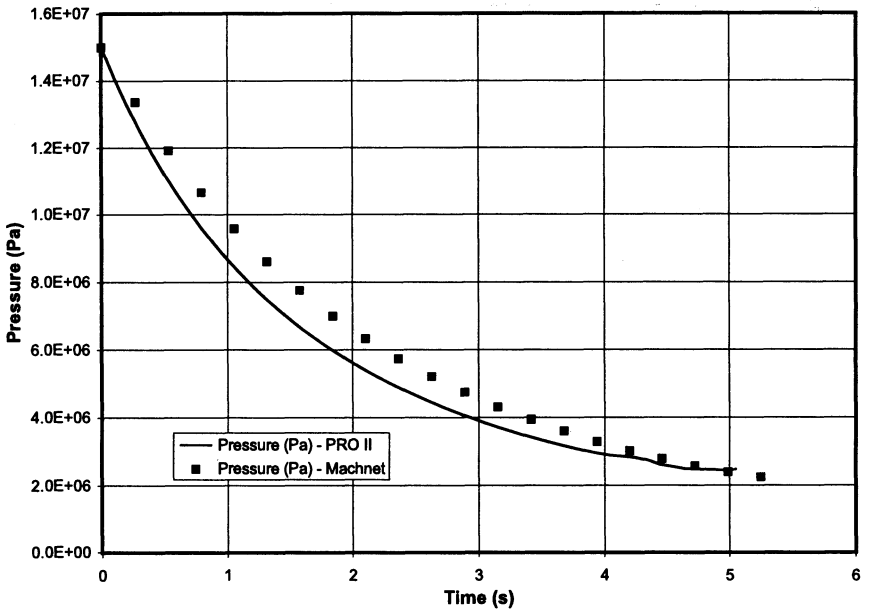

(a)

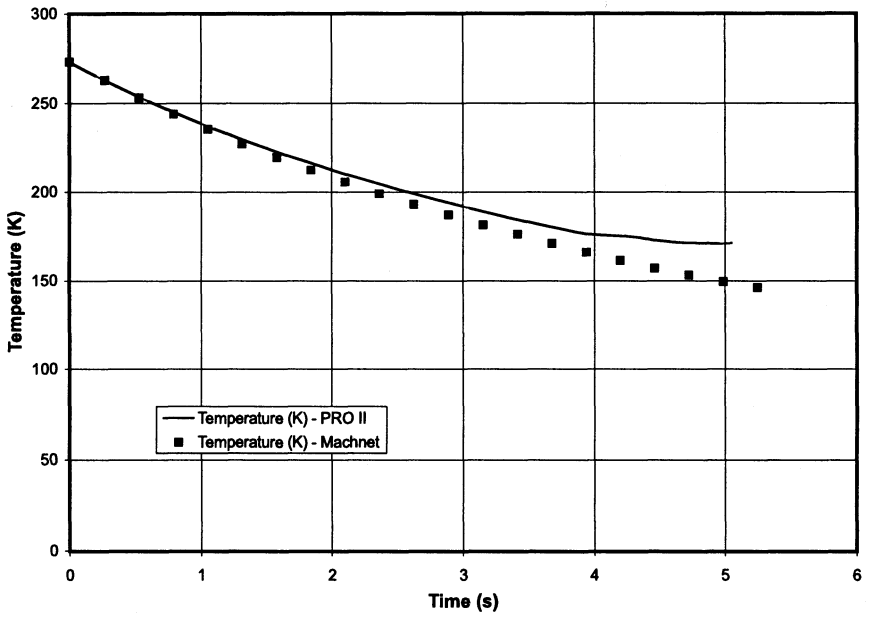

(b)

Figure 3.B.9 — Adiabatic vessel venting with methane initially at 150 bar. (a) Pressure time evolution. (b) Temperature time evolution.

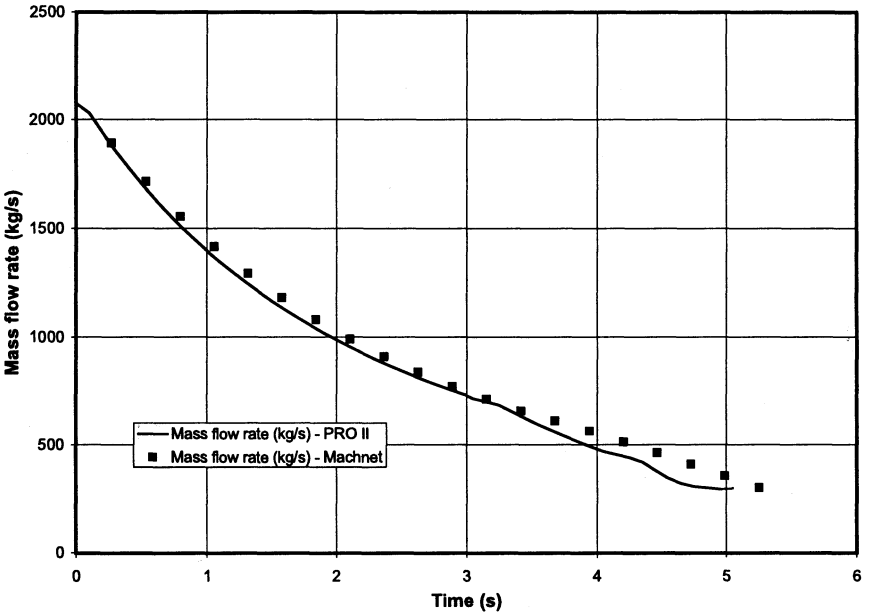

(c)

Figure 3.B.9 — (*Continued*) (c) Mass flow rate time evolution.

Experimental values of pressure and wall and fluid temperatures are available for comparison. In Figure 3.B.10 experimental and predicted (by Machnet) values are shown as time functions. The simulation has been carried out considering heat transfer phenomena, both from the still internal gas to the vessel wall and from the vessel external wall to the exterior.

Test Case No. 8: Pipeline Flow with Combined Friction and Heat Transfer

In the following, two examples of gas flow with combined effects of heating and friction in a pipe with constant wall temperature are presented, along with comparison to referenced calculations.

The calculations refer to the steady flow of a gas in a constant-area tube supplied by an infinite vessel and discharging to atmosphere. The inlet to external pressure ratio is chosen in such a way as to have a Mach number of 0.5 at the pipe inlet. Each calculation is distinguished by a specific value of the ratio between the wall temperature and the gas inlet temperature. The wall temperature is held constant along the pipeline. The gas is air treated as perfect gas having:

Molecular mass = 29 kg/kmol

Isentropic coefficient = 1.4

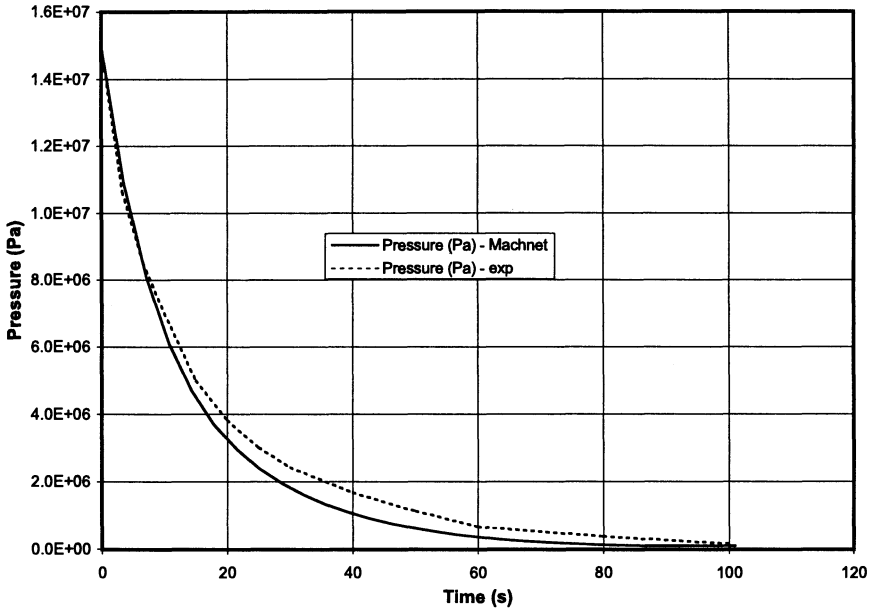

(a)

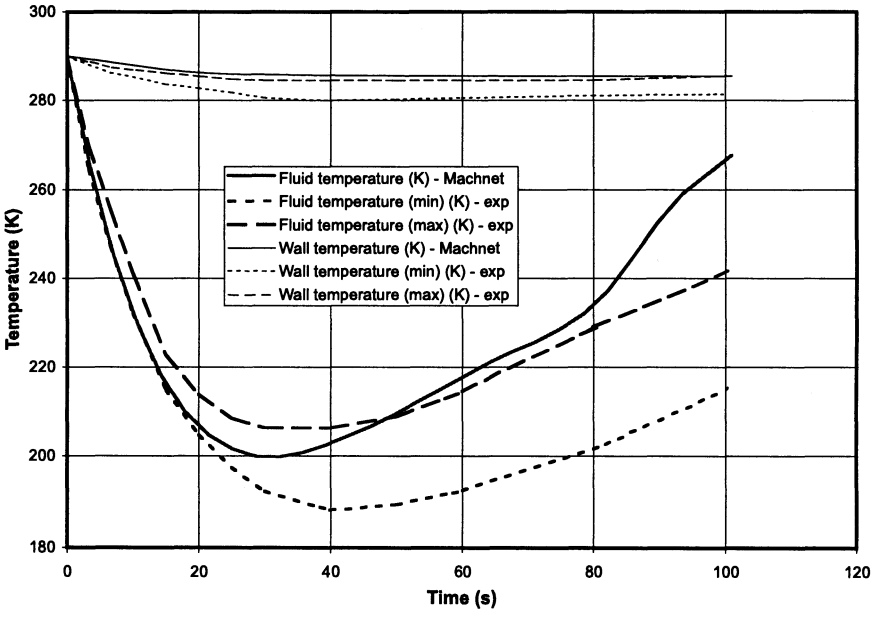

(b)

Figure 3.B.10 — Blowdown of a vessel containing nitrogen initially at 150 bar with heat transfer. Comparison Machnet vs. experimental results. (a) Pressure time evolution. (b) Temperatures time evolution.

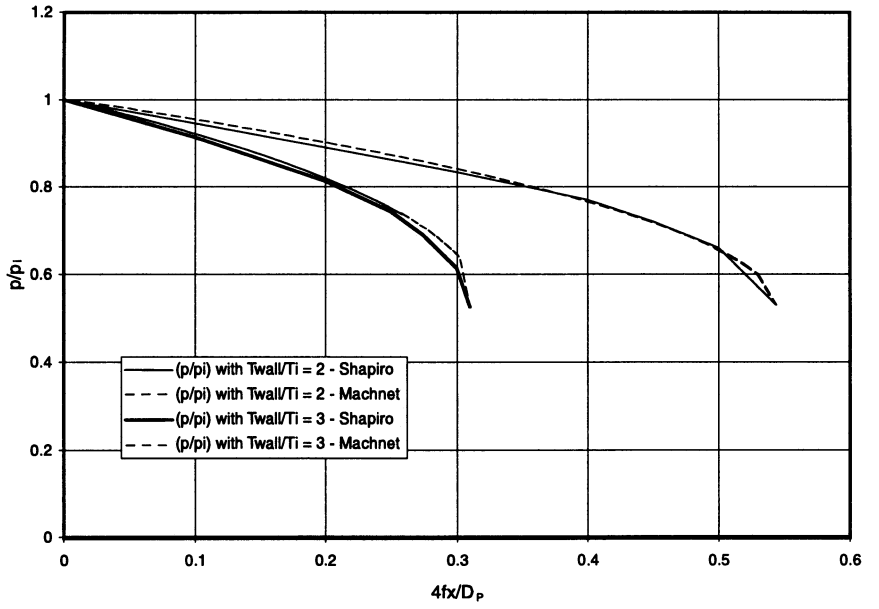

(a)

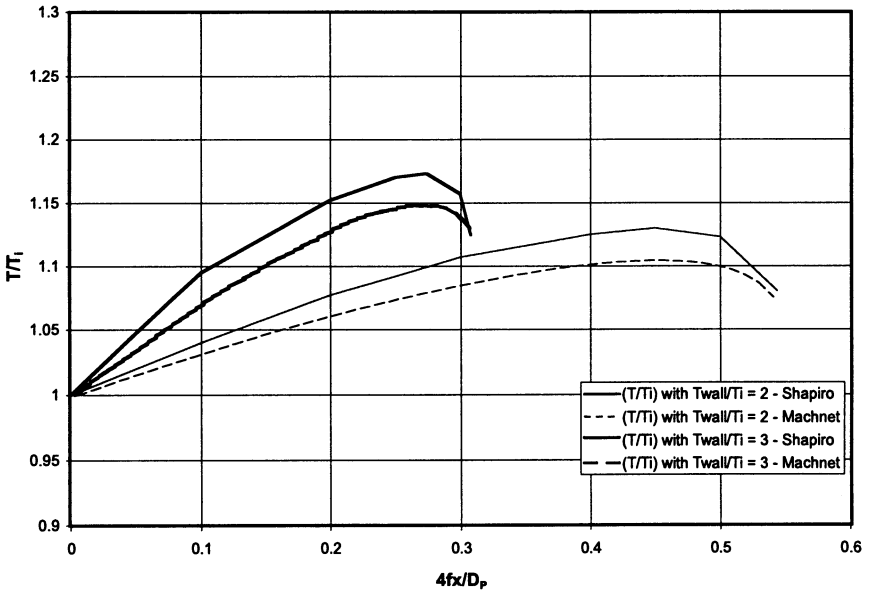

(b)

Figure 3.B.11 — Results of calculations for combined friction and heat transfer for steady gas flow in a constant-area pipe. (a) Pressure vs. distance. (b) Temperature vs. distance.

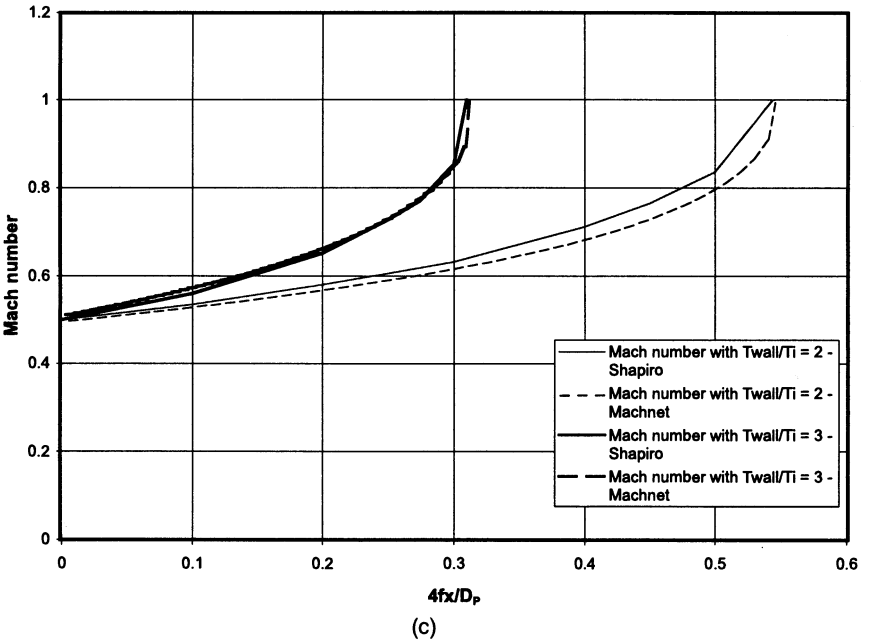

Figure 3.B.11 — (*Continued*) (c) Mach number vs. distance.

Viscosity = 0.0161 m Pa·s

Thermal conductivity = 0.0224 W/m/K

Limiting steady flow profiles are obtained as a result of frictional and wall-fluid heat transfer processes. In Figure 3.B.11 pressure, temperature, and Mach number distributions calculated by Machnet as function of the quantity $4fx/D_p$ are shown, with similar profiles reported by Shapiro [18] referred to analogous calculations. Pressure and temperatures are normalized with respect to inlet conditions p_i, T_i.

Test Case No. 9: Blowdown of a Buried Pipeline

This test case is concerned with the blowdown of a buried pipeline through a composed vent pipe caused by an instantaneous valve opening. The fluid is a perfect "corrected" gas with

Molecular mass = 18.1 kg/kmol

$\gamma_V = 1.33$

$\gamma_T = 1.33$

Viscosity = 0.0124 m Pa.s

Thermal conductivity = 0.037 W/m/K

$Z = 0.85$

The initial and boundary conditions are:

Pipe pressure = $64.5 \cdot 10^5$ Pa

Pipe temperature = 286 K

External pressure = $1.013 \cdot 10^5$ Pa

External temperature = 286 K

The pipe characteristics are:

Pipe diameter = 0.4888 m

Pipe length = 2700 m

Pipe roughness = 25 μm

The pipe wall properties are:

Layer 1

Thickness = 0.0096 m

Thermal conductivity = 45 W/m/K

Density = 7850 kg/m^3

Thermal capacity = 445 J/kg/K

Layer 2

Thickness = 0.03 m

Thermal conductivity = 0.04 W/m/K

Density = 100 kg/m^3

Thermal capacity = 837 J/kg/K

The external ambient is ground at 286 K, and the pipe depth is 1 m. The venting pipe is composed by two sections with:

Section 1

Pipe diameter = 0.0794 m

Pipe length = 250 m

Pipe roughness = 25 μm

Layers are of the same material as buried pipeline, but the first layer thickness is 0.0103 m.

Section 2

Pipe diameter = 0.742 m

Pipe length = 790 m

Pipe roughness = 25 μm

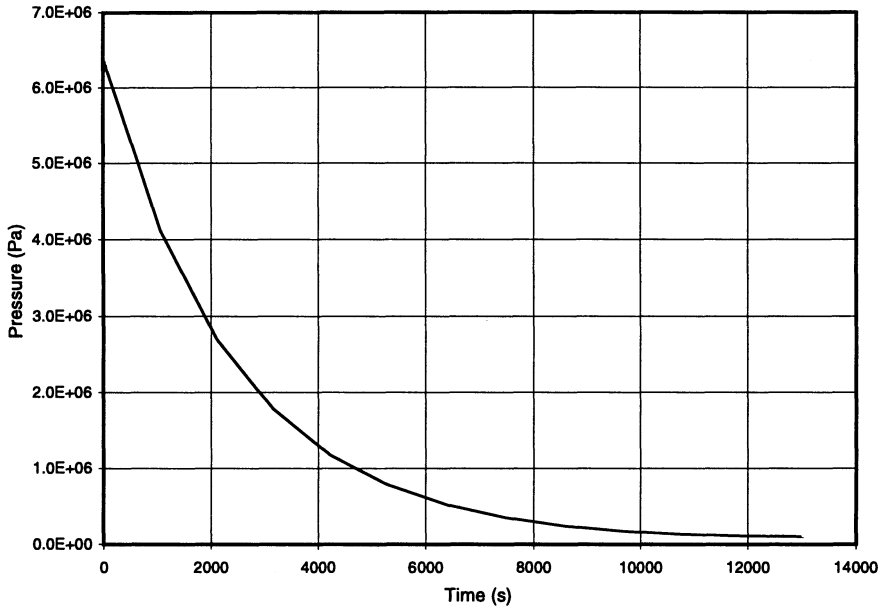

(a)

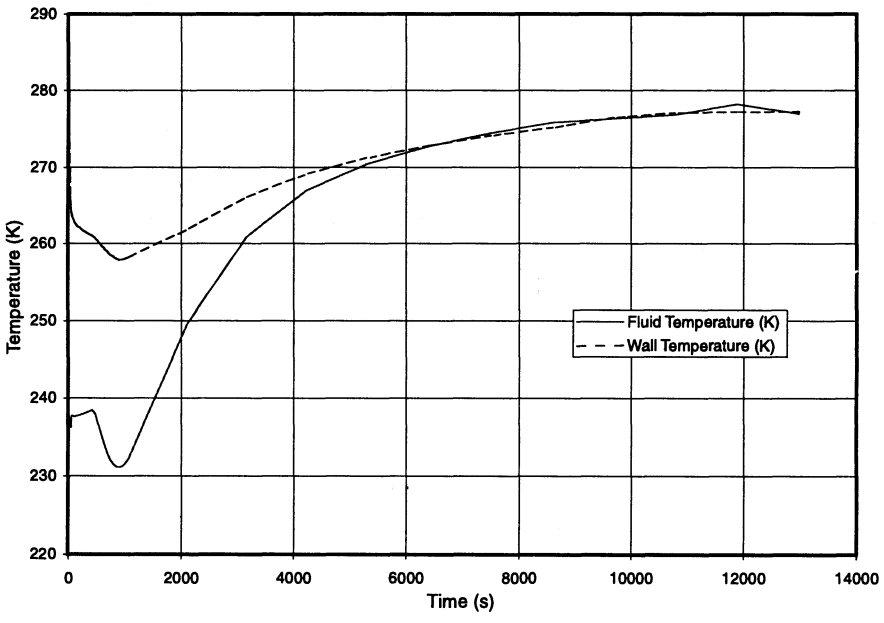

(b)

Figure 3.B.12 — Blowdown of a buried pipeline. (a) Pressure time evolution inside the buried pipeline. (b) Fluid and wall temperatures time evolution in the area change region of the venting pipe.

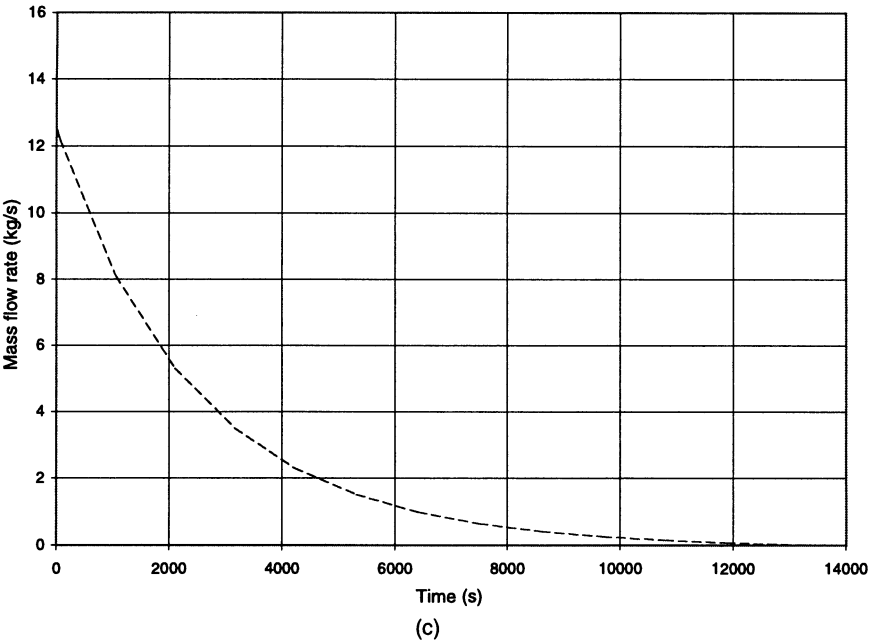

Figure 3.B.12 — (*Continued*) (c) Mass flow rate time evolution.

Layers are of the same material as buried pipeline, but the first layer thickness is 0.0048 m.

The external ambient of venting pipe is air at 286 K and flowing around it at 4.7 m/s. In Figure 3.B.12 pressure inside the buried pipeline and mass flow rate time evolutions are shown, along with fluid and wall temperature time trends in a point located in the region of area change between section 1 and section 2 of the venting pipe.

3.B.10 Conclusions

The program Machnet can be used for simulation of thermal and hydraulic transients in gases undergoing rapid blowdown processes. It is especially concerned with wave propagation during the "strong-wave period," and with temperature predictions along a pipeline with fittings (valves, orifices). The adopted thermodynamic model (corrected perfect gas) can be considered an acceptable approximation unless liquid formation occurs (because liquid formation delivers latent heat and causes an increase in the fluid temperature).

Calculation tests are in good agreement with referenced results, and the code can be considered validated.

Appendix A: The Riemann Problem

The shock tube problem represents the limit case of a depressurization process, in which two ambients at different pressures are connected through a valve opened in a finite time; in the Riemann problem a long tube is initially divided into two parts by a diaphragm, on the left-hand side of which there is high-pressure stagnant gas, and on the right-hand side low-pressure stagnant gas.

If viscous effects can be neglected along the tube walls and if an infinitely long tube is considered, avoiding reflections at the tube ends, the exact solution to the Euler equations can easily be obtained on the basis of simple waves separating regions of uniform conditions. At the bursting of the diaphragm, at time $t = 0$, the pressure discontinuity propagates to the right in the low-pressure gas and simultaneously an expansion fan propagates to the left in the high-pressure gas. In addition, a contact discontinuity separating the two gas regions propagates to the right in the tube.

We will distinguish the following regions (see Fig. 3.B.13). Region 1 contains the undisturbed gas at the low pressure p_1. It is separated by a shock wave from region 2, which represents the disturbed low-pressure gas. The contact discontinuity separates region 2 from the disturbed high-pressure gas in region 3, which in turn has been influenced by the expansion fan propagating to the left into the undisturbed high-pressure region 4.

The pressure in regions 2–3 can be derived by combining the Rankine–Hugoniot relations that are valid across a shock with the rarefaction wave equations; the implicit equation for $\Pi = p_2/p_1$, to be solved by an iterative method, is:

$$\sqrt{\frac{2}{\gamma(\gamma-1)}}\frac{\Pi-1}{(1+\Gamma\Pi)^{1/2}} - \frac{2}{\gamma-1}\frac{c_4}{c_1}\left[1-\left(\Pi\frac{p_1}{p_4}\right)^{(\gamma-1)/2\gamma}\right] = 0 \qquad (3.B.50)$$

$$\Gamma = \frac{\gamma+1}{\gamma-1}$$

The flow configuration depends on the initial pressure ratio across the diaphragm (p_1/p_4). If it assumes a critical value given by (for $c_1 = c_4$):

$$\left(\frac{p_1}{p_4}\right)_{CR} = \left(\frac{2}{\gamma+1}\right)^{2\gamma/(\gamma-1)} \frac{1}{\left[1+\frac{(1+\sqrt{5})}{\gamma+1}\gamma\right]} \qquad (3.B.51)$$

the flow acceleration through the expansion fan reaches sonic conditions at the original diaphragm position, which remain blocked in this state for infinite time.

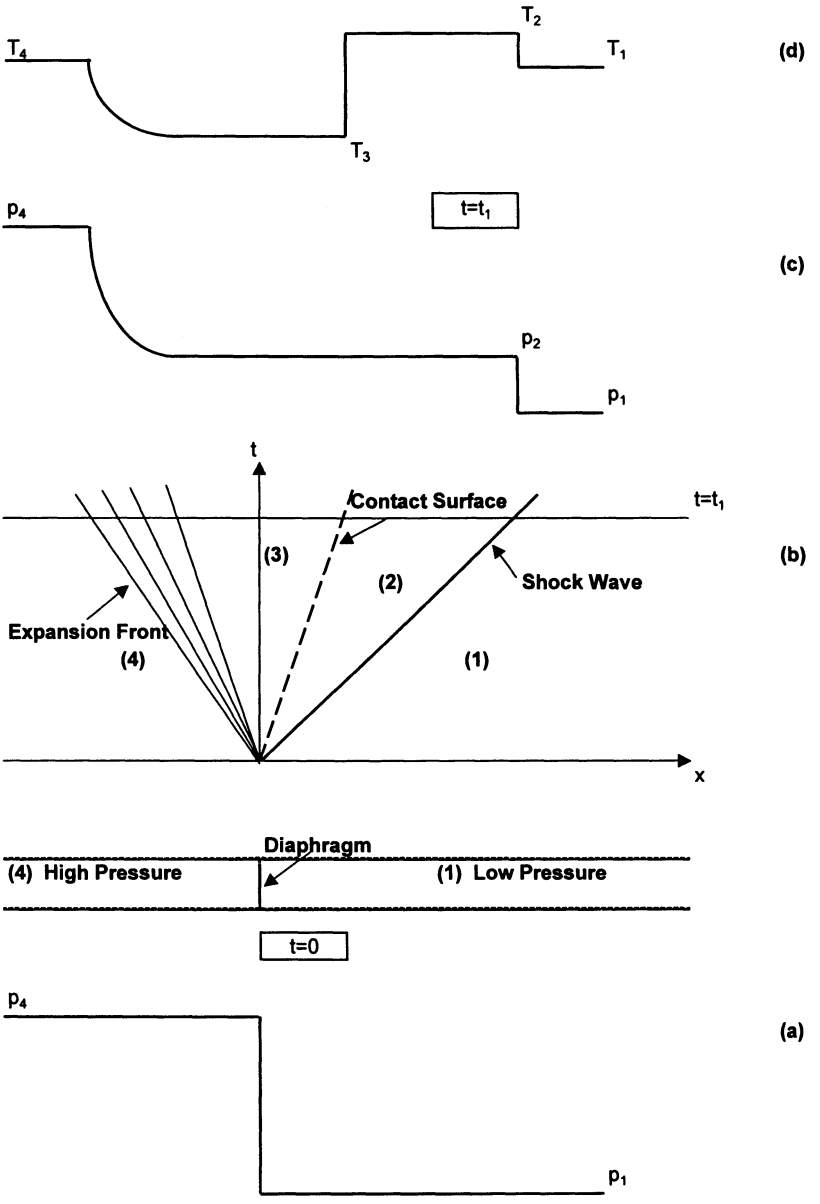

Figure 3.B.13 — Flow pattern in a shock tube. (a) Initial conditions. (b) x-t diagram. (c) Pressure distribution at $t = t_1$ (d) Temperature distribution a $t = t_1$.

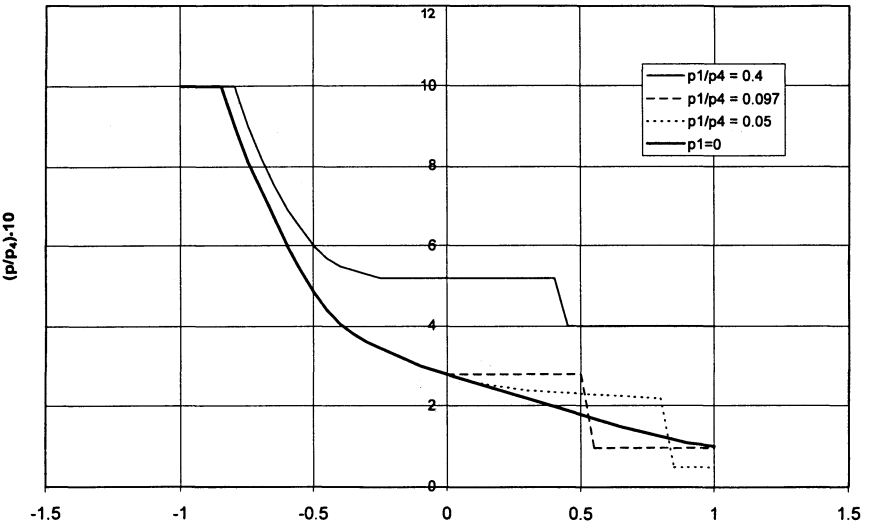

Figure 3.B.14 — Pressure distribution for different initial pressure ratios in the shock tube problem.

If $(p_1/p_4) > (p_1/p_4)_{\mathrm{CR}}$, the rear part of the wave travels to the left, while for $(p_1/p_4) < (p_1/p_4)_{\mathrm{CR}}$ it travels to the right.

If $p_1/p_4 = 0$ (expansion in empty space) the rarefaction wave accelerates the gas to the escape speed $U_{\max}$:

$$U_{\max} = \frac{2}{\gamma - 1} c_4 \tag{3.B.52}$$

The situation can be represented by Figure 3.B.14, valid for $\gamma = 1.4$ when $(p_1/p_4)_{\mathrm{CR}} = 0.097$.

The Riemann problem includes all possible initial discontinuities, giving different flow configurations from the shock–tube scheme. Considering that left and right states can have initial velocity u_4 and u_1 and nonhomogeneous properties ($\gamma_1 \neq \gamma_4$), the pressure of intermediate regions 2–3 between extreme waves is the solution of the following equation:

$$f(P, p_1, \rho_1) + f(P, p_4, \rho_4) - (u_4 - u_1) = 0 \tag{3.B.53}$$

with

$$f(P, p_k, \rho_k) = \begin{cases} c_k \sqrt{\dfrac{2}{\gamma_k (\gamma_k - 1)}} \dfrac{P - 1}{(1 + \Gamma_k P)^{1/2}} & \text{for } P \geq 1 \\ -\dfrac{2}{\gamma_k - 1} c_k \left(1 - P^{(\gamma_k - 1)/(2\gamma_k)}\right) & \text{for } P < 1 \end{cases} \tag{3.B.54}$$

$$\Gamma_k = \frac{\gamma_k + 1}{\gamma_k - 1}; \qquad P = \frac{p_2}{p_k} \quad k = 1, 4.$$

By putting

$$\mathcal{J}(P) = f(P, p_1, \rho_1) + f(P, p_4, \rho_4) \tag{3.B.55}$$

according to Godunov et al. [5] the following quantities can be defined:

$$U_{\text{shock}} = \mathcal{J}\left(P_4 = \frac{p_4}{p_1}\right) = c_1 \sqrt{\frac{2}{\gamma_1(\gamma_1 - 1)}} \frac{\left(\frac{p_4}{p_1}\right) - 1}{\left(1 + \frac{\gamma_1 + 1}{\gamma_1 - 1}\frac{p_4}{p_1}\right)^{1/2}} \tag{3.B.56}$$

$$U_{\text{rar}} = \mathcal{J}\left(P_1 = \frac{p_1}{p_4}\right) = -\frac{2c_4}{\gamma_4 - 1}\left[1 - \left(\frac{p_1}{p_4}\right)^{(\gamma_4 - 1)/(2\gamma_4)}\right] \tag{3.B.57}$$

$$U_{\text{void}} = \mathcal{J}(P = 0) = -\frac{2c_1}{\gamma_1 - 1} - \frac{2c_4}{\gamma_4 - 1}. \tag{3.B.58}$$

Based on the value of initial relative velocity between the left and right states, four configurations can be realized; following Landau and Lifshitz [11] notation, in which S indicates shock wave, T indicates tangential or contact discontinuity, R indicates rarefaction wave, and I is the initial discontinuity, configurations are:

1) $u_4 - u_1 > U_{\text{shock}}$

In this case, which we write $I \rightarrow S \leftarrow TS \rightarrow$, the initial discontinuity I gives two shock waves S, propagated in opposite directions, and a tangential discontinuity T between them. This case occurs when two masses of gas collide with a large relative velocity.

2) $U_{\text{rar}} < u_4 - u_1 < U_{\text{shock}}$

In this case $I \rightarrow R \leftarrow TS \rightarrow$ a shock wave is propagated on one side of the tangential discontinuity, and a rarefaction wave R on the other side. This case occurs, for example, if two masses of gas at relative rest ($u_4 - u_1 = 0$) and at different pressures are brought into contact at the initial instant. Of all the cases considered, the second is the only one in which gases 1 and 4 are moving in the same direction, so the equation $u_4 = u_1$ is possible.

3) $U_{\text{void}} < u_4 - u_1 < U_{\text{rar}}$.

In the third case ($I \rightarrow R \leftarrow TR \rightarrow$) a rarefaction wave is propagated on each side of the tangential discontinuity.

4) $u_4 - u_1 < U_{\text{void}}$.

Two rarefaction waves are generated, but gases 1 and 4 separate with a sufficiently great relative velocity so as to form a vacuum between waves.

An interesting feature of the Riemann problem (cfr. [6]) is that the flow direction may be determined without computing the full solution by

iteration. This can be accomplished rather simply by introducing an artificial stationary boundary or wall between the left and right states and calculating the pressures that would act on the left and right sides of this boundary. The flow direction will then be from the side with higher pressure to the side with lower pressure. If the flow at the left state is positive ($u_4 > 0$) a shock will be reflected from the left side of this boundary. On the other hand, if the flow is away from the left side of the boundary ($u_4 \leq 0$), a rarefaction wave will be reflected instead. The procedure may be repeated for the right side of the boundary. If we indicate by p_L and p_R the artificial pressures with respect to the stationary boundary, and introduce

$$\begin{aligned} M_4 &= \frac{u_4}{c_4} \\ M_1 &= \frac{u_1}{c_1} \\ \tilde{u}_4 &= u_4 + \frac{2c_4}{\gamma_4 - 1} \\ \tilde{u}_1 &= u_1 - \frac{2c_1}{\gamma_1 - 1} \end{aligned} \tag{3.B.59}$$

the flow direction, represented by the sign of u_2 can be obtained by applying the flow chart reported in Figure 3.B.15.

Using equation (3.B.53), which considers gases with different values of γ, the critical ratio $(p_1/p_4)_{\mathrm{CR}}$ producing sonic conditions at the diaphragm position in configuration 2 is given by:

$$\begin{aligned} \left(\frac{p_1}{p_4}\right)_{\mathrm{CR}} &= \frac{\alpha}{1 + x_+} \\ \alpha &= \left(\frac{2}{\gamma_4 + 1}\right)^{2\gamma_4/(\gamma_4 - 1)} \end{aligned} \tag{3.B.60}$$

with

$$x_+ = \left(\frac{c_4}{c_1}\right)^2 \frac{2\gamma_1^2}{(\gamma_4 + 1)^2} \left\{ \frac{\gamma_1 + 1}{2\gamma_1} + \sqrt{\frac{(\gamma_1 + 1)^2}{4\gamma_1^2} + \frac{(\gamma_4 + 1)^2}{\gamma_1^2} \left(\frac{c_1}{c_4}\right)^2} \right\}.$$

For example, with $\gamma_1 = 1.2$, $\gamma_4 = 1.4$, $c_1 = c_2$, equation (3.B.60) gives $(\frac{p_1}{p_4})_{\mathrm{CR}} = 0.109$. Configuration 3, with two rarefaction waves, is characterized by two critical ratios relevant to the two waves.

Rarefaction Wave in Region 4

$$\left(\frac{p_1}{p_4}\right)_{\mathrm{CR}} = \frac{X_{\mathrm{CR}} \cdot H^{1/\theta_1}}{\left[N + G + H - G X_{\mathrm{CR}}^{\theta_4}\right]^{1/\theta_1}} \tag{3.B.61}$$

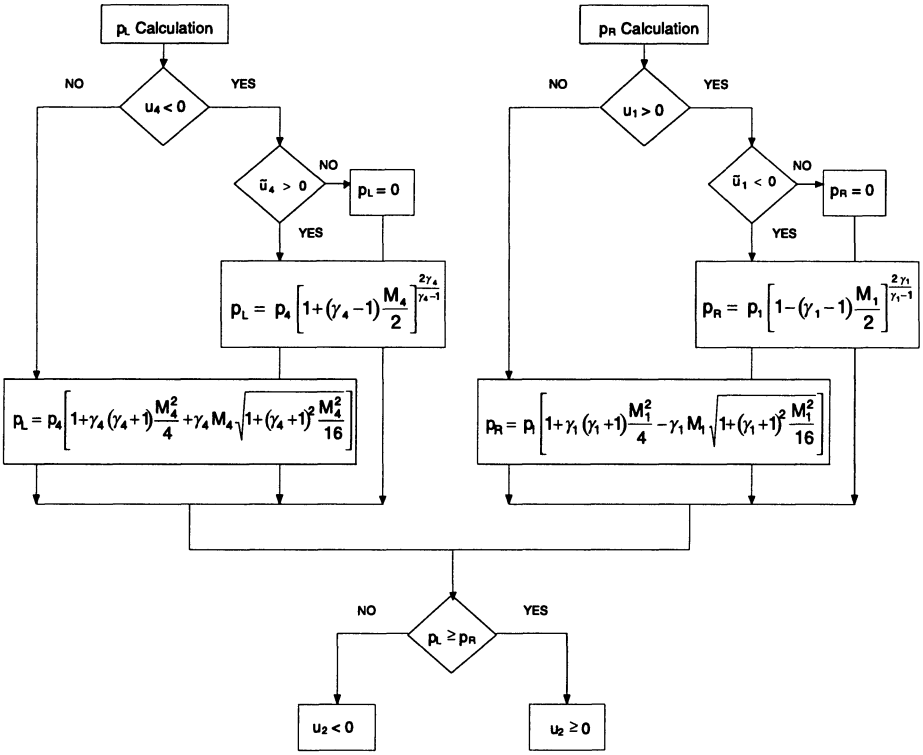

Figure 3.B.15 — Flow chart for determination of the flow direction in the Riemann problem.

where

$$X_{CR} = \text{critical pressure ratio at sonic point} = \left[1 - \frac{\gamma_4 - 1}{\gamma_4 + 1} \cdot \left|1 - \frac{u_4}{c_4}\right|\right]^{1/\theta_4} \tag{3.B.62}$$

$$\begin{aligned} N &= u_4 - u_1 \\ G &= \frac{2c_4}{\gamma_4 - 1} \\ H &= \frac{2c_1}{\gamma_1 - 1} \\ \theta_1 &= \frac{\gamma_1 - 1}{2\gamma_1} \\ \theta_4 &= \frac{\gamma_4 - 1}{2\gamma_4} \end{aligned} \tag{3.B.63}$$

Rarefaction Wave in Region 1

$$\left(\frac{p_1}{p_4}\right)_{CR} = \frac{1}{G^{1/\theta_1} Y_{CR}} \cdot \left[N + G + H - H Y_{CR}^{\theta_1}\right]^{1/\theta_1} \qquad (3.B.64)$$

where

$$Y_{CR} = \text{critical pressure ratio at sonic point} = \left[1 - \frac{\gamma_1 - 1}{\gamma_1 + 1} \cdot \left|1 + \frac{u_1}{c_1}\right|\right]^{1/\theta_1} \qquad (3.B.65)$$

References

1. Aziz, K., and Govier, G.W., *The Flow of Complex Mixtures in Pipes*, Van Nostrand Reinhold Co., New York (1972).
2. Bird, R.B, Stewart, W.E., and Lightfoot, E.N., *Transport Phenomena*, John Wiley & Sons, New York (1960).
3. Crane, Ltd. *Flow of Fluids through Valves, Fitting and Pipe*, Technical Paper no. 410M, Suffolk, England: Author (1988).
4. Ford, P.E., Pipelines for viscous fuels, *Fourth World Petroleum Congress*, 115 (1955).
5. Godunov, S., Zabrodine, A., Ivanov, M., Kraiko, A., and Prokopov, G., *Resolution Numerique des Problemes Multidimensionnels de la Dynamique des Gaz*, Editions MIR, Moscow (1979).
6. Gottlieb, J.J., and Groth, C.P.T., Assessment of Riemann solvers for unsteady one-dimensional inviscid flows of perfect gas, *J. Computational Phys.*, **78**, 437 (1988).
7. Haque, M.A., Richardson, S.M., Saville G., Chamberlain, G., and Shirvill, L., Blowdown of pressure vessels II experimental validation of computer model and case studies, *Trans. IChemE*, **70**, 10 (1992).
8. Hirsch, C., *Numerical Computation of Internal and External Flows*, John Wiley & Sons, New York (1990).
9. Keenan, J.H., and Neumann, E.P., Measurements of friction in a pipe for subsonic and supersonic flow of air, *J. Appl. Mech.*, **13**, A91 (1946).
10. Kuehn, T.H., and Goldstein, R.J., Correlating equations for natural convection heat transfer between horizontal circular cylinders, *Int. J. Heat Mass Transfer*, **19**, 1127 (1976).
11. Landau, L.D., and Lifshitz, E.M., *Fluid Mechanics, 2nd edition*, Pergamon Press, Oxford (1987).

12. Lax, P.D., Weak solutions of non linear hyperbolic equations and their numerical computation, *Comm. Pure and Applied Mathematics*, **7**, 159 (1954).
13. Lelchuk, V.L., Heat transfer and hydraulic flow resistance for streams of high velocity, *NACA Tech. Memo.*, no. 1054 (1943).
14. Liepmann, H.W., and Roshko, A., *Elements of Gas Dynamics*, John Wiley & Sons, New York (1957).
15. Pintabona, R., and Colacicco, P., Il calcolo delle valvole di sicurezza per gas, *La Termodinamica*, **5**, 101 (1994).
16. Roe, P.L., Approximate Riemann solvers, parameter vectors and difference schemes, *J. Computational Phys.*, **43**, 357 (1981).
17. Romiti, A., *Meccanica dei fluidi*, ISEDI (1974).
18. Shapiro, A.H., *The Dynamics and Thermodynamics of Compressible Fluid Flow*, John Wiley & Sons, New York (1953).
19. Terenzi, A., Mancini, N., and Podenzani, F., Transient compressible flow in pipelines: A Godunov-type solver for Navier-Stokes equations, to appear.
20. Truitt, W.R., *Fundamentals of Aerodynamics Heating*, Ronald Press, New York (1960).
21. Yee, H.C., Beam, R.M., and Warming, R.F., Boundary approximation for implicit schemes for one-dimensional inviscid equations of gas dynamics, *AIAA J.*, **20**, 1203 (1982).

4

Spurt in the Extrusion of Polymeric Melts: Discrete Models for Relaxation Oscillations

A.A.F. VAN DE VEN

Eindhoven University of Technology
Eindhoven, The Netherlands

ABSTRACT. In the extrusion of polymer melts, several types of flow instability can occur. One example of this is spurt. Spurt is manifested by periodic oscillations in the pressure and volumetric flow rate. These oscillations are of relaxation type. An extrusion through a cylindrical die is considered. A discrete model to describe spurt or relaxation oscillations is constructed. This model is based on observations from three-dimensional theory. When spurt occurs, the shear rates very near the wall of the die (i.e., in the spurt layer) are much higher than those in the kernel of the extruded polymeric melt. Therefore, the viscosity in the spurt layer is taken much smaller than in the kernel. In both regions a linear Newtonian fluid model is used. A no-slip boundary condition at the wall is maintained. The model developed here is compared to an analogous model, allowing for slip at the wall of the die. It is shown that corresponding results can be obtained from both models. Application of the model to a piston-driven extrusion flow shows the occurrence of spurt oscillations for a restricted range of prescribed inlet flow rates. The found oscillations are qualitatively in correspondence with experimental results.

A. Fasano (ed.), *Complex Flows in Industrial Processes*

4.1 Introduction

The manufacturing of plastic products from polymer melts is an industrial branch of strongly increasing economic importance. Many large companies are occupied with this kind of production process. Polymers are frequently used in industrial applications because of their excellent material and mechanical properties, and their range of applications is extremely wide (from daily products as plastic bags to very advanced applications in the automotive and aerospace industry). Industrial manufacturing of plastic products from polymer melts can be performed by processes such as extrusion, injection molding, film-blowing, spinning, or cable-coating; the final products were plastic household goods, sheets, wires or fibers, and coated cables, among others. Increase of operational profits requires higher production rates, however, without distorting the quality of the final product. Qualitative requirements on the final product concern strength, homogeneity, transparency, visual aspects, and the like. The often contradictory requirements mentioned earlier have inspired both the rheological world and scientists from applied mathematical physics and continuum mechanics to produce an immense amount of literature (see, for example, journals such as the *Journal of Non-Newtonian Fluid Mechanics* and the *Journal of Rheology*). In this area of research both material aspects, such as constitutive behavior of highly nonlinear viscoelastic fluids, and description of flow patterns (inclusive boundary conditions, e.g., slip or no-slip, and entrance and exit effects in dies or molds) play a role. In many of these investigations, stability comes into sight. Owing to the nonlinearity of the problems concerned, mostly numerical methods can lead to quantitative results, but several analytical approaches have also been published. It is evident that all the results obtained should ultimately be compared with, or supported by, experimental data, which are extensively reported in the literature.

In an extrusion process, molten polymer is pressed through a die, which can be cylindrical, plane, or annular. In injection molding, molten polymer is pressed through a die into a mold, having the shape of the desired product (e.g., cups, spoons, or complete dashboards for cars). In fiber spinning, molten polymer is pressed through a small hole and stretched to a fiber. Finally, in cable-coating, molten polymer is extruded from an annular die on a solid (e.g., copper) wire traveling at high speed, thus covering the wire with a thin shield of polymer (e.g., for electric insulation).

In all the processes described here, distortions can show up when raising the production rate. These distortions always show up at the surface of the final product. In addition to the smoothness of the surface, they diminish qualitative requirements regarding strength and transparency. Therefore,

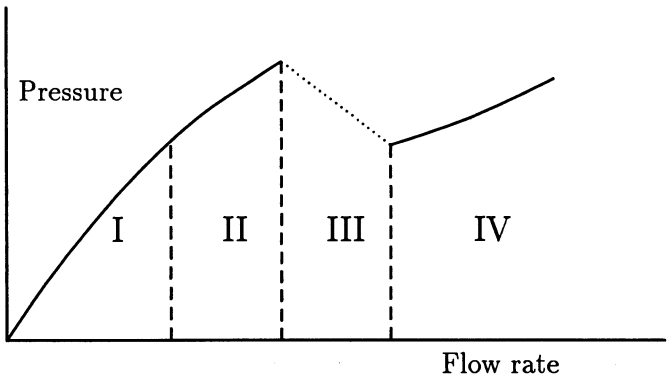

Figure 4.1 — Stationary flow curve with (in)stability regimes.

these distortions are highly unwished-for and should be avoided at all cost. It is an important subject of research to find the origins of these distortions and to discover how to improve the polymer and/or geometry of the process in order to get rid of them.

In this case, we concentrate on the extrusion of polymeric melts through a cylindrical capillary. The industrial aim of the process is to produce, at as high a rate as possible, great lengths of smooth plastic wires. However, when the production rate is increased above a certain critical level, distortions show up at the surface of the wire, making the final product worthless. These distortions are collected under the general name *extrusion instabilities*. The distortions can be of several types, with names such as *sharkskin* (small periodic surface distortions), *spurt* (larger periodic surface and volume distortions), or *gross-melt fracture* (a complete nonperiodic global distortion). As shown in Figure 4.1, all of these types have their own specific regime of flow rates. In Figure 4.1 a typical flow curve (i.e., the stationary pressure in the extrusion barrel as a function of the stationary flow rate through the die) for an extrusion process is drawn. Four regimes are distinguished in this figure:

- **Regime I**: the flow is regular here, yielding a smooth extrudate.
- **Regime II**: the sharkskin regime; small periodic disturbances show up at the surface of the layer.
- **Regime III**: the spurt regime, showing alternate smooth and disturbed extrudate.
- **Regime IV**: gross melt fracture, a strongly distorted spiral-shaped extrudate.

Here, we restrict ourselves to spurt-type instabilities. When an extrusion process is in the spurt regime, the extrudate shows alternating smooth and

distorted regions. In this regime, the volumetric flow rate Q periodically jumps between a lower value ($\Rightarrow$ *smooth surface: classical flow*) and a much higher value ($\Rightarrow$ *distorted surface: spurt flow*). In addition, the pressure, driving the capillary flow, shows oscillations. These oscillations are often observed in experiments; they look like relaxation oscillations (cf. [10]). Therefore, we shall refer to them as *spurt* or *relaxation oscillations.*

In spurt, as is understood here, the flow profile looks strongly different in two regions:

- In the inner region (the kernel) the velocity gradient is small and the flow profile is flat, looking very much like cork flow; in this inner region the flow is similar to classical Poiseuille flow.
- In a very small region near the wall the velocity profile is very steep, yielding very large values for the velocity gradient, or shear rate; this region is called the *spurt zone.*

In the literature, spurt flow is explained in two different ways:

- as a result of slip at the wall of the capillary; in this explanation, the spurt zone is in fact reduced to a surface layer in which slip takes place. The velocity at the wall is then no longer zero ([6], [11], among others).
- as a result of nonmonotone constitutive behavior ([1], [2], [9]).

Here, we shall adhere to the second explanation in which spurt is called a *constitutive instability* and in which the no-slip boundary condition is maintained.

4.2 Extrusion Model

The extrusion device we consider here is modeled as a capillary rheometer, consisting of a huge barrel filled with polymeric melt, closed at one side by a movable plunger, and on the other side connected to a narrow capillary (see Figure 4.2). The plunger moves with velocity V_0 and has an area A, whereas

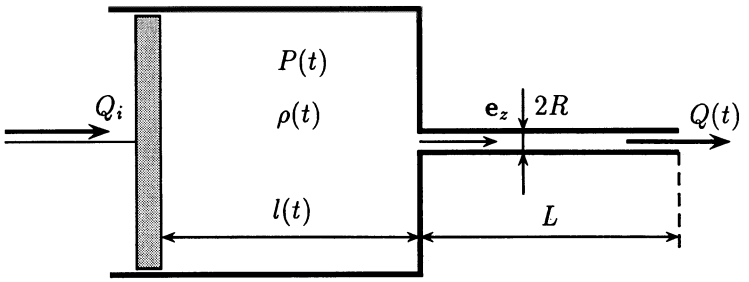

Figure 4.2 — Capillary rheometer.

the barrel has length l ($l = l(t) = l_0 - Vt$). Due to the plunger movement, a pressure P is built up inside the barrel, and the melt is forced to leave the barrel and flow into the capillary, with volumetric flow rate Q. At the end of the capillary, the melt leaves the capillary and the extrudate is formed. Because the flow in the barrel and in the capillary are of essentially different types, the two flows are also modeled in different ways. In the main part of the barrel the flow is an almost uniform compression flow (*plug flow*). The pressure becomes very high here due to the narrow inlet of the capillary, but the velocity is rather low because the barrel is very wide (compared to the capillary). Hence, in the barrel the flow is compression dominated, and shear is negligible here. Thus, the compressibility of the melt inside the barrel must be taken into account, and the melt density ρ is variable. Because the flow in the barrel is uniform, P and ρ are only time-dependent, i.e., $P = P(t)$ and $\rho = \rho(t)$. On the other hand, the flow in the capillary is strongly shear dominated, due to the no-slip condition, which is assumed at the wall, and the relatively high velocity compared to that in the barrel. Then the influence of compressibility is small, and the melt flowing through the capillary may be assumed to be incompressible. Hence, the melt flows through the whole capillary with uniform volumetric flow rate $Q = Q(t)$.

We first model the flow inside the barrel. The unknowns here are the density $\rho(t)$, the pressure $P(t)$, and the volumetric flow rate $Q(t)$ flowing from the barrel into the capillary. The relations to be used are:

- a global balance law for the total melt in the barrel:

$$\frac{d}{dt}(\rho A l) = -\rho A V_0 + \dot{\rho} A l = -\rho Q$$

  where $\dot{l} = -V_0$.

- a constitutive (linearly elastic) compressibility law, relating the pressure to the density:

$$\frac{1}{\rho}\frac{d\rho}{dt} = \frac{1}{K}\frac{dP}{dt}$$

  where K is the compression or bulk modulus of the polymer melt.

From these two laws the following relation between Q and P can be derived

$$\frac{dP(t)}{dt} = -\frac{1}{\chi}(Q(t) - Q_i). \tag{4.1}$$

Here, $Q_i = AV_0$, the rate of volume displaced by the plunger, and $\chi = Al/K$, a material coefficient related to the compressibility.

For the shear dominated flow in the capillary (length L, radius R, $\pi R^2 \ll A$) we assume (r and z are cylindrical coordinates defined in the capillary):

- laminar incompressible flow:

$$\mathbf{v} = v(r,t)\mathbf{e}_z$$

- pressure linear in z and equal to $P(t)$ at the inlet ($z = 0$) and zero at the outlet ($z = L$) of the capillary; this yields

$$\frac{\partial p}{\partial z} = -\frac{P(t)}{L}$$

- body force and inertia term are negligible ($\rho\dot{v} \approx 0$) in the equation of motion; this reduces this equation to its stationary version:

$$\nabla \cdot \mathcal{T} = 0$$

- constitutive equation for the stress of the (general) form

$$\mathcal{T} = -p\mathcal{I} + 2\eta_s\mathcal{D} + \mathcal{S}$$

$$(\mathcal{D} = \frac{1}{2}(\nabla\mathbf{v} + (\nabla\mathbf{v})^T))$$

  where $2\eta_s\mathcal{D}$ represents a small Newtonian viscous component (which can be due to a small-molecule solvent, but just as well can represent the contribution due to a higher relaxation rate (cf. [1, section 2.6] or [3]), which becomes apparent for high shear rates), while $\mathcal{S}$ is the extra viscoelastic stress characterizing the polymer contribution. For moderate shear rates the viscoelastic stress $\mathcal{S}$ dominates the Newtonian term $2\eta_s\mathcal{D}$, but for higher shear rates (as in the spurt zone), the opposite is true.

Using the four points listed earlier, it turns out that only the equation of motion in the axial z-direction is not trivially zero. This equation reads

$$\frac{1}{r}\frac{\partial}{\partial r}(\eta w - S_{rz}) = \frac{\partial p}{\partial z} = -\frac{P(t)}{L}$$

where $w = w(r,t) = -\partial v/\partial r$; the shear rate, and $S_{rz} = S_{rz}(r,t)$. After one integration with respect to r, where $(\partial v/\partial r)(0,t) = S_{rz}(0,t) = 0$, this equation can be evaluated to

$$\eta w(r,t) - S_{rz}(r,t) = \frac{P(t)}{2L}r. \tag{4.2}$$

Equations (4.1) and (4.2) must be supplemented by

- a constitutive equation for the extra shear stress S_{rz} (see Section 4.3)
- the no-slip boundary condition at the wall of the capillary ($r = R$):

$$v(R,t) = 0 \tag{4.3}$$

- a relation for the volumetric flow $Q(t)$ reading

$$Q(t) = 2\pi \int_0^R rv(r,t)\,dr = \pi \int_0^R r^2 w(r,t)\,dr \tag{4.4}$$

where the latter result is derived after one integration by parts in which the no-slip boundary condition is used.

We proceed by making the basic equations (4.1) to (4.2) dimensionless. For the normalization of the shear stress, we use its initial viscosity η_0 and its first relaxation rate λ, both representative for small shear rates (see Section 4.3). That is, we take $S_{rz} = -\eta_0 \lambda \hat{S}$, where $\hat{S}$ is the dimensionless shear stress. As we shall see in the next section, $\eta_0 \gg \eta_s$. The radial coordinate r is normalized on R ($\hat{r} = r/R$), the velocity on λR ($\hat{v} = v/\lambda R$), and the shear on λ ($\hat{w} = w/\lambda$). The dimensionless flow rate and pressure are defined as

$$\hat{Q}_{(i)} = \frac{Q_{(i)}}{\pi \lambda R^3}, \qquad \hat{P} = \frac{R}{8\eta_0 \lambda L} P$$

respectively. Finally, a time scale T, such that $\hat{t} = t/T$, is chosen as

$$T = \frac{8\eta_0 \chi}{\pi} \frac{L}{R^4}$$

making the time derivative in (4.1) of $O(1)$. Note the dependence of T on the geometry of the die by the factor L/R^4. This factor is often encountered in experiments.

This normalization leads to the following set of equations (omitting the hats):

$$\frac{dP(t)}{dt} = Q_i - Q(t) \tag{4.5}$$

$$\varepsilon w(r,t) + S(r,t) = 4P(t)r \tag{4.6}$$

$$Q(t) = \int_0^1 r^2 w(r,t)\,dr \tag{4.7}$$

$$v(1,t) = 0 \tag{4.8}$$

In (4.6), $\varepsilon = \eta_s/\eta_0 \ll 1$ is a small parameter, relating the (very small) viscosity at high shear rates to the viscosity at moderate shear rates.

4.3 Constitutive Model for the Shear Stress

In [1], [2], and [9], several constitutive models (JSO, KBKZ, with one or more relaxation rates) are studied, all having one common feature: a

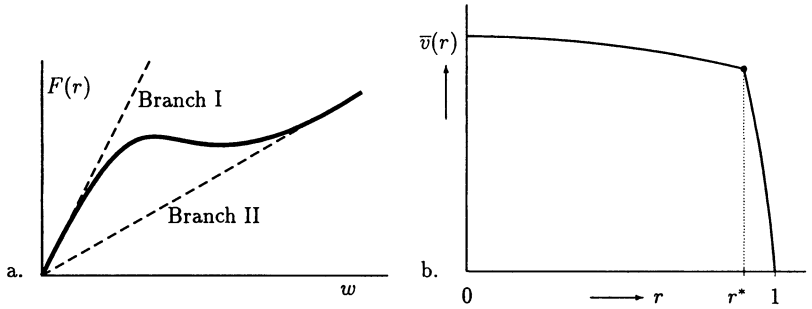

Figure 4.3 — (a) A nonmonotone stationary shear curve; (b) the steady-state velocity profile $\bar{v}(r)$ in spurt flow showing a kink at $r = r^*$ (from [1]).

nonmonotone stationary shear curve (total stationary shear stress versus shear rate). An example of such a shear curve is shown in Figure 4.3(a). For our consideration, the most important consequence of this nonmonotonicity is that the apparent viscosity for very high shear rates, as they occur in the spurt zone, is much smaller than the viscosity for the moderate shear rates in the kernel.

To visualize this, we consider a stationary solution of the system described in the preceding section. Let $\omega(r) = \lim_{t\to\infty} w(r,t)$ be the stationary value of the shear rate and $F(r) = \lim_{t\to\infty}(4P(t)r)$, $r \in [0,1]$, the stationary value of the total shear stress. Then, as shown in [2, section 3], for small enough ε-values, the stationary shear curve is nonmonotone. This implies that for certain values of F the stationary solution of (4.6) is not unique. More relevant for our considerations, however, is the following observation: If $F(1)$ is large enough, there is a jump in $\omega(r)$ from a branch with rather low ω-values to a branch with much higher ω-values (see Figure 4.2). We refer to a stationary solution on the first branch as *classical flow* and to one on the latter branch as *spurt flow.*

To distinguish between classical flow (moderate shear rates) and spurt flow (high shear rates) we propose the following (simplified) discrete model:

- In the classical flow zone we assume $\bar{S} = \omega$ and we neglect $\varepsilon\omega$ with respect to ω. In that case (4.6) reduces to (here $\bar{S}(r)$ and $\bar{P}$ are the stationary values of S and P)

$$\bar{S}(r) = \omega(r) = 4\bar{P}r \tag{4.9}$$

  This corresponds to Branch I in Figure 4.3(a).

- In the spurt zone, we neglect (motivated by the very low values of the viscosity at these high shear rates) $\bar{S}$ with respect to $\varepsilon\omega$, and then (4.6) yields

$$\varepsilon\omega(r) = 4\bar{P}r \tag{4.10}$$

  corresponding to Branch II.

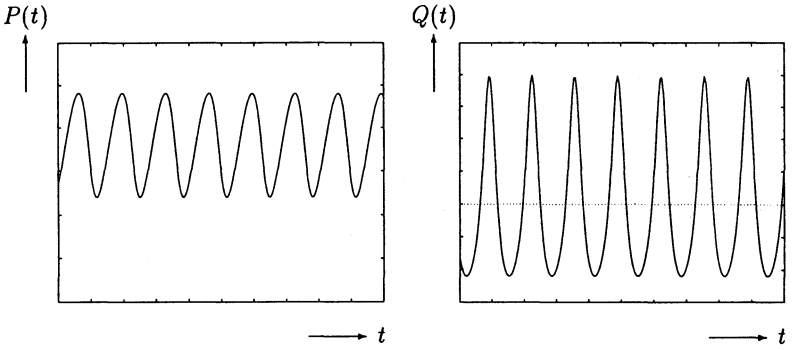

Figure 4.4 — The pressure $P(t)$ and the volumetric flow rate $Q(t)$ as functions of time t, showing persistent oscillations (from [1]).

From the three-dimensional theories presented in [1] and [3], we mention the following results (which will form the basis for our discrete model to be presented in the next section):

1. For a certain range of prescribed inlet flow rates Q_i (piston-driven flow), spurt is found to occur. Spurt is manifested by a kink in the velocity profile ([1, figure 2.2], or Figure 4.3(b)); a narrow zone of very high shear rates is developed at the capillary wall. This results in a sudden increase in the outgoing flow rate $Q(t)$. This kinked velocity profile can be obtained by integration with respect to r of (4.9) and (4.10) (with $\omega(r) = -\partial v/\partial r$).
2. For a certain range of prescribed inlet flow rates Q_i periodic oscillations in both the pressure and the flow rate are found ([1, figure 4.11], or Figure 4.4).
3. The transition from classical to spurt flow, and vice versa, is always very fast ([1, figure 3.3], or Figure 4.5). During this fast transition the

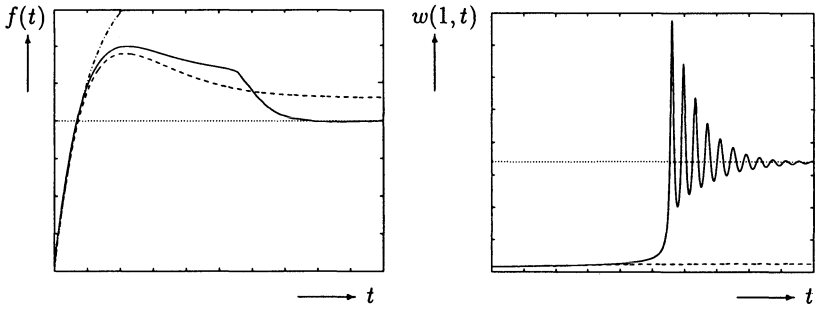

Figure 4.5 — The pressure gradient $f(t) = P(t)/L$ and the velocity gradient $w(1,t)$, directly related to $Q(t)$, for spurt flow (from [1]). Notice the very fast increase of $w(1,t)$ or $Q(t)$ at the transition to spurt ($t \approx 5.5$), and the rather flat behavior of $f(t)$ or $P(t)$ at the same instance of time.

pressure remains (approximately) constant, whereas the flow rate suddenly jumps. The transition classical → spurt (loading trajectory) takes place at a higher pressure than the reverse transition spurt → classical (unloading trajectory) ([1, section 4.5]). This difference between loading and unloading explains *hysteresis*, a phenomenon that is observed in experiments by Kissi and Piau [7]. A constitutive model in which loading and unloading trajectories coincide excludes hysteresis, and is therefore in our view inappropriate to our purposes.

4. During spurt the thickness of the spurt zone remains constant. This result is referred to as *shape memory* ([1, sections 4.3 and 4.5] or [9]).

In the next section we construct, on the basis of these observations, from three-dimensional constitutive theories a simplified discrete model. This mathematically simple model will be able to predict relaxation oscillations in pressure and flow rate that are, at least qualitatively, similar to experimentally observed relaxation oscillations, reported in [4], [5] and [8].

4.4 Discrete Model

The starting point for our discrete model is the possible existence of a spurt zone in capillary flow. During spurt, the spurt zone reaches from, say, $r = r^* < 1$ to $r = 1$ $(1 - r^* \ll 1)$, whereas in classical flow no spurt zone exists $(r^* = 1)$. Hence, in accordance with (4.6), (4.9) and (4.10) we take

$$\begin{aligned} w(r,t) &= 4rP(t), \qquad 0 \le r < r^* \\ w(r,t) &= \frac{4rP(t)}{\varepsilon}, \qquad r^* < r \le 1. \end{aligned} \tag{4.11}$$

With use of (4.11) in (4.7) the volumetric flow rate can be evaluated into

$$\begin{aligned} Q(t) &= \int_0^1 r^2 w(r,t)\, dr \\ &= P(t)\left((r^*)^4 + \frac{(1-(r^*)^4)}{\varepsilon}\right) \\ &\approx P(t)\left(1 + \frac{4}{\varepsilon}(1-r^*)\right) \end{aligned} \tag{4.12}$$

because $(1 - r^*) \ll 1$. Assuming that $(1 - r^*) = O(\varepsilon)$, we define the normalized thickness of the spurt zone by

$$R(t) = (1 - r^*)/\varepsilon. \tag{4.13}$$

Substitution of (4.13) into (4.12) yields

$$Q(t) = (1 + 4R(t))P(t). \tag{4.14}$$

To make the model complete, we need an evolution equation for $R(t)$. This equation must match the four points listed in Section 4.3, especially points 3 and 4. On the analogy of the slip model proposed by Greenberg and Demay in [6], which is also used in [8], we introduce the following evolution equation for the normalized thickness of the spurt zone,

$$\frac{dR}{dt} = -\lambda[R(t) - \alpha H(P - B(Q))] \tag{4.15}$$

with λ and α material parameters, H the Heaviside function, and $B(Q)$ a switch curve, defined by

$$B(Q) = \begin{cases} Q_1, & Q < Q_1 \\ Q_1 + \frac{Q-Q_1}{Q_2-Q_1}\left[\frac{Q_2}{1+4\alpha} - Q_1\right], & Q_1 < Q < Q_2 \\ \frac{Q_2}{1+4\alpha}, & Q > Q_2 \end{cases} \tag{4.16}$$

where Q_1 and Q_2 are two fixed values, such that $Q_2/(1 + 4\alpha) < Q_1 < Q_2$. This accounts for the fact that the transition spurt $\rightarrow$ classical takes place at a lower pressure than the transition classical $\rightarrow$ spurt, in accordance with point 3 in Section 4.3. It follows from (4.15) (see Section 4.6) that $R(t) = 0$ in classical flow, and that $R(t) = \alpha(=$ constant) in spurt flow, in accordance with point 4.

The switch curve $B(Q)$ is depicted in Figure 4.6. Because by assumption the transition from classical to spurt flow, and vice versa, is very fast, we have $\lambda \gg 1$ in the normalized time scale used here.

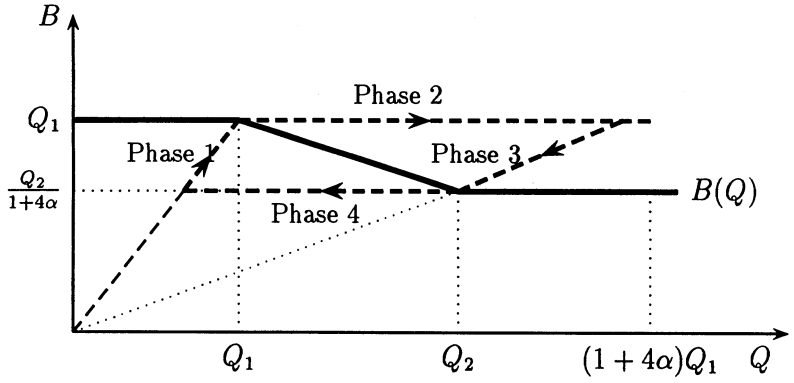

Figure 4.6 — The switch curve $B(Q)$ (bold line); the dashed line represents the relaxation loop.

Recapitulating, we have the following discrete model for the unknowns: $P(t), Q(t)$, and $R(t)$:

$$\frac{dP(t)}{dt} = Q_i - Q(t)$$

$$Q(t) = (1 + 4R(t))P(t) \tag{4.17}$$

$$\frac{dR(t)}{dt} + \lambda R(t) = \alpha\lambda H(P - B(Q)).$$

Assuming that the process starts from rest, we have as initial conditions

$$P(0) = R(0) = 0. \tag{4.18}$$

This system can be solved either numerically (see [5]) where results show relaxation oscillations in $P(t)$ and $Q(t)$ or analytically (see Section 4.6).

4.5 Comparison with Slip Model

Our discrete model presented in the preceding section will now be compared with a more or less analogous discrete slip model derived by den Doelder et al. [5]. They used a model for slip at the capillary wall in agreement with a slip law first proposed by Greenberg and Demay [6]. In this slip model, $v(1,t)$ can be either larger than zero or equal to zero, depending on whether slip occurs. When slip starts, the flow rate suddenly increases. The slip velocity at the wall is taken proportional to the maximum shear stress at the wall, which in its turn is proportional to the pressure $P(t)$. The appearance of slip is governed by an evolution equation of the same type as the one for $R(t)$. Thus,

$$v(1,t) = G(t)P(t)$$

where $G(t)$ satisfies (4.15) with $R(t)$ replaced by $G(t)$.

When slip occurs, the volumetric flow rate equals (instead of (4.7))

$$Q(t) = 2\int_0^1 rv(r,t)\,dr = v(1,t) + \int_0^1 r^2 w(r,t)\,dr.$$

In [5], the fluid is assumed to be Newtonian everywhere in the flow region, yielding

$$S(r,t) = w(r,t) = 4rP(t), \qquad \forall_{r\in[0,1]}.$$

Substitution of this relation for w into the equation for the flow rate leads to

$$Q(t) = (1 + G(t))P(t).$$

Hence, by comparing the latter relation with (4.14), we see that if

$$G(t) \to 4R(t)$$

exactly the same model follows. Thus we conclude that in this approach, and in a mathematical sense, no difference between the two models based on either no-slip, spurt zone or slip, no spurt zone exists.

4.6 Analytical Calculations

The nonlinear system (4.17) can be solved analytically if we make use of asymptotics that are based on $\lambda \gg 1$ (fast transitions)(see also [12]). For this, we distinguish four phases, of which phase 1 represents classical flow, phase 3 spurt flow, and phases 2 and 4 are transition phases from classical to spurt flow and vice versa, respectively. In phases 1 and 3 the evolution equation (4.15) yields constant values for $R(t)$ (the very fast exponential evolution ($\propto \exp(-\lambda t)$, $\lambda \gg 1$) takes place in the transition phases). Hence, in phase 1, $R(t) = 0$, whereas in phase 3, $R(t) = \alpha$. During very short ($O(\lambda^{-1})$) phases 2 and 4, $R(t)$ jumps from $0 \to \alpha$ and from $\alpha \to 0$, respectively. Because $R(t)$ is constant during phases 1 and 3 (shape memory), the system (4.17) is linear and can be easily solved. On the other hand, the transition phases are so short ($O(\lambda^{-1})$) that the changes in $P(t)$ according to (4.17) are also of ($O(\lambda^{-1})$) and, hence, negligible in an approximation for $\lambda \gg 1$. Thus, $P(t)$ may be taken constant during these phases, and again the system (4.17) is linear and easy to solve.

Therefore, we distinguish the following four phases.

Phase 1. $0 < t < t_1$: Classical Flow

In this initial phase $P < B(Q)$ and hence $H(P - B(Q)) = 0$. Then (4.17; eq. 3), with $R(0) = 0$, yields $R(t) = 0$. This reduces (4.17) and (4.18) to

$$\begin{aligned} \frac{dP}{dt} &= Q_i - Q(t), \qquad P(0) = 0 \\ Q(t) &= P(t) \end{aligned} \tag{4.19}$$

the solution of which reads

$$P(t) = Q(t) = Q_i(1 - e^{-t}). \tag{4.20}$$

The end of phase 1 is at $t = t_1$, where t_1 is the time where $P(t)$ reaches for the first time the switch curve $B(Q)$. Hence (see Figure 4.6), $P(t_1) = Q_1$,

yielding

$$t_1 = \ln\left(\frac{Q_i}{Q_i - Q_1}\right) \tag{4.21}$$

provided $Q_i > Q_1$. We note that $t_1 = O(1)$, which justifies our time scaling.

Phase 2. $t_1 < t < t_2$: Transition from Classical to Spurt Flow

Because $P(t)$ crosses $B(Q)$ from below at $t = t_1$, we assume that during this phase $P > B(Q)$, so $H(P - B(Q)) = 1$. For this phase we introduce a new time scale: $\tau = \lambda(t - t_1)$, such that (4.17) becomes ($R = R(\tau)$, etc.)

$$\begin{aligned} &\frac{dR}{d\tau} + R(\tau) = \alpha, \qquad R(0) = 0 \\ &\frac{dP}{d\tau} = \frac{1}{\lambda}(Q_i - Q(\tau))(= O(\lambda^{-1})) \qquad P(0) = Q_1 \\ &Q(\tau) = (1 + 4R(\tau))P(\tau). \end{aligned} \tag{4.22}$$

The solution of this system reads

$$\begin{aligned} P(\tau) &= P(0)(1 + O(\lambda^{-1})) \approx Q_1 \\ R(\tau) &= \alpha(1 - e^{-\tau})(\to \alpha) \\ Q(\tau) &= [1 + 4\alpha(1 - e^{-\tau})]Q_1(\to (1 + 4\alpha)Q_1). \end{aligned} \tag{4.23}$$

We define the end of phase 2 as $\tau = \tau_2$, such that $e^{-\tau_2} = \lambda^{-1}$. This yields

$$\tau_2 = \ln\lambda \quad \text{or} \quad t_2 = t_1 + \frac{\ln\lambda}{\lambda} = t_1(1 + O(\lambda^{-1})). \tag{4.24}$$

So, indeed, $\tau_2 = O(1)$, implying that the time that phase 2 lasts is very short ($O(\lambda^{-1})$) compared to phase 1.

Phase 3. $t_2 < t < t_3$: Spurt Flow

In this phase we assume $P > B(Q)$ (see Figure 4.6), so $H(P - B(Q)) = 1$. Because (4.23 eq. 3) yields $R(t_2) = \alpha(1 + O(\lambda^{-1})) \approx \alpha$, for $\lambda^{-1} \to 0$, (4.17 eq. 3) renders $R(t) = \alpha$, for all $t \in (t_2, t_3)$.

With the new time scale $\tau = (t - t_2)$, (4.17) reduces to ($P = P(\tau)$, etc.)

$$\begin{aligned} &\frac{dP}{d\tau} = Q_i - Q(\tau), \qquad P(0) = Q_1 \\ &Q(\tau) = (1 + 4\alpha)P(\tau). \end{aligned} \tag{4.25}$$

The solution of this system reads

$$P(\tau) = \frac{Q(\tau)}{1+4\alpha} = \frac{Q_i}{1+4\alpha} + \left[Q_1 - \frac{Q_i}{1+4\alpha}\right] e^{-(1+4\alpha)\tau}. \tag{4.26}$$

Because phase 3 always runs along the line $P = Q/(1+4\alpha)$ in a $P-Q$-diagram, it must be so that if this line crosses the switch curve $B(Q)$ this happens in the point $P = B(Q_2) = Q_2/(1+4\alpha)$. According to (4.26), $Q(\tau) \to Q_i$, for $\tau \to \infty$. As $Q \to Q_i$, there are now two possibilities:

1. If $Q_i > Q_2$, then $P(\tau) \to Q_i/(1+4\alpha) > B(Q_i) = Q_2/(1+4\alpha)$. In this case no transition takes place, and phase 3 tends to a final stationary spurt state, in which $(P(\tau), Q(\tau)) \to (Q_i/(1+4\alpha), Q_i))$, for $\tau \to \infty$.
2. If $Q_i < Q_2 (< (1+4\alpha)Q_1$, see (4.16)), then a transition to classical flow takes place when $Q(t)$ reaches $Q_2 > Q_i$, and phase 4 starts at $t = t_3 (< \infty)$. Here, t_3 is such that $Q(t_3) = Q_2$, yielding

$$t_3 = t_2 + \frac{1}{(1+4\alpha)} \ln\left(\frac{(1+4\alpha)Q_1 - Q_i}{Q_2 - Q_i}\right) \tag{4.27}$$

We assume case 2 holds, and we proceed with phase 4. We shall see that in this case relaxation oscillations occur.

Phase 4. $t_3 < t < t_4$: Transition from Spurt to Classical Flow

At $t = t_3$, $P(t)$ crosses the switch curve coming from above, so during this phase we assume $P < B(Q)$, and thus $H(P - B(Q)) = 0$. With the new time scale $\tau = \lambda(t - t_3)$, (4.17) reduces to ($R = R(\tau)$, etc.)

$$\begin{aligned} &\frac{dR}{d\tau} + R(\tau) = 0 \qquad R(0) = \alpha \\ &\frac{dP}{d\tau} = \frac{1}{\lambda}(Q_i - Q(\tau)) (= O(\lambda^{-1})) \qquad P(0) = Q_2/(1+4\alpha) \\ &Q(\tau) = (1+4R(\tau))P(\tau). \end{aligned} \tag{4.28}$$

The solution of this system reads

$$\begin{aligned} P(\tau) &= \frac{Q_2}{(1+4\alpha)}(1 + O(\lambda^{-1})) \\ R(\tau) &= \alpha e^{-\tau} \ (\to 0) \\ Q(\tau) &= \frac{Q_2}{(1+4\alpha)}(1 + 4\alpha e^{-\tau}). \end{aligned} \tag{4.29}$$

Analogous to phase 2, phase 4 ends at $t = t_4 = t_3(1 + O(\lambda^{-1}))$. At $t = t_4$, phase 1 starts anew, not from $P(0) = Q(0) = 0$, but from

$$P = Q = Q_2/(1 + 4\alpha)$$

This brings us to the fifth phase.

Phase 5. $t_4 < t < t_5$: Classical Flow

Analogous to phase 1, the solution now reads

$$P(t) = Q(t) = Q_i + \left(\frac{Q_2}{1 + 4\alpha} - Q_i\right) e^{-(t-t_4)}. \tag{4.30}$$

This phase ends at $t = t_5$ when $Q(t_5) = Q_1$, yielding

$$t_5 = t_4 + \ln\left(\frac{Q_i - Q_2/(1 + 4\alpha)}{Q_i - Q_1}\right) \tag{4.31}$$

after which a phase identical to phase 2 follows.

Thus, a loop is followed as depicted by the dashed line in Figure 4.6. Because this dashed line is a closed loop, it represents a periodic phenomenon. Its behavior is of relaxation type, because phases 2 and 4 are extremely short. Therefore, we call this a relaxation oscillation. The period of one oscillation is $(t_3 - t_2) + (t_5 - t_4)$, or

$$T_{os} = \ln \frac{((1 + 4\alpha)Q_1 - Q_i)((1 + 4\alpha)Q_i - Q_2)}{(1 + 4\alpha)(Q_2 - Q_i)(Q_i - Q_1)} \tag{4.32}$$

for $\lambda^{-1} \approx 0$. The behavior of the pressure $P(t)$ and the volumetric flow rate $Q(t)$ during these relaxation oscillations is depicted in Figure 4.7.

Hence, the conclusion is that the obtained analytical results clearly predict relaxation oscillations. These relaxation oscillations occur if

$$Q_1 < Q_i < Q_2 < (1 + 4\alpha)Q_1 \tag{4.33}$$

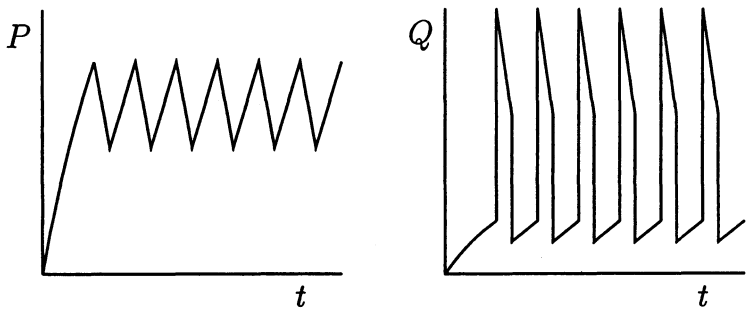

Figure 4.7 — Relaxation oscillations for the pressure $P(t)$ and the volumetric flow rate $Q(t)$ ($Q_1 = 1, Q_2 = 3, Q_i = 2, \alpha = 1$, and $\lambda = 1000$).

A relaxation loop consists of four distinct phases: in phase 1 the flow is classical, whereas in phase 3 spurt occurs; phases 2 and 4 are relatively short transition phases.

4.7 Results

Our model described by the system (4.17) is characterized by the parameter set $\{Q_1, Q_2, \alpha, \lambda\}$ plus the prescribed inlet flow rate Q_i. In the preceding section we have seen that dependent on the value of Q_i different types of capillary flow can occur. We distinguish three regimes for Q_i, knowing $Q_i < Q_1, Q_1 < Q_2 < Q_1$, and $Q_i > Q_2$. For the numerical results in this section, the following fixed values for the parameters are used:

$$Q_1 = 1, Q_2 = 3, \alpha = 1, \lambda = 1000.$$

- In the first regime, $Q_i < Q_1$, the flow is classical, like a Poiseuille flow. Because there is no spurt zone, the velocity profile is smooth. The pressure and flow rate tend monotonically to their stationary values, according to (4.20). This behavior is depicted in Figure 4.8.
- In the second regime $Q_1 < Q_i < Q_2$, persistent relaxation oscillations occur. The flow periodically jumps from classical to spurt and vice versa, and large jumps in the pressure and, especially, the flow rate are found. The value of the flow rate is relatively high during spurt, and low during classical flow. Typical relaxation oscillations in $P(t)$ and $Q(t)$ in the case where $Q_i = 2$ are depicted in Figure 4.7.

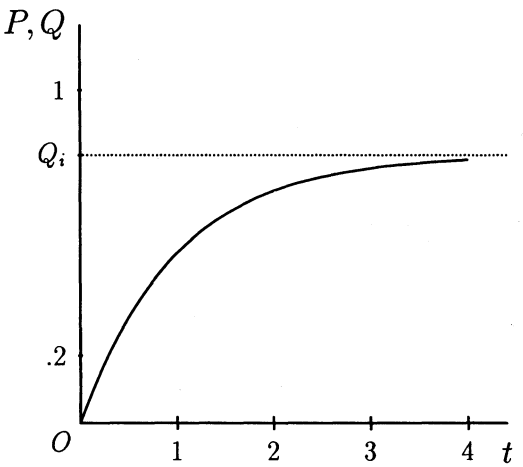

Figure 4.8 — The pressure $P(t)$ and the flow rate $Q(t)$ as a function of time t for $Q_i = 0.8 < Q_1$ (classical flow).

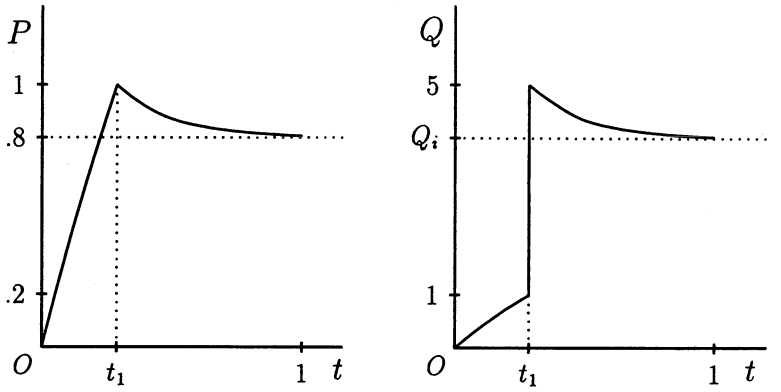

Figure 4.9 — The pressure $P(t)$ and the flow rate $Q(t)$ as a function of time t for $Q_i = 4 > Q_2$ (spurt flow).

- In the third regime $Q_i > Q_2$, the flow again tends to a stationary state, but now to one in which spurt occurs. The spurt zone is fixed to $R = \alpha$, and the pressure and flow reach the stationary values $\bar{P} = Q_i/(1+4\alpha)$, and $\bar{Q} = Q_i$, respectively, according to (4.26). In this regime we can further distinguish between $Q_i < (1 + 4\alpha)$ and $Q_i > (1 + 4\alpha)$. If $Q_i < (1 + 4\alpha)$, an overshoot in both $P(t)$ and $Q(t)$ occurs, before they reach their final state. This overshoot at $t = t_1$ is depicted in Figure 4.9, for the case when $Q_i = 4$. If $Q_i > (1 + 4\alpha)$, no overshoot occurs; in this case the steady state is reached in a monotone way.

4.8 Conclusions

In this case study, we have presented a discrete model for the capillary flow of a polymeric fluid, allowing for the occurrence of spurt flow. In spurt flow a very thin layer of very high shear rates exists near the wall of the capillary, while in the kernel the flow is almost uniform (like plug flow). Our model was built on the assumption that the flow in both the kernel and the spurt layer can be described by linear Newtonian fluid laws, however, with quite distinct viscosities: The viscosity in the spurt layer is taken to be much smaller ($O(\varepsilon^{-1}), 0 < \varepsilon \ll 1$) than the one in the kernel. At the wall of the capillary, a no-slip condition is maintained.

Our model is based on the fundamental concepts of:

- global mass balance for the compressible fluid in the barrel.
- equation of motion for the shear flow in the capillary.

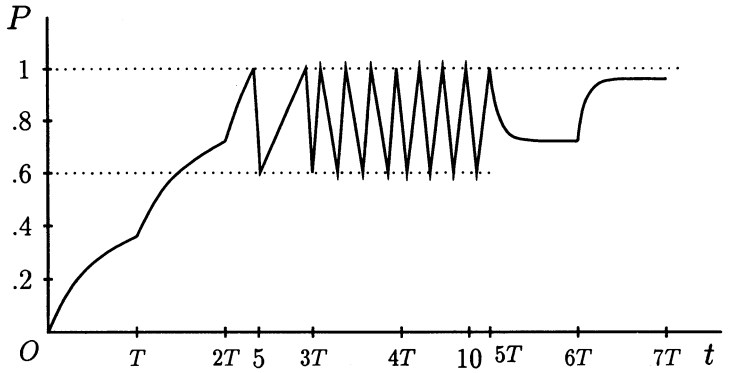

Figure 4.10 — The pressure $P(t)$ as a function of time t for a loading process in which Q_i is stepwise increased at time steps T, with $T = 2.1$, according to the sequence $\{0.4, 0.8, 1.2, 1.8, 2.4, 3.6, 4.8\}$.

- a global relation for the total flow rate through the capillary.
- a postulated evolution relation for the thickness of the spurt layer (including a switch relation describing the forming or vanishing of a spurt layer).

We have shown that the model thus obtained was able to describe the distorted extrusion flow phenomenon called spurt. Spurt is manifested by relaxation oscillations in both the pressure in the barrel and the flow rate through the capillary or die of the extruder. The relaxation oscillations found here are of the type depicted in Figure 4.7. Moreover, a finite range of prescribed inlet flow rates Q_i was found for which relaxation oscillations can occur. This was shown by the simulation of a realistic loading process, depicted in Figure 4.10, in which only for a restricted range of Q_i-values spurt oscillations show up. For Q_i-values below this range ($Q_i < Q_1$) the flow tends to a stationary classical (Poiseuille) flow, whereas for values beyond this range ($Q_i > Q_2$) the flow tends to a stationary spurt flow (having a fixed spurt layer).

We consider it important to note here that the discrete model presented in Section 4.4 satisfies each of the four points listed in Section 4.3, which emanate from a three-dimensional theory (from [1]):

1. According to (4.33) spurt only occurs for a restricted range ($Q_i \in (Q_1, Q_2)$). The sudden increase in flow rate Q at the time spurt starts, mentioned in Section 4.3, is clearly depicted in Figure 4.9.
2. For the range (Q_1, Q_2) mentioned in 1, relaxation oscillations are found as in Figures 4.7 and 4.10.
3. The very fast transition from classical to spurt flow and vice versa is manifested by the high numerical value for λ in the evolution equation

(4.15). In Section 4.6, it is shown that during transition phases 2 and 4 the pressure remains constant, but the flow rate makes large jumps. The transition from classical to spurt flow takes place at a normalized pressure value $P = Q_1$, and that from spurt to classical flow at the *lower* value $P = Q_2/(1 + 4\alpha) < Q_1$.

4. During the spurt phase (i.e., phase 3 in Section 4.6) the normalized thickness of the spurt layer remains $R(t) = \alpha$, hence constant (*shape memory*).

Hence, so far our discrete model is in accordance with the three-dimensional theory of [1].

In Section 4.5, we have shown that our discrete no-slip model renders exactly the same results as the discrete model of [5], which is based on a model with slip at the capillary wall (and without an internal spurt layer). Hence, in a mathematical sense, no differences between these two models exist.

Relaxation oscillations in extrusion are often observed in experiments and in the literature. A lot of experimental data, especially on extrusion instabilities, can be found in the new book by Koopmans and Molenar, [8]. Comparison of our analytical results as depicted in Figures 4.7 to 4.10 with experimental results as they can be found in, e.g., [9, figure 9], [4, figure 3], and [8] indicates a good *qualitative* agreement. However, for a *quantitative* agreement, further modifications of the model presented here are needed. As shown in [4], at least a nonlinear evolution equation is needed. That this can lead to an essentially improved quantitative agreement is shown by den Doelder et al. [4], where, among others, a nonlinear slip relation, relating the slip velocity to the square of the wall shear stress, is used. Translated to our model, this would imply that relation (4.14) must become nonlinear (in that $P(t)$ must be replaced by $P^2(t)$). It remains a point for further research to investigate what are the consequences of this modification. Moreover, it again stresses the fact that a theoretical basis for the (empirical) evolution equation for $R(t)$ is still missing. A further analysis of the results of the three-dimensional theory of the thesis of Aarts [1] could render some new insights in this aspect.

References

1. Aarts, A.C.T., Analysis of the flow instabilities in the extrusion of polymeric melts, *Ph.D. Thesis*, Eindhoven University of Technology (1997).
2. Aarts, A.C.T., and van de Ven, A.A.F., Instabilities in the extrusion of polymers due to spurt, *Progress in Industrial Mathematics at*

ECMI94, H. Neunzert; ed., Wiley and Teubner, Chichester (1996), 216–23.

3. Aarts, A.C.T., and van de Ven, A.A.F., The occurrence of periodic distortions in the extrusion of polymeric melts. *Continuum Mechanics and Thermodynamics*, **11** (1999), 113–139.
4. den Doelder, C.F.J., Koopmans, R. J., and Molenaar, J., Quantitative modelling of HDPE spurt experiments using wall slip and generalised Newtonian flow. *J. Non-Newtonian Fluid Mech*, **79** (1998), 503–514.
5. den Doelder, C.F.J., Koopmans, R.J., Molenaar, J., and van de Ven, A.A.F., Comparison of wall slip and constitutive instability spurt models, *J. Non-Newtonian Fluid Mechanics*, **75** (1998), 25–41.
6. Greenberg, J.M., and Demay, Y., A simple model of the melt fracture instability, *European J. Appl. Math.*, **5** (1994), 337–58.
7. Kissi, N.E., and Piau, J.M., The different capillary flow regimes of entangled polydimethylsiloxane polymers: Macroscopic slip at the wall, hysteresis and cork flow, *J. Non-Newtonian Fluid Mech.*, **37** (1990), 55–94.
8. Koopmans, R.J., and Molenaar, J., *Polymer Melt Fracture*, Marcel Dekker Inc., New York, to appear (1999).
9. Malkus, D.S., Nohel, J.A., and Plohr, B.J., Dynamics of shear flow of a non-Newtonian fluid, *J. Computational Phy.*, **87** (1990), 464–87.
10. Molenaar, J., and Koopmans, R.J., Modeling polymer melt-flow instabilities, *J. Rheology*, **38** (1994), 99–109.
11. Piau, J.M., and Kissi, N.E., Measurement and modelling of friction in polymeric melts during macroscopic slip at the wall, *J. Non-Newtonian Fluid Mech.*, **54** (1994), 121–42.
12. van de Ven, A.A.F., Comparing stick and slip models for spurt in the extrusion of polymeric melts. In: *Progress in Industrial Mathematics*, Eds. L. Arkeryd, J. Bergh, P. Brenner, R. Petterson; Proc. ECMI 98, Teubner, Stuttgart, 1999; pp.154–162.

Part II

Flows Accompanied by Thermal Processes

5

Isobaric Crystallization of Polypropylene

ANTONIO FASANO, A. MANCINI, AND S. MAZZULLO

Università di Firenze
Dipartimento di Matematica "U. Dini"
Firenze, Italy

ABSTRACT. Crystallization of polymers is an extremely complex process exhibiting several peculiar properties that makes it substantially different from usual transitions from liquid to solid state. Starting from the experimental data on isobaric crystallization of polypropylene provided by Montell (Ferrara, Italy), we illustrate a mathematical model based mainly on the papers [18], [30], and [31] that leads to a correct physical description of the process.

5.1 Introduction

The determination of *pressure-volume-temperature* diagrams for polymers in ranges including solidification processes presents experimental and theoretical difficulties because of the particular complexity of the chemical structure of polymers. On the other hand, knowing the behavior of polymers during cooling from a molten to solid state is of fundamental importance, for example, in injection molding processes. This explains the abundance of experimental literature on the subject (see, e.g., [5], [16], [17]).

There is also a great deal of literature about mathematical modeling of polymer crystallization (see, in particular, the survey papers [5] and [17] as well as [2], [3], [4], [6], [10], [14], [19], [20], and [23]) with an impressive

A. Fasano (ed.), *Complex Flows in Industrial Processes*

variety of proposed models. Due to the complexity of the phenomenon all models have been formulated on a heuristic basis, although crystallization models are often inspired by the well-known Avrami–Kolmogorov phase change model ([7]), which has been given a rigorous justification by Kolmogorov, grounded on a probabilistic argument [24]. The effort of using probability as the basic tool for the mathematical description of crystal growth and nucleation over a range of temperature has been successfully undertaken in recent years by V. Capasso and coworkers ([11], [33]). The study of the thermodynamics of nucleation has been performed in [1], [21], [39], [40], [41], [42], and [43].

A discussion of phase change models for polymers is out of the scope of this chapter, and for this reason we refer to the survey papers. Let us just recall the main features of polymer solidification. Crystallization takes place over a relatively large temperature interval, depending on pressure, and is a two-step process (nucleation and growth) proceeding at a rate that depends on pressure, temperature, and the crystal volume fraction already in the system. The influence of the last factor must be attributed to the so-called *impingement* phenomenon with a twofold mechanism: (1) The presence of crystals reduces the volume available (and thus the probability) for nucleation (this is the essential core of Kolmogorov's argument), and (2) the collision between two growing crystals stops their radial growth in all directions of contact points (as a consequence, there are sharp interfaces among crystals that are clearly observable).

Remark 5.1. *This situation is not peculiar to polymer crystallization; it occurs in other processes, like solid–solid transitions in steel, for which Avrami and Kolmogorov theories have been developed.*

What is really typical of polymer crystallization is that what we have so far called crystals *are in fact* crystal aggregates with amorphous inclusions. *The really crystalline components of such complexes are thin laminar elements (*lamellae*) growing approximately along radii from the nucleus (with possible branching) and giving rise to a structure called* spherulite, *having typical dimensions ranging from several microns to ten and hundreds of microns.*

Clearly the density and size distribution of spherulites at the end of the process depend on the time spent in the phase change temperature range and are going to critically influence the mechanical properties of the system. Even when spherulites occupy the entire available volume, an amorphous fraction will be present and the crystal volume fraction never reaches unity.

It is usually assumed that for any given temperature in the crystallization range there is a known amount of residual amorphous phase. This leads to the definitions of an experimental function: the *maximum* (or *equilibrium*) crystal volume fraction $w_{eq}(T)$, whose properties will be discussed later.

As we said, phase change occurs when the absolute temperature T ranges in some pressure-dependent interval $(T_{\text{glass}}, T_{\text{melt}})$. For $T \geq T_{\text{melt}}$ (*melting point*) the system is *liquid* (in the thermodynamical sense; the rheology of polymers is another wide and fascinating research field with many still-open questions), while for T approaching T_{glass} (*glassy transition temperature*) the viscosity of the amorphous phase increases to a point that the mobility of the polymer chains is no longer sufficient to arrange them according to a crystalline pattern, so that phase change stops completely.

To this already complex picture we should add other peculiar effects, like secondary crystallization, effects of nucleation seeds (owing, e.g., to impurities), memory effects (in melting-solidification cycle sites occupied by crystals prior to melting are more likely to become nucleation sites during the next cooling stage), the influence on nucleation rate by the stress history experienced by the molten phase, thermally induced flows, and the like. Such an extremely complex scenario is in itself an explanation of the diversity of models proposed in the literature.

The objective of this chapter is quite specific: investigating a model that correctly describes the solidification process of a polymer sample under a prescribed pressure, taking into account the shrinking flow induced by thermal contraction and crystal growth. We refer explicitly to the experimental data on polypropylene provided by *Montell Italia SpA*.

This is the experimental procedure that, carried out for several values of the pressure, leads to the determination of P-V-T diagrams. The model is designed according to the experimental apparatus in use at Montell's laboratories (see Fig. 5.1).

Although we adopt a specific crystallization kinetic law, from a mathematical point of view such a choice is not critical, in the sense that it could be replaced by another with similar mathematical characterization. The paper summarizes the results of research based on the experimental data obtained at Montell, which has gone through several steps:

- analysis of the most important features of the measurement device;
- formulation of a mathematical model coupling the thermal problem and the flow problem;
- numerical simulation of the process, indicating the admissibility of some substantial simplifications;
- theoretical investigation of the simplified model, aimed at showing existence and uniqueness of a classical solution; and
- physical conclusions.

We will follow this plan in our exposition. The main reference is [18].

The model helps us to better understand the development of the cooling process, in particular for what concerns the role of the function $w_{eq}(T)$, acting as a constraint for the crystallization kinetics. It has been shown, for example, that for polypropylene the switch from the unconstrained kinetics

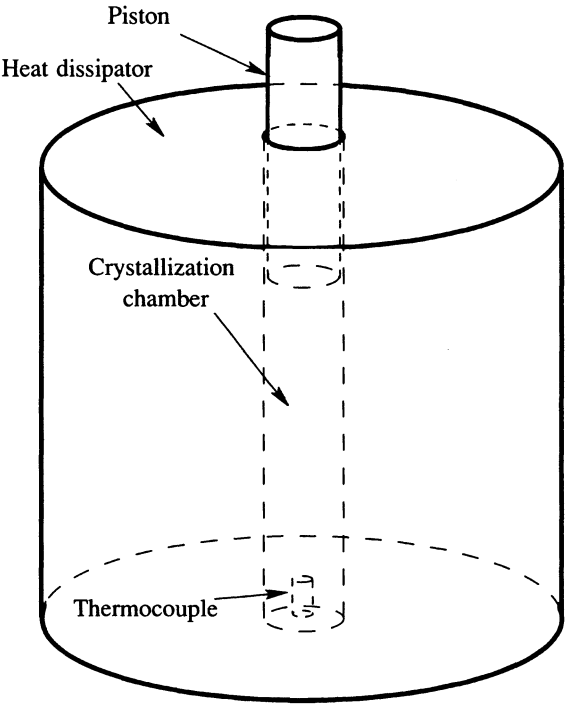

Figure 5.1 — The measurement device.

to the crystallization stage fully described by the function $w_{eq}(T)$ occurs at temperatures very close to the melting point. Information like this has an obvious practical relevance: The kinetic law for the crystallization does not have to be specified over the whole phase change interval. On one hand, this saves a great deal of heavy, difficult, and costly experimental work; on the other it explains the flexibility in choice of the kinetic law by various authors.

The material presented here is based on [15], [18], [27], [28], [29], [30], and [32].

5.2 The Experiments

The development of the model stems from the experimental data obtained at Montell's laboratories. The basic equipment consisted of a device providing simultaneous measurements of temperature and average specific volume and ensuring a constant pressure during the entire cooling process.

5.2.1 Measurement Device

The device can be roughly described as follows: a cylindrical chamber (radius $R \simeq 0.5$ cm) with a thermocouple, on the cylinder axis, supported by a metallic rod, and a piston on the top side to maintain the pressure constant at the desired value. The chamber is surrounded by a thick metallic heat dissipator. The device measures the temperatures at the thermocouple, the heat-dissipator, and the piston, and the height of the sample at the same time.

5.2.2 Measurements

Experiments for different pressures in the range of 1 to 1600 bars have been performed. The modus operandi is as follows. The chamber is filled with a fixed quantity of polymer (the mass m is known) and pressure is kept constant at the chosen value during the whole experiment. The temperature of the material is initially about 250°C (the polymer is completely molten and crystallinity is absent). The material is observed for about an hour until it approaches a temperature near room temperature (20–30°C). At this temperature the polymer is solid and the crystallization process is not active, from a practical point of view, because we are outside the crystallization interval.

During each experiment the following quantities are plotted as functions of time: the temperature measured by the thermocouple, the temperature of the heat dissipator, and the height of the sample (thus the specific volume).

In Figure 5.2, results obtained for some "typical" values of the pressure (p) are shown.

5.3 Analysis of Experimental Data

The first part of the model is a careful analysis of the experimental data to set up a background. What is important here is to obtain information about the state equation and the crystallization kinetics observed for different values of the pressure and for a large range of temperatures.

5.3.1 Analysis of PVT Diagrams

5.3.1.1 The State Equation (S.G.M.)

The qualitative analysis of PVT diagrams of semicrystalline polymers shows some general characteristics that can be useful in applications [31].

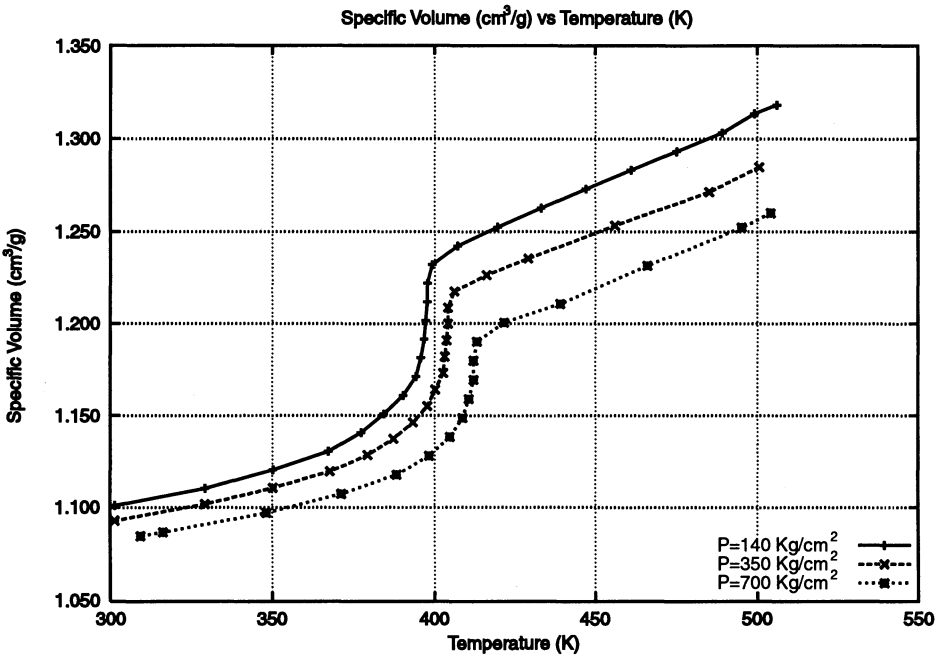

Figure 5.2 — $P - V - T$ diagrams from experiments.

In a typical V–T diagram (see Fig. 5.2) for a fixed pressure P, the behavior of the isobaric curves is linear for relatively high temperatures. Then we have the liquid–solid phase transition with a relevant decreasing of the specific volume, but this phenomenon interests a small temperature range (10–15°C). After phase transition, the isobaric curve tends to resume a linear behavior.

The experimental data can be thus described using the semi-empirical law (S.G.M.):

$$\frac{1}{\rho} = v_c + \frac{(1-w)}{P+\pi} R^*(T - T_0) \tag{5.1}$$

where v_c, π, R^*, T_0 are parameters of the material; w is the crystal volume fraction of the polymer, T the temperature, P the pressure, and ρ the volumetric density. This relation is in agreement with the linear behavior for high temperatures (when the crystallinity is zero) and for low temperatures (crystallinity having reached a constant value).

The S.G.M. law is a generalization of the Spencer–Gilmore state equation, modified to take into account the crystallinity by means of the term $(1 - w)$ ([31]).

5.3.1.2 Shift of the Phase Transition Temperature Range

The range of temperature where phase change is active depends on pressure; more exactly, it shifts to higher temperatures and shrinks when pressure increases.

This behavior can be incorporated in the model as follows:

- The Clausius–Clapeyron equation ([25],[35]) can describe the variation of T_{melt}. This relation for polypropylene can be estimated from Figure 5.2, obtaining:

$$\frac{dT_{\text{melt}}}{dP} = \frac{1}{40}\frac{\text{K}}{\text{kg/cm}^2} \tag{5.2}$$

- the Ehrenfest equation ([13],[22],[35]) is used to predict the shift of T_{glass}. Its estimate, from Figure 5.2, gives rise to:

$$\frac{dT_{\text{glass}}}{dP} = \frac{1}{27}\frac{\text{K}}{\text{kg/cm}^2}. \tag{5.3}$$

Figure 5.3 shows the functions T_{melt} and T_{glass} used in our simulations.

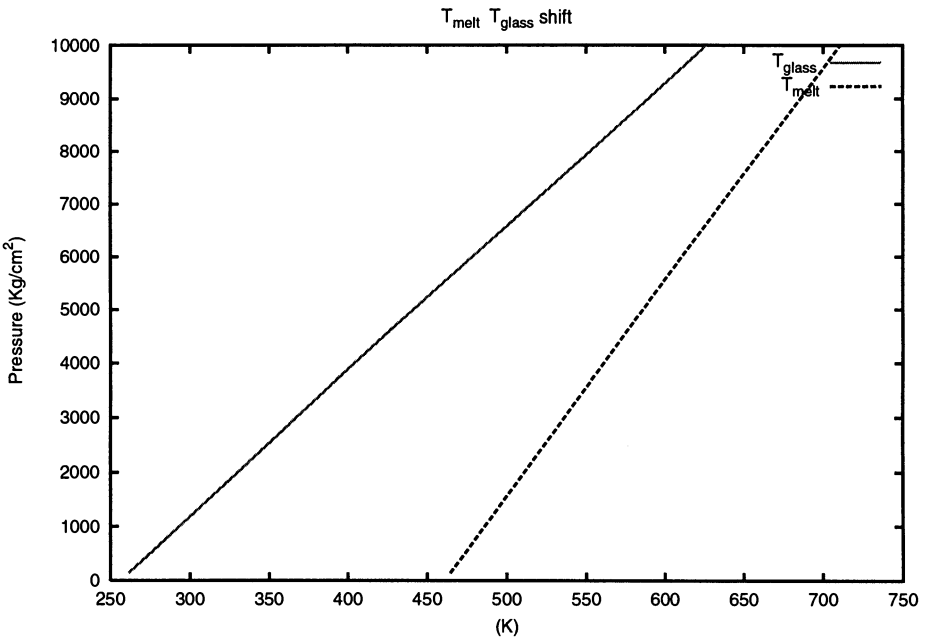

Figure 5.3 — T_{melt} and T_{glass} vs. pressure.

5.3.1.3 Crystallization Kinetics: Generalized Tobin Law

The kinetics used in our model is the one proposed in [15], because it seems to provide the best fit of the experimental data. On the other hand the model is mathematically flexible from this point of view and most of the results concerning existence and uniqueness remain valid for a large class of kinetic laws. The specific choice made here is the following generalization of Tobin's law [38]

$$\frac{dw}{dt} = K(T,P)w^{\alpha}(w_{eq} - w)^{\beta}w_{eq}^{1-\alpha-\beta} \tag{5.4}$$

where

$$K(T,P) = K_0 \exp\left[\frac{-u/R}{T - T_{\text{glass}}(P)}\right] \exp\left[-\frac{K_g(T_{\text{melt}}(P) + T)}{2T^2(T_{\text{melt}}(P) - T)}\right] \tag{5.5}$$

and w_{eq} is the equilibrium crystallinity that depends on temperature; α, β, and K_0 are positive parameters (with $\alpha + \beta < 1$) obtained by experiments ([15]); u is the viscosity activation energy; R the gas constant; and K_g the nucleation constant.

5.3.1.4 Modeling $w_{eq}(T)$

All the tests carried out experimentally and numerically have shown that an essential feature needed to produce a reasonable model for nonisothermal crystallization is the dependence of w_{eq} on temperature. In our experiments (and in some ad hoc numerical simulations and qualitative analysis) we compared three different models for this dependence.

The first is the Malkin model [9], already known in the literature, and the other two are new empirical models that have been proposed to better understand the influence of this parameter.

A plot of the three models is shown in Figure 5.4, together with a curve representing the average crystallinity observed in a typical experiment, while values of the constants a, T_M, T_{II}, c, and T_I used, respectively, in (5.6), (5.7), and (5.8) can be found in Table 5.1; of course discrepancies in regions when $w_{eq} > w$ are of little interest.

- Malkin's law:

$$w_{eq} = a\sqrt{T_M - T} \tag{5.6}$$

  (it underestimates crystallinity by a large extent).

- Our first empirical guess is the piecewise linear law (5.7): constant ($= 70\%W_{\max}$) for T in an interval of about 70 K near T_{melt}, then growing linearly up to $W_{\max}$, and finally again constant ($= W_{\max}$). The value of $W_{\max}$ used is the same obtained experimentally and used in [12] (=0.456). This simple choice of w_{eq} produces surprisingly

Table 5.1. $w_{eq}(T)$

Malkin Model		
a	5.124	—
T_M	471.2	K
Piecewise Linear Model		
T_{II}	T_{melt}-70	K
Rational Model		
T_I	474.5	K
A	1/75.0	—
c	8	—

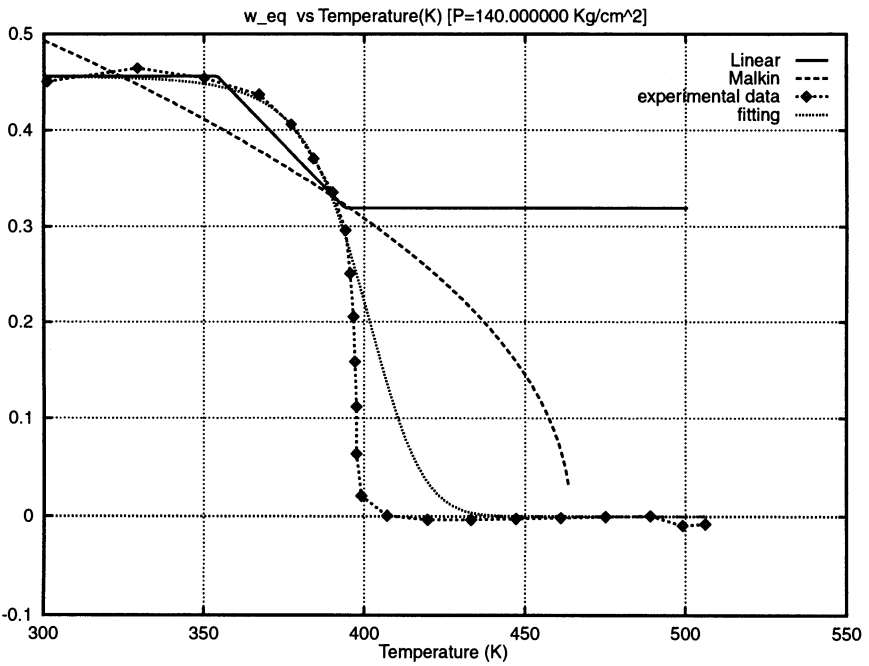

Figure 5.4 — Different models for w_{eq} compared with the measured mean crystallinity.

good agreement with the data.

$$w_{eq}(T) = \begin{cases} 0.7\, W_{\max} & T \in (T_{II}, T_{\text{melt}}) \\ W_{\max}\left[0.7 + \min\left(0.3, \frac{T_{II}-T}{T_{II}-T_{\text{glass}}}\right)\right] & T \in (T_{\text{glass}}, T_{II}) \end{cases} \tag{5.7}$$

- Formulating a relation between w_{eq} and the temperature as a rational fitting allows us to obtain the best representation of the measured data for low temperatures. For the data at hand the result is the following (see Table 5.2)

$$w_{eq}(T) = w_{\max}\frac{[A(T_I - T)]^c}{1 + [A(T_I - T)]^c} \tag{5.8}$$

In what follows, until the end of this section, we compare the results obtained using the three models, and we present the qualitative analysis developed for a simplified model that shows the importance of w_{eq} for the understanding of the nonisothermal crystallization phenomenon (see Figures 5.5, 5.6 and 5.7).

The influence of w_{eq} as a constraint for w can be emphasized by the following argument. Let us consider the simple case of a spatially uniform

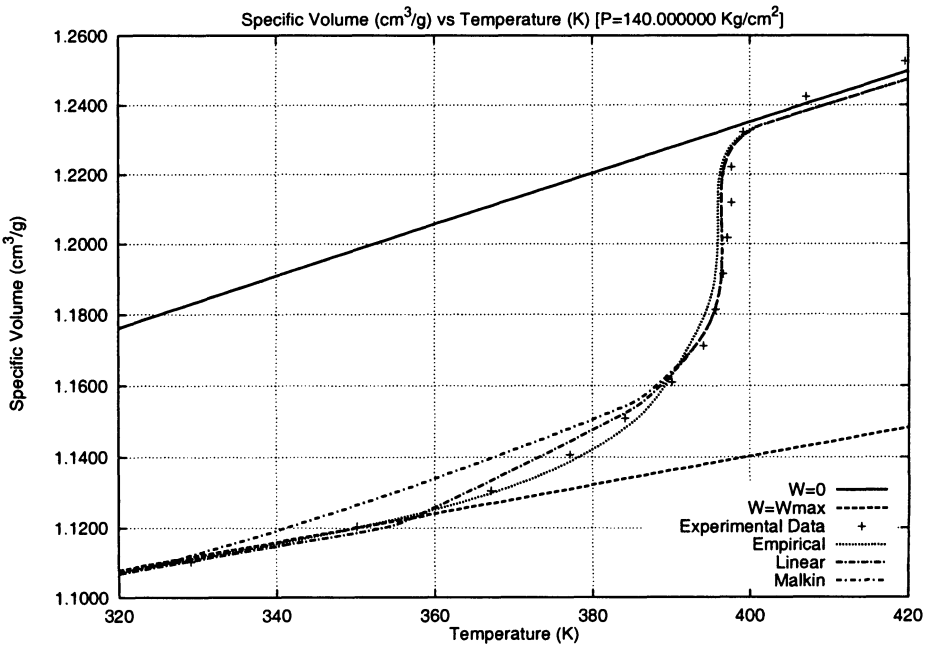

Figure 5.5 — Low pressure (140 Kg/cm^2).

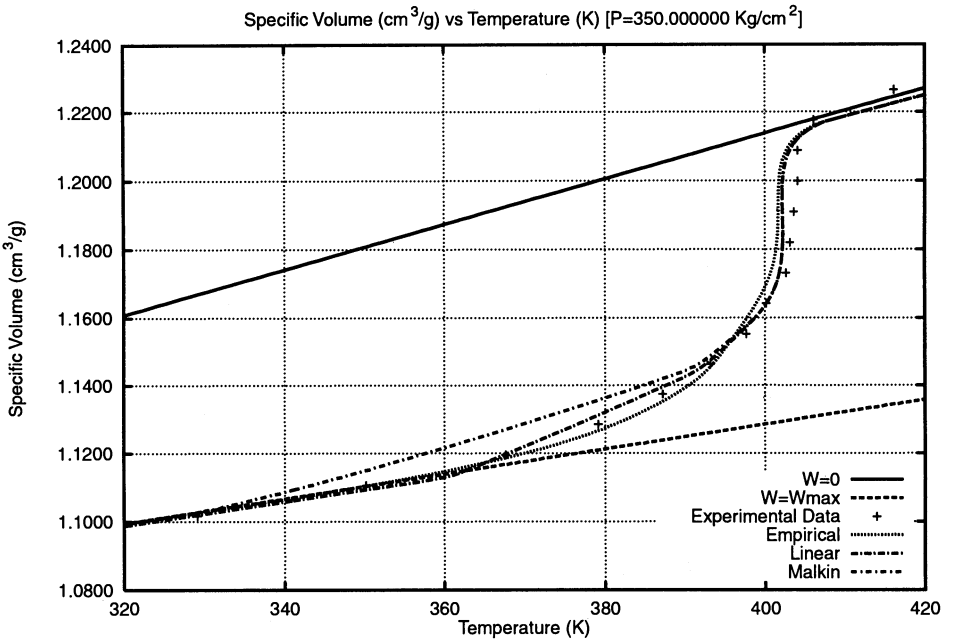

Figure 5.6 — Mean pressure (350 Kg/cm^2).

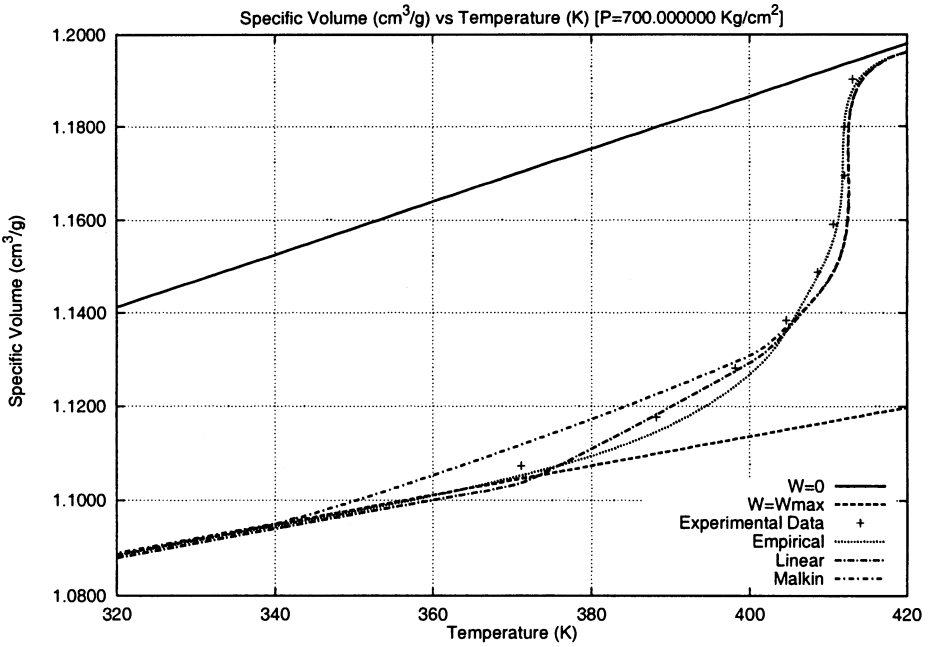

Figure 5.7 — High pressure (700 Kg/cm^2).

cooling process, governed by the ODE

$$\dot{w} = K(T(t))w^{\alpha}(w_{eq} - w)^{\beta} w_{eq}^{1-\alpha-\beta} \tag{5.9}$$

where $w = w(t)$ and we suppose to know $T(t)$ as a function of time t. We can assume a linear behavior of $T(t) = T_{\text{melt}} - \omega t$ and $w_{eq} = \text{constant} = 0.456$, where $\frac{1}{3}\ \frac{\text{K}}{\text{sec}} < \omega < \frac{1}{6}\ \frac{\text{K}}{\text{sec}}$, as in the experimental situation.

The differential equation is solved by separation of variables:

$$\int_{w_0}^{w(t)} \frac{ds}{s^{\alpha}(w_{eq} - s)^{\beta}} = \frac{w_{eq}^{1-\alpha-\beta}}{\omega} \int_{T_{\text{melt}} - \omega t}^{T_{\text{melt}}} K(\nu)\, d\nu \tag{5.10}$$

which holds until $w(t) < w_{eq}$.

With the help of this equation we want to show two facts:

1. The crystallinity w_{eq} is actually reached during experiments.

   Substituting in (5.10) the data found in [15] we get:

$$\omega \int_{w_0}^{w_{eq}} \frac{ds}{s^{\alpha}(w_{eq} - s)^{\beta}} < w_{eq}^{1-\alpha-\beta} \int_{T_{\text{glass}}}^{T_{\text{melt}}} K(\nu)\, d\nu$$

   In fact, for $T \notin [T_{\text{glass}}, T_{\text{melt}}]$ we have $K(T) = 0$. This implies that the crystal volume fraction of the material reaches w_{eq} before T reaches T_{glass}. We observed this behavior in simulations; in fact

$$\int_{w_0}^{w_{eq}} \frac{ds}{s^{\alpha}(w_{eq} - s)^{\beta}} \simeq 6.2$$

   while

$$w_{eq}^{1-\alpha-\beta} \int_{T_{\text{glass}}}^{T_{\text{melt}}} K(\nu)\, d\nu \simeq 14.7$$

   With this kind of data we can get regions with $w_{\infty} < w_{eq}$ only with cooling rates larger than 2 K/sec, i.e., about one order of magnitude larger than the cooling rates in our experiments.

2. w_{eq} is reached very fast.

   The equation

$$\int_{w_0}^{w_{eq}} \frac{ds}{s^{\alpha}(w_{eq} - s)^{\beta}} = \frac{w_{eq}^{1-\alpha-\beta}}{\omega} \int_{T_{\text{melt}} - \omega t}^{T_{\text{melt}}} K(\nu)\, d\nu$$

   is solved by $t \simeq 265$ sec with $\omega = 1/3$, $t \simeq 486$ sec for $\omega = 1/6$. In other words, the kinetic law (5.4) is active only in a temperature range close to T_{melt}. This feature is confirmed by the experiments. Of course the evolution of crystallinity after the constraint w_{eq} comes into play is correctly described only by taking into account the temperature dependence of w_{eq}.

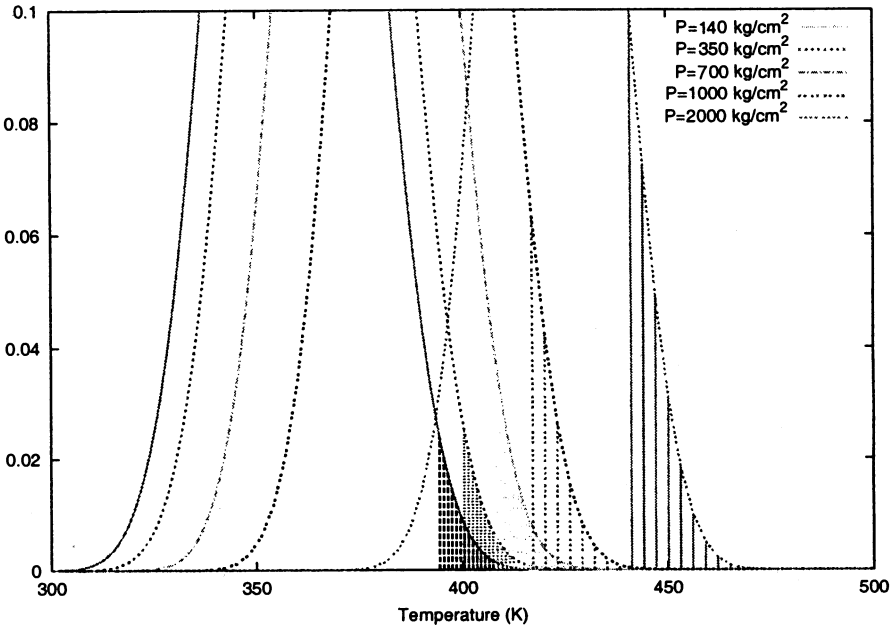

Figure 5.8 — Fraction of the crystallization temperature range where the effect of the kinetics (5.4) is operative (dashed zone).

We may conclude that it is possible to distinguish two different regions in the crystallization kinetics: first where the behavior is controlled by (5.4) and second, for lower temperatures, where the crystallinity is exactly the maximum attainable crystal volume fraction (w_{eq}).

It is interesting to note that in the first region, near T_{melt}, we observe a fast growth of w, following the equation $\dot{w} = Kw^{\alpha}(w_{eq} - w)^{\beta} w_{eq}^{1-\alpha-\beta}$. Here we remark that the choice of w_{eq} has very little influence (see Figs. 5.5 to 5.7) on the short range of temperatures in which w experiences a sharp variation. In conclusion, roughly speaking, for each fixed pressure the crystallization process is governed by (5.4) only for a relatively small temperature interval near T_{melt}. Therefore the kinetic constant $K(T, P)$ must be accurately measured only in such an interval. Figure 5.8 shows the regions in which (5.4) is active.

5.4 Formulation of the Mathematical Model

From analysis of the experimental data we obtained information concerning the kinetics and the state equation (the law relating pressure and density

of the material). Now we want to develop a suitable model for the evolution of the following quantities:

- the thermal field T,
- the crystal volume fraction w, and
- the velocity $\vec{V}$ of displacement of the material.

The first attempt at modeling was a full system including the fluid dynamics (with some approximation). Using this model we proved that some effects are negligible, and we formulated a second simpler model. For the latter model we developed a complete well-posedness theory proving the existence and uniqueness of a regular (classical) solution.

5.4.1 The Velocity Field—$\vec{V}$

We are in the presence of a velocity field produced in the material due to thermal contraction and phase change. The velocity measured in experiments is the velocity of the piston, i.e., the global contraction of the material. Of course the Reynolds number is very low because of the high value of the viscosity and the low velocity[1] ($Re \simeq 10^{-6}$). Thus it is largely justified to simplify the equation of motion neglecting the inertia terms, although we must consider that the viscosity is not constant but depends on temperature (T) and crystallinity (w). Remembering that $\operatorname{div} \vec{V} \neq 0$, we write the simplified Navier-Stokes equation for a compressible Newtonian fluid ([8],[34]):

$$\operatorname{div}\left[\eta(\nabla\vec{V} + \nabla\vec{V}^T) - \frac{2}{3}\eta I \operatorname{div}\vec{V}\right] = \nabla P \tag{5.11}$$

with the coupled continuity equation

$$\rho_t + \nabla\rho \cdot \vec{V} = -\rho \operatorname{div}\vec{V}. \tag{5.12}$$

From (5.12) we get an equation for $\operatorname{div}\vec{V}$ (neglecting the influence of pressure variation on ρ):

$$\operatorname{div}\vec{V} = -\frac{\frac{\partial\rho}{\partial T}(T,w)D_tT + \frac{\partial\rho}{\partial w}(T,w)D_tw}{\rho(T,w)} \tag{5.13}$$

with

$$D_t = \frac{\partial}{\partial t} + \vec{V}\cdot\nabla.$$

[1] The maximum velocity attained in the system is at the piston surface. In experiments, this quantity does not exceed $1 - 2$ cm/h.

The movement of the piston is obtained by imposing conservation of the total mass. If $h(t)$ is the coordinate of the piston (i.e., the height of the sample), we have

$$2\pi \int_0^{h(t)} \int_0^R r\rho(r,z,t)\,dr\,dz = m \tag{5.14}$$

and we denote by h_0 the initial value of h. Differentiating with respect to t we get

$$\dot{h}(t) \int_0^R r\rho(r,h(t),t)\,dr = -\int_0^{h(t)} \int_0^R r\left(\frac{\partial \rho}{\partial T}\frac{\partial T}{\partial t} + \frac{\partial \rho}{\partial w}\frac{\partial w}{\partial t}\right)\Big|_{(r,z,t)} dr\,dz. \tag{5.15}$$

Boundary data for the dynamical problem must be written. We denote by u, v the radial and longitudinal components of $\vec{V}$, respectively. Then we write the conditions

$$u(r,h(t),t) = 0, \quad v(r,h(t),t) = \dot{h}(t) \tag{5.16}$$

$$u(r,0,t) = 0, \quad v(r,0,t) = 0 \tag{5.17}$$

while on the lateral wall we have

$$u(R,z,t) = 0, \quad 0 < z < h \tag{5.18}$$

$$v(R,z,t) = \nu\left(\frac{z}{h(t)}\right)\dot{h}(t), \quad 0 < z < h \tag{5.19}$$

with $\nu(1) = 1$ and $\nu(\zeta)$ decreasing to zero in $\zeta_0 < \zeta < 1$ for a fixed $\zeta_0 \geq 0$.

Equation (5.19) introduces a slip at the boundary near the piston regularizing the velocity field at corner points. Of course this choice is artificial, but it greatly simplifies our analysis, and it is largely justified by the not-crucial role played by $\vec{V}$.

Remark 5.2. *It is interesting to note that if there is a part of the lateral boundary of a nonzero measure with a no-slip condition, then we cannot have a completely longitudinal flow (that is, with $u = 0$). This can be proved trying to solve (5.11) with $u = 0$.*

5.4.2 Crystallinity—w

The crystal volume fraction obeys a first-order partial differential equation.

$$w_t + \nabla w \cdot \vec{V} + w \operatorname{div} \vec{V} = W(P,T,w) \tag{5.20}$$

where W describes the crystallization kinetics (crystal diffusion is neglected). Equation (5.20) is solvable, integrating along characteristic curves, that is, along the flow lines of $\vec{V}$.

It is easy to see that $\vec{V}$ is pointing inward only on the surface of the piston $z = h(t)$, where we can obtain the value of w integrating the following

ordinary differential equation

$$w_t(r, h(t), t) = W(w, T, p_0)|_{z=h(t)}, \quad w(r, h(0), 0) = 0. \tag{5.21}$$

As already observed, (5.4) produces a crystallization field that, when we reach sufficiently low temperatures, is coincident with w_{eq}. We think that this is an important feature of the crystallization of polypropylene, and we prefer to write (5.20) stressing the presence of this constraint:

$$w_t + \nabla w \cdot \vec{V} + w \ \mathrm{div}\, \vec{V} = W(P, T, w) \quad \text{if } w < w_{eq}(T) \tag{5.22}$$

$$w = w_{eq}(T) \quad \text{otherwise.} \tag{5.23}$$

5.4.3 The Thermal Field—T

The important phenomena for a correct formulation of the thermal problem can be grouped as follows:

- The presence of the flow produces a thermal convection that we have to consider (at least in the first instance).
- The phase change process involves the release of latent heat.
- The piston and the support of the thermocouple (metallic bodies and thus a thermal conductivity much larger than the one of the polymer) are better described as "concentrated capacities," i.e., with spatially uniform temperature.

All the preceding produces:

$$\rho C(T_t + \nabla T \cdot \vec{V}) = k\Delta T + \nabla k \cdot \nabla T + \rho_c \mathcal{H} w_t \tag{5.24}$$

where ρ_c is the density of the pure crystal $\rho_c = \rho(T, P, 1)$ and $\mathcal{H}$ is the latent heat. To solve (5.24) we need two equations for the evolution of temperatures T_p and T_c of the piston and thermocouple supporting rod, respectively. If we use the symbol C_p for the thermal capacity of the piston, the evolution of $T_p(t)$ is described by

$$C_p \dot{T}_p(t) = -k_p \int_0^R T_z(r, h(t), t)\ 2\pi r\ dr \tag{5.25}$$

with a condition on the heat exchange between the polymer and the contact surface of the type:

$$-k_p T_z(r, h(t), t) = \varphi_p(T(r, h(t), t) - T_p(t)) \tag{5.26}$$

with $\varphi_p(\cdot)$ a known smooth, increasing function, with $\varphi_p(0) = 0$. A similar equation is valid for the rod (of length l) on the axis of the chamber. Let C_c be its heat capacity and $T_c(t)$ its temperature; then

$$C_c \dot{T}_c(t) = -k_c\ 2\pi r_c \int_0^l T_r(0, z, t)\, dz \tag{5.27}$$

where r_c is the radius of the rod and heat exchange through the endpoints is neglected. Similarly we have the flux condition

$$-k_c T_r(0,z,t) = \varphi_c(T(0,z,t) - T_c(t)), \quad 0 < z < l \tag{5.28}$$

where φ_c is analogous to φ_p.

5.4.4 The Complete Model

Collecting the previous equations, we have the following system:

$$w_t + \nabla w \cdot \vec{V} + w \operatorname{div} \vec{V} = W(p,T,w) \tag{5.29}$$

$$T_t + \nabla T \cdot \vec{V} = \frac{k}{\rho}\Delta T + \frac{\rho}{\rho_c}\mathcal{H} w_t \tag{5.30}$$

$$\operatorname{div} \vec{V} = -\frac{\frac{\partial \rho}{\partial T}(T,w) D_t T + \frac{\partial \rho}{\partial w}(T,w) D_t w}{\rho(T,w)} \tag{5.31}$$

$$\operatorname{div}\left[\eta(\nabla \vec{V} + \nabla \vec{V}^T) - \frac{2}{3}\eta I \operatorname{div} \vec{V}\right] = \nabla P \tag{5.32}$$

for $t > 0$ in $[0,R] \times [0,h(t)]$ and for $w < w_{eq}$. In addition we have the following ordinary differential equations on the boundary

$$\dot{h}(t) \int_0^1 r\rho(r,h(t),t)\, dr$$

$$= -\int_0^{h(t)} \int_0^R r\left(\frac{\partial \rho}{\partial T}\frac{\partial T}{\partial t} + \frac{\partial \rho}{\partial w}\frac{\partial w}{\partial t}\right)\Big|_{(r,z,t)} dr\, dz \tag{5.33}$$

$$C_c \dot{T}_c(t) = -k_c\, 2\pi r_c \int_0^l T_r(0,z,t)\, dz \tag{5.34}$$

$$C_p \dot{T}_p(t) = -k_p \int_0^R T_z(r,h(t),t)\, 2\pi r\, dr. \tag{5.35}$$

In Figure 5.9 all boundary and initial conditions are shown.

The first approach to the study of this model was numerical. Simulations, as described in the next section, provided sufficient clues for some significant simplifications:

1. The influence of convective terms in equations (5.30) and (5.29) is negligible because the velocity field is quite modest and mainly longitudinal while the crystallization and thermal gradients are predominantly radial (see Figs. 5.10 to 5.14). On the contrary, we remark that $-\operatorname{div} \vec{V}$ (the relative volume contraction rate) has some influence in (5.29) during some stage of the process. However, in our approximation, $\operatorname{div} \vec{V}$ is predicted by (5.31) with no need of solving the fluid dynamic problem.

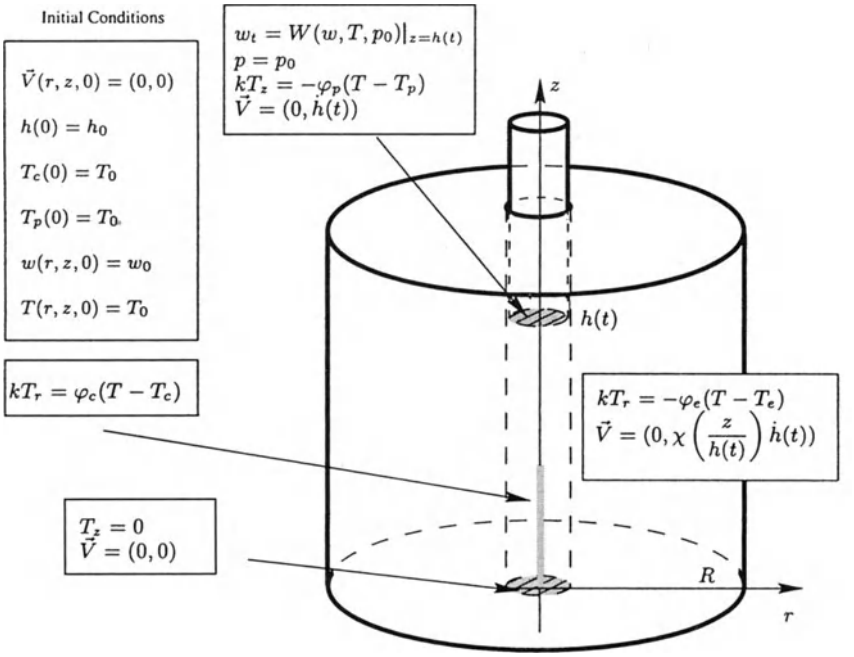

Figure 5.9 — Initial and boundary conditions.

2. According to the previous assumption, Lagrangian derivatives D_t are identified with their Eulerian counterpart $\frac{\partial}{\partial t}$.
3. Pressure gradients are so small that we can safely neglect this variation assuming a constant pressure (equal to the imposed pressure on the piston surface) throughout the sample.

5.4.5 The Reduced Model

After the simplifications discussed, the system of partial differential equations we are going to consider is the following:

$$\rho C T_t = k\Delta T + \rho_c \mathcal{H} w_t \tag{5.36}$$

$$w_t + w \operatorname{div} \vec{V} = W(P,T,w), \quad w < w_{eq}(T) \tag{5.37}$$

$$\operatorname{div} \vec{V} = -\frac{1}{\rho(T,w)}\left[\frac{\partial \rho}{\partial T}T_t + \frac{\partial \rho}{\partial w}w_t\right] = -\frac{\partial}{\partial t}\left(ln\frac{\rho}{\rho_0}\right) \tag{5.38}$$

with ρ_0 a reference density (e.g., $\rho_0 = \rho(P, T_m, 0)$).

Remark 5.3. *Since we are considering isobaric cooling processes, from now on we will drop the symbol P in all formulas.*

(continued on page 172)

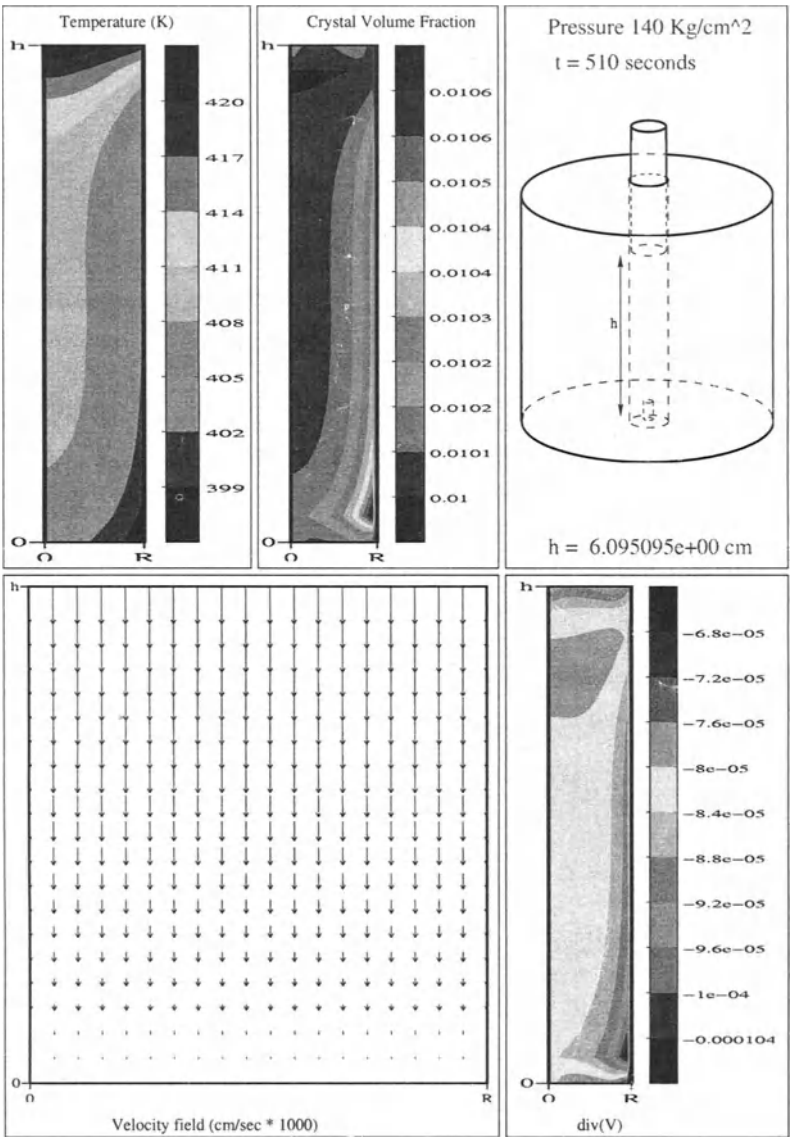

Figure 5.10 — 510 sec.

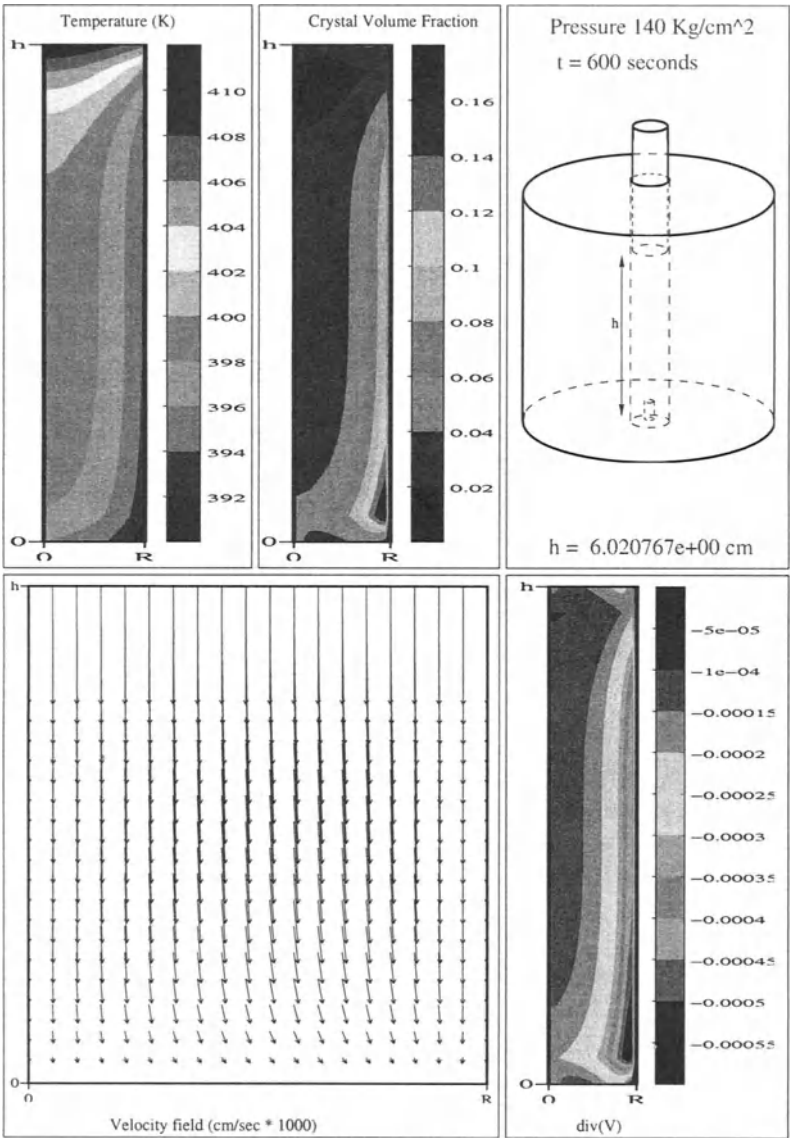

Figure 5.11 — 600 sec.

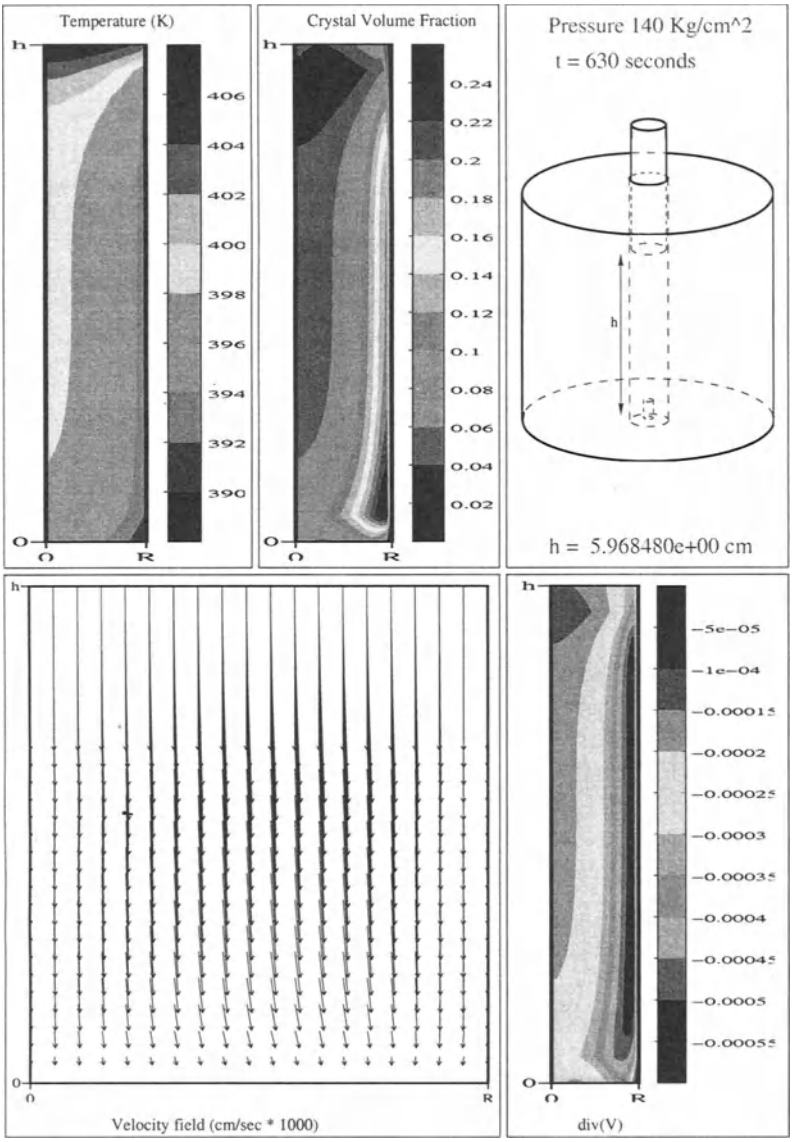

Figure 5.12 — 630 sec.

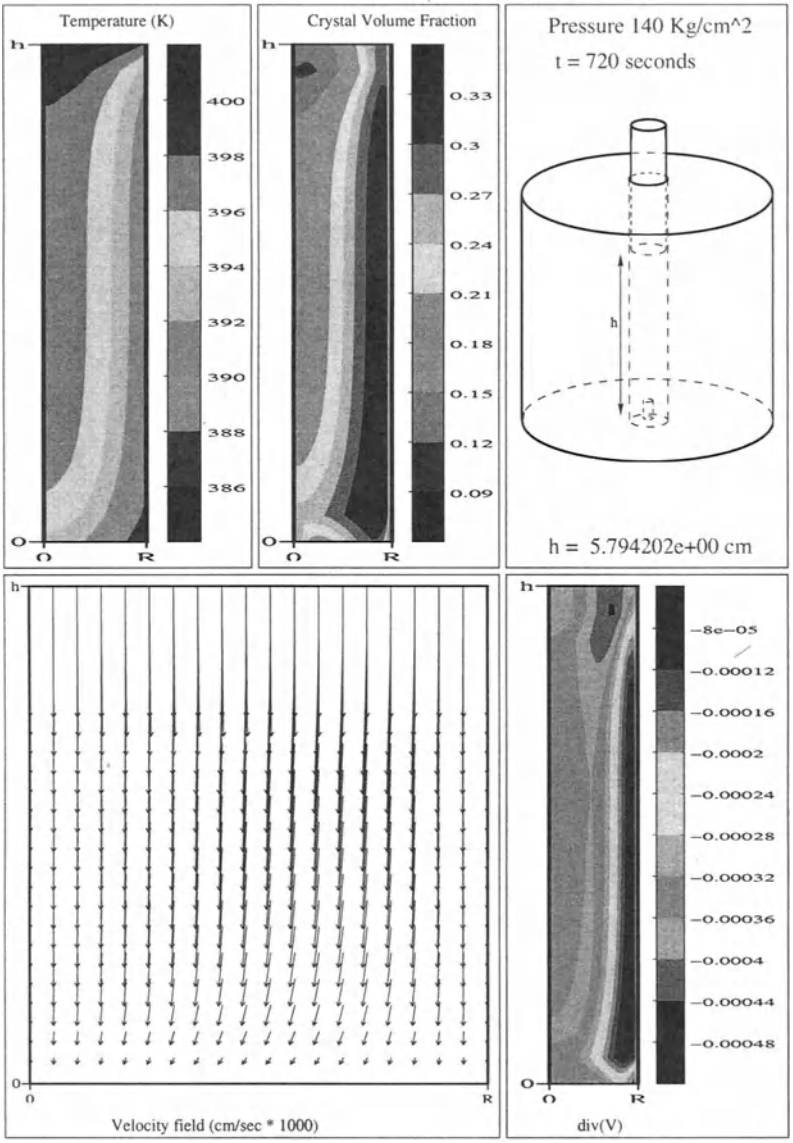

Figure 5.13 — 720 sec.

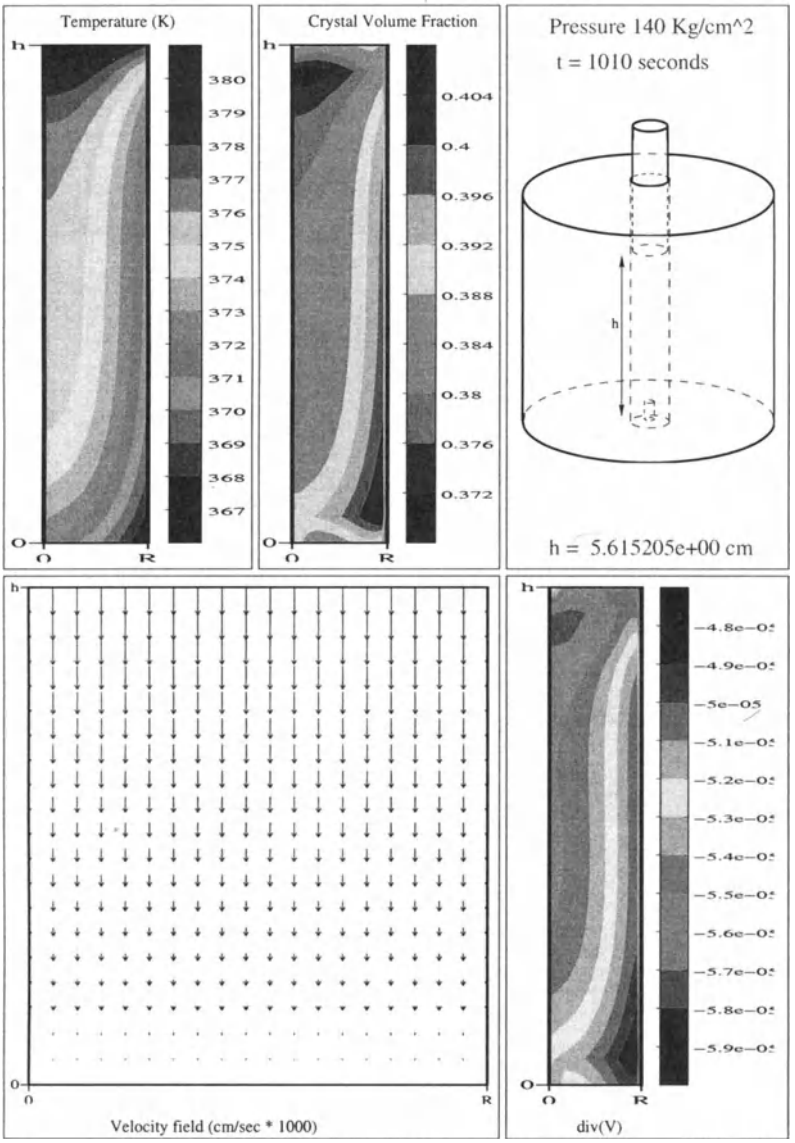

Figure 5.14 — 1010 sec.

Equations (5.36) to (5.38) must be solved in the moving domain

$$R_\theta = \{(r,z,t) \in \mathbb{R}^3 \mid (r,z,t) \in \Omega_t,\ 0 < t < \theta\}$$

with Ω_t the cylinder defined by the conditions

$$(r,z) \in \Omega_t \text{ iff} \begin{cases} r_c < r < R \quad \text{and} \quad 0 < z < l \\ 0 < r < R \quad \text{and} \quad l < z < h(t) \end{cases}$$

where R, l, and r_c known quantities (R radius of the cylindrical sample, l, r_c height, and radius of the thermocouple support) and $h(t)$ is unknown.

5.4.6 Boundary and Initial Conditions for the Reduced Model

As we said, the initial conditions are

$$T(r,z,0) = T_0 > T_m \text{ everywhere in } \Omega_0. \tag{5.39}$$

At the bottom surface Γ_b (where the presence of the thermocouple can be disregarded) we take

$$T_z(r,0,t) = 0, \qquad \text{on } \Gamma_b, 0 < t < \theta. \tag{5.40}$$

On the lateral surface Γ_e we have

$$-kT_r(R,z,t) = \phi_e(T - T_e), \quad 0 < z < h(t), \quad 0 < t < \theta \tag{5.41}$$

where $T_e < T_g$ is the outside temperature and ϕ_e is a positive constant.

On the piston surface Γ_p we write

$$-kT_z(r,h(t),t) = \phi_p(T - T_p(t)), \quad 0 < r < R, \quad 0 < t < \theta \tag{5.42}$$

where $T_p(t)$ is the still unknown temperature of the piston and $\phi_p > 0$ is constant.

A similar condition holds on the boundary Γ_c of the thermocouple support (radius $r_c << R$, length $l \simeq h_0/3$).

Because the heat exchange through the tip of the thermocouple is negligibly small in comparison with the whole heat flow through the support, we may smooth the support boundary Γ_{0c} to Γ_{0c}^ε in some arbitrary way. So we write the following boundary condition

$$-k\nabla T \cdot \vec{n} = \phi_{0c}^\varepsilon(z)(T - T_c(t)) \quad \text{on } \Gamma_{0c}^\varepsilon \tag{5.43}$$

$\vec{n}$ being the outside normal to the boundary Γ_{0c}^ε,

$$\Gamma_{0c}^\varepsilon = \begin{cases} (r_c, z), & 0 < z < l - \varepsilon \\ (\mu(z), z), & l - \varepsilon \le z \le l + \varepsilon \\ (0, z), & l + \varepsilon < z < h(t) \end{cases}$$

and

$$\phi_{0c}^{\varepsilon}(z) = \begin{cases} \phi_c, & 0 < z < l - \varepsilon \\ \phi_0, & l - \varepsilon \le z \le l + \varepsilon \\ 0, & l + \varepsilon < z < h(t) \end{cases}$$

for some smooth monotone functions $\mu(z)(\mu(l-\varepsilon) = r_c,\ \mu(l+\varepsilon) = 0)$, and $\phi_0(z)$ $(\phi_0(l-\varepsilon) = \phi_c,\ \phi_0(l+\varepsilon) = 0)$.

The evolution of temperatures T_p, T_c is determined by the balance equations

$$C_p \dot{T}_p(t) = -k \int_0^R 2\pi r T_z(r, h(t), t)\, dr, \quad 0 < t < \theta \tag{5.44}$$

$$C_c \dot{T}_c(t) = k 2\pi r_c \int_0^l T_r(r_c, z, t)\, dz, \quad 0 < t < \theta \tag{5.45}$$

with the initial conditions $T_p(0) = T_c(0) = T_0$; C_p, C_c are the respective heat capacities.

Note that in (5.45) we have neglected the heat exchange through the endpoint of the thermocouple.

Inserting (5.42) in (5.44) we obtain a linear ordinary differential equation for T_p that gives:

$$T_p(t; T, h) = e^{-\lambda_p t} \left[T_0 + \frac{2\lambda_p}{R^2} \int_0^t \left(e^{\lambda_p s} \int_0^R r T(r, h(s), s)\, dr \right) ds \right] \tag{5.46}$$

with $\lambda_p = \frac{2\pi\phi_p R^2}{C_p}$.

Likewise we get

$$T_c(t; T) = e^{-\lambda_c t} \left[T_0 + \frac{\lambda_c}{l} \int_0^t \left(e^{\lambda_c s} \int_0^l T(r_c, z, s)\, dz \right) ds \right] \tag{5.47}$$

with$\lambda_c = \frac{2\pi r_c \phi_c l}{C_c}$.

Equations (5.46) and (5.47) must be put back into (5.42) and (5.43).

Remark 5.4. *In the thermal problem we have taken, k and C constant for the sake of simplicity, but it would not be too difficult to let them depend on T and w. Another possible generalization is to replace (5.41) to (5.43) with nonlinear radiation laws.*

Introducing the functions Φ and T_{ext} defined on the boundary of D_θ as:

$$\Phi(r, z, t) = \begin{cases} \phi_{0c}^{\varepsilon} & \text{on } \Gamma_{0c}^{\varepsilon} \\ 0 & \text{on } \Gamma_b \\ \phi_e & \text{on } \Gamma_e \\ \phi_p & \text{on } \Gamma_p \end{cases} \tag{5.48}$$

$$T_{\text{ext}}(r,z,t;T_c,T_p) = \begin{cases} T_c & \text{on } \Gamma_c \cup \Gamma_0 \\ 0 & \text{on } \Gamma_b \\ T_e & \text{on } \Gamma_e \\ T_p & \text{on } \Gamma_p \end{cases} \tag{5.49}$$

we can write the boundary condition for the thermal field in the following compact form

$$-k\nabla T \cdot \vec{n} = \Phi(T - T_{\text{ext}}) \quad \text{on } \Gamma. \tag{5.50}$$

Remark 5.5. *The elimination of the term $\nabla w \cdot \vec{V}$ in the equation for w reduces it to an ordinary differential equation, although quite nontrivial due to the presence of $\operatorname{div} \vec{V}$. We shall see how to deal with (5.37). The only data we need to know are for $t = 0$:*

$$w(r,z,0) = 0, \quad \text{in } D_0. \tag{5.51}$$

Remark 5.6. *The regularization procedure is in the spirit of the general framework of the model, which incorporates several approximations. However, it may not look elegant from a mathematical point of view. It is not essential, and it could be removed replacing the Hölder norms used in the existence proof (Section 5.6.3) by the weighted norms and the corresponding estimates to be found in [36]. Such a remark has been suggested by V.A. Solonnikov.*

5.5 Numerical Simulations

We will briefly describe the numerical integration procedure used in our simulations referring to [28] for a complete justification and evaluation of this approach.

Actually we approximate the solution of "the complete model" (see Section 5.4.4) by means of a sort of time splitting procedure advancing each variable separately.

More precisely, let us use the symbols

$$T_n(r,z),\ w_n(r,z),\ \vec{V}_n(r,z),\ p_n(r,z),\ h_n,\ \dot{h}_n, (T_p)_n, (T_c)_n$$

for the known quantities for $t = t_n$ and dt_{n+1} for a chosen time step such that

$$|dt_{n+1}\dot{h}| < h\,\text{Toll}$$

(for a given tolerance $h\,\text{Toll}$). The integration is based on the assumption that for $t \in [t_n, t_{n+1}], t_{n+1} = t_n + dt_{n+1}$ we can write

$$h(t) = h_n + \dot{h}_n(t - t_n) \tag{5.52}$$

and

$$\vec{V}(r,z,t) \equiv \vec{V}(r,z,t_n), \quad p(r,z,t) \equiv p(r,z,t_n) \tag{5.53}$$

We can thus compute scalar fields $T_{n+1}^{(0)}$, $w_{n+1}^{(0)}$ integrating (5.29) and (5.30) for $t \in [t_n, t_{n+1}]$ by means of a transformation of the free domain in a cylindrical one. Substituting $T_{n+1}^{(0)}, w_{n+1}^{(0)}$ in (5.33) we get $\dot{h}_{n+1}^{(0)}$. Finally, with the help of (5.34) and (5.35), we can get $(T_p)_{n+1}$ and $(T_c)_{n+1}$.

Remark 5.7. *Knowing $\dot{h}_{n+1}^{(0)}$ we try to verify if the hypothesis on (5.52) is too stringent, causing $|dt_{n+1}\dot{h}| > h$ Toll, approximating, for example, $\dot{h}(t)$ linearly. In this case we divide the step size and restart the process.*

Using $T_{n+1}^{(0)}$, $w_{n+1}^{(0)}$ in (5.13) we compute $\operatorname{div} \vec{V}_{n+1}^{(0)}$. Then with (5.32) and the already known value of $\dot{h}_{n+1}$ we integrate equations for the velocity field obtaining $\vec{V}_{n+1}^{(0)}$.

A projection-like process allows us to refine the velocity field.

Remark 5.8. *Knowing $\vec{V}_{n+1}^{(0)}$, $p_{n+1}^{(0)}$ is possible to estimate the error caused by (5.53): We can impose $\|\vec{V}_{n+1}^{(0)} - \vec{V}_n\| < v$ Toll for a fixed tolerance v Toll, otherwise reducing the step size.*

Now we can iterate our process obtaining $T_n^{(i)}(r,z)$, $w_n^{(i)}(r,z)$, $\vec{V}_n^{(i)}(r,z)$, $p_n^{(i)}(r,z)$, $h_n^{(i)}$, and $\dot{h}_n^{(i)}$, for $i = 0, \ldots, \nu$ until some chosen convergence criterion is satisfied. Finally we obtain the desired quantities at $t = t_{n+1}$ as:

$$T_{n+1}(r,z) := T_n^{(\nu)}(r,z), \quad w_{n+1}(r,z) := w_n^{(\nu)}(r,z), \quad \vec{V}_{n+1}(r,z) := \vec{V}_n^{(\nu)}(r,z),$$
$$p_{n+1}(r,z) := p_n^{(\nu)}(r,z), \quad h_{n+1} := h_n^{(\nu)}, \quad \dot{h}_{n+1} := \dot{h}_n^{(\nu)}$$

Remark 5.9. *In our experiments we obtained every time $p \simeq$ constant, and we actually removed completely the variable p assuming $p \equiv p_0$.*

Remark 5.10. *The proposed scheme requires for $t = 0$ the values of $\vec{V}_0 = \vec{V}(r,z,0)$, $P_0 = p(r,z,0)$, and $\dot{h}_0 = \dot{h}(0)$, which is not in agreement with the kind of equations under consideration but is just a requirement of the numerical approach. We can prove that with the hypothesis $T(r,z,0) \geq T_{\text{melt}}$ (that implies $W(P_0, T_0, w_0) = 0$ [12]) and $\Delta T = 0$ (an equilibrium temperature distribution), the choice $\vec{V}_0 = (0,0)$, $\dot{h}_0 = 0$ is the right one.*

5.5.1 Input Data

In Tables 5.2, 5.3 and 5.4 numerical values of the parameters used in simulations are listed. Simulations are performed for 3600 seconds with an initial time step chosen between 0.5 and 3 seconds, depending on the spatial discretization and the problem. We considered many different partitions of the (r,z) domain (in any case we observed that partitions with step size

Table 5.2. Rheological parameters

		Value	Unit
Viscosity	η	$1.0E3$	Pa/sec
Thermal diffusivity	k	$1.6E-3$	W/(cm°K)
Thermal capacity	C	$2.093E3$	J/(°K * Kg)
Latent heat	$\mathcal{H}$	$1.0E5$	J/Kg

Table 5.3. Parameters of S.G.M.

	Value	Unit
ω	1.0245	cm^3/g
π	1730.0	Atm
T_0	114.0	°K
R^*	1.393	$cm^3 * Atm/g * °K$

Table 5.4. Crystallization kinetics

	Value	Unit
α	(2.0/3.0)	—
β	(0.765)	—
u/R	(6280.0/8.314)	K
Kg	4.87E5	K^2
K_0	(1.6E9)	

$dx \simeq 0.01$ cm are largely sufficient for our purposes. It is important to note that spatial refinements have little influence on the obtained PVT diagrams. This allows us to use a relatively fine spatial discretization when we were interested in spatial distributions of quantities.

5.5.2 Some Results

Numerical simulations can produce more information (i.e., spatial distributions of temperature, crystallinity, and velocity field in the sample) that is impossible to measure directly.

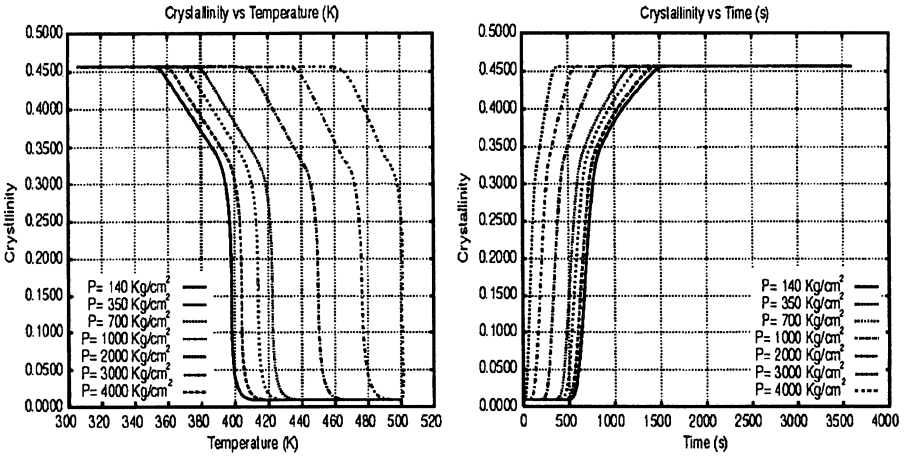

Figure 5.15 — Average crystallinity as a function of temperature (left) and as a function of time.

Remark 5.11. *Knowing the velocity field in the sample could be useful to better understand the effects of dynamical stresses on nucleation and crystal growth.*

As already said, the agreement with experimental data is quite satisfactory (see Figures 5.5, 5.6, and 5.7). In Figures 5.10, 5.11, 5.12, 5.13, and 5.14 we show the output obtained for a pressure of 140 Kg/cm^2 in different instants.

In Figure 5.15 the average crystallinity for high pressures (up to 4000 Kg/cm^2) is shown. In all tests the initial temperature was $T = 500$ K and the final was $T = 300$ K.

In the same range of temperatures/pressures, the PVT diagrams are shown in Figure 5.16.

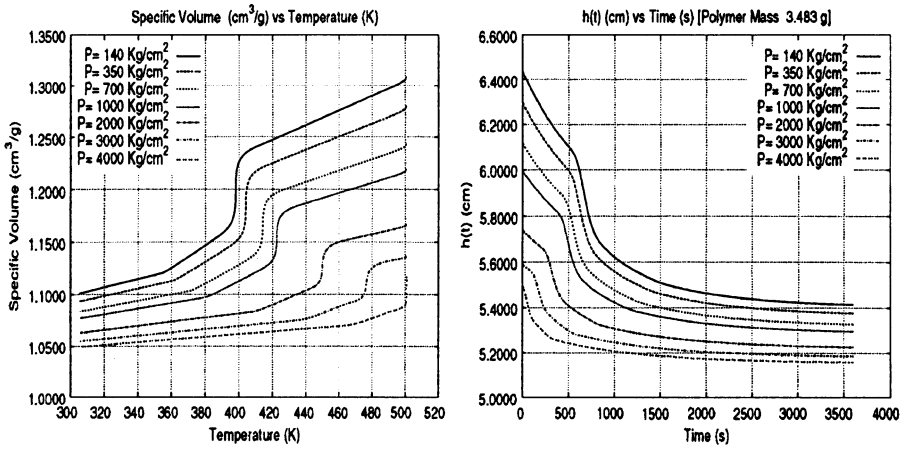

Figure 5.16 — PVT (left) and kinetics of piston displacement.

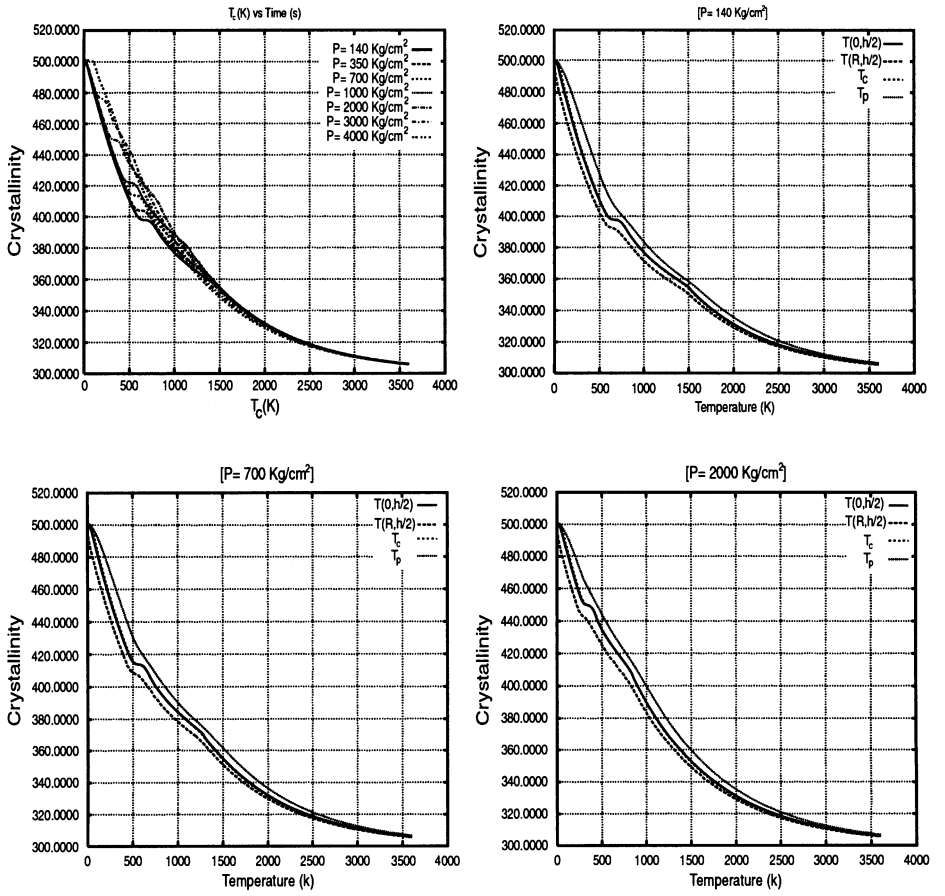

Figure 5.17 — Temperatures for different pressures.

Finally, in Figure 5.17 we show the temperatures of the piston and the thermocouple support for different pressures. Note the shift of the crystallization interval to higher temperatures as pressure increases, emphasized by the corresponding shift of the temperature plateau.

5.6 Well-Posedness of the Mathematical Model

5.6.1 Statement of the Problem

Problem. (P) Find a triple (T, w, h) satisfying equations (5.36), (5.39), (5.43), (5.46), and (5.33) in some time interval $(0, \theta)$ in the classical sense. By solution to (5.37) we mean a *maximal solution.*

A condition on $\rho(T,w)$ that plays an important role is that for some $\mathcal{K}<1$

$$\frac{\rho_w}{\rho}w \leq \mathcal{K} < 1, \quad \forall w \in [0,1], \ T \in [T_e, T_0] \tag{5.54}$$

which is indeed satisfied in our case.

We will show that problem P has one unique solution in a suitable time interval $(0,\theta)$ in the Hölder space $H^{2+a,1+a/2}$ (see Theorem 5.1). Next we will extend the solution for all times.

Remark 5.12. *The existence theorem refers to the modified model illustrated in Section 5.3, which differs from the one just stated only by some convective terms whose contribution, consistently with the approximations adopted so far, is immaterial (see Remark 5.14).*

5.6.2 Reformulation of the Problem and Some a Priori Results

First, we eliminate w_t from (5.36). This step is necessary to find the condition guaranteeing the parabolicity of (5.36), because w_t is linked to T_t through (5.37), and (5.38).

Let us first suppose $w < w_{eq}$. Let us rewrite (5.36) to (5.38) in the form

$$\begin{pmatrix} \rho C & -\rho_c \mathcal{H} & 0 \\ 0 & 1 & w \\ \rho_T & \rho_w & \rho \end{pmatrix} \begin{pmatrix} T_t \\ w_t \\ \operatorname{div} \vec{V} \end{pmatrix} = \begin{pmatrix} k\Delta T \\ W(T,w) \\ 0 \end{pmatrix}$$

from which we deduce

$$T_t = A_0(T,w)\Delta T + A_1(T,w)W(T,w) \tag{5.55}$$

with

$$A_0(T,w) = \frac{(1-w\hat{\rho}_w)}{\mathcal{Z}}k, \quad A_1(T,w) = \frac{\rho_c \mathcal{H}}{\mathcal{Z}} \tag{5.56}$$

$$\mathcal{Z} = \rho C \left[1 - w\hat{\rho}_w - \frac{\hat{\rho}_c \hat{\rho}_T \mathcal{H}}{C} w\right] \tag{5.57}$$

$$\hat{\rho}_w = \frac{\rho_w}{\rho}, \quad \hat{\rho}_T = \frac{\rho_T}{\rho}. \tag{5.58}$$

Therefore parabolicity is guaranteed by (5.54). When $w = w_{eq}(T)$, the source term in (5.36) becomes $\rho_c \mathcal{H} w_{eq} T_t$ and the equation remains parabolic because $w_{eq} \leq 0$. Thus we can state the following.

Proposition 5.1. *Equation (5.55) is uniformly parabolic if (5.54) holds.*

From now on, we replace (5.36) with (5.55) as long as $w < w_{eq}$. Now we transform (5.37), eliminating $\operatorname{div} \vec{V}$ and writing it in the form

$$\frac{\partial}{\partial t} ln \frac{w}{\rho/\rho_0} = Bw^{a-1}(w_{eq} - w)^b \tag{5.59}$$

from which we deduce the following integral equation for w

$$w = \rho(T, w) \left\{ (1-a) \int_0^t \rho^{a-1}(T, w) B(T) (w_{eq} - w)^b \, dt \right\}^{\frac{1}{1-a}}. \tag{5.60}$$

An a priori result can be obtained as a consequence of the maximum principle for the thermal problem.

Proposition 5.2. *During the whole process we have* $T_e \leq T \leq T_0$.

We conclude this section by introducing some minor changes in the model. First, we remark that it is convenient to deal with a domain that does not depend on time. For this reason, given a smooth function $\psi(\zeta, h(t)) \geq 0$ such that $\psi \equiv 0$ for $\zeta \leq 0$ and $\psi(h(t) - \frac{h_0}{2}, h(t)) = 1$, we introduce the change of variable

$$y = z + (h_0 - h(t))\psi(z - \frac{h_0}{2}, h(t)) \tag{5.61}$$

which leaves the domain unchanged for $z \leq \frac{h_0}{2}$ and maps the remaining part onto the cylinder $0 < r < R$, $\frac{h_0}{2} < y < h_0$, $0 < t < \theta$. In this way the new boundary is fixed in time. We will denote the new domain by D_θ.

Therefore defining the unknowns

$$\tilde{T}(r, y, t) = T(r, z, t), \quad \tilde{w}(r, y, t) = w(r, z, t)$$

equation (5.55) becomes ($\tilde{T} \simeq T_t$, see Remark 5.13)

$$\tilde{T}_t = A_0(\tilde{T}, \tilde{w}) \left[\Delta_h \tilde{T} + \tilde{T}_y (h_0 - h) \psi_{\zeta\zeta} \right] + A_1(\tilde{T}, \tilde{w}) W(\tilde{T}, \tilde{w}) \tag{5.62}$$

where

$$\Delta_h = \frac{1}{r} \frac{\partial}{\partial r} \left(r \frac{\partial}{\partial r} \right) + \psi_\zeta^2. \tag{5.63}$$

Remark 5.13. *When applying transformation (5.61), we neglect the terms in* $\dot{h}$ *appearing in the differential equation, consistently with the approximation of suppressing convection.*

In the same spirit we keep the form (5.37), i.e., (5.59) for the equation to be satisfied by $\tilde{w}$ implying (by means of (5.60))

$$\tilde{w} = \rho(\tilde{T}, \tilde{w}) \left\{ (1-a) \int_0^t \rho^{a-1}(\tilde{T}, \tilde{w}) B(\tilde{T}) (w_{eq} - \tilde{w})^b \, dt \right\}^{\frac{1}{1-a}} \tag{5.64}$$

The equation for the free boundary becomes

$$2\pi \int_0^{h_0} \int_0^R r\rho(\tilde{T}, \tilde{w})(1 + (h_0 - h)\psi_\zeta) \, dr \, dy = m \tag{5.65}$$

and the boundary condition for $\tilde{T}$ has the form

$$\begin{aligned} -k\nabla_h \tilde{T} \cdot \vec{n} = \tilde{\Phi}(r, y, t)\big(\tilde{T} - \tilde{T}_{\text{ext}}(r, y, t; \tilde{T}_c, \tilde{T}_p)\big) \text{ on} \\ \Gamma = \partial D_\theta \backslash \big\{(r, z, t) |\ t = 0,\ t = \theta\big\} \end{aligned} \tag{5.66}$$

with obvious definitions of the functions $\tilde{\Phi}$, $\tilde{T}_{\text{ext}}$, $\tilde{T}_c$, and $\tilde{T}_p$.

Remark 5.14. *Equations (5.62) and (5.64) do in fact replace equation (5.36), i.e., (5.55), and (5.37), i.e. (5.60).*

Remark 5.15. *A final change introduced in the model is that the domain $D_\theta \cap \{t = \text{const.}\}$ is approximated in a standard way by a set with a smooth boundary, say D_θ^ε. This implies that we have to define a new couple of functions Φ^ε, $T_{\text{ext}}^\varepsilon$ defined on the new smooth boundary and approximating smoothly Φ^ε and $T_{\text{ext}}^\varepsilon$.*

5.6.3 Local Existence and Uniqueness Theorem

Theorem 5.1. *Under the regularity assumptions specified for $\rho(T, w)$ for a suitably small θ there exists a unique solution $(\tilde{T}, \tilde{w}, h)$ of (5.62), (5.64), and (5.65) with the boundary condition (5.66) and the initial condition*

$$\tilde{T}(r, y, 0) = T_0 \tag{5.67}$$

Under these conditions the function $\tilde{T}$ belongs to the Hölder space $\mathcal{H}^{2+\alpha, 1+\frac{\alpha}{2}}$.

Remark 5.16. *In (5.66) the functions T_c and T_p are defined by means of (5.46) and (5.47).*

Remark 5.17. *The proof of the theorem is performed assuming a smooth domain with smooth boundary conditions in the sense of Remark 5.15. Here we keep the simpler notation D_θ (instead of D_θ^ε) but we mean that ∂D_θ is smooth.*

Proof of Theorem 5.1. The proof of Theorem 5.1 is based on a fixed-point argument.

Let us first define the set

$$\mathcal{B} = \Big\{(\tau,\omega,\chi) \mid \|\tau\|_{\mathcal{H}^{\alpha,\frac{\alpha}{2}}} \le M_1, \|\tau\|_{\mathcal{H}^{1+\alpha,\frac{1}{2}+\frac{\alpha}{2}}} \le M_2, \|\tau\|_{\mathcal{H}^{2+\alpha,1+\frac{\alpha}{2}}} \le M_3,$$

$$\tau(r,y,0) = T_0, \tau_t(r,y,0) = 0, \frac{1}{2}T_e \le \tau \le 2T_0$$

$$\sup_{D_\theta} |\nabla\omega| \le N_1, \sup_{D_\theta} |\omega_t| \le N_2, \omega(r,y,0) = 0,$$

$$\omega(r,y,t) \le w_{eq}(T) - \delta, \|\chi\|_{\mathcal{H}^{\frac{1}{2}+\frac{\alpha}{2}}}(0,\theta) \le Q,$$

$$\chi(0) = h_0 = \frac{m}{\pi R^2 \rho(T_0,0)}, l < \frac{h_0}{2} < h_{min} = \frac{m}{\pi R^2 \rho_{max}} \le \chi \le h_0\Big\} \tag{5.68}$$

where the constants M_i have to be chosen and δ is given less than the inf of $w_{eq}(\tau)$ in the range of τ.

Now we define the functions

$$\tau_p(t) = e^{-\lambda_p t}\left[T_0 + \frac{2\lambda_p}{R^2}\int_0^t \left(e^{\lambda_p s}\int_0^R r\tau(r,h_0,s)\,dr\right)ds\right] \tag{5.69}$$

$$\tau_c(t;h) = e^{-\lambda_c t}\left[T_0 + \frac{\lambda_c}{l}\int_0^t \left(e^{\lambda_c s}\int_0^{l/h} \tau(r_c,z,s)\,dz\right)ds\right] \tag{5.70}$$

and for a given $(\tau,\omega,\chi) \in \mathcal{B}$ we state the problem

$$\hat{\tau}_t = A_0(\tau,\omega)\left[\Delta_h\hat{\tau} + \tau_y(h_0-h)\psi_{\zeta\zeta}\right] + A_1(\tau,\omega)W(\tau,\omega) \tag{5.71}$$

$$-k\nabla_h\hat{\tau}\cdot\vec{n} = \tilde{\Phi}(r,y,t)\big(\tau - \tilde{T}_{ext}(r,y,t;\tau_c,\tau_p)\big) \text{ on } \Gamma. \tag{5.72}$$

Existence and uniqueness of a solution in $\mathcal{H}^{2+\alpha,\frac{2+\alpha}{2}}$ of problem (5.71) to (5.72) is now assured by Theorem 5.3 pag. 320 [26].

For such a problem it is possible to obtain a chain of inequalities that define the constants M_1, M_2, M_2 and the time interval $(0,\theta)$ so that the function $\hat{\tau}(r,z,t)$ satisfies the same requirements on τ specified in the definition of the set $\mathcal{B}$. The proof is technical and we refer to [18] for the details.

Now we define the second element of the triple $(\hat{\tau},\hat{\omega},\hat{\chi})$:

$$\hat{\omega} = \rho(\tau,\omega)\left\{(1-a)\int_0^t \rho^{a-1}(\tau,\omega)B(\tau)(w_{eq}-\omega)^b\,dt\right\}^{\frac{1}{1-a}} \tag{5.72}$$

and we compute

$$\hat{\omega}_t = (\rho_T\tau_t + \rho_w\omega_t)\frac{\hat{\omega}}{\rho} + \hat{\omega}^{\frac{a}{1-a}}\rho^{a-1}B(w_{eq}-\omega)^b \tag{5.73}$$

from which we get

$$|\hat{\omega}_t| \leq C_1(M_3 + N_2)t^{\frac{1}{1-a}} + C_2 t^{\frac{a}{1-a}} \tag{5.74}$$

where C_i denote uniform constants.

Likewise we get

$$|\nabla_h \hat{\omega}| \leq C_4(M_1 + N_1)\theta^{\frac{a}{1-a}}. \tag{5.75}$$

Putting together these estimates we realize that we can select the constants N_i and θ so that $\hat{\omega}$ satisfies the same inequalities as ω, including the constraint $\hat{\omega} \leq w_{eq}(\hat{\tau}) - \varepsilon$. Next we complete the mapping $(\tau, \omega, \chi) \to (\hat{\tau}, \hat{\omega}, \hat{\chi})$ by means of

$$2\pi \int_0^{h_0} \int_0^R r\rho(\hat{\tau}, \hat{\omega})(1 + (h_0 - h)\psi_\zeta)\, dr\, dy = m \tag{5.76}$$

from which we realize that $\|\hat{\chi}\|_{\mathcal{H}^{\frac{1}{2}+\frac{a}{2}}}$ is estimated in terms of the Hölder coefficients of $\hat{\tau}(\cdot, t)$, $\hat{\omega}(\cdot, t)$, which as we have seen can be made as small as desired by reducing θ. Therefore we obtain the last estimate

$$\|\hat{\chi}\|_{\mathcal{H}^{\frac{1}{2}+\frac{a}{2}}} \leq Q \tag{5.77}$$

with arbitrary Q.

The last step of the proof consists in showing that the mapping $(\tau, \omega, \chi) \to (\hat{\tau}, \hat{\omega}, \hat{\chi})$ is contractive with respect to the sup-norm of the three elements. Denoting such a norm by $\|(\tau, \omega, \chi)\|_{\mathcal{B}}$ we have to show that for any pair $(\tau_1, \omega_1, \chi_1), (\tau_2, \omega_2, \chi_2) \in \mathcal{B}$, we have

$$\|(\hat{\tau}_1 - \hat{\tau}_2, \hat{\omega}_1 - \hat{\omega}_2, \hat{\chi}_1 - \hat{\chi}_2)\|_{\mathcal{B}} \leq \lambda \|(\tau_1 - \tau_2, \omega_1 - \omega_2, \chi_1 - \chi_2)\|_{\mathcal{B}} \tag{5.78}$$

for some positive $\lambda < 1$.

Writing equation (5.76) for $(\hat{\tau}_1, \hat{\omega}_1)$ and $(\hat{\tau}_2, \hat{\omega}_2)$ and subtracting we get, using the regularity of ρ and F, the estimate

$$\sup_{D_\theta} |\hat{\chi}_1 - \hat{\chi}_2| \leq C_\chi \sup_{D_\theta} \{|\hat{\tau}_1 - \hat{\tau}_2| + |\hat{\omega}_1 - \hat{\omega}_2|\} \tag{5.79}$$

where by means of the boundedness of ρ, B, and w_{eq} in (5.72), we obtain

$$\sup_{D_\theta} |\hat{\omega}_1 - \hat{\omega}_2| \leq t\, C_\omega \sup_{D_\theta} \{|\tau_1 - \tau_2| + |\omega_1 - \omega_2|\}. \tag{5.80}$$

Finally Theorem 2.2 pg. 15 of [26] applied to the parabolic equation we can obtain for $\hat{\tau}_1 - \hat{\tau}_2$ (which has zero initial data), guarantees that we can estimate from above the sup-norm of $|\hat{\tau}_1 - \hat{\tau}_2|$ with $\sup_{D_\theta} \{|\tau_1 - \tau_2| + |\omega_1 - \omega_2|\}$ times an increasing function of time.

$$\sup_{D_\theta} |\hat{\tau}_1 - \hat{\tau}_2| \leq \mathcal{F}(\theta) \sup_{D_\theta} \{|\tau_1 - \tau_2| + |\omega_1 - \omega_2|\} \tag{5.81}$$

with $\mathcal{F}(0) = 0$.

Putting back (5.80) and (5.81) in (5.79) we obtain that (5.78) can be satisfied for θ sufficiently small. This concludes the proof thanks to the Banach–Caccioppoli contraction lemma. □

5.6.4 Continuation of the Solution

As it is formulated, the model cannot produce a sufficiently regular solution. Indeed when w crosses the value $w_{eq}(T)$, then w_t jumps from $w_{eq}\ \mathrm{div}\,\vec{V}$ to $W - w_{eq}\ \mathrm{div}\,\vec{V}$, producing a discontinuity of the latent heat release rate. Such a discontinuity derives from a crude representation of the switch of the crystallization mechanism. The physics of such a change are not completely clear, and it may be that it occurs only in a cooling regime ($T_t < 0$), due to secondary crystallization within the spherulites. Therefore it seems quite reasonable to slightly modify the model to eliminate that artificial singularity. This can be done redefining w_t for values of w in the interval $(w_{eq} - \varepsilon, w_{eq})$. Setting

$$F_\varepsilon(T) = -(w_{eq} - \varepsilon)\ div\,\vec{V} + W(T, w_{eq} - \varepsilon) \tag{5.82}$$

and

$$z_\varepsilon(T, w) = \frac{w_{eq} - w}{\varepsilon}, \quad z_\varepsilon(T, w) \in [0, 1] \tag{5.83}$$

for all w in the preceding interval, we write the following evolution equation:

$$\varepsilon z_{\varepsilon t} + z_\varepsilon^b \left[F_\varepsilon(T) - \frac{\partial}{\partial t} w_{eq}(T)\right] = 0, \quad z_\varepsilon(t^*) = 1 \tag{5.84}$$

(t^* being such that $w(\cdot, t^*) = w_{eq}(T(\cdot, t^*)) - \varepsilon$), which gives

$$z_\varepsilon = \left\{1 - \frac{1-b}{\varepsilon}\left[\int_{t^*}^t F_\varepsilon(T(\cdot,\tau))\,d\tau - \left(w_{eq}(T(\cdot,t)) - w_{eq}(T(\cdot,t^*))\right)\right]\right\}^{\frac{1}{1-b}} \tag{5.85}$$

as long as $z > 0$ (note that $z = 0$ is reached in a finite time), and finally

$$w(\cdot,t) = w_{eq}(T(\cdot,t)) - \varepsilon \left\{1 - \frac{1-b}{\varepsilon}\left[\int_{t^*}^t F_\varepsilon(T(\cdot,\tau))\,d\tau - (w_{eq}(T(\cdot,t)) - w_{eq}(T(\cdot,t^*)))\right]\right\}^{\frac{1}{1-b}}. \tag{5.86}$$

The source term in the heat balance equation is proportional to

$$w_t = \frac{\partial}{\partial t} w_{eq}(T) - \varepsilon \frac{\partial z}{\partial t} = w'_{eq}(T) T_t + \left\{1 - \frac{1-b}{\varepsilon}\left[\int_{t^*}^t F_\varepsilon(T(\cdot,\tau))\,d\tau - (w_{eq}(T(\cdot,t)) - w_{eq}(T(\cdot,t^*)))\right]\right\}^{\frac{1}{1-b}}$$

$$\left[F_\varepsilon(T(\cdot,t)) - w'_{eq}(T)\right] T_t = \mathcal{A}_3 w'_{eq}(T) T_t + \mathcal{A}_4. \tag{5.87}$$

Note that $\mathcal{A}_3 \in [0,1]$, and $w'_{eq} < 0$, so that the equation replacing (5.67) remains parabolic.

In conclusion, the heat balance equation has the form (5.67) as long as $w < w_{eq} - \varepsilon$; otherwise the evolution of the temperature field is given by (5.36) with w_t replaced by (5.87).

At this point is not difficult to get the continuation of the solution for all times by means of obvious modifications of the proof of Theorem 5.1. Thus we can state the following.

Theorem 5.2. *The problem with a modified model for the switch from growth regime to the constrained regime $w = w_{eq}(T)$ has a unique classical solution in any time interval.*

5.7 Physical Implications

A basic feature of this chapter is the introduction of an empirical equation of state able to describe the pressure-volume-temperature (PVT) data during polypropylene crystallization under isobaric conditions [31].

Equation (5.1), proposed by one of the authors (S.M.), is an extension from amorphous to semicrystalline polymers of the Spencer-Gilmore equation by adding the effects of both thermal contraction and overall crystallinity developed during polymer phase change.

The evaluation of the actual crystallinity requires the solution of a mathematical model for the crystallization process.

In this chapter, on the basis of the analysis performed in [18] it is shown that accurate fitting to the experimental data is the result of two key pieces of information: the kinetics of crystallization (5.4) and the equilibrium crystallinity w_{eq} (5.7) or (5.8) as a function of temperature.

The phenomenology described by the chosen model is the following: The kinetics of crystallization (5.4) act as a switch that starts the phase change process during cooling. However, caused by the fast growth of the kinetic constant (5.5) as the temperature decreases (Figure 5.8), very soon the equilibrium crystallinity w_{eq} is reached and crystallization kinetics (5.4) are switched off. From this instant on, the attainable crystallinity coincides with the equilibrium crystallinity w_{eq}.

Finally, the new state equation (5.1) suggests the possible existence of a critical triple point ($P^*V^*T^*$) where, by analogy with real fluids, phase change takes place without volume contraction. This effect can be foreseen from the behavior of the kinetic constant $K(T,P)$ at high pressures (Figure 5.18).

For pressures higher than 7000 Kg/cm^2 the kinetic constant becomes vanishingly small, and consequently crystallization is no longer allowed. In practice, phase change from liquid to solid takes place without

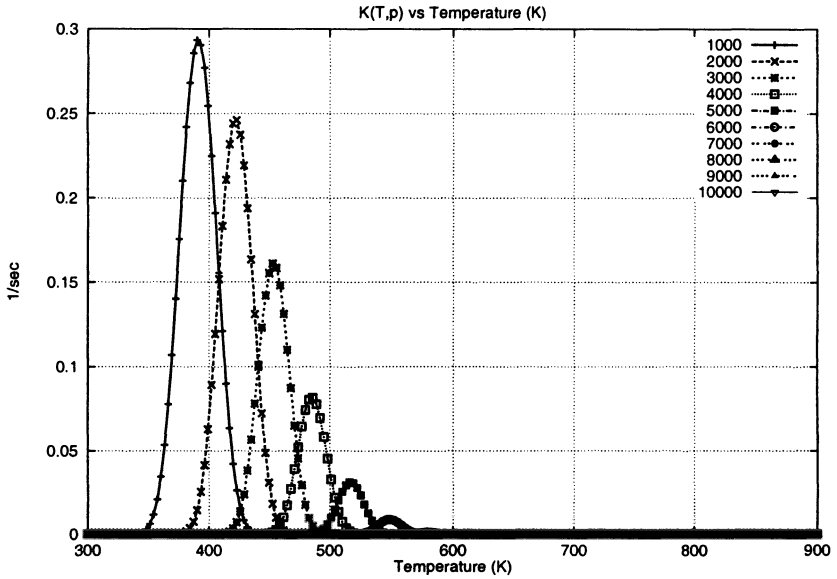

Figure 5.18 — $K(T, P)$.

crystallization. From a technological point of view, this effect may have formidable implications in the future when such ultra-high pressures will be accessible in commercial machines; processing of polymers in "near critical" conditions may become the key to solving such problems as shrinkage warping during injection molding and, in general, all problems where the dimensional stability is an issue.

The technology of ultra-high pressures during phase change is actively being investigated for the generation of nanostructures in semicrystalline polymers [37].

Acknowledgment

This work is partially supported by Federchimica, ASI (Italian Space Agency) and CNR (Italian Research Council).

References

1. Andreucci, D., Fasano, A., Gianni, R., Primicerio, M., and Ricci, R., Modelling nucleation in crystallization of polymers, *Conf. Free*

Boundary Problems, edited by M. Niezgodka and P. Strzelecki (1995), Zakopane, 359–67.

2. Andreucci, D., Fasano, A., Paolini, M., Primicerio, M., and Verdi, C., Numerical simulation of polymer crystallization, *Math. Models & Meth. Appl. Sci.*, **4** (1994), 135–45.
3. Andreucci, D., Fasano, A., and Primicerio, M., A mathematical model for non isothermal crystallization, *Proc. R.I.M.S.* (1991), Kyoto, 112–20.
4. Andreucci, D., Fasano, A., and Primicerio, M., On a mathematical model for the crystallization of polymers, *4th Europ. Conf. Math. in Industry*, edited by Hj. Wacker and W. Zulehner, Teubner Stuttgart (1991), 3–16.
5. Andreucci, D., Fasano, A., Primicerio, M., and Ricci, R., Mathematical models in polymer crystallization, *Survey Math. Ind.*, **6** (1996), 7–20.
6. Astarita, G., and Ocone, R., Continuous and discontinuous models for transport phenomena in polymers, *A.I.Ch.E.J.*, **33** (1987), 423–35.
7. Avrami, M., Kinetics of phase change I, II, III, *J. Chem. Phys.*, **7**, **8**, **9** (1939, 1940, 1941), 1103–12, 212–24, 117–84.
8. Batchelor, G.K., An Introduction to Fluid Dynamics, Cambridge University Press, (1973).
9. Beghishev, V.P., Bolgov, S.A., Keapin, I.A., and Malkin, A.Y., General treatment of polymer crystallization kinetics. Part 1: A new macrokinetic equation and its experimental verification, *Polym. Eng. Sci.*, **24** (1984), 1396–401.
10. Berger, J., and Schneider, W., A zone model of rate controlled solidification, *Plast. Rubber Process. Appl.*, **4** (1986), 127–33.
11. Capasso, V., Micheletti, A., De Giosa, M., and Mininni, R., Stochastic modelling and statistics of polymer crystallization processes, *Surv. Math. Ind.*, **6** (1996), 109–32.
12. Caselli, R., Mazzullo, S., Paolini, M., and Verdi, C., Models, experiments and numerical simulation of isothermal crystallization of polymers, *ECMI VII*, edited by A. Fasano and M. Primicerio, Teubner Stuttgart (1993), 167–74.
13. Chow, T.S., Molecular kinetic theory of the glass transition, *Polym. Eng. Sci.*, **24** (1984), 1079–86.
14. Clark, E.J., and Hoffman, J.D., Regime III crystallisation in polypropylene, *Macromolecules*, **17** (1984), 878–85.
15. De Luigi, C., Corrieri, R., and Mazzullo, S., Modello matematico di cristallizzazione isobara, non isoterma, di polipropilene, *XII Convegno*

italiano di scienza e tecnologia delle macromolecole (1995), Altavilla Milicia.

16. Eder, G., and Janeschitz-Kriegl, H., Structure development during processing: Crystallization. In *Proceedings of Polymers* (H.E.H. Mcijer ed.), *Material Science and Technology* **18**, VCH (1997).
17. Fasano, A., Modelling the solidification of polymers. An example of an ECMI cooperation, *ICIAM 91*, edited by R.E. O'Malley (1991), Washington, D.C.
18. Fasano, A., and Mancini, A., Existence and uniqueness of a classical solution for a mathematical model describing the isobaric crystallization of a polymer, *Interfaces and Free Boundaries* **2** (2000), 1–19.
19. Fasano, A., and Primicerio, M., An analysis of phase transition models, *EJAM*, **7** (1996), 1–12.
20. Fasano, A., and Primicerio, M., On a class of travelling wave solutions to phase change problems with an order parameter, *Workshop on non linear analysis an applications*, Warsaw, (1995), 113–23.
21. Fasano, A., and Primicerio, M., On mathematical models for nucleations and crystal growth processes, *Boundary Value Problems for PDE's and Applications*, edited by J. L. Lions and C. Baiocchi, Masson, Paris (1993), 351–58.
22. Ferry, J.D., Viscoelastic Properties of Polymers, John Wiley & Sons, Inc., New York (1970).
23. Kamal, M.R., and Lafleur, P.G., A structure oriented simulation of the injection molding of viscoelastic crystalline polymers. Part 1: Model with fountain flow, packing, solidification, *Polym. Eng. Sci.*, **26** (1986), 92–102.
24. Kolmogorov, A.N., Statistical theory of crystallization of metals, *Bull. Acad. Sci. USSR Mat Ser.*, **1** (1937), 355–59.
25. Kovarskij, A.L., High-Pressure Chemistry and Physics of Polymers (Compressibility of Polymers), CRC Press, London (1994).
26. Ladyzenskaja, O.A., Solonnikov, V.A., and Ural'ceva, N.N., Linear and quasi-linear equations of parabolic type, *Transl. of Mathematical Monographs*, **23**, American Mathematical Society (1968).
27. Mancini, A., A model for the crystallization of polypropylene under pressure, *ECMI* **98**, edited by Philip Brenner, Leif Arkerys, Jöran Bergh, and Rolf Pettersson (1999), Göteborg, 146–53.
28. Mancini, A., Non isothermal crystallization of polypropilene: Numerical approach, to appear.
29. Mancini, A., Processo di cristallizzazione non isoterma di polipropilene in condizioni isobare, Internal Report, Dip. Matematica "U.Dini," Università degli Studi di Firenze, (1997).

30. Mazzullo, S., Corrieri, R., and De Luigi, C., Mathematical model for isobaric non-isothermal crystallization of polypropylene, *Progress in Industrial Mathematics at ECMI 96*, edited by M. Brons, B.G. Teubner, Stuttgart (1997).

31. Mazzullo, S., Ferrari, M.C., and Mancini, A., A modified Spencer-Gillmore equation of state (SGM) for polypropylene during crystallization under isobaric conditions, *XIII National Macromolecular Meeting*, Genova, (1997).

32. Mazzullo, S., Paolini, M., and Verdi, C., Polymer crystallization and processing: Free boundary problems and their numerical approximation, *Math. Eng. Ind.*, **2** (1989), 219–32.

33. Micheletti, A., Problemi di geometria stocastica nei processi di cristallizzazione di polimeri. aspetti modellistici, statistici e computazionali, Ph.D. thesis, Università degli Studi di Milano (1997).

34. Pironneau, O., Finite Element Methods for Fluids, John Wiley & Sons, New York (1989).

35. Trotignon, J.P., and Verdu, J., Skin core structure fatigue behaviour relationships for injection molded parts of polypropylene. I: Influence of molecular weight and injection conditions on the morphology, *J. App. Polym. Sci.*, **34** (1987), 1–18.

36. Solonnikov, V.A., Solvability of the classical initial-boundary-value problems for the heat conduction equation in a dihedral angle, *J. Soviet Math*, **32** (1986), 526–46, (translated from Russian).

37. Stribeck, N., Zachmann, H.G., Bayer, R.K., and Balta Colleja, F.J., SAXS investigation of the structure of high-pressure crystallized polyetilene terephtalate—A new nanostructured material ?, *J. Mat. Sci.*, **32** (1997), 1639–47.

38. Tobin, M.C., Theory of phase transition kinetics with growth site impingement, *J. Polym. Sci. Polym. Phys. Ed.*, **12** (1974), 394–406.

39. Visintin, A., Motion by mean curvature and nucleation, *C.R. Acad. Sci. Paris*, **325(I)** (1997), 55–60.

40. Visintin, A., Nucleation and mean curvature flow, *Commun. P.D.E.'s*, **23** (1998), 17–53.

41. Visintin, A., Two-scale model of phase transitions, *Physica D*, **106** (1997), 66–80.

42. Ziabicki, A., Generalized theory of nucleation kinetic I, II, *J. Chim. Phys.*, **48** (1968), 4368–80.

43. Ziabicki, A., Theoretical analysis of oriented and non-isothermal crystallization, *Colloid Polymer Sci.*, **252** (1974), 207–21, 433–47.

6

Mathematical Modeling of Some Glass Problems

K. LAEVSKY AND R.M.M. MATTHEIJ

Eindhoven University of Technology
Department of Mathematics and Computer Science
Eindhoven, The Netherlands

ABSTRACT. In studying glass morphology one often uses models, which describe it as a strongly viscous Newtonian fluid. In this chapter we shall study two types of problems encountered in glass technology. One is dealing with so-called sintering, which plays a role in producing high-quality glasses, for example, and the other with producing packing glass by so-called pressing. We give a Stokes model to describe these processes and discuss various aspects of the evolution of both forming problems. The sintering problem is solved by a boundary element method, for which we use an interesting analytical tool to avoid numerical instabilities. The pressing problem actually deals with the morphology of a bottle or jar. Here we focus on simulating the glass flow. We first show how to deal with the temperature separately, by a suitable dimension analysis. Then we consider the flow of the glass in a domain with a partially free and partially moving boundary. We give a number of numerical examples to sustain our result.

6.1 Introduction

For many years, glass technology has been a craft based on expertise and experimental knowledge, reasonably sufficient to keep the products and production competitive. Over the last twenty years mathematical modeling

A. Fasano (ed.), *Complex Flows in Industrial Processes*

of the various aspects of production has become increasingly decisive, however. This is induced in part by fierce competition from other materials, notably polymers, which, for example, have found their way into the food packing industry. This is also a consequence of environmental concerns. It is not so much the waste (glass is 100% recyclable, a strong advantage to most competitors) as the energy consumption. One should realize that the melting process of sand to liquid glass makes up the largest cost factor of the product. For the relative importance of the current industry, look at some figures: In the European Union about 25 megatons of glass is being produced, which represents 30 billion ECU worth. The industry employs more than 200,000 people. Two-thirds of the glass production is meant for packing (jars and bottles). Float glass (used for panes) makes up most of the other quarter. The rest is for special products like CRTs and fibers.

Production of glass forms goes more or less along the following lines: First grains and additives, like soda, are heated in a tank. This can be a device several tens of meters long and a few meters high and wide (width being larger than height). Gas burners or electric heaters provide the heat necessary to heat the material to some 1400°C. At one end, the liquid glass comes out and is either led to a pressing or blowing machine or it ends up on a bed of liquid tin, where it spreads out to become float glass (panes, windshields, etc.). In the latter case the major problems are the need for a smooth flow from the oven on the bed and controlling the spreading and flattening. The pressing and blowing process is used in producing packing glass. To obtain a glass form a two-stage process is often used: First a blob of hot glass is pressed into a mould to form a so-called *parison.* It is cooled down (the mould is kept at 500°C) such that a small skin of solid glass is formed. The parison is then blown into its final shape. Such pressing/blowing machinery can produce a number of products at the same time; as a result a more or less steady flow of glass products is coming out on a belt. The products then have to be cooled down in a controlled way such that the remaining stresses are as small as possible (and thus the strength is optimal).

Sometimes only pressing is needed. This is the case in the production of CRTs, where a stamp is pressed into liquid glass and after being lifting, a certain morphology should have been transferred onto the glass screen.

As a final application of glass we may mention fibers. Glass fibers are, e.g., used to produce insulation material. A modern application is for transmitting optical signals. These optical fibers need to consist of very pure glass and have a low porosity. One of the processes to produce this is through a so-called *sol-gel process*, which amounts to chemical purification. The result of this is pure, strong glass particles. Through heating they melt together to a larger compact, a process called *sintering.* The eventual outcome of this is should be a dense glass compact [9].

All these processes involve the flow of the (viscous) glass in combination with heat exchange. Although these two are closely intertwined we shall show in this chapter that they can often be decoupled, thus effectively leading to isothermal flow problems on one hand and temperature problems on the other. For some overviews, see, e.g., [2], [10], [10] and [13].

This chapter is written as follows. In Section 6.2 we shall derive the basic flow equations that will play a role in our models. Section 6.3 is devoted to the sintering problem. We shall explain how we can describe the sintering of two cylinders (circles) numerically. This is typical for a more general compact of glass particles, which, however, is too complicated to deal with. Section 6.4 also gives an analytical method that can even handle the touching of two such cylinders. Then, in Section 6.5, we discuss the second problem, the pressing of glass in a mould. We describe the model and pay special attention to the heat exchange problem. In Section 6.6 the evolutionary process of the glass flow is considered numerically. An important practical problem here is the numerical conservation of mass, which is discussed in Section 6.7.

6.2 Modeling

Glass may be viewed as a frozen liquid, i.e., it has an amorphous structure. At sufficiently high temperatures (higher than 600°C) it behaves like an incompressible Newtonian fluid, which means that for a given dynamic viscosity η, a velocity $\mathbf{v}$ and a pressure p, the stress tensor τ is given by

$$\tau = -p\mathbf{I} + \eta(\operatorname{grad}\mathbf{v} + \operatorname{grad}\mathbf{v}^{\mathrm{T}}) \tag{6.1}$$

This constitutive relation should be used to close the equations that actually describe the motion of a glass blob, the momentum equation (2) and the continuity equation (3):

$$\rho\left(\frac{\partial \mathbf{v}}{\partial t} + (\operatorname{grad}\mathbf{v})^{\mathrm{T}}\mathbf{v}\right) = \rho\mathbf{f} + \operatorname{div}\tau \tag{6.2}$$

where ρ denotes the mass density, $\mathbf{f}$ the volume forces on the blob, and

$$\operatorname{div}\mathbf{v} = 0. \tag{6.3}$$

Using (6.1) in (6.2) we obtain

$$\rho\left(\frac{\partial \mathbf{v}}{\partial t} + (\operatorname{grad}\mathbf{v})^{\mathrm{T}}\mathbf{v}\right) = \rho\mathbf{f} - \operatorname{grad}\mathrm{p} + \operatorname{div}(\eta(\operatorname{grad}\mathbf{v} + \operatorname{grad}\mathbf{v}^{\mathrm{T}})). \tag{6.4}$$

In the two problems we shall study in this chapter we anticipate the viscous forces (div τ) to dominate in (6.2). To see this we shall reformulate our

equations in dimensionless form, for which we need some characteristic quantities.

First we remark that the only acting volume force in the process is gravity, so $||\mathbf{f}|| \approx 10\,\mathrm{m/s^2}$. We define

$$\tilde{\mathbf{f}} := \frac{1}{||\mathbf{f}||}\mathbf{f}. \tag{6.5}$$

The viscosity η is assumed to be constant, say $\eta_0 \approx 10^4\,\mathrm{kg/ms}$. Normally there is no need to introduce a dimensionless viscosity, but we shall do this. Thus, because it may be highly temperature-dependent, let

$$\tilde{\eta} := \frac{1}{\eta_0}\eta. \tag{6.6}$$

A typical average velocity V_0 (which is 10^{-1} m/s or much slower), say $V_0 \approx 10^{-1}\,\mathrm{m/s}$, can be used as a characteristic velocity. As a characteristic length scale we take $L(\approx 10^{-2}\,\mathrm{m}$ or smaller). We now define the dimensionless quantities

$$\tilde{\mathbf{x}} := \frac{\mathbf{x}}{L}, \quad \tilde{\mathbf{v}} := \frac{\mathbf{v}}{V_0}, \quad \tilde{p} := \frac{L}{\eta_0 V_0}p. \tag{6.7}$$

A proper choice of characteristic time scale is the ratio $L/V_0(\approx 10^{-1}\,\mathrm{s})$. So, let us finally define

$$\tilde{t} := \frac{V_0}{L}t. \tag{6.8}$$

Substituting all dimensionless quantities into (6.3) and (6.4) yields

$$Re\left(\frac{\partial\tilde{\mathbf{v}}}{\partial\tilde{t}} + (\operatorname{grad}\tilde{\mathbf{v}})^{\mathrm{T}}\tilde{\mathbf{v}}\right) = \frac{Re}{Fr}\tilde{\mathbf{f}} - \operatorname{grad}\tilde{\mathrm{p}} + \operatorname{div}\left(\tilde{\eta}(\operatorname{grad}\tilde{\mathbf{v}} + \operatorname{grad}\tilde{\mathbf{v}}^{\mathrm{T}})\right),$$
$$\operatorname{div}\tilde{\mathbf{v}} = 0. \tag{6.9}$$

All spatial derivatives in (6.9) have to be taken with respect to the dimensionless variable $\tilde{\mathbf{x}}$. In (6.9) two dimensionless numbers appear, namely, the Reynolds number (Re) and the quotient of the Reynolds number and the Froude number (Re/Fr), defined by

$$Re := \frac{V_0 L\rho}{\eta_0}, \quad \frac{Re}{Fr} := \frac{\rho||\mathbf{f}||L^2}{\eta_0 V_0}.$$

The Reynolds number indicates the ratio between inertial forces, and viscous forces and the quotient of the Reynolds number and the Froude number indicates the ration between volume forces (i.e., gravity) and viscous forces. The two numbers are estimated by

$$Re \approx 10^{-4}, \quad \frac{Re}{Fr} \approx 10^{-3}. \tag{6.10}$$

From this we conclude that the viscous forces indeed dominate. Thus, the flow describing the equations are (rewritten in their dimensionless form)

$$\begin{aligned} \operatorname{grad} \mathrm{p} &= \operatorname{div}\left(\eta(\operatorname{grad}\mathbf{v} + \operatorname{grad}\mathbf{v}^{\mathrm{T}})\right) \\ \operatorname{div}\mathbf{v} &= 0. \end{aligned} \tag{6.11}$$

These equations are the *Stokes creeping flow equations.* They require further boundary conditions in order to solve the vector $\mathbf{v}$. Actually they will be kinematic constraints, changing with time t, describing the evolution of the blob. We shall specify these boundary conditions for the two situations in the subsequent section. They have in common that at least one part of the boundary is free. Hence, besides finding the velocity $\mathbf{v}(t)$ we then need to find this free boundary. The actual displacements $\mathbf{x}$ satisfy the ordinary differentional equation

$$\frac{d\mathbf{x}}{dt} = \mathbf{v}(\mathbf{x}). \tag{6.12}$$

Numerically we shall deal with these problems in a two-stage sweep: Suppose we have a domain $\mathcal{G}(t)$ describing the glass blob. Then solve (6.11) (approximately) and use velocity field on the boundary to compute a new domain $\mathcal{G}(t + \Delta t)$ using (12) and the boundary conditions.

6.3 Viscous Sintering

Sintering is the process of bringing a powder of metals, ionic crystals, or glasses (a compact) to such a high temperature that there is sufficient mobility to release the excess free energy of the surface of the powder, thereby joining the particles together. The driving force arises from the excess free energy of the surface of the powder over that of the solid material. For a survey of the most important papers about sintering we refer to the book edited by Sōmiya and Moriyoshi [12].

We are interested in the case of sintering glasses; see also [9] and [11]. There the material transport can be modeled as a viscous incompressible Newtonian volume flow, driven solely by surface tension (*viscous sintering*), i.e., the Stokes creeping flow equations hold. The geometry of such a sintering compact is usually very complex. Because of this it is impossible to give a deterministic description of the flow in such a compact as a whole. We shall therefore investigate simple geometries in two dimensions only. For more general compacts see, e.g., [8], [15], and [16].

Let us denote the compact (blob) at time t by Ω_t and its boundary by Γ_t; see Figure 6.1. Then the driving force of the boundary movement is a tension in the direction of the normal $\mathbf{n}$; the latter is proportional to the

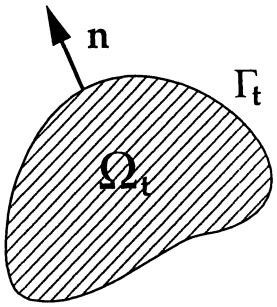

Figure 6.1 — Compact domain at time t.

local curvature, κ of the boundary. Thus we obtain

$$\tau \mathbf{n} = (\operatorname{div} \mathbf{n})\mathbf{n} = \kappa \mathbf{n}. \tag{6.13}$$

Our only interest is the movement of the boundary Γ, i.e., only the velocity at the boundary is required (from which we can calculate the shape evolution of the body directly). Therefore this problem is ideally suited to be solved numerically by a boundary element method (BEM). To do this, we have to reformulate the problem as an integral equation over the boundary. This is done in terms of a boundary distribution of hydrodynamic single- and double-layer potentials: see also Ladyzhenskaya [7].

When the boundary is sufficiently smooth, the integral formulation that can be derived for the Stokes equations at a point, say $\mathbf{x}$, reads in matrix notation (see also [6])

$$\mathcal{C}\mathbf{v}(\mathbf{x}) + \int_\Gamma \mathcal{Q}(\mathbf{x},\mathbf{y})\mathbf{v}\, d\Gamma_y = \int_\Gamma \mathcal{U}(\mathbf{x},\mathbf{y})\mathbf{b}\, d\Gamma_y. \tag{6.14}$$

Here $\mathcal{C}, \mathcal{Q}(\mathbf{x},\mathbf{y})$, and $\mathcal{U}(\mathbf{x},\mathbf{y})$ are 2×2 matrices with coefficients c_{ij}, q_{ij}, and $u_{ij}, i,j = 1,2$, respectively:

$$c_{ij} = \begin{cases} \delta_{ij} & \mathbf{x} \in \Omega \\ \frac{1}{2}\delta_{ij} & \mathbf{x} \in \Gamma \end{cases} \tag{6.15}$$

$$q_{ij} = \frac{r_i r_j}{\pi(r_1^2 + r_2^2)^2} r_k n_k \tag{6.16}$$

$$u_{ij} = \frac{1}{4\pi}\left[-\delta_{ij}\frac{1}{2}\, log[r_1^2 + r_2^2] + \frac{r_i r_j}{r_1^2 + r_2^2}\right] \tag{6.17}$$

where δ_{ij} is the Kronecker delta, $r_i := x_i - y_i, i,j = 1,2$, and the vector $\mathbf{b}$ is the boundary curvature in the normal direction, i.e.,

$$\mathbf{b} = \kappa \mathbf{n} \tag{6.18}$$

The integral equation (6.14), which has to be solved for a fixed boundary, does not ensure a unique solution $\mathbf{v}$. Clearly, we need to add three extra conditions (equations) to account for the degrees of freedom with respect to translation and rotation.

We follow the approach of Hsiao, Kopp, and Wendland [5] to make the integral equation (6.14) uniquely solvable for a fixed boundary. This is done by adding three additional variables w_i to this integral equation, which prescribe the translation and rotation, i.e.,

$$\mathcal{C}\mathbf{v}(\mathbf{x}) + \int_\Gamma \mathcal{Q}(\mathbf{x},\mathbf{y})\mathbf{v}\, d\Gamma_y + \mathcal{V}(\mathbf{x})\mathbf{w} = \int_\Gamma \mathcal{U}(\mathbf{x},\mathbf{y})\mathbf{b}\, d\Gamma_y \tag{6.19}$$

where $\mathcal{V}$ is a 2×3 matrix defined by

$$\mathcal{V} = \begin{bmatrix} 1 & 0 & x_2 \\ 0 & 1 & -x_1 \end{bmatrix}. \tag{6.20}$$

Three additional equations have to be given to ensure that the boundary velocity is defined uniquely. In order to prescribe the translation freedom, we formulate the problem to be stationary at a (reference) point in the fluid, say $\mathbf{x}^r$. With regard to this reference point the velocity of the boundary points is computed. The most natural choice for this reference point is the center of mass: the point where the gravity forces would grip the body, thus:

$$\mathbf{v}(\mathbf{x}^r) = 0. \tag{6.21}$$

Using this, we derive from the integral formulation (6.14) and $\mathbf{x} = \mathbf{x}^r$ the following equation

$$\int_\Gamma \mathcal{Q}(\mathbf{x}^\nabla,\mathbf{y})\mathbf{v}\, d\Gamma_y = \int_\Gamma \mathcal{U}(\mathbf{x}^\nabla,\mathbf{y})\mathbf{b}\, d\Gamma_y. \tag{6.22}$$

Furthermore we assume the tangential component of the velocity at the boundary to be zero, i.e.,

$$\int_\Gamma (\mathbf{v},\tau)\, d\Gamma = 0 \tag{6.23}$$

where τ is the tangential vector of the boundary. Combining this with the Stokes formula, it follows from equation (6.23) that the flow in Ω is *irrotational*.

In a practical implementation we have to determine the grid on Γ in an appropriate way; for more see [16]. Special care has to be taken with respect to the computation of the curvature. Indeed, if we use finite differences to approximate differential quotients we are facing problems when the distance between grid points is too small. In Figure 6.2 we illustrated this for the coalescence of two circles (actually cylinders in a three dimentional setting) a time after the actual touching took place. At this

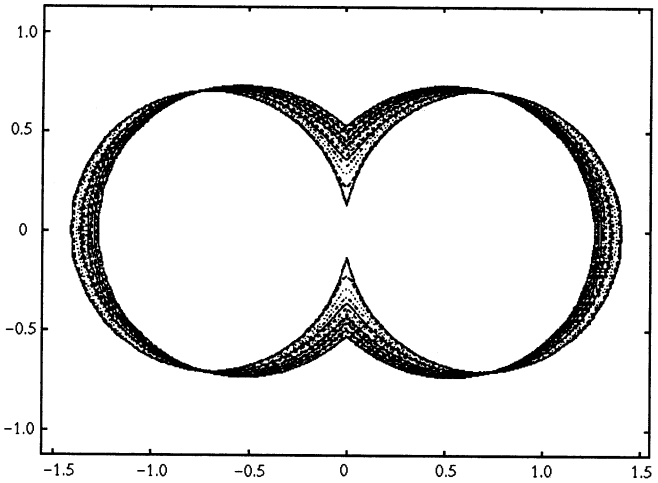

Figure 6.2 — Two sintering cylinders with equal diameters. The same mesh is used through the entire simulation.

touching point a so-called *neck* is developing, at which the curvature is still extremely high. The results show numerical instability. To cure this problem, we shall invoke some analytical tools first.

6.4 The Analytical Solution for the Coalescence of Two Equal Circles

In this section we give the analytical solution for the coalescence of two equal circles and we introduce some notation for the main properties of this solution. These are the initial radii R of both circles, the measure of contact between both circles, and the boundary curvature at the contact.

The analytical solution for the evolution of two equal coalescing circles was derived by Hopper [4]. He described the evolution of these circles in terms of a time-dependent mapping function $z = x + \mathbf{i}\mathbf{y} = \Omega(\xi, \mathbf{t})$ of the unit circle, conformal on $|\xi| \leq 1$. The time evolution of the map was given in parametric form. In these papers, the equations derived are valid for the coalescence of two circles with initial radius 1. Here it turns out that we may take

$$z = \frac{\sqrt{2}(1-\nu^2)e^{\frac{1}{2}\mathrm{i}\theta}}{1-\nu e^{2\mathrm{i}\theta}\sqrt{1+\nu^2}} \tag{6.24}$$

where $e^{\mathrm{i}\theta}$ describes the contour of the unit circle and $\nu = \nu(t)$ is a function with values $\in [0, 1]$. For $\nu \to 1$ we have a touching of the two circles.

Following Hopper [3], we can derive parametric equations for the evolution of two coalescing circles both with initial radius R and centers $(R,0)$ and $(-R,0)$ respectively ($R=1$ follows from (6.24))

$$\begin{aligned} x(\theta,\nu) &= \frac{(1-\nu^2)(1-\nu)R\sqrt{2}\cos\theta}{(1-2\nu\cos 2\theta+\nu^2)\sqrt{1+\nu^2}} \\ y(\theta,\nu) &= \frac{(1-\nu^2)(1+\nu)R\sqrt{2}\sin\theta}{(1-2\nu\cos 2\theta+\nu^2)\sqrt{1+\nu^2}} \end{aligned} \tag{6.25}$$

and for the time t (as a function of ν)

$$t(\nu) = \frac{\pi R}{\sqrt{2}} \int_{\nu}^{1} \frac{dk}{k\sqrt{1+k^2\mathrm{K(k)}}} \tag{6.26}$$

Here K(k) is the complete elliptic integral of the first kind defined by

$$\mathrm{K(k)} = \int_{v}^{\frac{\pi}{2}} (1-\mathrm{k}^2\sin^2\phi)^{-\frac{1}{2}}\, d\phi. \tag{6.27}$$

The degree of coalescence is specified by the parameter ν, which decreases from 1 to 0 if time increases (t is going to infinity as $\nu \to 0$), and the boundary curve is specified by the parameter θ, which is varying from 0 to 2π. Of course, at $t=0$, both circles are making contact at the origin.

Of special interest is the region where the circles are touching. In our example, the line of contact is the y-axis during the evolution. Let r be the *contact radius* between both circles and denote the point on the boundary at the line of contact in the positive direction by $\mathbf{x}^n$, i.e., $\mathbf{x}^n = (0,r)$. Recall that we called this point the *neck*.

In the analytical solution (6.25) the neck is occurring at $\theta = \pi/2$ during the evolution. Thus for the contact radius r, as a function of the parameter ν, the following holds

$$r(\nu) = y\left(\frac{\pi}{2},\nu\right) = \frac{(1-\nu)R\sqrt{2}}{\sqrt{1+\nu^2}}. \tag{6.28}$$

Note that as $\nu \to 0$, i.e., $t \to \infty$, $r \to R\sqrt{2}$, which is the radius of the circle the shape evolution is approaching as time increases.

By solving for the parameter ν as function of the contact radius r, we obtain from (6.28)

$$\nu = \nu(r) = \frac{2R^2 - r\sqrt{4R^2-r^2}}{2R^2-r^2}. \tag{6.29}$$

For the curvature of the neck, say κ_n, we can derive from the parametric

equations (6.25)

$$\kappa_n(\nu) = \left.\frac{x_{\theta\theta}y_\theta - x_\theta y_{\theta\theta}}{(x_\theta^2 + y_\theta^2)^{\frac{3}{2}}}\right|_{\theta=\frac{\pi}{2}} = -\frac{(1-6\nu+\nu^2)\sqrt{1+\nu^2}}{(1-\nu)^3 R\sqrt{2}}. \tag{6.30}$$

Remark that as $\nu \to 0$, i.e., $t \to \infty$, $\kappa_n \to -1/R\sqrt{2}$, as assumed. The derived neck curvature (6.30) can be written as a function of the contact radius r; from equations (6.29) and (6.30), we obtain

$$\kappa_n(r) = \frac{4R^2}{r^3} - \frac{3}{r}. \tag{6.31}$$

Using this formula, rather than a numerical derivation of the curvature, gives satisfactory results, see Figure 6.3.

We can now also analyze the effect of a small perturbation of the initial contact radius $r, r+\varepsilon$, say, both circles having initial radius R (see Figure 6.4). Although depicted in one graph they may represent the boundaries at different time points. So consider the parametric equations (6.25) as a function of R and t (i.e., ν). A measure for the difference between both shapes is given by the derivative of x, y with respect to R.

Using (6.27), the parametric equations (6.25) can be written as

$$\begin{aligned} x(\theta,\nu) &= \frac{r(1-\nu^2)\cos\theta}{1+\nu^2-2\nu\cos 2\theta} \\ y(\theta,\nu) &= \frac{r(1+\nu^2)\sin\theta}{1+\nu^2-2\nu\cos 2\theta} \end{aligned} \tag{6.32}$$

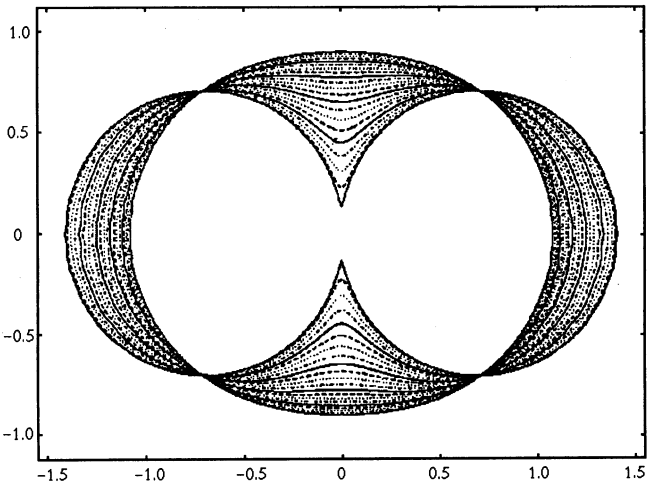

Figure 6.3 — Two sintering cylinders with equal diameters. A mesh verification is done at each time step.

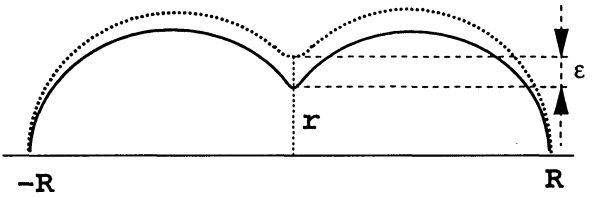

Figure 6.4 — The coalescence of two equal circles.

We have to consider equations (6.25) as a function of r (and t). The derivative of x and y with respect to r will then be a measure for the deviation between the two curves.

For the derivative of ν with respect to r, we obtain after squaring, taking the derivative of equation (6.28) and using the relation (6.29)

$$\frac{\partial \nu}{\partial r} = -\frac{2R^2(1-\nu)^2}{r^2\sqrt{4R^2-r^2}} \tag{6.33}$$

Now define a normalized radius

$$\tilde{r} := r/(R\sqrt{2})$$

then derive the following relation between ν and $\tilde{r}$ (so r)

$$\frac{1-\nu}{1+\nu} = \frac{\tilde{r}}{\sqrt{2-\tilde{r}^2}}. \tag{6.34}$$

If we then write

$$\xi = \cos\theta$$

we find, by taking the derivatives of (6.31) with respect to r, and restricting ourselves to the first quadrant, using (6.32),

$$\begin{aligned}
\frac{\partial x}{\partial r} &= \frac{(1-\nu^2)\xi}{(1+\nu)^2-4\nu\xi^2} + \frac{2(1-\nu)^2[(1+\nu)^2-2(1+\nu^2)\xi^2]\xi}{\tilde{r}\sqrt{2-\tilde{r}^2}((1+\nu)^2-4\nu\xi^2)^2} \\
\frac{\partial y}{\partial r} &= \frac{(1-\nu)^2\sqrt{1-\xi^2}}{(1+\nu)^2-4\nu\xi^2} - \frac{4(1+\nu)(1-\nu)^3\xi^2\sqrt{1-\xi^2}}{\tilde{r}\sqrt{2-\tilde{r}^2}((1+\nu)^2-4\nu\xi^2)^2}.
\end{aligned} \tag{6.35}$$

Again our interest is mainly the neck region, i.e., ξ is small. Using (6.31) and (6.33) we derive for (6.24)

$$\frac{\partial x}{\partial r} = \frac{y\xi}{R\sqrt{2(1-\xi^2)(2-\tilde{r}^2)}} + \frac{y^2\xi\sqrt{2}[(1+\nu)^2-2(1+\nu^2)\xi^2]}{R(1-\xi^2)(1+\nu)^2(2-\tilde{r}^2)^{\frac{3}{2}}} \tag{6.36}$$

$$\frac{\partial y}{\partial r} = \frac{y}{r} - \frac{2\sqrt{2}xy\xi}{rR(2-\tilde{r}^2)^{\frac{3}{2}}}.$$

Using $0 \leq \tilde{r} < 1$, one may check that maximum absolute values in (6.36) are given by

$$\left|\frac{\partial x}{\partial r}\right| \leq \frac{y\xi}{R\sqrt{2(1-\xi^2)}}\left(1+\frac{2y}{\sqrt{1-\xi^2}}\right), \quad \left|\frac{\partial y}{\partial r}\right| \leq \frac{y}{r}\left(1+\frac{2\sqrt{2}x\xi}{R}\right). \tag{6.37}$$

In the neck region y is $\mathcal{O}(\nabla)$ and x is small, i.e., from (6.31) we conclude that a small change of the contact radius r of the coalescing circles will not perturb the shape of the neck region, even when r is small.

The relation (6.31) for the (exact) neck curvature also gives information about the effect of a change of the contact radius r on this curvature. From (6.31) it follows that the derivative of the neck curvature, with respect to r, is given by

$$\frac{\partial \kappa_n}{\partial r} = -\frac{12R^2}{r^4} + \frac{3}{r^2}. \tag{6.38}$$

Thus a small change of the radius r has an $\mathcal{O}(\frac{\infty}{\nabla^\Delta})$ effect on the neck curvature, i.e., when the contact radius is small the curvature is changed dramatically. Conversely, we also have

$$\frac{\partial r}{\partial \kappa_n} = -\frac{r^4}{12R^2+3r^2}$$

i.e., a change of the neck curvature gives only an $\mathcal{O}(\nabla^\Delta)$ effect on the contact radius r.

A measure for the time difference between the shapes at time t and $\tilde{t}$ is given by the derivative of t with respect to r, i.e., taking the derivative of equation (6.26) and using (6.26), (6.32), we derive

$$\frac{\partial t}{\partial R} = \frac{\pi\sqrt{1+\nu^2}}{2\nu K(\nu)\sqrt{2-\tilde{r}^2}}. \tag{6.39}$$

Using asymptotic expansions for $K(\nu)$ one can show that $\left|\frac{\partial t}{\partial R}\right|$ is small when the time t is not too large. We conclude that neck evolution is a smooth function of time.

The preceding analysis shows that a small change of the contact radius is hardly perturbing the global shape of the neck region. Only the curvature of the neck (a local effect) is changed dramatically when r is small.

We finally remark that the curvature approximations here can be used more generally in the computation of rather complicated blobs. For more details see [16].

6.5 Pressing of Glass

As stated in Section 6.1, there is a large variety of applications of glass products. Previous sections dealt with particles of millimeter size. In this section we consider viscous flows arising in the production of packing glass, such as bottles and jars, which are of order of 10 cm size. Typically this is a two-stage process. First a blob of glass is pressed in a *mould* by a *plunger* to a certain preform, the so called *parison* (see Figure 6.5), which is then blown into the finally desired shape (see Figure 6.6). Here we will only consider the first stage, i.e., the pressing. Because the mould and the plunger are axisymmetric we shall assume the entire problem to be so. In practice, the initial form of the glass blob may not be axisymmetric, but it will not deviate too much from this form in a well-controlled production process.

Thus we can study an essential two-dimensional flow/energy problem in a time-varying domain Ω_t as depicted in Figure 6.7.

In cylindrical coordinates the Stokes equations (6.11) can be written as

$$\begin{aligned} \frac{\partial p}{\partial z} &= \eta\left[\frac{\partial^2 u}{\partial z^2} + \frac{\partial^2 u}{\partial r^2} + \frac{1}{r}\frac{\partial u}{\partial r}\right] \\ \frac{\partial p}{\partial r} &= \eta\left[\frac{\partial^2 v}{\partial z^2} + \frac{\partial^2 v}{\partial r^2} + \frac{1}{r}\frac{\partial v}{\partial r} - \frac{v}{r^2}\right] \end{aligned} \tag{6.40}$$

$$0 = \frac{\partial u}{\partial z} + \frac{\partial v}{\partial r} + \frac{v}{r}. \tag{6.41}$$

Here u and v are the velocities in the z and r directions, respectively.

In contrast to the sintering problem we do not have an isothermal situation here, at least not in principle. As a consequence the viscosity η

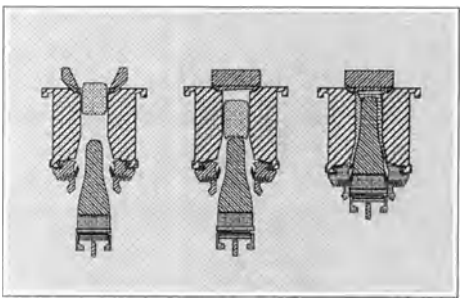

Figure 6.5 — The pressing phase.

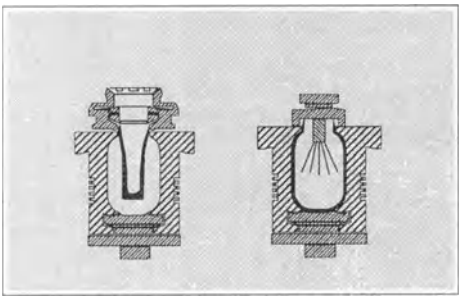

Figure 6.6 — The blowing phase.

may not be constant, and in fact it may vary wildly as a function of the temperature. Note that the temperature T and the viscosity η of glass are related through the Vogel–Fulcher–Tamman relation [10]

$$\eta = K \exp(E_o/(T - T_0)). \tag{6.42}$$

Here K is some constant, E_0 the viscosity activation energy, and T_0 a fixed temperature.

In dimensionless quantities (Section 6.2) the velocity and temperature are coupled through the energy equation, written for the axisymmetric case for an incompressible stationary flow with constant heat conductivity and

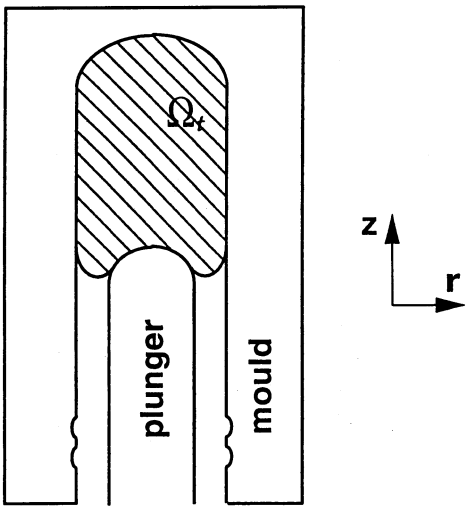

Figure 6.7 — 2-D problem.

heat capacity as (cf [1])

$$\left(v\frac{\partial T}{\partial r}+u\frac{\partial T}{\partial z}\right)=\frac{1}{Pe}\left(\frac{\partial^2 T}{\partial r^2}+\frac{1}{r}\frac{\partial T}{\partial r}+\frac{\partial^2 T}{\partial z^2}\right)$$
$$+\frac{Ec}{Re}\left(2\left(\frac{\partial u}{\partial z}\right)^2+2\left(\frac{\partial u}{\partial r}\right)\left(\frac{\partial v}{\partial z}\right)\right.$$
$$\left.+2\left(\frac{\partial v}{\partial r}\right)^2+\left(\frac{\partial v}{\partial z}\right)^2+\left(\frac{\partial u}{\partial r}\right)^2\right). \tag{6.43}$$

Here Ec is the Eckhard number, defined as (cf Section 6.2)

$$Ec := \frac{U^2}{c_p \Delta T} \tag{6.44}$$

where c_p is the specific heat and ΔT the temperature drop. Pe is the Peclet number, defined as

$$Pe := \frac{\rho U L c_p}{k} \tag{6.45}$$

where k is the thermal conductivity. For glass we obtain

$$\frac{1}{Pe} = 6.2 \cdot 10^{-4}, \quad \frac{Ec}{Re} = 1.2 \cdot 10^{-4}.$$

Both are very small, so we can ignore the heat conduction and thermal production terms (the second and third terms in equation (6.42)); thus the energy equation simplifies to:

$$u\frac{\partial T}{\partial z}+v\frac{\partial T}{\partial r}=0. \tag{6.46}$$

This equation is solved by the system

$$\frac{dz}{dt}=u, \quad \frac{dr}{dt}=v, \quad \frac{dT}{dt}=0 \tag{6.47}$$

from which we see that the temperature remains constant along the streamlines. If we start with a uniform temperature field, it will remain uniform everywhere.

If we include the cooling of the wall we can do the following: Let Ω_p, Ω_g, and Ω_m denote the plunger (p), glass (g), and mold (m) domains, respectively (see Figure 6.8) and $k_i, i \in \{p, g, m\}$, their thermal diffusitivity. One can estimate the numerical values of these to find $k_m = k_g = 6.2 \cdot 10^{-7}[\mathrm{m}^2/\mathrm{s}]$ and $k_p = k_m = 1.7 \cdot 10^{-5}[\mathrm{m}^2/\mathrm{s}]$. We observe that $k_p = k_m \gg k_g$, and this implies that when the heat process of the

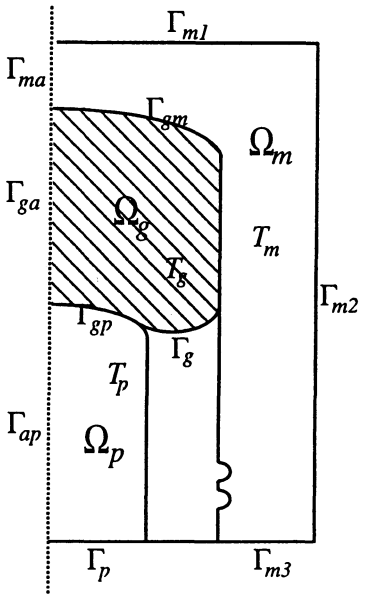

Figure 6.8 — 2-D domain.

glass starts, the heat processes of the plunger and the mould are already in the steady state. This means that the temperature $T_p = T_p(0)$ and $T_m = T_m(0)$. Hence the three heat processes are not coupled.

We therefore conclude that we may actually compute the temperature from the simple heat equation

$$\frac{1}{k_g}\frac{\partial T_g}{\partial t} = \Delta T_g \quad \text{in}\,\Omega_g \tag{6.48}$$

subject to the boundary conditions

$$\frac{\partial T_g}{\partial \eta} = 0 \text{ on } \Gamma_g \cup \Gamma_{ga},$$

$$k_g \frac{\partial T_g}{\partial n} = h_{gp}(T_g - T_{0p}) \text{ on } \Gamma_{gp}, \text{ and}$$

$$k_g \frac{\partial T_g}{\partial n} = h_{gm}(T_g - T_{0m}) \text{ on } \Gamma_{gm}.$$

Here h_{gp} is the contact conductance between the glass and the plunger and h_{gm} is the contact conductance between the glass and the mold. The contact conductance depends on the surface roughness, the interface pressure and temperature, the thermal conductivities of the contacting materials and the type of fluids or gas in the gap, and is about $h_{gp} = h_{gm} = 2.10^3[\text{W/m}^2/.\text{c}]$.

On the two boundaries Γ_{gp} and Γ_{gm} we have a temperature drop, depending on the contact conductances, and a boundary layer, depending on the thermal diffusivity of the glass. One can prove that the asymptotic behavior of the boundary layer is the error function $\operatorname{erfc}(r/\sqrt{4k_g t})$.

6.6 Computation of the Flow

Because we may now assume the flow to be isothermal after all, we can concentrate on solving the Stokes equation, subject to kinematic boundary conditions. Consider the configuration in Figure 6.9. Let $\Gamma_t = \partial\Omega_t$ be the boundary of Ω_t. It is easy to see that Γ_t consists of four parts:

$$\Gamma_t = \Gamma_m \cup \Gamma_f \cup \Gamma_p \cup \Gamma_s$$

corresponding to the mold, free boundary, plunger, and symmetric part, respectively. Because glass during the process is assumed to be a fluid, no-slip boundary conditions can be assumed for correspondent parts of the boundary Γ_t:

$$\begin{aligned} \mathbf{v} &= V_p \\ \mathbf{v} &= 0 \end{aligned} \tag{6.49}$$

where V_p is the velocity of the plunger.

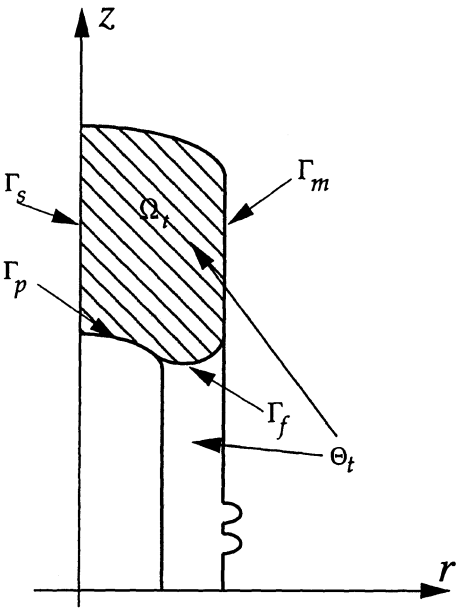

Figure 6.9 — 2-D domain.

A symmetry boundary condition is required for Γ_s:

$$\begin{aligned} v_n &= 0 \\ \frac{\partial v_s}{\partial n} &= 0 \\ \frac{\partial p}{\partial n} &= 0. \end{aligned} \tag{6.50}$$

Here we have denoted by v_n and v_s the normal and tangential components of $\mathbf{v}$ respectively.

At the free boundary the normal stress must be equal to the external pressure p_0, which is assumed to be constant. The tangential stress must be equal to zero. Hence:

$$\begin{aligned} p - 2\eta \frac{\partial \mathbf{v}_n}{\partial n} &= p_0 \\ \frac{\partial \mathbf{v}_n}{\partial s} + \frac{\partial \mathbf{v}_s}{\partial n} &= 0. \end{aligned} \tag{6.51}$$

One should note that (50) provides for kinematic boundary conditions. Indeed, the domain Ω_t, corresponding to the region occupied by the glass at time t, is time-dependent and changes during the process. The method of solution is now to use a Stokes solver (we actually use a finite element method) on the domain Ω_t, and we use the found velocity field to simulate the evolution.

Let $\mathbf{x} : [0, T] \times \Omega_0 \rightarrow \mathrm{IR}^2$ be a mapping such that:

$$\mathbf{x}(0) = \Omega_0, \quad \mathbf{x}(t) = \Omega_t$$

where Ω_t is the problem domain as defined before. Then the relation between the velocity field and the domain geometry can be described by the initial value problem:

$$\begin{aligned} \frac{d\mathbf{x}(t)}{dt} &= \mathbf{v}(\mathbf{x}(t)) \quad t \in [0, T], \\ \mathbf{x}(0) &= \Omega_0. \end{aligned} \tag{6.52}$$

The velocity field $\mathbf{v}(\mathbf{x}(t))$ can be obtained by solving the Stokes equations in Ω_t. However, one should realize that the geometry of Ω_t depends on that velocity field.

To overcome this problem we will use the following strategy. Let us define

$$t_n = n\Delta t, \quad n = 1, \ldots, N$$

such that $t_0 = 0, t_N = T$. After discretization and solving the Stokes equations with correspondent boundary conditions in Ω_{t_n} (which are assumed to be defined), we obtain the velocity field $\mathbf{v}^n$. Instead of (6.53) we solve

the initial value problem:

$$\frac{d\mathbf{x}(t)}{dt} = \mathbf{v}^n, \quad t \in [t_n, t_{n+1}] \qquad \mathbf{x}(t_n) = \Omega_{t_n}. \tag{6.53}$$

At a particular time t_n for any point $\mathbf{x}_i^n$ on the free boundary Γ_f we may consider this as a Lagrangian displacement, which we may, e.g., discretize by the explicit Euler method:

$$\mathbf{x}_i^{n+1} = \mathbf{x}_i^n + \Delta t \mathbf{v}_i^n. \tag{6.54}$$

The local error for this algorithm is of the first order in Δt.

The geometry of $\Omega_{t_{n+1}}$ can be obtained now, and hence the boundary conditions required for solving the flow equations at t_{n+1} can be defined. The same procedure is repeated until the final geometry Ω_{t_N} and corresponding flow quantities have been computed. Instead of Euler explicit it is possible to use more sophisticated integration schemes. For our problem it turns out to be one of the most important aspects.

Consider first in more detail the deformation of the free boundary during a time step. Applying formula (6.54) for a point $\mathbf{x}_i^n$ at the boundary Γ_f^n (i.e., the boundary Γ_f at time t_n) with corresponding velocities $\mathbf{v}_i^n$, we see that some of the points $\mathbf{x}_i^{n+1}$ don't belong to the domain as defined by the mould and the plunger. Let us denote the latter by $\Theta_{t_{n+1}}$. This configuration is changed explicitly by moving the plunger at each time iteration. We now simply clip displacement outside this $\Theta_{t_{n+1}}$; see Figure 6.10. So the position of $\mathbf{x}_i^{n+1}$ is defined by the intersection of $\mathbf{x}_i^{n+1} + \text{span}\{\mathbf{v}_i^n\}$ and $\Theta_{t_{n+1}}$

$$\mathbf{x}_i^{n+1} = \mathbf{x}_i^n + \alpha_i \Delta t \mathbf{v}_i^n, \quad \alpha_i \in (0, 1]. \tag{6.55}$$

Here α_i is chosen such that

$$\Omega_{t_{n+1}} \subset \Theta_{t_{n+1}}.$$

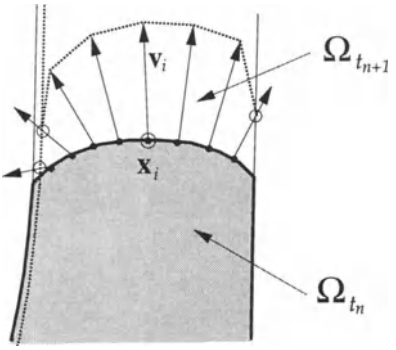

Figure 6.10 — Clip algorithm.

We shall call this the *clip algorithm*. Note that for the local error in (6.55) we have

$$\begin{aligned}\frac{||\mathbf{x}_i(t_{n+1}) - \mathbf{x}_i^{n+1}||}{\Delta t} &= \frac{||\mathbf{x}_i(t_n) + \Delta t\dot{\mathbf{x}}_i(t_n) - \mathbf{x}_i^n - \alpha_i \Delta t \mathbf{v}_i^n||}{\Delta t} + O(\Delta t) \\ &= \frac{||\mathbf{x}_i(t_n) + \Delta t\dot{\mathbf{x}}_i(t_n) - \mathbf{x}_i(t_n) - \alpha_i \Delta t\dot{\mathbf{x}}_i(t_n)||}{\Delta t} + O(\Delta t) \\ &= (1 - \alpha_i)||\dot{\mathbf{x}}_i(t_n)|| + O(\Delta t).\end{aligned}$$

For the velocities that must be clipped ($\alpha_i < 1$) the error is apparently $\mathcal{O}(\infty)$, although their contribution to the global error is still $\mathcal{O}(\langle)$. The actual values of α_i depend on the characteristics of the process, Δt, and the mesh size h. In a practical implementation the term $(1 - \alpha_i)||\dot{\mathbf{x}}_i(t_n)||$ should be of order Δt.

6.7 Mass Conservation

In the previous section we described one step of the actual solution process, i.e., solving Stokes, doing one Euler step, and clipping "nonphysical" values. Clearly the latter procedure leads to the question of whether mass is still conserved. The finite volume of glass (which can be associated with the mass because of incompressibility) is given a priori and equal to Θ_{t_N}, i.e., the volume of the mold-plunger system in its final position, when the final domain is filled with glass. Numerically we may find the mass decreasing or increasing. If this is significant (say more than 1%) the simulation process is useless. For example, in the case of mass decreasing we can see that there is space left in Θ_{t_N} and $\Theta_{t_N} \backslash \Omega_{t_N} \neq \{\emptyset\}$.

To solve this problem we can perform the process with a smaller time step, which requires more computational time to solve the flow equations or increase accuracy of numerical integration by using a scheme of higher order. Increasing mass (Figure 6.11) arises because of Euler explicit, as it is not a conservative scheme. Instead of (6.52) we shall use the following trapezoidal-like algorithm:

$$\begin{aligned}\mathbf{y}_i^0 &= \mathbf{x}_i^0 \\ \mathbf{y}_i^{n+1} &= \mathbf{x}_i^n + \Delta t \mathbf{v}_i^n \\ \mathbf{x}_i^{n+1} &= \mathbf{x}_i^n + \frac{\Delta t}{2}(\mathbf{v}_i^n + \mathbf{v}_i^{n+1})\end{aligned} \tag{6.56}$$

where $\mathbf{v}_i^n$ now is the velocity at $\mathbf{y}_i^n$. The advantage of this explicit predictor–corrector scheme is that the velocity field has to be calculated only once each time step. It is still not conservative but at least of higher

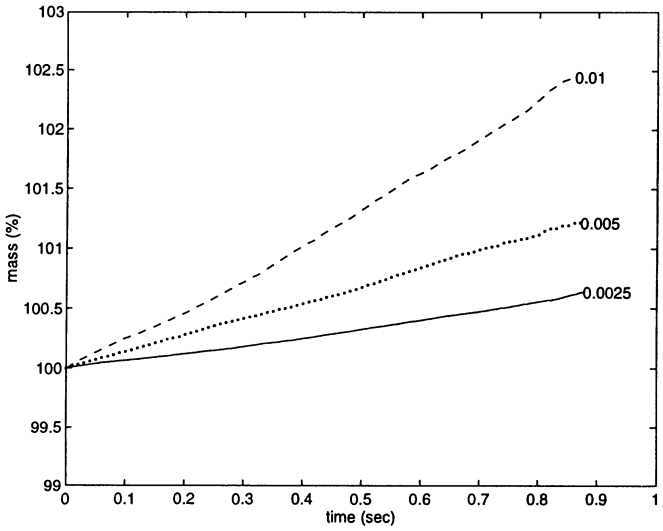

Figure 6.11 — Volume graph using Euler explicit and different time steps.

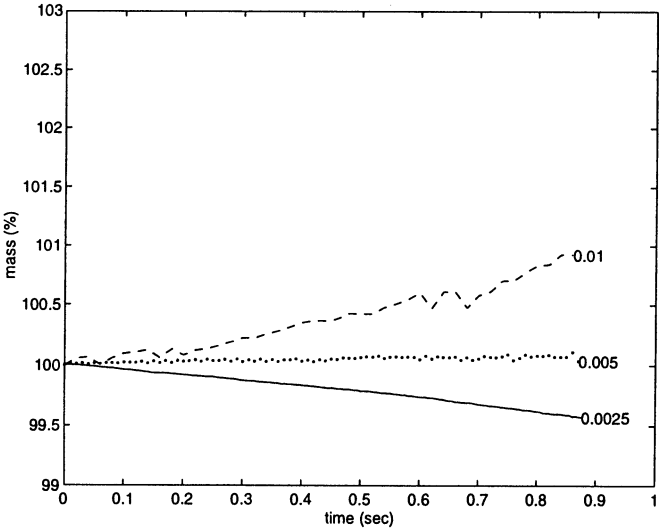

Figure 6.12 — Volume graph for second-order scheme and different time steps.

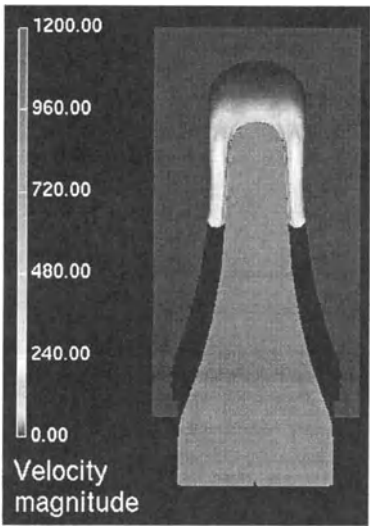

Figure 6.13 — Velocity magnitude.

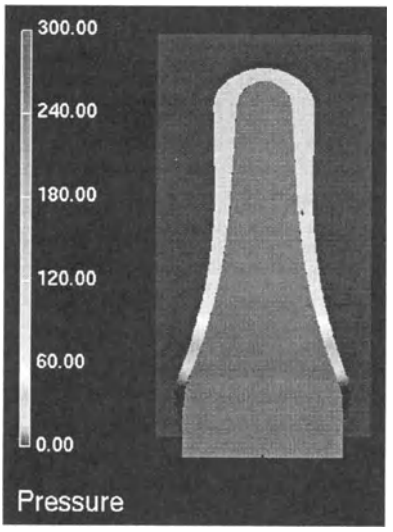

Figure 6.14 — Pressure.

order. With respect to mass conservation, simulation using the combination of the clip algorithm and (6.54) is illustrated by Figure 6.12. The mass still increases for $\Delta t = 0.01$ because the scheme is still explicit. The local error in (6.54) is of second order with respect to Δt, the discretization error in the clip algorithm is of lower order; hence, for a smaller time step ($\Delta t = 0.0025$) we can see that the clip algorithm, which decreases mass by clipping the velocities, dominates. The graph for $\Delta t = 0.005$, which gives almost mass conservation, is a case where Euler explicit and clip algorithm errors more or less cancel.

Using a FEM method to solve the Stokes equations and (6.57) to obtain the changing geometry of Ω_t we can run numerical simulations up to the final stage. The final results are depicted in Figures 6.13 and 6.14.

References

1. Chandra, T.D., and Rienstra, S. W., Analytical approximation to the viscous glass flow problem in the mould-plunger pressing process, *RANA 97-08*, Technical University of Eindhoven (1997).
2. Doyle, P.J., *Glass Making Today*, R.A.N. Publisher, Ohio (1994).
3. Hopper, R.W., Plane Stokes flow driven by capillarity on a free surface, *J. Fluid Mech.*, **213**, (1990), 349–75.
4. Hopper, R.W., Plane Stokes flow driven by capillarity on a free surface, 2: Further developments, *J. Fluid Mech.*, **230**, (1991), 355–64.
5. Hsiao, G.C., Kopp, P., and Wendland, W.L., Some applications of a Galerkin-collocation method for boundary integral equations of the first kind, *Math. Methods in the Appl. Sciences*, **6**, (1984), 280–325.
6. Kuiken, H.K., Mattheij, R.M.M., and van de Vorst, G.A.L., A boundary element solution for 2-dimensional viscous sintering, *J. Comput. Phys.*, **100** (1992), 50–63.
7. Ladyzhenskaya, O.A., *The Mathematical Theory of Viscous Incompressible Flow*, Godon and Beach, New York (1963).
8. Mattheij, R.M.M., van de Vorst, G.A.L., Mathematical modelling and numerical simulation of viscous sintering processes, *Surv. Math. Ind.*, **7** (1998), 255–81.
9. Mulder, C.A.M., van Lierop, J.G., and Frens, G., Densification of SiO_2-xerogels to glass by Ostwald ripening, *J. Noncryst. Solids*, **82** (1986), 92–6.
10. Rawson, H., Properties and applications of glass, *Glass Sci. and Tech.*, **3**, Elsevier (1980).

11. Reed, J.S., *Introduction to the Principles of Ceramic Processing*, Wiley-Interscience, Chichester (1988).
12. Sōmiya, S., and Moriyoshi, Y., Eds., *Sintering Key Papers*, Elsevier Applied Science, London (1990).
13. Stokes, Y.M., Very viscous flows driven by gravity, with particular application to slumping of molten glass, Ph.D. Thesis, University of Adelaide (1998).
14. Uhlmann, D.R., and Kreidl, V.J., eds., *Glass Science and Technology*, Academic Press, London (1986).
15. van de Vorst, G.A.L., Integral method for a two-dimensional Stokes flow with shrinking holes, applied to viscous sintering, *J. Fluid Mech.*, **257** (1993). 667–89.
16. van de Vorst, G.A.L., Modelling and numerical simulation of axisymmetric viscous sintering, Ph.D. Thesis, Eindhoven (1994).

7

Mathematical Problems in the Ziegler–Natta Polymerization Process

DANIELE ANDREUCCI

Università di Roma "La Sapienza"
Dipartimento Metodi e Modelli Matematici
Roma, Italy

AND
RICCARDO RICCI

Università di Milano
Dipartimento di Matematica "F.Enriques"
Milano, Italy

ABSTRACT. Some models describing the Ziegler–Natta polymerization are reviewed, and their mathematical aspects are discussed. A model for the heterogeneous polymerization is developed assuming a continuous approximation of the catalyst site distribution. Some mathematical results about these models are presented.

7.1 Introduction

This chapter is concerned with mathematical models for the industrial process known as Ziegler–Natta polymerization.

Polymerization is the process in which polymer chains are generated as sequences of identical elements, provided by the molecules of a given substance (the monomers). For a large class of polymers the presence of a

A. Fasano (ed.), *Complex Flows in Industrial Processes*

catalyst is required to make it possible for a monomer to join the chain. In Ziegler–Natta-type polymerization the catalyst is a metal (titanium in the form of a titanium halide), and the monomer is gaseous. Much technological ingenuity has been required to develop an efficient and versatile way to manage this process. The article by Cecchin [3] and the book by Moore [10] give a complete historical account of the quest for the best support for Ziegler–Natta polymerization.

The current technology is based on the so-called fourth-generation supported catalyst, which has proved to be the most efficient way to achieve a very good balance between the two most impelling requests made on the process: the conversion factor (i.e., the ratio of weights of produced polymer to catalyst material) and the control of the spatial form of the product (known in the literature as *replica*). However, most of the changes from the first-generation supported catalyst to the fourth-generation one are in the materials used in preparation of the porous support and the catalyst metal, belonging therefore to the domain of the chemical-physical investigations. The general physical structure of the process remains basically the same throughout the different "generations" and can be described as follows.

The catalyst particles are fixed on the surface of a porous matrix formed by a crystallite. The monomer, in the form of a gas, diffuses through this porous pellet to reach the catalyst sites, where polymerization takes place. After a rather short time the small stress generated by the polymer so accumulated is enough to start a fragmentation of the support into a large number of very small particles, which are kept together by the entangled growing chains of polymer. In the next stage of polymer growth, monomer molecules have to reach the catalyst particles diffusing through the growing polymer. This very rough description is the base for the models used in the literature.

Let us quote from the paper by Nagel, Kirillov, and Ray [11]: "Polymerization is heterogenous and proceeds by a coordination mechanism. It is thought that the growing polymer is directly attached to an active titanium atom on the catalyst surface, and propagation occurs by insertion of monomer between the metal atom and the growing chain."

This point needs some clarification. The growing polymer surrounds the catalyst site so that after a small time the catalyst surface is coated by the polymer. At this stage, the porous pellet supporting the process is no longer the original crystallite but is formed by the entangled polymer chains where the catalyst sites are now scattered. The situation presents two natural scales. From an "external" observation, the system looks like a growing porous medium, through which the monomer gas has to diffuse. A closer "internal" observation reveals the structure of closely entangled polymer chains coating the catalyst particles that have been trapped by the polymer during fragmentation. Then a monomer molecule, which can join a chain only if it reaches the catalyst surface, has to "travel" through the polymer coating as well, before becoming available for polymerization.

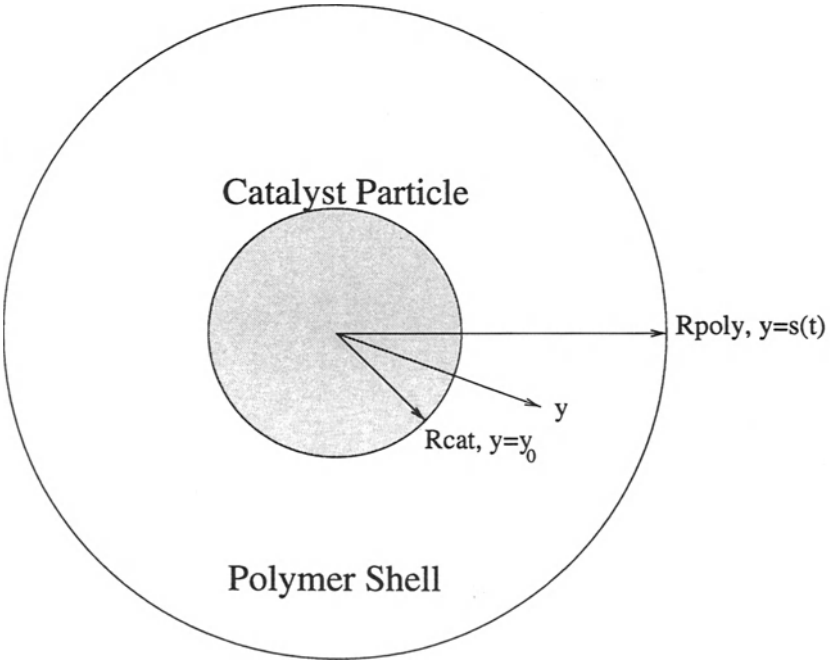

Figure 7.1 — The solid core model.

It is then convenient to separately analyze the neighborhood of a catalyst site and the global process in the whole pellet.

7.2 The Solid Core Model

A well-accepted approach consists in describing the process in the vicinity of a single catalyst particle using the so-called *solid core model* for polymerization Figure 7.1. Let us quote again from [11]: "The solid core model for polyolefin polymerization is simply based on a spherical catalyst particle with a spherical shell of polymer growing around it.... Growth of the polymer shell results directly from the rate at which polymer is produced. The kinetics depend on both the temperature at the surface of the catalyst and the monomer concentration at that point. Particle growth, the kinetics, and mass and heat transfer are all interrelated."

According to this description the newly formed polymer surrounds the catalyst, and the polymer shell has to expand to accommodate the new inner layer. However, this picture poses a number of nontrivial problems when we try to translate it into a coherent mathematical model. The first question is: How does the polymer shell move? Even if we assume a priori

a simple spherically symmetrical geometry, i.e., that the catalyst particle is a sphere and that the polymer shell is a growing sphere at any time, the equations determining the velocity field should include the structural assumptions about the mechanical behavior of the polymer shell itself. Moreover, this velocity field generates a convection term in the monomer diffusion equations through the shell, which is usually not negligible.

None of these considerations are taken into account in the relevant literature on the subject. In [11] the diffusion equation for the monomer gas in the shell, which contains the accumulation term, has no convection, and the whole question of the expansion of the polymer shell is not given specific attention.

A much more clearly stated mathematical problem can be found in [8], which is a standard reference for the so-called *multigrain model.* In that paper, the solid core model is the basic ingredient of what is called the "microproblem" (we will return to this later). Here the rate of expansion of the external radius of the particle formed by the polymer shell is directly related to the amount of momomer reacting at the catalyst surface, giving (equation (22) of [8])

$$3R^2\frac{dR}{dt} = C_1 M(R_c, t) \tag{7.1}$$

where R indicates the external radius of the particle, R_c is the catalyst radius, $M(r,t)$ is the monomer concentration, and $C_1 > 0$ is a conversion constant.

Equation (7.1) says that all the polymerized material (according to a first-order reaction law for polymerization) produces a volume increase of the shell at a constant rate not depending on the mechanical state of the shell itself. This, however, is correct only if the porosity (i.e., the ratio polymer/void) of the coating forming the shell remains constant. This assumption can be reformulated into an equation for the expansion velocity field v_p, namely,

$$\left(\frac{\partial}{\partial y} + \frac{2}{y}\right) v_p = 0. \tag{7.2}$$

The constant porosity assumption seems reasonable if the polymer chains in the shell are free to rearrange with virtually no mechanical effort.

Equation (7.2) is sufficient to determine the expansion velocity field inside the shell only if spherical symmetry of the shell is assumed a priori. In a more general situation where this assumption is not realistic, this single equation is not sufficient to determine the three components of the velocity field, and some specific mechanical assumptions on the behavior of the shell have to be made.

A convection term will be present in the diffusion equation, which takes into account the effect of the velocity field in a Eulerian frame of reference. Summing up these remarks, we can formulate a consistent problem for the solid core model in the hypothesis of spherical symmetry [2].

The model has the form of a "free boundary problem" for the diffusion-convection equation, exhibiting the peculiarity that the free boundary condition, i.e., the differential law for the increase of the external radius of the particle, involves the process occurring at the fixed boundary (the catalyst surface). This means that the free boundary condition is *nonlocal*, i.e., it depends on the complete spatial distribution of the concentration within the shell.

Let us pass to a description of the detailed mathematical setting of the model.

We denote by y the radial coordinate in the polymer shell (we call it *microsphere* in the following).

The catalyst is a small sphere of radius $y_0 > 0$. At time $t > 0$ the polymeric microsphere has radius $s(t) > 0$, i.e., the growing polymer occupies the region between $y = y_0 > 0$ and $y = s(t)$. This region is assumed to be a porous medium where the monomer molecules diffuse to reach the catalyst. Here the polymer is produced, which pushes apart the outer polymeric shell.

We indicate by $m(y,t)$ the monomer concentration in the pores.

The monomer flux inside the microsphere is given by a diffusive term and a convective term due to expansion. As we said earlier, in order to determine the form of the convective term we have to stipulate some assumptions on the mechanical behavior of the microparticle. A simple choice is to assume that the polymerization does not affect the porosity (or the diffusivity) inside the microsphere. Then the convective velocity is divergence-free, i.e., it satisfies (7.2). Equation (7.2) can be easily integrated, giving $v_p(y,t)y^2$ constant with respect to y so that v_p can be determined at any point in terms of its value at the surface of the catalytic particle. In turn, v_p at $y = y_0$ is related to the monomer concentration in the vicinity of the catalyst (mathematically at $y = y_0$) according to a first-order reaction law. In other words, the polymerization rate is proportional to the monomer concentration at the catalyst surface. In this way the rate of increase of the particle radius, $\dot{s}(t) = v_p(s(t),t)$ depends on the monomer concentration at $y = y_0$.

Finally, the monomer concentration at the external boundary $y = s(t)$ is assumed to be known at this modeling level. In a more complete model, the "multigrain" model, which we will discuss later, the value of the monomer concentration at $y = s(t)$ is determined by the "macroscopic" monomer concentration in the porous matrix formed by a large number of microspheres.

Then the resulting mathematical problem we have to study is the following free boundary problem.

FBP

Find $(m(y,t), s(t), \bar{t})$ with $\bar{t} > 0$, $s \in C^1[0,\bar{t}]$, $s(0) = y_0 > 0$, $m \in C^{2,1}(Q_{\bar{t}}) \cap C^{1,0}(\overline{Q}_{\bar{t}})$, $Q_{\bar{t}} = \{(y,t) : y_0 < y < s(t), 0 < t < \bar{t}\}$ such that the following

equations are satisfied:

$$\varepsilon_p \frac{\partial}{\partial t} m + \left(\frac{\partial}{\partial y} + \frac{2}{y} \right) \left(-d \frac{\partial}{\partial y} m \right) + \varepsilon_p \frac{\dot{s} s^2}{y^2} \frac{\partial}{\partial y} m = 0, \quad (y,t) \in Q_{\bar{t}} \tag{7.3}$$

$$d \frac{\partial}{\partial y} m(y_0, t) = \lambda m(y_0, t) \left[\nu + \varepsilon_p m(y_0, t) \right], \quad 0 < t < \bar{t} \tag{7.4}$$

$$m(s(t), t) = M(t), \quad 0 < t < \bar{t} \tag{7.5}$$

$$\dot{s}(t) = \lambda \frac{y_0^2}{s^2(t)} m(y_0, t), \quad 0 < t < \bar{t} \tag{7.6}$$

where $M(t) > 0$ is a given function and $\varepsilon_p, \lambda, \nu$, and d are positive constants (d indicates the diffusivity in the porous medium).

Problem **FBP** has been analyzed in [2], where existence and uniqueness of solution has been proved for $M(t)$ in a suitable class.

The proof is based on a fixed-point argument for a family of approximating problems obtained by solving the diffusion problem (7.3) to (7.5) with a moving boundary $\sigma(t)$, determined by integrating the ordinary differential equation (7.6) with a trial function $f(t)$ replacing $m(y_0, t)$. The resulting value of $m(y_0, t)$ is then taken as the new trial function $\hat{f}(t)$. We find a solution of the problem if $\hat{f}$ coincides with f.

In [2] the map $f \to \hat{f}$ is proved to be a contraction in the norm of $C^0([0, t'])$, for a suitably small time interval $[0, t']$. However it is only defined in a closed subset of the space $C^0([0, t'])$ formed by functions that are uniformly Hölder continuous of class $1/2$ in any time interval $[\tau, t']$, $\tau > 0$. Estimates are given showing that the subspace is mapped into itself and that the map is actually a contraction in the C^0 norm, obtaining uniqueness and existence of the solution.

Notice that each of the approximating problems is also nonstandard because of the vanishing of the spatial domain as t decreases to zero. The solution of this problem is obtained by an extra approximation procedure, solving the diffusion equation in domains of the form $\{y_0 < y < \sigma(t), t_n < t < t'\}$ with $t_n \to 0$, with appropriate initial conditions. The sequence of approximating solutions tends to the solution of our problem by virtue of a compactness argument and noting that uniqueness follows directly from the maximum principle.

A considerable mathematical simplification is obtained assuming a quasi-stationary approximation, i.e., dropping the accumulation term $\varepsilon \frac{\partial}{\partial t} m$ and the convection term $\varepsilon_p \frac{\dot{s} s^2}{y^2} \frac{\partial}{\partial y} m$ from (7.3). This approach is followed in [13]. Equation (7.3) then reduces to the assertion that the diffusive flux $-d \frac{\partial}{\partial y} m$ is divergence-free; then the quantity $y^2 \frac{\partial}{\partial y} m$ is constant

in space, i.e.,

$$y^2 \frac{\partial}{\partial y} m = C_1(t) \tag{7.7}$$

where $C_1(t)$ is an unknown function of time to be calculated from the boundary conditions. Integrating (7.7) once more with respect to y and using (7.4) and (7.5) we can find a close expression for m and $\frac{\partial}{\partial y} m$ in terms of y, the front location $s(t)$, and the boundary value $M(t)$, namely,

$$m(y,t) = M(t) \left[1 - \frac{\frac{1}{y} - \frac{1}{s(t)}}{\frac{d}{\lambda \nu y_0^2} + \left[\frac{1}{y_0} - \frac{1}{s(t)} \right]} \right] \tag{7.8}$$

$$\frac{\partial}{\partial y} m(y,t) = \frac{1}{y^2} \frac{M(t)}{\frac{d}{\lambda \nu y_0^2} + \left[\frac{1}{y_0} - \frac{1}{s(t)} \right]}. \tag{7.9}$$

Finally inserting these expressions into (7.6), we find an ordinary differential equation for $s(t)$ involving only $M(t)$, namely,

$$\left[\frac{s^2}{\lambda y_0^2} + \frac{\nu}{d} \left(\frac{s^2}{y_0} - s \right) \right] \dot{s} = M(t). \tag{7.10}$$

Equation (7.10) can be explicitly solved in terms of rational powers of $\int_0^t M(\tau)\, d\tau$, but its solution is more readable in the implicit form

$$g(s) \equiv \left[\frac{1}{3\lambda y_0^2} + \frac{\nu}{3 d y_0} \right] s^3(t) - \frac{\nu}{2d} s^2(t) = \frac{y_0}{3\lambda} - \frac{\nu y_0^2}{6d} + \int_0^t M(\tau)\, d\tau \tag{7.11}$$

where we used the initial condition $s(0) = y_0$. A qualitative description of the solution is deduced from the inspection of Figure 7.2, observing that y_0 is larger than the value where $g(s)$ attains its minimum and that $s(t)$ is obtained as the abscissa of the only intersection of the cubic $z = g(s)$ with the line $z = \frac{y_0}{3\lambda} - \frac{\nu y_0^2}{6d} + \int_0^t M(\tau)\, d\tau = g(y_0) + I(t)$ at the right of y_0. It follows immediately that $s(t)$ is monotonically increasing, recalling that $M(t) > 0$.

7.3 The Multigrain Model

The solid core model is too simple to account for all the features of the polymerization process. A considerable improvement consists in the so-called "multigrain" model, introduced in [8] and [11] (see also [5], [6], and [9]) and describing the process after fragmentation. The inclusion of fragmentation leads to the introduction of a new free boundary (the fragmentation front) with Stefan-type conditions, whose presence influences the velocity field of

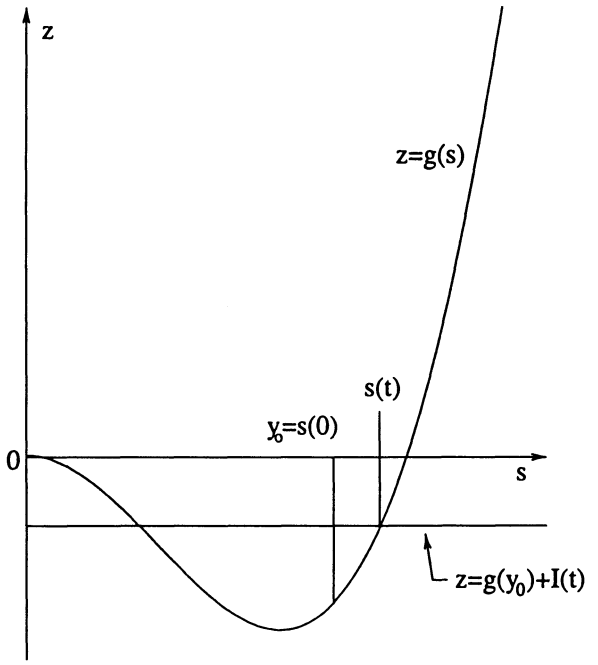

Figure 7.2 — $g(s) = [\frac{1}{3\lambda y_0^2} + \frac{\nu}{3dy_0}]s^3 - \frac{\nu}{2d}s^2$.

the whole system. The initial pellet of crystallite with catalyst metal particles is penetrated by the monomer gas, which starts to build up polymer chains as soon as it reaches the catalyst. When enough polymer has been produced, the stress against the porous matrix breaks the catalyst structure. However, entangled polymer molecules attached to different active sites keep the growing microparticles together in a system that can be reasonably considerd a porous medium.

The catalyst phase is not continuous any longer, but each catalyst microparticle is surrounded by a polymer layer that remains in contact with similar layers. Then the overall pellet can be considered a cluster of such microparticles.

The multigrain model describes the process, from the macroscopic point of view, as a collection of individual processes based on the "solid core" model. The growing layer surrounding the catalyst will be referred to as the "microparticle" and the corresponding mathematical description as the "microproblem."

The pellet itself is a porous aggregate of such microparticles in which the monomer gas diffuses. At this level the mathematical model is based on a diffusion equation (Fick's law) for the monomer gas. We refer to it as the "macroproblem."

The interaction between the macro- and microproblems occurs through various factors.

Postponing the discussion of thermal interactions, a first coupling of the two problems comes from mass exchange: The local gas concentration in the macroproblem provides the outer concentration for the equations of the microproblem; see (7.5), and it is generally assumed that the microparticle is small enough to justify the assumption that the monomer concentration is constant all around its surface. In turn, the influx of monomer gas into microparticles gives the sink term for the diffusion problem in the macroparticle.

A more complex coupling comes from the growth of the particles, inducing the global expansion of the system. Indeed, as we noticed in the previous section, in the solid core model each microparticle grows according to the solution of the free boundary problem we described in the previous section. The buildup of local swelling produces an expansion of the aggregate. Here again the correct description of this phenomenon is complex, and so far not fully investigated.

The expansion model proposed in [8] can be pictorially represented by Figure 7.3. It assumes that the sphere representing the macroparticle is made of layers of microparticles disposed in spherical annuli. Each annulus grows according to the growth law for the microparticle.

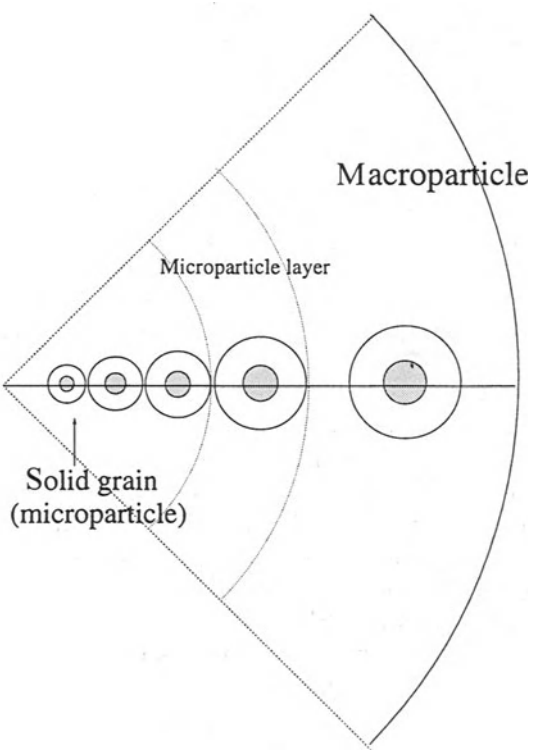

Figure 7.3 — The multigrain model.

Although suggestive, Figure 7.3 can be misleading, if taken literally, because we must allow some local transversal motion (not seen on the average), so that the spheres can rearrange themselves according to some given (ideal) scheme.

This description is widely accepted as a reasonable scheme for a qualitative interpretation of the phenomenon and as a numerical scheme, based on the spherically symmetric "layered" growth of the particles; see [8].

In the chemical literature, it is generally assumed that the expansion of the macroparticle is such that no significant change in the porosity of the macroparticle is present; see [3]. This is (almost) achieved if we suppose that the microparticles rearrange during the expansion according to a packing mode as closed as possible. Although the microparticles at different distances from the center of the aggregate have different radii, we can assume that layers of particles in a thin spherical shell do not deviate much from the ideal packing of equal spheres, so that porosity can be considered constant throughout the agglomerate. (Remember that microparticles have different radii, depending on their expansion history.)

To overcome the geometrical difficulty implicit in the packing problem, a "continuum" approach to the problem has been developed [4] based on the fact that the number of catalyst sites is very large and each microparticle has a small dimension compared to the whole pellet. The catalytic site distribution is then approximated with a continuous distribution characterized by a density function ρ representing the number of sites per unit of volume in the pellet. Because the total number of catalytic sites is preserved, the site density will decrease in time, as a consequence of the swelling of the porous matrix.

The assumption of constant porosity of the pellet is then transformed into an equation for the expansion (velocity) field. However, as we noticed for the microproblem, this is not enough to determine the velocity unless some a priori geometrical assumptions are made on the velocity field itself. Again a possible solution is to assume that the expansion is spherically symmetric.

This gives a coherent mathematical framework, which is described later, under the assumption of spherical symmetry.

Four relevant macroscopic variables are found in the model: the monomer concentration M in the porous channels of the matrix, the site density ρ, the velocity field $\mathbf{v}$ induced by the matrix swelling, and the temperature T (in the preceding discussion we purposely decided not to discuss the role of temperature for the sake of simplicity, although it plays a crucial role in the catalyst process). Other variables are needed when we look at the growth of polymer around each microscopic particle, that is, those introduced in the discussion of the solid core model. However, we now have a continuous family of microproblems parameterized by an appropriate microparticle "label" (i.e., a Lagrangian coordinate).

Let us first clarify the following difficulty. As we said, the macroparticle exchanges matter with the microparticles: The monomer flux entering the microparticles located at a distance r from the center is related to the sink term in the diffusion equation for the monomer concentration M in the pellet; on the other hand, $M(r,t)$ is the boundary condition for the solid core model describing the expansion of the microparticle which, at time t, occupies the position r in the pellet. However, different *microparticles will occupy this position at different times* (of course this is strictly true for the idealized continuum approximation, but it is also true, with an appropriate time delay, in the real situation). This is important when writing the correct form of the sink term, because the quantity of monomer absorbed by the microparticles depends on their history. So we have to label each microparticle (for example) by its initial location, and we have to follow the motion of every microparticle to know which is occupying a given position at a given time.

This is the peculiarity of the model. Moreover, the model, being a double-scale scheme coupling micro- and macroproblems, is better described in a mixed Eulerian–Lagrangian approach.

Temperature is also important in this process. Polymerization is exothermic, and latent heat is released when monomers attach to the polymer chains. Moreover the rate of polymerization is temperature-dependent, and this has to be taken into account in the microproblem equations. An additional, even more dramatic, thermal effect is the possible change from the almost crystalline structure to the rubber phase. If the polymer coating of the catalyst changes its state from crystalline to rubber, the porosity almost vanishes and the catalyst remains impervious to the incoming monomer. As a consequence the site is not active in the polymerization.

It is then necessary to include an equation for the temperature evolution in the pellet according to Fourier's law. Temperature of the microparticle is generally considered to be uniform (it changes only in time) and equal to the temperature in the pellet at the location occupied by the microparticle.

Accordingly, the equation for the temperature has the same mathematical structure as the one determining monomer diffusion in the pellet. However, a source term, rather than a sink, must be introduced to account for the heat released by polymerization.

7.4 The Mathematical Model

Following the arguments in the previous section we can write the mathematical problem for the continuous version of the multigrain model. Let us first write the equations in Eulerian form, i.e., in a frame of reference at rest with respect to the initial location of the catalyst pellet (disregarding

a possible "rigid" motion of the pellet). We denote by M the monomer concentration inside the pores of the macrosphere, by v the expansion field velocity (which we assume to be radial), and by ρ the density of the catalyst particles. Then we have

$$\frac{\partial}{\partial t}\rho + \left(\frac{\partial}{\partial r} + \frac{2}{r}\right)(\rho v) = 0\,, \quad \text{in } \Sigma \tag{7.12}$$

$$\frac{\partial}{\partial t}(\varepsilon M) - \left(\frac{\partial}{\partial r} + \frac{2}{r}\right)\left(D\frac{\partial}{\partial r}M - \varepsilon M v\right) = -\rho Q\,, \quad \text{in } \Sigma \tag{7.13}$$

$$\left(\frac{\partial}{\partial r} + \frac{2}{r}\right) v = \rho\hat{Q}(1-\varepsilon)^{-1}\,, \quad \text{in } \Sigma \tag{7.14}$$

where Σ is the moving domain $\Sigma = \{0 < r < R(t), t > 0\}$. In turn, $R(t)$ must be found by solving the ordinary differential equation

$$\dot{R} = v(R,t). \tag{7.15}$$

Equation (7.12) expresses the conservation of the number of catalytic sites. Equation (7.13) is almost self-explanatory except for the sink term $-\rho Q$, where Q accounts for the decrease of monomer concentration in the pellet, due to the polymerization process in a single microparticle. Equation (7.14) relates the local expansion rate of the pellet (in the radial direction, by assumption) with the growth rate of the microparticles via the quantity $\hat{Q}$, representing the contribution of a single microparticle. A precise definition of Q and $\hat{Q}$ is given in the sequel (see (7.30) and (7.27)).

We must also prescribe initial and boundary data as follows:

$$M(r,0) = M_0(r), \quad 0 < r < R_0 \tag{7.16}$$

$$\frac{\partial}{\partial r}M(0,t) = 0, \quad 0 < t \tag{7.17}$$

$$M(R(t),t) = M_1(t), \quad 0 < t \tag{7.18}$$

$$\rho(r,0) = \rho_0(r), \quad 0 < r < R_0 \tag{7.19}$$

$$R(0) = R_0 > 0. \tag{7.20}$$

The choice $M_0(r) \equiv 0$ and $\rho_0(r) \equiv$ constant is natural in view of the physical meaning of the model. See also (7.26).

We assume that the microparticles are so small that the temperature T can be considered uniform across each of them, so that heat diffusion is relevant only at the macroscopic scale. Then the heat balance equation takes the form

$$c\frac{\partial T}{\partial t} - \left(\frac{\partial}{\partial r} + \frac{2}{r}\right)(k\nabla T - cTv) = \mu\hat{Q}\rho\,, \qquad \text{in } \Sigma \tag{7.21}$$

where the source $\mu\rho\hat{Q}$ accounts for the heat released by polymerization; the latent heat $\mu > 0$ is assumed to be constant. The heat source term is proportional to the local expansion rate of the pellet, because the latter is proportional to the quantity of monomer that polymerizes (per unit time), having chosen a first-order polymerization dynamics in the microproblem (see Section 7.2).

Of course, (7.21) must be complemented with suitable initial and boundary data, e.g.,

$$T(r,0) = T_0(r)\,, \quad 0 < r < R_0 \tag{7.22}$$

$$\frac{\partial}{\partial r}T(0,t) = 0\,, \quad 0 < t \tag{7.23}$$

$$-k\frac{\partial}{\partial r}T(R(t),t) = h(T(R(t),t) - T_1(t))\,, \quad 0 < t \tag{7.24}$$

$h > 0$ is a (constant) heat exchange coefficient.

Problem (7.21) to (7.24) is coupled with the macroscopic gas diffusion problem, and with the microscopic free boundary problem described in Section (7.2), through the term $\rho\hat{Q}$ in (7.21). In the following, we neglect the possible dependence of the coefficients on temperature, which seems to be reasonable, at least in a first stage of the process. For large times, different temperature-driven phenomena, like the possible change of the polymer from crystalline to rubber should be taken into account. We also recall that R is a free boundary to be found as the solution of (7.15) and (7.20).

Finally, we give an explicit form for the quantities $\hat{Q}$ and Q appearing in the equations for v and M. Here is where the Lagrangean–Eulerian coupling comes into play. In fact, the quantities $\hat{Q}$ and Q are related to the growth rate of a microparticle and to the monomer sorption by a microparticle, respectively, but their values depend on which microparticle is actually passing through the point r. Let us indicate from now on by x the initial location of a microparticle (i.e., at the time $t = 0$ of the first exposure of the system to the monomer). This will be the Lagrangian coordinate (label) of our particle, and we refer to this particle as the particle x. Let us also indicate by $\sigma(x,t)$ the position of the particle x at a time $t \geq 0$; of course $\sigma(x,0) = x$ (in the following we shall drop the dependence of σ on x when no ambiguity is possible). Moreover $s(x,t)$ (or simply $s(t)$) indicates the radius of the particle x, y_0 is the radius of the catalyst particle (which we assume to be the same for every microparticle) and v_p the expansion velocity of the microparticle at the catalyst surface, according to the scheme in Section 7.2.

As for the microparticle, a structural assumption on the way the pellet expands is necessary to have a closed set of equations. A reasonable constitutive law for it is that the porosity ε remains unchanged during expansion;

see [3]. Assuming that ε inside the macrosphere stays constant, and that locally we can describe the macroparticle as a closely packed sphere, we get the following relation between the radius $s(x,t)$ of the microsphere and the density of the sites $\rho(\sigma(x,t),t)$

$$1-\varepsilon=\frac{4}{3}\pi\rho(\sigma(x,t),t)s^3(x,t)\,. \tag{7.25}$$

Equation (7.25) determines the evolution of the radius of the microsphere as a function of the local site density. Also note that the radius of the catalytic particle $y_0 > 0$ and the initial density $\rho_0(r) = \rho(r,0)$ must be connected by

$$1-\varepsilon=\frac{4}{3}\pi\rho_0 y_0^3\,. \tag{7.26}$$

Then we can give an expression for the quantity $\hat{Q}$ in terms of the microparticle radius

$$\rho\hat{Q}(\sigma(x,t),t)=\rho 4\pi y_0^2 v_p(y_0,t)=\rho 4\pi s^2\dot{s}=3(1-\varepsilon)\dot{s}/s\,. \tag{7.27}$$

Therefore we replace (7.14) with

$$\left(\frac{\partial}{\partial r}+\frac{2}{r}\right)v=\frac{3\dot{s}}{s}\,,\qquad \text{in } \Sigma \tag{7.28}$$

and we recover (7.25) a posteriori, as a consequence of (7.26),(7.12), and (7.28).

Notice that the expansion velocity $v(r,t)$ of the macroparticle is related to the position $\sigma(x,t)$ of a microparticle by

$$\frac{\partial}{\partial t}\sigma(x,t)=v(\sigma(x,t),t) \tag{7.29}$$

so that (7.28) can be used to construct a closed expression for σ, which is given later.

The sink term $-\rho Q$ in the diffusion equation for the monomer in the macrosphere equals the flux of monomer entering the microspheres, i.e., Q is given by

$$Q(\sigma(x,t),t)=4\pi s^2(x,t))d\frac{\partial m}{\partial y}(s(x,t),t;x) \tag{7.30}$$

which has to be substituted into (7.13). In (7.30) we indicate by $m(y,t;x)$ the concentration in the pores of the microparticle x.

Finally it remains to relate the value of the concentration $M(r,t)$ of the monomer gas diffusing in the pellet with the microparticle surface concentration $m(s(x,t),t)$. We simply assume that

$$m(s(x,t),t)=M(\sigma(x,t),t). \tag{7.31}$$

The preceding equations, coupled with the family, parameterized by x, of equations (7.6) to (7.13) are the complete mathematical model describing the continuous multigrain model.

We can simplify the set of equations by expressing σ in terms of the function $s(x,t)$. According to equation (7.29), σ can be found as the solution of the integral equation

$$\sigma(x,t) = x + \int_0^t v(\sigma(x,\tau),\tau)\,\mathrm{d}\tau\,. \tag{7.32}$$

The function σ can be explicitly calculated by means of the following argument; let $\xi(\cdot,t)$ be the inverse function of $\sigma(\cdot,t)$ at a given $t>0$. Then

$$v(r,t) = \sigma_t(\xi(r,t),t)\,. \tag{7.33}$$

Thus, using (7.28),

$$\frac{3\dot{s}}{s} = \frac{\partial}{\partial r}\big(\sigma_t(\xi,t)\big) + \frac{2}{r}\sigma_t(\xi,t) = \frac{\sigma_{xt}(\xi,t)}{\sigma_x(\xi,t)} + \frac{2\sigma_t(\xi,t)}{\sigma(\xi,t)} \tag{7.34}$$

where $\xi = \xi(r,t)$. Passing to the variable x,

$$\frac{3\dot{s}(x,t)}{s(x,t)} = \frac{\sigma_{xt}(x,t)}{\sigma_x(x,t)} + \frac{2\sigma_t(x,t)}{\sigma(x,t)}\,. \tag{7.35}$$

Let us remark that, in fact, $\dot{s}(x,t)$ is the partial derivative with respect to t of the function $(x,t)\mapsto s(x,t)$; we keep this notation for reasons of consistency with the previous part of the paper. Integrating this equality with respect to t, after trivial calculations we get

$$\sigma^2(x,t)\sigma_x(x,t) = \Lambda(x)s^3(x,t) \tag{7.36}$$

for a function Λ to be determined. But, at time $t=0$, $\sigma(x,0)\equiv x$ and $s^3(x,0)\equiv y_0^3$. Then

$$\Lambda(x) = \frac{x^2}{y_0^3}\,. \tag{7.37}$$

Substituting in (7.36) and integrating with respect to x, we find, using the initial condition $\sigma(0,t)=0$ for all $t>0$,

$$\sigma(x,t) = \left[3\int_0^x z^2\frac{s^3(z,t)}{y_0^3}\,\mathrm{d}z\right]^{1/3}. \tag{7.38}$$

By differentiating with respect to t, (7.38) and substituting r for $\sigma(x,t)$ we get

$$v(r,t) = \frac{3}{r^2}\int_0^{\xi(r,t)} \frac{z^2 s^2(z,t)\dot{s}(z,t)}{y_0^3}\,\mathrm{d}z\,. \tag{7.39}$$

These expressions allow us to restate the problem in a more compact way. Indicating by $L_M[v]$ and $L_T[v]$ the linear parabolic differential operator on the left-hand side of (7.13) and (7.21), respectively (here we have stressed their dependence on the velocity v; in fact the operators are linear once v is given: In our problem v actually depends on the solution of the equation (7.41), so this is not a linear equation), the problem can be summarized as follows.

Problem 7.1. Find four real valued functions M, T, m, and s with $M(r,t)$ and $T(r,t)$ defined in $\{(r,t) \mid r \in [0, R(t)]], t \geq 0\}$, and $s(x,t)$ defined in $\{(x,t) \in [0, R_0] \times \{t \geq 0\}\}$ and $m(y,t;x)$ in $\{(y,t;x) \mid y \in [y_0, s(x,t)], t \geq 0, x \in [0, R_0]\}$ solving, respectively,

$$L_M[v]M = -\frac{3(1-\varepsilon)}{s(\xi(r,t),t)} d \frac{\partial}{\partial y} m(s(\xi(r,t),t),t;\xi(r,t)) \tag{7.40}$$

$$L_T[v]T = \frac{3(1-\varepsilon)\dot{s}(\xi(r,t),t)}{s(\xi(r,t),t)} \tag{7.41}$$

and FBP of Section 7.2 for each $x \in [0, R_0]$, with boundary condition (7.31), where $R(t) = \sigma(R_0, t)$, σ is given by (7.38), $\xi(r,t)$ is the inverse function of σ, and $v(r,t)$ is defined by (7.39).

In order to complete the mathematical formulation of the problem, we have also to specify what kind of solution we are looking for, i.e., what regularity we require for the solutions of Problem 7.1. There are many difficulties related to the unusual coupling of parabolic partial differential equations with the same time variable but different space domains. A similar two-scale problem is found in a model for polymer crystallization [12], where the macroscale was related to heat conduction and the microscale was one of the aggregation dynamics of chain segment clusters, described by a Fokker–Planck-type equation in a suitable parameter space; see [14]. In [12] existence of solution in the classical sense (i.e., the $C^{2+\alpha,1+\alpha/2}$ theory of parabolic partial differential equations) was proved.

Here again it seems that the problem has to be dealt with in the classical framework. In fact the **FBP** has no weak formulation, as far as we know. This implies that the boundary value on the free boundary has to be a suitably regular function of time ($C^{1+\beta}$ regularity is required in [2]). The latter is, in turn, the solution of the diffusion problem in the macroparticle, i.e., the concentration $M(r,t)$, so we must look for a classical solution of equation (7.40) as well ((7.41) does not pose additional regularity problems if we neglect the possible dependence on temperature of the coefficients, as we did earlier). Thus we need smooth coefficients in equation (7.40), according to the classical theory of parabolic partial differential equations see [9]. Such a remark is indeed quite critical. The convection coefficient, as well as the free term in (7.12), depend on the solution of free boundary

problem. In particular, any estimate of the Hölder regularity with respect to the radial variable r of those terms involves a delicate study of the dependence of the solution of free boundary problem on the boundary data (remember that in fact free boundary problem is now a family of free boundary problems parameterized, essentially, by the spatial variable r).

7.5 Some Mathematical Results

A considerable simplification of the mathematical problem stated in the previous section can be obtained if we assume the validity of the quasi-steady approximation for the diffusion problem in the microparticle. In this case, all the relevant quantities from the microproblem entering the coupling term in equations (7.40) and (7.41) can be expressed in terms of the monomer gas concentration in the pellet, $M(r,t)$. A different approximation has been considered in [1].

In fact, as we observed in Section 7.2, $s(x,t)$ is now the solution of an ordinary differential equation in which the monomer concentration M is the free term. Things are a little more complex now because the value of M entering (7.10) is calculated at the actual location of the microparticle. So the precise form of the equation for $s(x,t)$ is

$$\left[\frac{s^2}{\lambda y_0^2}+\frac{\nu}{d}\left(\frac{s^2}{y_0}-s\right)\right]\dot{s}=M(\sigma(x,t),t)\,,\quad s(x,0)=y_0 \tag{7.42}$$

with $\sigma(x,t)$ defined by (7.38), so that, even if we regard M as a given function, (7.42) is actually an integral–differential equation for $s(x,t)$.

We can also substitute $\frac{\partial}{\partial y}m(s(x,t),t)$ into (7.40) using equation (7.9). In this way we obtain a new problem where any reference to the concentration m in the microspheres has disappeared.

Problem for Quasi-Steady System (PQS)

Find three real valued functions M, T, and s with $M(r,t)$ and $T(r,t)$ defined in $\{(r,t)\mid r\in[0,R(t)]],t\geq 0\}$, and $s(x,t)$ defined in $\{(x,t)\in[0,R_0]\times\{t\geq 0\}\}$ solving, respectively,

$$\begin{aligned}\varepsilon\frac{\partial}{\partial t}M-D\left(\frac{\partial}{\partial r}+\frac{2}{r}\right)\left(\frac{\partial}{\partial r}M\right)+\varepsilon v\frac{\partial}{\partial r}M=-\varepsilon\frac{3\dot{s}(\xi(r,t),t)}{s(\xi(r,t),t)}M\\ -\frac{3d(1-\varepsilon)y_0}{s^2(\xi(r,t),t)}\frac{M}{\left[1+\frac{d}{\lambda\nu y_0}\right]s(\xi(r,t),t)-y_0}\end{aligned} \tag{7.43}$$

$$c\frac{\partial}{\partial t}T-k\left(\frac{\partial}{\partial r}+\frac{2}{r}\right)\left(\frac{\partial}{\partial r}T\right)+cv\frac{\partial}{\partial r}T=\frac{3(1-\varepsilon-c)\dot{s}(\xi(r,t),t)}{s(\xi(r,t),t)} \tag{7.44}$$

together with boundary and initial conditions (7.16) to (7.18), and (7.22) to (7.24), and equation (7.42) for each $x \in [0, R_0]$, where $R(t) = \sigma(R_0, t)$, σ is given by (7.38), $\xi(r,t)$ is the inverse function of σ and $v(r,t)$ is defined by (7.39).

The rest of this chapter is devoted to the proof of the existence and uniqueness of a solution of problem PQS (see also [1] for a similar approach). We proceed as follows: First we solve the problem for a modified version of equations (7.43) and (7.44), with initial and boundary data in the domain $\{(r,t) \mid r \in [0, R(t)]], t \geq 0\}$, for a given function $s(x,t)$ (and the associated σ and ξ). Then we construct a new function S solving the ordinary differential equation (7.42) with M provided by the previously solved diffusion problem (and the function σ defined using the "old" s, in such a way that (7.42) is a genuine ordinary differential equation). The solution of **PQS** will result from the proof that the mapping $s \to S$ has a unique fixed point. For the sake of simplicity we neglect the temperature equation in the following. Solving the problem with the inclusion of temperature does not introduce any additional mathematical difficulty if the coefficients in the problem are not temperature-dependent, because in this case the temperature equation can be solved a posteriori once the function $s(x,t)$ has been determined.

7.5.1 Auxiliary Problem

Let $s(x,t)$ be a given function in the space

$$\mathcal{X} = \{s \in \mathrm{Lip}([0, R_0] \times [0, t^*]) \mid s(x,0) = y_0, 0 \leq \dot{s} \leq \lambda, \|s_x(\cdot, t)\|_\infty \leq H\} \tag{7.45}$$

and define $\sigma_s(x,t)$ according to (7.38), $R_s(t) = \sigma(R_0, t)$, and $\xi_s(r,t)$ the inverse function of σ_s with respect to x. The auxiliary problem consists in solving the following modification of (7.43)

$$\varepsilon \frac{\partial}{\partial t} M - D\left(\frac{\partial}{\partial r} + \frac{2}{r}\right)\left(\frac{\partial}{\partial r} M\right) + \varepsilon v_s \frac{\partial}{\partial r} M = -G_a[s]M - G_b[s]M^2 \tag{7.46}$$

in $\Sigma_{s,t^*} = \{0 < r < R_s(t), 0 < t < t^*\}$ with the initial and boundary conditions (7.16) to (7.18), where the function s is to be understood as calculated at the point $(\xi_s(r,t), t)$ and with σ, R, and ξ substituted by $\sigma_s(x,t)$, R_s, and ξ_s. Here v_s is given by

$$v_s(r,t) = \frac{3}{r^2} \int_0^{\xi(r,t)} \frac{z^2 s^2(z,t) M(\sigma(z,t),t)}{y_0^3 f(\sigma(z,t))} \, \mathrm{d}z \tag{7.47}$$

where

$$f(z) = \left[\frac{z^2}{\lambda y_0^2} + \frac{\nu}{d}\left(\frac{z^2}{y_0} - z\right)\right] \qquad z \geq y_0 \,.$$

Finally, we denote

$$G_a[s] = \frac{3d(1-\varepsilon)y_0}{s^2} \frac{1}{\left[1 + \frac{d}{\lambda \nu y_0}\right] s - y_0} \tag{7.48}$$

and

$$G_b[s] = \varepsilon \frac{3}{s\left[\frac{s^2}{\lambda y_0^2} + \frac{\nu}{d}\left(\frac{s^2}{y_0} - s\right)\right]}. \tag{7.49}$$

Note that both $G_a[s]$ and $G_b[s]$ are positive functions once s is chosen in the space $\mathcal{X}$. Moreover, we have

$$\frac{1}{\lambda} \leq f(s(x,t)) \leq \left[\frac{1}{\lambda y_0^2} + \frac{\nu}{d y_0}\right](y_0 + \lambda t)^2 \tag{7.50}$$

for any $s \in \mathcal{X}$.

The auxiliary problem so defined can be solved using standard results on the linear parabolic equation from [7]. In fact, the equation is nonlinear because of the functional coupling due to the definition of v_s, and of the quadratic term M^2. The sign of the latter, however, allows us to use the maximum principle for positive solutions, so that the equation can be easily solved by a fixed-point argument. Because of our assumption on the function s, all the coefficients in the operator are Hölder-continuous functions, so we can apply the results about linear parabolic equations with smooth coefficients in Chapter IV of [7]. Those results are stated for cylindrical domains, while our domain Σ_{s,t^*} is not a cylinder; however, a standard rectangularization procedure can be used (i.e., a change of variable from r to $r/R_s(t)$), without any regularity reduction of the coefficients of the resulting parabolic equation (the most delicate coefficient appearing in the transformed equation is $\dot{R}_s/R_s^2 = v_s(\sigma(R_0,t),t))/(\sigma(R_0,t),t))^2$).

It follows that the resulting solution $M_s(r,t)$ belongs to $C^{2+\alpha,1+\alpha/2}(\overline{\Sigma}_{s,t^*})$ for any $\alpha \in (0,1)$, and its norm is controlled by a constant depending only on α, the initial and boundary data, and the $C^{\alpha,\alpha/2}$ norms of the coefficients of the equation, which in turn are controlled by the corresponding norm of s. In particular it follows that $M_s(\sigma_s(x,t),t)$ has the same regularity as the function σ_s and that

$$|M_r(r,t)| \leq \overline{M} \tag{7.51}$$

where $\overline{M}$ is a constant depending only on the space $\mathcal{X}$ and on the initial and boundary data.

Moreover, a direct application of the maximum principle gives

$$0 \leq M_s(r,t) \leq 1 \tag{7.52}$$

throughout the domain Σ_{s,t^*}.

Now we define $S(x,t)$ to be the solution of the ordinary differential equation

$$\left[\frac{S^2}{\lambda y_0^2} + \frac{\nu}{d}\left(\frac{S^2}{y_0} - S\right)\right]\dot{S} = M_s(\sigma_s(x,t),t) \tag{7.53}$$

with initial condition $S(x,0) = y_0$ for any x.

As we observed in Section 7.2, (7.53) can be explicitly solved in terms of an algebraic function of the time integral $I_s(x,t) = \int_0^t M_s(\sigma_s(x,\tau),\tau)\,\mathrm{d}\tau$ involving only quadratic and cubic roots. Let us call this function $Q(I)$. Then $S(x,t) = Q(I_s(x,t))$ would be, at least, as regular as the free term, unless some of the quantities under a root in the expression of Q vanish for some (x,t). An investigation of the regularity of S based on its explicit expression would be rather tedious because of the complicated form of Q. But we can easily show that S is a regular function directly from the differential equation.

In fact, because $S(x,0) = y_0$, we have $\left[\frac{S^2}{\lambda y_0^2} + \frac{\nu}{d}\left(\frac{S^2}{y_0} - S\right)\right](x,0) = \frac{1}{\lambda} > 0$; then (7.52) implies that S is a monotone increasing continuous function. Consequently, its time derivative $\dot{S}$ is bounded from above by λ.

To estimate the space derivative S_x, we can differentiate (7.53) with respect to x. It turns out that $S_x(x,t)$ is the solution of a linear ordinary differential equation (still parameterized by x)

$$\dot{S}_x + \alpha(x,t)S_x = \beta(x,t) \tag{7.54}$$

where

$$\alpha(x,t) = \frac{\dot{S}(x,t)(2aS(x,t) - b)}{aS^2(x,t) - bS(x,t)} \tag{7.55}$$

$$\beta(x,t) = \frac{\frac{\partial}{\partial\tau}M_s(\sigma_s(x,t),t)\frac{\partial}{\partial x}\sigma_s(x,t)}{aS(x,t)^2 - bS(x,t)} \tag{7.56}$$

and $a = \frac{1}{\lambda y_0^2} + \frac{\nu}{dy_0}$, $b = \frac{\nu}{d}$. Moreover we have the initial condition $S_x(x,0) = 0$, because $S(x,0) \equiv y_0$, so that

$$S_x(x,t) = \int_0^t \beta(x,\tau)\exp\left(-\int_0^\tau \alpha(x,\theta)\,\mathrm{d}\theta\right)\mathrm{d}\tau. \tag{7.57}$$

Now we observe that $\alpha(x,t) \geq 0$. Moreover, from (7.38) and the definition of the space $\mathcal{X}$, it follows that $0 \leq \frac{\partial}{\partial x}\sigma(x,t) \leq 1 + \frac{\lambda^3}{y_0^3}t^3$, which, together with (7.51), gives $|\beta(x,t)| \leq \frac{1}{\lambda}\overline{M}(1 + \frac{\lambda^3}{y_0^3}t^3)$. Inserting this estimate into (7.57) we obtain

$$|S_x(x,t)| \leq \frac{1}{\lambda}\overline{M}\left(t + \frac{\lambda^3}{4y_0^3}t^4\right). \tag{7.58}$$

This implies that the operator $s \to S$ maps the space $\mathcal{X}$ into itself if the time t^* is sufficiently small.

7.5.2 Existence and Uniqueness for Short Time

We now want to show that the map $s \to S$ has a unique fixed point. Because the space $\mathcal{X}$ is a closed subspace of the space of continuous function $C^0([0, R_0] \times [0, t^*])$ it is enough to prove that the map is a contraction in the sup norm.

Let s_1 and s_2 be two given functions in $\mathcal{X}$. We denote by $\hat{S} = S_1 - S_2$ the difference between the two solutions of (7.53) corresponding to s_1 and s_2, respectively (and of course containing the corresponding solutions M_1 and M_2 of problem (7.46)). Let us also indicate by

$$f_i = f(S_i) = \left[\frac{S_i^2}{\lambda y_0^2} + \frac{\nu}{d}\left(\frac{S_i^2}{y_0} - S_i\right)\right], \quad i = 1, 2.$$

Then $\dot{\hat{S}}$ is given by

$$\dot{\hat{S}} = \frac{(f_1 - f_2)M_1 + f_2(M_1 - M_2)}{f_1 f_2} \tag{7.59}$$

yielding

$$\left|\dot{\hat{S}}\right| \leq \lambda^2(|f_1 - f_2| + C(1+t)^2|M_1 - M_2|) \tag{7.60}$$

where C is an appropriate constant.

The difference $|f_1 - f_2|$ is easily dominated by

$$|f_1 - f_2| < C(1+t)|S_1 - S_2| \leq C(t + t^2) \sup \left|\dot{\hat{S}}\right| . \tag{7.61}$$

A more delicate estimate is needed to dominate the term $|M_1 - M_2|$ because the two functions M_i are calculated at two different points, namely, $M_1(\sigma_1(x,t),t)$ and $M_2(\sigma_2(x,t),t)$, where again $\sigma_i = \sigma_{s_i}$. Define $j = j(t)$ such that $\sigma_{j(t)}(R_0, t) = \max_{i=1,2} \sigma_i(R_0, t)$, $k = k(t)$ such that $\sigma_{k(t)}(R_0, t) = \min_{i=1,2} \sigma_i(R_0, t)$, and $\Sigma_{j,t} = \Sigma_{s_1,t} \cup \Sigma_{s_2,t}$, $\Sigma_{k,t} = \Sigma_{s_1,t} \cap \Sigma_{s_2,t}$.

Let us start from the case in which one of the points $\sigma_i(x,t)$ belongs to $\Sigma_{j,t} \setminus \Sigma_{k,t}$. Without loss of generality, assume that (x,t) is such that $\sigma_2(x,t) > R_1(t) = \sigma_1(R_0,t) > \sigma_1(x,t)$. In this case we write the difference

$$\begin{aligned} M_2(\sigma_2(x,t),t) - M_1(\sigma_1(x,t),t) &= M_2(\sigma_2(x,t),t) - M_R(t) \\ &\quad - M_1(\sigma_1(x,t),t) + M_R(t) \end{aligned}$$

and use the fact that $M_R(t) = M_2(\sigma_2(R_0,t),t) = M_1(\sigma_1(R_0,t),t)$. Then

$$\begin{aligned} |M_2(\sigma_2(x,t),t) - M_R(t)| &\leq \overline{M}\,(\sigma_2(R_0,t) - \sigma_2(x,t)) \\ &\leq \overline{M}\,(\sigma_2(R_0,t) - \sigma_1(R_0,t)) \end{aligned}$$

and

$$|M_R(t) - M_1(\sigma_1(x,t),t)| \le \overline{M}\,(\sigma_1(R_0,t) - \sigma_1(x,t)) \le \overline{M}\,(\sigma_2(x,t) - \sigma_1(x,t))\,.$$

We can estimate the L^∞ norm of the difference $\sigma_1 - \sigma_2$ using the finite increment formula for the function $[\cdot]^{1/3}$ in (7.38)

$$|\sigma_1(x,t) - \sigma_2(x,t)| \le \frac{1}{(\overline{z}(x,t))^2}\int_0^x \frac{z^2}{y_0^3}|s_1^3(z,t) - s_2^3(z,t)|dz \le \frac{R_0(y_0+\lambda t)^2}{y_0^3}\|s_1 - s_2\|_{\infty,t} \tag{7.62}$$

where $\overline{z}(t) > x$ is an appropriate value between $\sigma_1(x,t)$ and $\sigma_2(x,t)$.

In order to estimate the term $\|M_1 - M_2\|_{\infty,\Sigma_{k,t}}$ we need to bound $|M_1 - M_2|$ on the curve $r = \sigma_{k(t)}(t)$. Clearly one of the M_i equals $M_R(t)$ on $r = \sigma_{k(t)}(t)$. The other function can be bounded in terms of its Lipschitz norm and of (7.62), giving

$$|M_1(\sigma_{k(t)}(t),t) - M_2(\sigma_{k(t)}(t),t)| \le C\|s_1 - s_2\|_{\infty,t}\,. \tag{7.63}$$

Now we can write the equation for the difference $u = M_1 - M_2$ in the domain $\Sigma_{k,t}$

$$\varepsilon\frac{\partial}{\partial t}u - D\left(\frac{\partial}{\partial r} + \frac{2}{r}\right)\left(\frac{\partial}{\partial r}u\right) + \varepsilon v_1\frac{\partial}{\partial r}u + G_a[s_1]u + G_b[s_1](M_1+M_2)u = -\varepsilon M_{2r}(v_1 - v_2) - M_2(G_a[s_1] - G_a[s_2]) - M_2^2(G_b[s_1] - G_b[s_2])\,. \tag{7.64}$$

The differences $(G_a[s_1] - G_a[s_2])$ and $(G_b[s_1] - G_b[s_2])$ can be expanded in terms of $\sigma_1 - \sigma_2$ because the functions G_a and G_b are both Lipschitz continuous in s. The only delicate point is that $G_a[s_1]$ and $G_a[s_2]$ (and $G_b[s_1]$ and $G_b[s_2]$) are calculated at the points $\xi_1(r,t)$ and $\xi_2(r,t)$, respectively. This problem is removed observing that, for any $C > 1$,

$$C^{-2/3} \le \sigma_x(x,t) \le C \;\text{ so that }\; C^{-1} \le \xi_r(r,t) \le C^{2/3} \tag{7.65}$$

at least if $t \le (C^{1/3} - 1)y_0/\lambda$, implying $s^3(x,t)/y_0^3 \le C^3$. Indeed, we only have to use $x \le \sigma(x,t)$, and $y_0 \le s(x,t) \le y_0 + \lambda t$ in

$$\frac{x^2}{\sigma^2(x,t)} \le \sigma_x(x,t) = \frac{x^2 s^3(x,t)}{\sigma^2(x,t)y_0^3} \le \frac{s^3(x,t)}{y_0^3}\,. \tag{7.66}$$

Because ξ_i is the inverse function of σ_i (for any fixed t), from (7.62) and (7.65) it follows that (in the common r domain)

$$|\xi_1(r,t) - \xi_2(r,t)| \le C^{2/3}\frac{R_0(y_0+\lambda t)^2}{y_0^3}\|s_1 - s_2\|_{\infty,t}\,. \tag{7.67}$$

Finally we estimate $v_1 - v_2$

$$
\begin{aligned}
&|v_1(r,t) - v_2(r,t)| \\
&\quad \leq \frac{1}{r^2} \int_0^{\xi_1(r,t)} \frac{z^2}{y_0^3} \left| \frac{s_1^2(z,t) M_1(\sigma_1(z,t),t)}{f(\sigma_1(z,t))} - \frac{s_2^2(z,t) M_2(\sigma_2(z,t),t)}{f(\sigma_2(z,t))} \right| dz \\
&\qquad + \frac{1}{r^2} \int_{\xi_1(r,t)}^{\xi_2(r,t)} \frac{z^2}{y_0^3} \frac{s_2^2(z,t) M_2(\sigma_2(z,t),t)}{f(\sigma_2(z,t))} dz
\end{aligned} \tag{7.68}
$$

assuming, without loss of generality, that $\xi_1(r,t) \leq \xi_2(r,t)$. Again the second term of the sum in (7.68) is easily bounded by a function that depends only on time (and is bounded as $t \to 0$) times the difference $\xi_1 - \xi_2$, while the first term, splitting the product $s_i^2 M_i / f_i$, is dominated by two terms bounded by $\|s_1 - s_2\|$ and a final term dominated by $|M_1 - M_2|$. Then, recalling (7.67), we have

$$
|v_1(r,t) - v_2(r,t)| \leq \bar{C} \left\{ \|s_1 - s_2\|_{\infty,t} + \|u\|_{\infty,t} \right\}. \tag{7.69}
$$

Finally we can use the maximum principle in (7.64) and get

$$
\|M_1 - M_2\|_{\infty,\Sigma_{k,t}} \leq C(t) \|s_1 - s_2\|_{\infty,t} \tag{7.70}
$$

where again $C(t)$ stays bounded as $t \to 0$.

We can now go back to (7.60) and get

$$
\|S_1 - S_2\|_{\infty,t} \leq C(t) t \|s_1 - s_2\|_{\infty,t} \tag{7.71}
$$

from which the contractive character of the map follows for a sufficiently small t^* in the definition of $\mathcal{X}$.

Acknowledgment

This work is partially supported by Progetto Strategico CNR Metodi Matematici in Fluidodinamica e Dinamica Molecolare.

References

1. Andreucci, D., Fasano, A., and Ricci, R., Existence of solutions for a continuous multigrain model for polymerization, to appear on M^3AS.
2. Andreucci, D., Fasano, A., and Ricci, R., On the growth of a polymer layer around a catalytic particle: A free boundary problem, *NoDEA*, 4 (1997), 511–20.

3. Cecchin, G., Reactor granule technology: The science of stuctural versatility, *Polypropylene, Past, Present and Future*, Conference, Ferrara Montell Polyolefins, Centro Ricerche "G. Natta," (1998).
4. Fasano, A., Andreucci, D., and Ricci, R., Modello matematico di replica nel caso limite di distribuzione continua di centri attivi, *Meccanismi di accrescimento di poliolefine su catalizzatori Ziegler-Natta*, Simposio Montell 96, edited by S. Mazzullo and G. Cecchin, Montell Polyolefins, Centro Ricerche "G. Natta" (1997), 155–74 .
5. Floyd, S., Choi, K.Y., Taylor, T.W., and Ray, W.H., Polymerization of olefins through heterogeneous catalyst. III. Polymer particle modelling with an analysis of interparticle heat and mass tranfer effects, *J. Appl. Polym. Sci.*, **32** (1986), 2935–60.
6. Hutchinson, R.A., Chen, C.M., and Ray, W.H., Polymerization of olefins through heterogeneous catalyst. X. Modeling of particle growth and morphology, *J. Appl. Polym. Sci.*, **44** (1992), 1389–414.
7. Ladyzenskaja, O.A., Solonnikov, V.A., and Ural'ceva, N.N., Linear and quasi–linear equations of parabolic type, *Translations of Mathematical Monographs*, **23**, Providence RI, American Mathematical Society (1968).
8. Laurence, R.L., and Chiovetta, M.G., Heat and mass transfer during olefin polymerization from the gas phase, Polymer Reaction Engng, edited by K.H. Reichert and W. Geiseler, Hanser, Munich (1983), 73–112.
9. Mei, G., Modello polimerico multigrain e double grain, *Meccanismi di accrescimento di poliolefine su catalizzatori Ziegler-Natta*, Simposio Montell 96, edited by S. Mazzullo and G. Cecchin, Montell Polyolefins, Centro Ricerche "G. Natta" (1997), 135–53.
10. Moore, E. P., Jr., *The Rebirth of Polypropylene: Supported Catalysts* Hanser Pub., Munich (1998).
11. Nagel, E.J., Kirillov, V.A., and Ray, W.H., Prediction of molecular weight distribution for high-density polyolefins, *Ind. Eng. Prod. Res. Dev.*, **19** (1980), 372–9.
12. Ricci, R., Andreucci, D., Fasano, A., Gianni, R., and Primicerio, M., Diffusion driven crystallization in polymers, free boundary problems: Theory and applications, *Res. Notes in Math.*, **363**, edited by M. Niezgodka and P. Strzelecki, Longman (1996), 359–67.
13. Schmeal, W.R., and Street, J.R., Polymerization in expanding catalyst particles, *AIChE J.*, **17** (1971), 1188–97.
14. Ziabicki, A., Generalized theory of nucleation kinetic, I, II., *J. Chem. Phys.*, **48**, (1968), 4368–80.

Part III

Nonlinear Flows in Porous Media

8

The Espresso Coffee Problem

ANTONIO FASANO AND F. TALAMUCCI

Università di Firenze
Dipartimento di Matematica "U. Dini"
Firenze, Italy

AND
M. PETRACCO

illycaffè s.p.a
Trieste, Italy

ABSTRACT. We review the results of a long research project on the espresso coffee brewing process, carried out jointly by the industrial mathematics research group at the Department of Mathematics "U. Dini" of the University of Florence and the Italian company illycaffè s. p. a. (Trieste).

We describe the main experimental steps of the research and present the mathematical models developed in order to interpret the data correctly. The models are of increasing complexity, the first being confined to the mechanical phenomena (experiments performed with cold water), while the most comprehensive includes the influence of dissolution. Particular emphasis is put on the fact that the process deviates significantly from usual filtration in standard porous media, although the classical Darcy's law is assumed as the fundamental flow mechanism.

8.1 Introduction

8.1.1 Percolation in the Espresso Coffee Machine

It is well known that there are several different ways of preparing a cup of coffee. Espresso coffee is the favorite in Italy and is becoming increasingly

A. Fasano (ed.), *Complex Flows in Industrial Processes*

popular in other countries. An espresso coffee machine is a rather sophisticated device designed to supply water with constant values of temperature and pressure (95°C and 9 bars at the typical operating conditions), forcing it through a layer of ground coffee in the form of a compact cake inside a container that allows the beverage to drip out while retaining the solid particles.

The corresponding flow (percolation) is a remarkably complex process, accompanied by at least two important chemical effects: the extraction of soluble substances in water and the emulsification of insoluble liquids. More than 1500 chemical compounds have been identified in coffee: Some of them are expected to be more or less polar and may exhibit such an affinity with water as to become water soluble. Moreover, the flow also exerts a mechanical action on the ground coffee cake.

The cake commercialized by illycaffè s. p. a., an Italian company based in Trieste, for home espresso machines consists of nearly 7 grams of ground coffee, pressed in a cylindrical form between two filters of permeable paper. The size of the particles forming the main body of the cake is in the range 100–200 μ, but much smaller particles are also produced during the grinding process, which normally adhere to the larger grains. A fraction of such smaller particles can be removed by the flow, according to the mechanism that will be illustrated later, and are transported through the pores. A slight compression of the coffee cake can be exerted by the flow, although this effect seems unimportant in normal conditions.

It should be mentioned that the mechanical and chemical aspects we pointed out are strongly coupled: Actually, extraction affects the properties of the liquid (density, viscosity) and to a much larger extent those of the porous medium (porosity, permeability). On the other hand, the filtration velocity plays a fundamental role in the extraction kinetics.

In recent years illycaffè s. p. a., with the help of ECMI promoted a theoretical and experimental research program, the aim of which was to understand the mechanical and chemical processes taking place during the filtration of water through the compact cake of ground coffee in the espresso coffee machine. The corresponding problem exhibits a number of peculiar features deriving from the mutual interaction between the flow and the evolution of the porous matrix. Such a complexity is reflected in the mathematical models we are going to discuss, which, roughly speaking, consist in systems of partial differential equations of various types, with the presence of a free boundary.

8.1.2 The Experimental Approach

The first attempt to set up a mathematical model for the espresso brewing process dates back to the early sixties ([7]). As a naive approximation, it is likely to assume that the percolation process can be hydraulically defined by an equation associating five variables, sufficient to characterize the process in its macroscopic physical aspect, in agreement with the

traditional rule stating: To prepare an espresso cup correctly, it is necessary to set the right temperature and the right pressure, then the hydraulic resistance must be adjusted (by grinding and compacting) until the right volume of beverage is obtained in the right time.

In order to model the phenomenon theoretically, a semi-empirical approach uses flow, pressure, and temperature continual sensors to obtain discharge curves as a function of time ([27]). The steady-state prediction of Darcy's law (with no gravity) gives simply

$$p = Rq \tag{8.1}$$

where p is the injection pressure, q the volumetric velocity, and R the hydraulic resistance of the cake.

But two observations that lie in evident contradiction with this equation emerge from the experimental curves (see Fig. 8.1):

1. Flow is not constant for constant injection pressure, but it displays an initial transient in which a sharp maximum is reached and then decreases in time toward an apparently asymptotic value (dependent on temperature and pressure).
2. Even the asymptotic value is not proportional to the injection pressure (as we would expect from Darcy's law), but it increases until a certain value and then remains constant or decreases for larger values of pressure, thus exhibiting a nonmonotone behavior.

This situation occurs not only during the ordinary espresso coffee brewing procedure, but also in the case in which water is injected at low temperature, clearly pointing out the mechanical origin of this surprising effect.

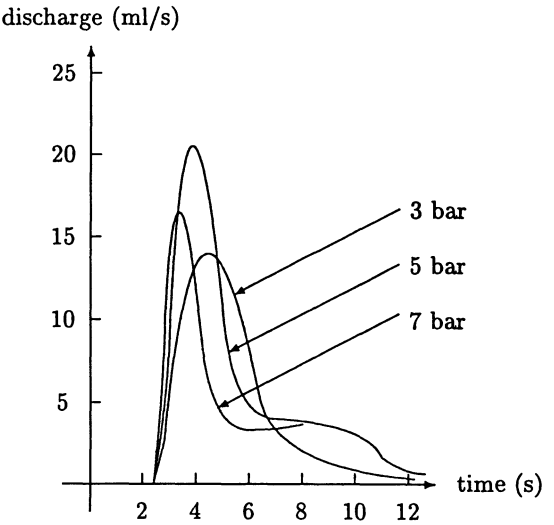

Figure 8.1 — Pressure dependence of flow during percolation.

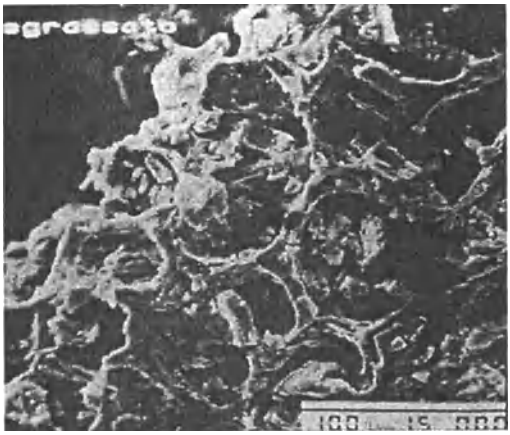

Figure 8.2 — Microstructure of ground coffee particles.

Such anomalous and clearly nonlinear behavior cannot be explained by just modifying Darcy's law in one of the ways suggested by the literature (see, e.g. [4]). On the contrary it must be attributed to other phenomena accompanying the flow, while Darcy's law can still be used as the basic flow equation.

The following equation (see [1]) approximates the experimental behavior of q as a function of time, excluding the initial transient peak (which is simply due to the way the apparatus builds up the required pressure):

$$q = a + be^{-ct} \tag{8.2}$$

where the values a, b, and c are deducible from the data. The flow exponential dependence on time suggests that the ground coffee particles may exhibit a progressive rearrangement under the action of the flow.

Electronic microscopy (see Fig. 8.2) shows that ground coffee contains a component of fine particles, fragments of the cell membranes, which become so fragile after roasting that it is not possible to keep the size of all the particles produced in the grinding operation within the desired range.

In such a setting, the fines are expected to migrate and eventually to accumulate in some part of the bed, typically at the outflow surface (Fig. 8.3).

An indirect convincing confirmation of this theory comes from a series of tests in which the direction of percolation can be reversed. Such tests are performed by percolating water through an over-turnable extraction chamber designed on purpose. The direct flow has the described behavior, and once the asymptotic discharge has been reached the cake seems to

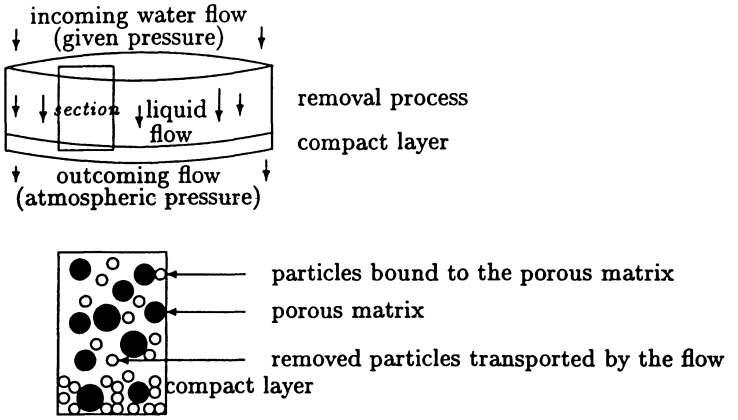

Figure 8.3 — A simplified scheme of the ground coffee layer: the cylinder is the coffee cake, and the lower rectangle is a transversal section of it.

behave like an ordinary porous medium (if the pressure is switched off and then applied again, the discharge immediately resumes the same value).

However, as the percolation chamber is rotated, the flow surprisingly goes through the exponential decay once more (see Fig. 8.4). This effect can be explained by assuming that the fine particles can be removed and transported by the flow; after the flow inversion the particles that accumulated first in a lower section of the cake (causing an increase of the hydraulic resistance) now counter-migrate, with an initial increase of the hydraulic conductivity in the opposite direction, subsequently leading the system to the previous steady state.

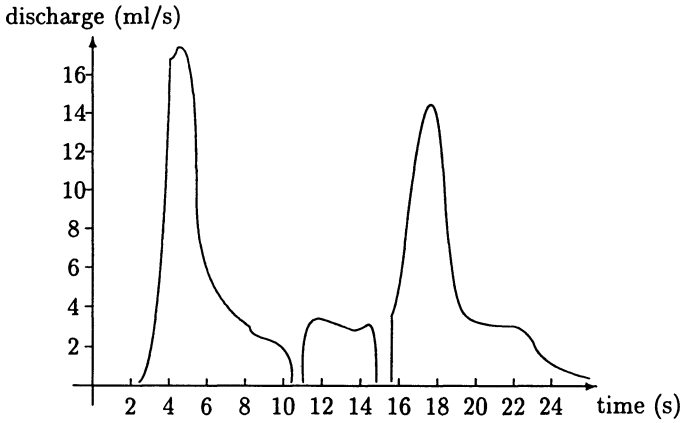

Figure 8.4 — Direct/inverse discharge curve.

8.2 Modeling the Percolation Process

A shortcut to formulating a model for a flow process through a progressively modified medium can be based on a *black box* philosophy, that is, establishing laws from a series of experimental data and disregarding the phenomena occurring at the microscopic scale. Such a semi-empirical approach, which has been used, for example, in approximation (8.2), has the advantage of simplicity, although it is of no help in investigating the real mechanism that governs the process.

A finer approach, which is more complex but more interesting, consists in looking at the real nature of the process and studying the local interactions between the flow and the porous matrix, in order to formulate a model providing a theoretical basis to the observed phenomena.

The rest of this chapter is devoted mainly to reviewing and discussing the mathematical models based on the second approach. We will not deal with space-independent models; we refer to [1] for an overview on the semi-empirical models and to [20] and [2] for further generalizations.

The complexity of the problem requires a separate analysis of the various aspects of the process. We will first introduce a simpler model (part I) that contains most of the peculiar features, focused on the consequences of removal and transport of a single species of fine particles. Next, (parts II and III), we will remove some simplifying assumptions and incorporate some generalizations (such as the deformability of the medium, the multi-species composition of the system, and the diffusion of some components).

In our conceptual model, the ground coffee layer will be saturated with the fluid. As a matter of fact, the first stage of the process, corresponding to the initial penetration of water through the dry cake, is not considered in this context. On the other hand, invasion problems with the specific features of filtration through ground coffee have been extensively investigated in [12], [13], [14], [15], and [23]. In principle, the two different processes of imbibition and filtration can be connected by considering the initial conditions of the latter as the state determined at the end of the invasion process.

We also assume, as a common feature, that the process is described by a one-dimensional model. Actually, the physical problem suggests that filtration can be considered in a good approximation predominant in the axial direction; the nozzle supplying water is designed to make the flow one-dimensional for a uniform exploitation of the ground coffee.

Finally, the liquid flowing through the porous medium is assumed to be incompressible.

For the sake of brevity we will not deal with other techniques that have been used to describe the process, although at a lower level of complexity.

We mention the approach based on the use of cellular automata ([3], [6]) and a first attempt to use homogenization techniques ([18]) and variational formulations, which allows us to describe the invasion process and looks susceptible of further developments.

The paper ([17]) reconsiders the problem in ([18]), adding a mass exchange kinetics between the grains and flowing liquid.

8.3 Part I: Single Species of Fine Particles, No Dissolution (References: [16], [20], [22])

As we said, the phenomena that at a microscopic level play a crucial role in the deviation of the studied process from the classical Darcyan filtration are the transport of fine particles of the porous medium by the flow and dissolution of substances. The latter process is virtually eliminated by percolating cold water. In this first approach we refer precisely to this situation, adding the further simplifying assumption that only one species of identical particles is present. Not all the fine particles are free to move; part of them are bound to the porous skeleton for various reasons. Nevertheless, some of the bound particles can be detached by the flow and subsequently transported by the flow.

If L is the thickness of the porous layer, we take a spatial coordinate $x, 0 < x < L$, such that x increases in the direction of the flow. In such a frame of reference, the boundaries $x = 0$ and $x = L$ correspond to the inflow and outflow surfaces, and we assume that the overall deformation of the medium is negligible.

We use two different symbols to denote the concentration (i.e., mass per unit volume of the total system) of fine particles when they are bound to the porous matrix (b) and when transported by the flow (m). The following equation expresses the mass balance for the moving fine particles (cfr. [29]):

$$\frac{\partial m}{\partial t} + \frac{\partial}{\partial x}(mV_m) = -\frac{\partial b}{\partial t} \tag{8.3}$$

where V_m is the particle velocity and the term on the right-hand side denotes the production rate of mobile particles, due to the action of the flow.

The velocity V_m can be related to the velocity of the fluid $V = q/\varepsilon$ by assuming reasonably that the fine particle average motion is in the direction of the flow:

$$V_m = \alpha V, \quad 0 < \alpha \leq 1 \tag{8.4}$$

where α is introduced to take account of possible slowing effects due to the shocks of the particles with the porous matrix during their motion.[1]

A crucial point in the model is to describe the release rate of fine particles. The predominant factors in such a process are the intensity of the flow q and the concentration of the particles susceptible to removal. For a specified value of q, we may suppose that not all the fine particles can be removed, just the fraction whose bonds are weak enough.

Such a behavior is modeled by introducing a threshold function $\beta(q)$ such that the particle removal process occurs only as long as the concentration b exceeds the value of β. Hence, the release kinetics of fine particles is summarized in the following equation:

$$\frac{\partial b}{\partial t} = -\gamma q[b - \beta(q)]^+. \tag{8.5}$$

By $[\cdot]^+$ we denote the positive part of $[\cdot]$. Note that the threshold β depends on q; actually, a more intense flux operates on a larger population of particles. For this reason β is a decreasing function of q.

We will prove that the threshold effect is essential in explaining the nonmonotone behavior of the asymptotic discharge on the injection pressure. Generalizations of the removal equation (8.5) will be considered in Section 8.4. Moreover, β may also depend on the concentration b (cfr. Section 8.4.1).

In a first modeling stage, it can be assumed that the porosity of the medium is not significantly affected by the removal process. Such an assumption, together with the incompressibility of the liquid, makes the flow intensity q depend on time only:

$$\frac{\partial q}{\partial x} = 0. \tag{8.6}$$

We shall see that dropping this assumption leads to a more complicated problem. As we said in Section 8.1, the moving particles accumulate in the proximity of the outflow surface $x = L$ due to the presence of a paper filter retaining the fine particles. As a consequence a low conductivity layer grows and a free boundary $x = s(t)$ (the layer top) appears in the problem. In other words, the porous layer is split into the two regions $0 < x < s(t)$, the removal-transport zone, and $s(t) < x < L$, the compact layer. Assuming that the fine particles are not compacted in any part of the layer at the initial time $t = 0$, we have $s(0) = L$.

[1] In some technical applications there are transported particles that are able to follow the paths of maximum velocity in the microscopic flow so that their average speed is larger than that of the fluid.

The flow is driven by the pressure gradient in each of the two regions:

$$\begin{aligned} q &= -K(b,m)\frac{\partial p}{\partial x} \quad 0 < x < s(t) \\ q &= -K_c\frac{\partial p}{\partial x} \quad s(t) < x < L. \end{aligned} \tag{8.7}$$

The hydraulic resistance in the compact layer is much higher than in the rest of the medium:

$$K_c \ll K(b,m).$$

We denote by M the concentration of fine particles in the compact layer. In the packing configuration the fine particles are assumed to occupy the maximum volume at their disposal, so that M is a given constant.

Arguing as in [28], the mass balance at the boundary $x = s(t)$ is given by the condition

$$[[m+b]]\,\dot{s}(t) - [[mV_m]] = 0 \tag{8.8}$$

where (here and in the sequel) $[[\chi]]$ denotes the jump of χ at $s(t)$:

$$[[\chi]] = \lim_{x \to s(t)^+} \chi(x,t) - \lim_{x \to s(t)^-} \chi(x,t) \tag{8.9}$$

Because the fine particles are at rest in the region $s(t) < x < L$, we find from (8.8) and (8.4) the following equation, which describes the growth rate of the compact layer:

$$(M - (m(s(t)^-,t) + b(s(t)^-,t)))\dot{s}(t) = \frac{\alpha}{\varepsilon} q(t) m(s(t)^-,t). \tag{8.10}$$

The physical meaning of (8.10) is evident: the number of particles needed per unit surface to complete the packed configuration, that is, the product $-\dot{s}(M-(m+b))$, is provided by the incoming flux of particles $\alpha q m/\varepsilon$. At the interface $s(t)$, we impose that p and q are continuous:

$$[[q]] = 0, \quad [[p]] = 0 \quad at\ x = s(t). \tag{8.11}$$

It has to be remarked that the correct jump condition for q would be $[[q - \varepsilon\dot{s}]] = 0$. However, the ratio between $\varepsilon|\dot{s}|$ and q on both sides of the interface is typically very small, so that (8.11) is justified as a first approximation. The model is completed by prescribing the initial conditions

$$b(x,0) = b_0 > 0, \quad m(x,0) = m_0 \leq 0 \tag{8.12}$$

which give the distribution of fine particles at $t = 0$, and the boundary conditions

$$\begin{cases} p(0,t) = p_0 & \text{injection pressure,} \\ p(L,t) = 0 & \text{atmospheric pressure,} \\ m(0,t) = 0 \end{cases} \tag{8.13}$$

Note that a constraint for the initial concentrations is given by $M > b_0 + m_0$. The third condition in (8.13) states that there is no injection of particles at the boundary $x = 0$. We also remark that the initial value of the flux q can be deduced from (8.7), (8.12), and (8.13):

$$q(0) = K_0 \frac{p_0}{L}, \quad K_0 = K(b_0, m_0)$$

8.3.1 The Mathematical Investigation of the Model

The mathematical analysis we will perform is based on the following assumptions:

(a) The threshold function $\beta(q)$ is continuously differentiable and

$$\beta'(q) \leq 0 \tag{8.14}$$

(b) $m_0 \geq 0$ and $p_0 > 0$ are constant.

(c) The initial concentration of bound particles $b_0 > 0$ is constant.

Before commenting on assumptions (a) to (c), we will summarize the complete mathematical model. After rescaling the variables as follows

$$\begin{array}{cccc} \bar{x} = x/L, & \bar{t} = t\gamma q_0, & \bar{q} = q/q_0, & \bar{p} = p/p_0 \\ \bar{b} = b/b_0, & \bar{m} = m/b_0, & \bar{M} = M/b_0, & \bar{m}_0 = m_0/b_0 \\ \bar{\beta}(\bar{q}) = \beta(\bar{q}q_0)/b_0, & \bar{s}(\bar{t}) = s(\bar{t}/\gamma q_0)/L, & \bar{K} = K/K_0, & \bar{K}_c = K_c/K_0 \end{array}$$

we define

$$\mu = \frac{\alpha L}{\varepsilon \gamma}$$

and we put the complete model (namely, eqs. (8.3), (8.4), (8.5), (8.7), (8.10), (8.11), (8.12), and (8.13)) in nondimensional form, omitting the bars to keep notation simple:

$$\frac{\partial m}{\partial t} + \mu q(t) \frac{\partial m}{\partial x} = -\frac{\partial b}{\partial t}, \quad 0 < x < s(t),\ t > 0 \tag{8.15}$$

$$\frac{\partial b}{\partial t} = -q(t)[b - \beta(q)]^+, \quad 0 < x < s(t),\ t > 0 \tag{8.16}$$

$$q = -K(b, m) \frac{\partial p}{\partial x}, \quad 0 < x < s(t),\ t > 0 \tag{8.17}$$

$$q = -K_c \frac{\partial p}{\partial x}, \quad s(t) < x < L,\ t > 0 \tag{8.18}$$

$$(M - (m(s(t)^-, t) + b(s(t)^-, t)))\dot{s}(t) = \mu q(t) m(s(t)^-, t), \quad t > 0 \tag{8.19}$$

$$\left[\left[-K \frac{\partial p}{\partial x}\right]\right] = 0, \quad [[p]] = 0, \quad x = s(t),\ t > 0 \tag{8.20}$$

$$b(x,0) = 1, \quad m(x,0) = m_0, \quad 0 < x < 1, \quad s(0) = 1 \tag{8.21}$$

$$p(0,t) = 1 \quad p(1,t) = 0 \quad m(0,t) = 0, \quad t > 0. \tag{8.22}$$

We now revert to assumptions (a) to (c) introduced at the beginning of this section. We have already discussed the meaning of property (a) of the threshold β with respect to flux q (cfr. the comment just below (8.5)). Point (b) is introduced to simplify the mathematical presentation.

The assumption that produces a significant simplification is (c). Actually, in that case b depends on time only (cfr. (8.5)) and $b(t)$ is nonincreasing. The essential advantage is that we can write the mass balance for the fine particles as a conservation equation:

$$\frac{\partial(m+b)}{\partial t} + \mu q(t) \frac{\partial(m+b)}{\partial x} = 0. \tag{8.23}$$

An important consequence of (8.23) is that $m + b$ remains constant along the characteristic curves of the transport equation (8.23). The characteristic line $\sigma(t)$ originating at $(0,0)$ bounds the region

$$Q_i = \{(x,t) | \sigma(t) < x < s(t), 0 < t < t^*\} \tag{8.24}$$

where t^* is the (finite) time at which $x = \sigma(t)$ intersects $x = s(t)$. The characteristic curves starting from points $(0,t)$, $t > 0$, lie in the region

$$Q_b = \{(x,t) | 0 < x < \sigma(t), t > 0\} \cup \{(x,t) | 0 < x < s(t), t \geq t^*\}$$

The regions Q_i and Q_b are sketched in Figure 8.5. Note that if $m_0 > 0$ the origin is a discontinuity line for $m(x,t)$.

By introducing the resistivity $R(b,m) = 1/K(b,m)$ and recalling (8.17) and (8.20) we obtain the following expression for the flux:

$$q(t) = \left(\int_0^{s(t)} R(b,m)\, dx + R_c(1 - s(t)) \right)^{-1} \tag{8.25}$$

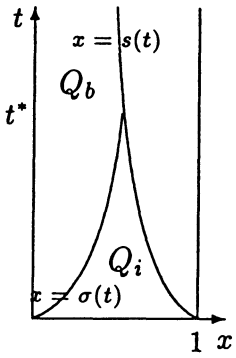

Figure 8.5 — The regions Q_b and Q_i.

where $R_c = 1/K_c$. Consistent with the physics of the problem we assume that two positive constant values R_m and R_M exist such that

$$0 < R_m \leq R(m,b) \leq R_M < R_c. \tag{8.26}$$

Lemma 8.1. *(a priori bounds). For any solution of (8.15) to (8.22), we have:*

$$s(t) \geq s_m = 1 - \frac{1+m_0}{M}, \quad t \geq 0 \tag{8.27}$$

$$q_m \equiv (R_M s_m + R_c(1-s_m))^{-1} \leq q(t) \leq R_m^{-1} \equiv q_M, \quad t \geq 0 \tag{8.28}$$

$$0 < b(t) \leq 1,\ t \geq 0, \quad 0 \leq m(x,t) \leq 1+m_0, \quad (x,t) \in Q_i \cup Q_b \tag{8.29}$$

$$0 \leq -\dot{s}(t) \leq \frac{\mu q_M (1+m_0)}{M-(1+m_0)} \quad t \geq 0. \tag{8.30}$$

Furthermore, the function $\theta(x,t)$ defined by

$$x = \int_{t-\theta(x,t)}^{t} \mu q(\tau)\, d\tau \tag{8.31}$$

corresponding to the time needed to transport particles across the distance x from the inflow surface is such that

$$\begin{cases} 0 \leq \theta \leq \dfrac{x}{\mu q_m} \\ 0 < \dfrac{\partial \theta}{\partial x} \leq \dfrac{1}{\mu q_m} \\ \left\| \dfrac{\partial \theta}{\partial t} \right\| \leq 1 + \dfrac{q_m}{q_M}. \end{cases} \tag{8.32}$$

The detailed proof of Lemma 8.1 is in [16]. We just mention the fact, physically expressive, that (8.27) comes from the global mass balance

$$\int_0^{s(t)} (m+b)\, dx + M(1-s(t)) = 1 + m_0 \tag{8.33}$$

obtained by integrating (8.15) separately in Q_b and Q_i and by taking account of (8.19) (note that $\dot{\sigma} = \mu q$). In (8.33) the partition of the global amount of particles $1 + m_0$ between the compact layer and the residual medium is in evidence. Balance (8.33) provides the least possible value s_m of s by setting $m + b = 0$:

$$(1 - s_m)M = 1 + m_0.$$

This proves (8.27).

On the other hand, (8.28) simply follows from (8.25), while (8.29) is a consequence of the following formula:

$$\begin{cases} m(x,t) + b(x,t) = m_0 + 1 & \text{if } (x,t) \in Q_i \\ m(x,t) = b(t - \theta(x,t)) - b(t) & \text{if } (x,t) \in Q_b \end{cases} \tag{8.34}$$

where θ is defined in (8.31). Note that (8.30), which easily follows from (8.28) and (8.29), provides an estimate for the time t^* introduced in (8.24). Finally, (8.32) comes from differentiating (8.31). In order to avoid the trivial problem that gives the stationary solution $q \equiv 1$, $s \equiv 1$, b, m constant (corresponding to the absence of the release process), we introduce the assumption

$$\beta(1) < 1. \tag{8.35}$$

Lemma 8.2. *(asymptotic behavior). For any solution of (8.15) to (8.22) existing for $t \in [0, +\infty)$, we have*

$$\dot{s}(t) \leq 0, \quad \lim_{t \to +\infty} s(t) = s_\infty \in [s_m, 1) \tag{8.36}$$

$$\dot{b}(t) \leq 0, \quad \lim_{t \to +\infty} b(t) = b_\infty \in [0, 1] \tag{8.37}$$

$$\lim_{t \to +\infty} m(x,t) = 0 \quad \textit{uniformly in} \quad (0, s_\infty) \tag{8.38}$$

$$\lim_{t \to +\infty} q(t) = q_\infty = \{s_\infty R(0, b_\infty) + R_c(1 - s_\infty)\}^{-1}. \tag{8.39}$$

Moreover

$$s_\infty = \frac{s_m}{1 - \dfrac{b_\infty}{M}}. \tag{8.40}$$

Proof. Eqs. (8.36) and (8.37) are evident (recall (8.19), (8.16), and (8.27)). Note that $b_\infty < 1$ because of (8.35). On the other hand, (8.38) is proved by observing that for $(x,t) \in Q_b$ $m(x,t) + b(t) = b(t - \theta(x,t))$ (cfr. (8.34)) and $t - \theta \to \infty$ for $t \to \infty$ because of the first estimate in (8.32). The boundedness of θ also provides the uniformity of the limit $m \to 0$. The asymptotic flux (8.39) is obtained simply by passing to the limit in (8.25). Finally, the value for s_∞ (8.40) comes from (8.33) (for $t \to \infty$) and from (8.27). □

The following results are aimed at showing that model (8.15) to (8.22) can predict the nonstandard behavior of the observed phenomena we described in Section 3. For this purpose, we need some additional assumption on the resistivity R.

Lemma 8.3. *(nonincreasing flux). Assume that*

$$R(m,b) = R(m+b) \tag{8.41}$$

with

$$R(\varrho) \in C^1[0,1+m_0),\ 0 < R_m \le R(\varrho) \le R_M < R_c,\ R'(\varrho) < \frac{R_c - R_M}{M}. \tag{8.42}$$

Then the flux $q(t)$ satisfies

$$\begin{cases} \dot{q}(t) > 0 & \text{as long as } m(s(t),t) > 0 \\ \dot{q}(t) = 0 & \text{otherwise} \end{cases} \tag{8.43}$$

Proof. From (8.25), by differentiating we get

$$\dot{q}(t) = -q^2(t) \left\{ \dot{s}(t) \left[R\left(\varrho(s(t),t)\right) - R_c \right] + \int_0^{s(t)} R'(\varrho(x,t)) \frac{\partial}{\partial t}(m+b)\, dx \right\}. \tag{8.44}$$

Recalling the free boundary condition (8.19) and noting that, thanks to (8.41) and (8.23), the term containing the integral in (8.44) is $-\mu q(t)$ $[R(\varrho(s,t)) - R(\varrho(0,t))]$, we obtain

$$\dot{q}(t) = \mu q^3(t) m(s(t),t) \left\{ \frac{R(\varrho(s(t),t)) - R_c}{M - \varrho(s(t),t)} + R'(\bar{\varrho}) \right\} \tag{8.45}$$

from which (8.43) follows. Note that $\varrho(s,t) - \varrho(0,t) = m(s(t),t)$, due to (8.21). □

Corollary 8.1.

(i) The function $b(t) - \beta(q(t))$ is nonincreasing (recall $\beta' \le 0$), thus implying that $\dot{b}(t)$ tends to zero at infinity. The positive part $(b(t) - \beta(q(t)))^+$ decreases from the initial value $1 - \beta(1) > 0$ (cfr. (8.35)) to zero, which is reached at infinity or at some finite time.

(ii) $\frac{\partial \theta}{\partial t} \ge 0$

(iii) $q(t) \le 1$

Property *(ii)* is a consequence of

$$\frac{\partial \theta}{\partial t} = 1 - \frac{q(t)}{q(t-\theta)}$$

which in turn comes from differentiating (8.31) with respect to t. In order to analyze the asymptotic behavior of the flux with respect to the applied

pressure, we further specialize to the case

$$R = \text{ constant } = 1. \tag{8.46}$$

Under such an assumption, (8.25) and (8.39) simplify, respectively, to

$$q(t) = (s(t) + R_c(1 - s(t))^{-1} \tag{8.47}$$

$$q_\infty = (s_\infty + R_c(1 - s_\infty))^{-1}. \tag{8.48}$$

The fact that $(b - \beta(q))^+$ vanishes either at infinity or at a finite time (as we pointed out in Corollary 8.1, (i)) makes the corresponding qualitative behavior of the system very different, as is shown in next proposition.

In order to investigate the dependence on injection pressure, we need to revert to the original variables, which we now denote by $\tilde{p}_0$, $\tilde{q}_0$, etc. Any quantity without a tilde will still denote the nondimensional scaled variable.

Proposition 8.1. *If*

$$b(t) - \beta(q(t)) > 0, \quad \forall t > 0 \tag{8.49}$$

then the asymptotic value of the flux $\tilde{q}_\infty$ is an increasing function of the applied pressure $\tilde{p}_0$.

Proof. The main consequence of (8.49) is that

$$b_\infty = \beta(q_\infty). \tag{8.50}$$

Note that (8.50) is equivalent to $\tilde{b}_\infty = \tilde{\beta}(\tilde{q}_\infty)$. Recalling (8.40), i.e.,

$$\tilde{s}_\infty = \frac{\tilde{s}_m}{1 - \dfrac{\tilde{\beta}_\infty(\tilde{q}_\infty)}{\tilde{M}}} \tag{8.51}$$

we obtain from (8.48):

$$\begin{aligned} \tilde{q}_\infty &= \tilde{q}_0 L \left(L\frac{\tilde{K}_0}{\tilde{K}_c} - \tilde{s}_\infty \left(\frac{\tilde{K}_0}{\tilde{K}_c} - 1 \right) \right)^{-1} \\ &= \left(\frac{\tilde{K}_0}{\tilde{K}_c} \right)^{-1} \left(1 - \frac{\tilde{s}_m}{L(1 - \tilde{\beta}(\tilde{q}_\infty)/\tilde{M}} \left(1 - \frac{\tilde{K}_0}{\tilde{K}_c} \right) \right)^{-1} \tilde{q}_0. \end{aligned} \tag{8.52}$$

Now we differentiate with respect to $\tilde{q}_0$:

$$\frac{d\tilde{q}_\infty}{d\tilde{q}_0} = \frac{\tilde{q}_\infty}{\tilde{q}_0} + \frac{\tilde{K}_c}{\tilde{K}_0}\tilde{q}_0\left(1 - \frac{\tilde{K}_c}{\tilde{K}_0}\right) \frac{\tilde{s}_m\tilde{\beta}'(\tilde{q}_\infty)\tilde{M}}{L\left(\tilde{M} - \tilde{\beta}(\tilde{q}_\infty) - \dfrac{\tilde{s}_m\tilde{M}}{L}\left(1 - \dfrac{\tilde{K}_c}{\tilde{K}_0}\right)\right)^2} \frac{d\tilde{q}_\infty}{d\tilde{q}_0} \tag{8.53}$$

Because $\tilde{\beta}'(\tilde{q}_\infty) < 0$, we get $\frac{d\tilde{q}_\infty}{d\tilde{q}_0} > 0$. □

Corollary 8.2. *Under assumption (8.46), a necessary condition for violating the nonmonotone dependence of $\tilde{q}_\infty$ on $\tilde{p}_0$ is that $(b - \beta(q))$ vanishes at a finite time.*

In Section 8.1.2 we discussed the experimental evidence of a possible nonmonotone dependence of the asymptotic flux velocity on the injection pressure. It is then of some interest to investigate whether the quantity $b-\beta(q)$ will vanish. This is the aim of the next section.

8.3.2 Reaching the Steady State in an Infinite or Finite Time

For a deeper analysis of the qualitative behavior of the solution, we keep the simplifying assumption (8.46). A simple case in which the occurrence of (8.49) takes place when

$$\beta(q) \equiv \beta_0 < 1. \tag{8.54}$$

Indeed, by setting

$$\Lambda(t) = b - \beta(q) \tag{8.55}$$

we can write (8.16) as

$$\frac{d\Lambda}{dt} + q\Lambda(t) = -\frac{d}{dt}\beta(q), \quad \Lambda(0) = 1 - \beta(1) > 0$$

which, under assumption (8.54), gives $\Lambda(t) > 0\ \forall t > 0$. Moreover, the asymptotic solution is given by coupling (8.48) with (cfr. (8.27), (8.40), and (8.50))

$$s_\infty = \frac{M - (1 + m_0)}{M - \beta(q_\infty)} \tag{8.56}$$

We are now going to prove that the solution can also reach the steady state in a finite time. First, we observe that if $b - \beta(q)$ vanishes at some time $\bar{t} > 0$, then $(b - \beta(q))^+ \equiv 0$ for $t > \bar{t}$, because $b(t)$ is nonincreasing and $\beta(q(t)) \geq \beta(q(\bar{t}))$ for $t > \bar{t}$ (Lemma 8.3). It follows that the solution of (8.16) for $t > \bar{t}$ is $b(t) \equiv b(\bar{t})$.

If we consider the characteristic $x = \hat{\sigma}(t)$ of (8.15) starting at $(0, \hat{t})$, $\hat{t} = \max(\bar{t}, t^*)$, we immediately have

$$m(x,t) \equiv 0 \quad for\ (x,t) \in Q_b \cap \{(x,t) | x \in (0,1), t > \bar{t}\}.$$

Therefore, the system reaches the steady state when $\bar{\sigma}(t)$ hits the free boundary $s(t)$ (and this will occur in a finite time after $\hat{t}$). We now prove the following.

Theorem 8.1. *A function $\beta(q)$ can be found such that system (8.15) to (8.22) reaches the steady state in a finite time.*

Proof. Take any $\beta(q)$ with properties (8.14) and (8.35) and any positive t' such that $\Lambda(t') > 0$. By virtue of (8.35), we can suppose that $\dot{s}(t') < 0$.

Now we freeze b at the value $b' = b(t')$ and solve the following problem for m', q', and s':

$$\frac{\partial m'}{\partial t} + \mu q' \frac{\partial m'}{\partial x} = 0, \qquad m'(0,t) = 0,\ t \geq t' \tag{8.57}$$

$$(M - (m' + b'))\dot{s}(t) = \mu q' m' \quad t > t' \tag{8.58}$$

Passing to the limit in the mass balance (8.33), which for $t > t'$ takes the form

$$\int_0^{s'(t)} m'(x,t)\, dx + M(1 - s'(t)) = 1 + m_0 - b' s'(t)$$

we get (cfr. also (8.56))

$$s'_\infty (M - b') = M - (1 + m_0). \tag{8.59}$$

Recalling (8.14), (8.48), and (8.56) we have

$$b' > b_\infty \Rightarrow s'_\infty > s_\infty \Rightarrow q'_\infty > q_\infty \Rightarrow \beta(q'_\infty) \leq \beta(q_\infty). \tag{8.60}$$

We also note that s'_∞ (hence q'_∞) depends on b' only, i.e., not on the choice of $\beta(q)$ for values of $q \leq q'$, because β plays no role in the modified system (8.57) to (8.58). At this point, two cases can occur:

(*i*) $\beta(q'_\infty) \geq b'$,
(*ii*) $\beta(q'_\infty) < b'$.

Owing to (8.60), case (*i*) means $\beta(q_\infty) > b_\infty$, so Λ has to vanish in a finite time. In case (*ii*) we modify the function $\beta(q)$ for $q \leq q(t')$ taking $\hat{\beta}(q)$ with the properties (8.14) and $\hat{\beta}(q'_\infty) > b'$. In this way, the original problem with the modified β reaches the steady equilibrium at a finite time. □

We remark that the theorem does not state that q_∞ may indeed be non-decreasing with the applied pressure. Actually, the vanishing of $b - \beta(q)$ is a necessary condition for such a behavior, as pointed out in Corollary 8.2.

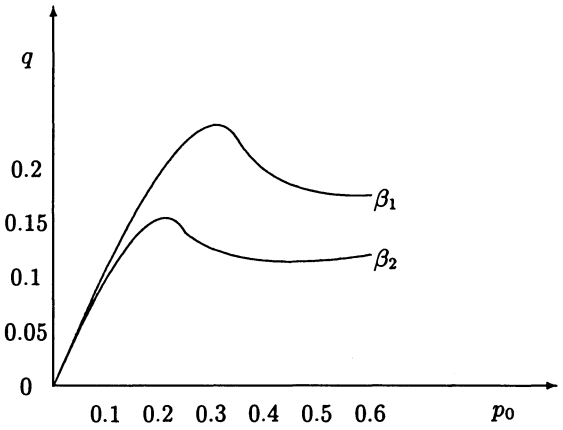

Figure 8.6 — Asymptotic discharge vs. applied pressure for different threshold functions β_1 and β_2 and $\mu = 0.5$ (normalized quantities).

Such an occurrence must be proved by an example. Some numerical simulations exhibiting the nonmonotone dependence of the asymptotic flux on the applied pressure have been provided in [22].

Figures (8.6) and (8.7) have been obtained by T. Suski of ICM, Warsaw.

8.3.3 Existence and Uniqueness of the Solution

The well-posedness for problem (8.15) to (8.22) is guaranteed by the following result, which is valid for the general case $R = R(m, b)$.

Theorem 8.2. *Suppose that $R = R(m, b)$ is a C^1 function for $m \in [0, m_0 + 1]$, $b \in [0, 1]$ satisfying (8.26). Then problem (8.15) to (8.22) has exactly*

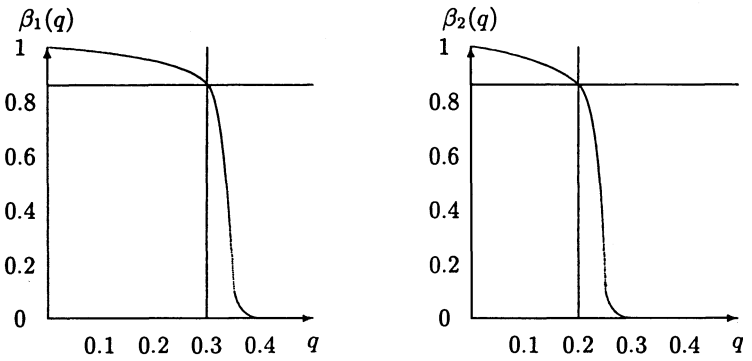

Figure 8.7 — Threshold concentrations β_1 and β_2.

one solution (m, b, q, s, p) globally in time. Moreover, if $R(m, b)$ is C^∞, the same is true for $q(t)$ and $s(t)$, except at $t = t^*$ (defined in (8.24)), where if $m_0 > 0$, $\dot{q}$ and $\dot{s}$ have a discontinuity (although bounded on both sides) and possibly at the time (if it exists) at which $b - \beta(q)$ vanishes, where some higher-order derivatives can be discontinuous.

The proof of this theorem is omitted; we refer to [16] and [20] for all details. We mention that the existence proof is based on a fixed-point procedure (which will also be used for the more general results quoted in the rest of this chapter), namely, taking an arbitrary $T > 0$ and introducing the set of functions

$$X(T) = \{(q, s) \in C([0, T]) \times C([0, T]) | q(0) = 1, s(0) = 1, q_m \leq q \leq q_M s_m \leq s \leq 1, s \downarrow, \text{Lip } s \leq \mu q_M \frac{1 + m_0}{M - (1 + m_0)}\} \tag{8.61}$$

where Lip s is the Lipschitz constant of s. For each $(q, s) \in X(T)$ we solve the problem for b and m in $[0, 1] \times [0, T]$, then we use the right-hand sides of (8.25) and of (8.19) to determine a new pair $(q^\star, s^\star)$. It can be seen that $(q^\star, s^\star) \in X(T)$ and the mapping $(q, s) \to (q^\star, s^\star)$ is precompact in it and Lipschitz continuous. Hence Schauder's fixed-point theorem can be used. The same techniques can be used to show the continuous dependence on the data (see [20]).

8.3.4 Numerical Calculation

Under the assumption $R_c \gg R$ the thickness of the compact layer is expected to be very small, i.e., $1 - s \ll 1$. In this context a reasonable approximation of the model consists in calculating the functions b and m in the whole domain $0 < x < 1$, $t > 0$ and the right-hand side of (8.19) for $x = 1$. For this problem, existence and uniqueness can be proved (see [5]).

The simplified model we introduced can be approximated by the numerical approach sketched later, based on the retarded argument method. Choose a time τ and set $\bar{s} = 1$, $\bar{q} = 1$ for $0 \leq t \leq \tau$. Then solve (8.15) and (8.5) and define a new q with the help of (8.20) and a new s with (8.19) (calculated for $x = 1$). Consider the interval $\tau \leq t \leq 2\tau$ and take $\bar{s}(t) = s(t - \tau)$, $\bar{q}(t) = q(t - \tau)$, and apply the same procedure to define $q(t)$ and $s(t)$ in $(0, 2\tau)$, imposing that m, b, and s take at $t = \tau$ the values found in the previous step.

It is not difficult to show that the family $(\bar{s}, \bar{q})$ indexed by τ is compact and that taking, e.g., $\tau = 1/n$, we get a sequence converging to the solution of the modified problem.

8.4 Part II: Several Species of Moving Particles and Deformation (References: [16], [19])

We now consider the simultaneous removal of several species, letting the porosity change, because of the mass loss from the porous matrix and the deformations induced by the friction of the incompressible fluid on the grains. The macroscopic deformation of the medium will be neglected, although it is supposed that a substantial variation in porosity can be produced by movement of the grains at a micrometric scale.

Contrary to this analysis, we allow all the transported particles to flow out from the medium, thus avoiding the difficulties due to the presence of an internal free boundary. This is because we will concentrate on the mass removal process and the combined influence of such a process and the flow on the porous medium. In some sense this analysis is complementary to the previous one, because the attention is shifted toward more complex mechanical phenomena, disregarding the formation of the compact layer.

In Part III the two aspects (interaction processes and formation of a compact layer) will be combined, including diffusion processes.

8.4.1 Statement of the Model

In order to describe the various species (either solid particles or soluble substances) we introduce two vectors of concentrations: $\mathrm{b} = (\mathrm{b}_1, \ldots, \mathrm{b}_n)$ for the species in the solid and $\mathrm{m} = (\mathrm{m}_1, \ldots, \mathrm{m}_n)$ for those in the liquid.

The transport equation for each species is written in the same way as (8.3) and (8.4):

$$\frac{\partial m_i}{\partial t} + \frac{\partial}{\partial x}\left(\alpha_i \frac{q}{\varepsilon} m_i\right) = -\frac{\partial b_i}{\partial t}, \quad i = 1, \ldots, n \tag{8.62}$$

where α_i, $i = 1 \ldots, n$ are slowing factors. Typically $\alpha_i = 1$ for solutes and $\alpha_i \leq 1$ for solid particles. The porosity ε is no longer constant (as in part I); it is an unknown function of x and t. Thus, the incompressibility condition (8.6) is replaced by the following:

$$\frac{\partial \varepsilon}{\partial t} + \frac{\partial q}{\partial x} = 0. \tag{8.63}$$

In writing (8.63) we neglect the rate of change of the specific volume occupied by the soluble substances in the porous matrix. This situation occurs when the volume made available for the flow by dissolution is large in comparison to the volume of substances in the porous matrix undergoing dissolution (for a discussion on this aspect see ([18]). The complete statement of the volume balance will be presented in the next section.

The removal rate is modeled in analogy with (8.5):

$$\frac{\partial b_i}{\partial t} = -F_i(q,b)G_i\left(b - \beta_i(q,b)\right), \quad i = 1,\ldots,n. \tag{8.64}$$

The functions F_i are bounded and vanish for $q = 0$. The functions $G_i(\zeta)$ are zero for $\zeta \leq 0$, bounded, and positive for $\zeta > 0$. The dependence of F_i and β_i on the whole vector b is explained by the possible interactions between different species (for example, the presence on the larger grains of a coating of fat substance can affect the dissolution of some underlying components).

The constitutive equation expressing the combined effects of mass removal and friction of the flow on the porous matrix is the following (the symbols introduced are explained next):

$$\frac{\partial \varepsilon}{\partial t} = -\sum_{i=1}^{n} \delta_i \frac{\partial b_i}{\partial t} - g(q)\xi_1(\varepsilon - \varepsilon_*(q,b)) + h(q)\xi_2(\varepsilon^*(b) - \varepsilon). \tag{8.65}$$

In (8.65) δ_i are nonnegative constants. The corresponding terms represent the porosity increase rate due to mass loss. The second term on the right-hand side of (8.65) represents the flow-induced reduction rate of porosity. The function g vanishes for $q = 0$ and is increasing, ξ_1 is zero when its argument is negative and bounded positive otherwise and increasing, $\varepsilon_*(q,b)$ is a lower limit for the porosity corresponding to the local values of q and b. The last (positive) term describes an elastic response of the medium. Here h is nonnegative and need not vanish for $q = 0$, ξ_2 has the same behavior as ξ_1. The function ε^* is an upper limit for ε. The functions ε_* and ε^* are bounded away from 0 and 1. Finally, we write Darcy's law as

$$q = -K(m,b,\varepsilon)\frac{\partial p}{\partial x} \tag{8.66}$$

in which we take into account that the porosity changes may also affect permeability.

After introducing a set of dimensionless quantities in the same way as in part I (for the nonconstant initial data we divide by some average value), we can write down the set of governing equations ((8.62), (8.64), (8.63), (8.65), and (8.66)) in the following way:

$$\frac{\partial m_i}{\partial t} + \frac{\partial}{\partial x}\left(\alpha_i \frac{q}{\varepsilon} m_i\right) = -\frac{\partial b_i}{\partial t}, \quad i = 1,\ldots,n \tag{8.67}$$

$$\frac{\partial b_i}{\partial t} = -F_i(q,b)G_i\left(b - \beta_i(q,b)\right), \quad i = 1\ldots,n \tag{8.68}$$

$$\frac{\partial \varepsilon}{\partial t} = -\sum_{i=1}^{n} \delta_i \frac{\partial b_i}{\partial t} - g(q)\xi_1(\varepsilon - \varepsilon_*(q,b)) + h(q)\xi_2(\varepsilon^*(b) - \varepsilon) \tag{8.69}$$

$$\frac{\partial \varepsilon}{\partial t} + \frac{\partial q}{\partial x} = 0 \tag{8.70}$$

$$q = -K(m, b, \varepsilon)\frac{\partial p}{\partial x} \tag{8.71}$$

to be satisfied in the classical sense in $(0, L) \times (0, T)$ for some given $T > 0$ (L is the thickness of the medium), together with the initial and boundary conditions:

$$b(x, 0) = b_0(x) > 0, \quad m(x, 0) = m_0(x) \geq 0, \quad 0 \leq x \leq L \tag{8.72}$$

$$m(0, t) = 0, \quad 0 \leq t \leq T \tag{8.73}$$

$$\varepsilon(x, 0) = \varepsilon_0(x) = \varepsilon^*(b_0), \quad 0 \leq x \leq L \tag{8.74}$$

$$p(0, t) = p_0(t), \quad p(L, t) = 0, \quad 0 \leq t \leq T. \tag{8.75}$$

The unknown quantities of system (8.67) to (8.75) are the concentrations b and m, the flux q, the porosity ε, and the pressure p. The given functions F_i, G_i, $i = 1, \ldots, n$, g, h, ξ_1, ξ_2, ε_*, ε^*, and β_i and all the data in (8.72) to (8.75) are assumed to be C^1 with Lipschitz derivatives, as well as the threshold functions β_i, $i = 1, \ldots, n$, for which we assume (in the same way as in (8.14)) $\beta_i' \leq 0$. Note that the initial value b_0 in (8.72) is not constant, as it was in part I (cfr. assumption (c) in Section 8.3.1).

As we will see, the mathematical character of (8.67) to (8.75) differs substantially from the problem studied in the previous section. To begin, the initial flux $q(x, 0)$ is not given and is not easily computable.

8.4.2 Determination of the Initial Flux

We start from the following.

Lemma 8.4. *The initial flux $q(x, 0)$ is determined in a unique way by the given initial conditions $b_0(x)$, $m_0(x)$, $\varepsilon_0(x)$, and $p(0, 0)$, $p(0, L)$.*

Proof. By combining (8.68), (8.69), and (8.70) we get the following ordinary differential equation for q:

$$\frac{\partial q}{\partial x} = \Gamma(q, \varepsilon, b) \tag{8.76}$$

with

$$\Gamma(q, \varepsilon, b) = -\sum_{i=1}^{n} \delta_i F_i(q, b) G_i\left(b - \beta_i(q, b)\right) + g(q)\xi_1(\varepsilon - \varepsilon_*(q, b)) - h(q)\xi_2(\varepsilon^*(b) - \varepsilon). \tag{8.77}$$

However, we miss the condition for $x = 0$. For $t = 0$, the right-hand side of (8.76) is a prescribed function of q and x, by virtue of (8.72) and (8.74) (note that the last term in (8.77) vanishes for $t = 0$). Thus, for $t = 0$ (8.76) is a nonlinear ordinary differential equation for the unknown $q(x, 0)$. The initial condition $q(0, 0) = q_0^* > 0$ must be determined in such a way that the corresponding solution $q(x, 0; q_0^*)$ is compatible with (8.71). Recalling that $p_0(0) = 1$, $p(1, 0) = 0$ (cfr. (8.75)), and integrating (8.71) we have

$$\int_0^1 \frac{q(x, 0; q_0^*)}{K(b_0, m_0, \varepsilon_0)} \, dx = 1 \tag{8.78}$$

We are now going to prove that equation (8.78) determines q_0^* uniquely. Indeed, we first observe that

$$\lim_{q_0^* \to +\infty} q(x, 0; q_0^*) = +\infty$$

uniformly in $(0, 1)$, because Γ is bounded, and that $q(x, 0; 0) = 0$, because $g(0) = 0$ and either $F_i(0) = 0$ or we assume that $(b_i - \beta_i(0))^+ = 0$. Next we define

$$Q(x, q_0^*) = \frac{\partial}{\partial q_0^*} q(x, 0; q_0^*)$$

which satisfies

$$\frac{\partial Q}{\partial x} = Q \frac{\partial \Gamma}{\partial q}, \quad Q(0, q_0^*) = 1, \quad \forall q_0^*.$$

Therefore $Q > 0$, i.e., $q(x, 0; q_0^*)$ increases with q_0^*, $\forall x$. Consequently the integral in (8.78) increases monotonically from 0 to ∞ as q_0^* goes from 0 to $+\infty$. We conclude that (8.78) has exactly one positive solution q_0^* and $q(x, 0)$ is uniquely determined. □

8.4.3 The Fixed-Point Argument

Although we are not going to reproduce in all details the proof of global existence and uniqueness for system (8.67) to (8.75), we will briefly sketch the argument on which it is based. We first remark that for a given $q(x, t)$ the quantities b, m, and ε can be calculated by using (8.68) to (8.67), and (8.70) together with the corresponding data (8.73) to (8.75). Then Darcy's law (8.71) can be used to construct a mapping on q in such a way that any possible fixed point of it corresponds to a solution of problem (8.67) to (8.75).

More specifically, this procedure goes through the following steps:

(i) For any $T > 0$ define the set

$$X_1 = \{q \in C([0,1] \times [0,T]) | q(x,0) = q_0(x), 0 < q_m \leq q \leq q_M$$

$$\frac{|q(x_1,t) - q(x_2,t)|}{|x_1 - x_2|} \leq A_x, x_1 \neq x_2, t \in [0,T] \tag{8.79}$$

$$\frac{|q(x,t_1) - q(x,t_2)|}{|t_1 - t_2|} \leq A_t, t_1 \neq t_2, x \in [0,1]\}$$

where q_m and q_M are positive constants that depend on the norms of the given data and on T. The initial flux $q_0(x) = q(x,0)$ is computed using the method illustrated in Lemma 8.4. Note that it is very important to keep distinct the two Lipschitz constants A_x and A_t.

(ii) Compute $b(x,t)$ by means of (8.68) and the initial condition in (8.72).

(iii) Calculate $\varepsilon(x,t)$ by integrating

$$\frac{\partial \varepsilon}{\partial t} = -\Gamma(q,b,\varepsilon), \quad \varepsilon(x,0) = \varepsilon_0(x) \tag{8.80}$$

with Γ defined by (8.77).

(iv) Compute $m(x,t)$: This step is more complicated because (8.67) requires the definition of the spatial derivatives of ε and q, which at this stage are not known to exist. To avoid such a difficulty, we use the modified system

$$\frac{\partial m_i}{\partial t} + \alpha_i \frac{q}{\varepsilon} \frac{\partial m_i}{\partial x} + \alpha_i \frac{1}{\varepsilon} \Gamma(q,\varepsilon,b) - \alpha_i \frac{q}{\varepsilon^2} E m_i$$

$$= F_i(q,b) G_i(b_i - \beta_i(q,b)), \quad i = 1, \ldots, n \tag{8.81}$$

where Γ is a natural replacement for $\frac{\partial q}{\partial x}$. The function $E(x,t)$, taking the place of $\frac{\partial \varepsilon}{\partial x}$, is obtained by integrating the following ordinary differential equation, which comes from differentiating formally (8.80) with respect to x:

$$\begin{aligned} \frac{\partial E}{\partial t} &= -\Gamma_q \Gamma - \Gamma - \varepsilon E - \nabla \Gamma \cdot B \\ E(x,0) &= \varepsilon_0'(x), \quad 0 \leq x \leq 1. \end{aligned} \tag{8.82}$$

The function $B(x,t)$ appearing in (8.82) plays the role of $\frac{\partial b}{\partial x}$ and is

the solution of the system

$$\begin{aligned}\frac{\partial B_i}{\partial t} &= \left(-\frac{\partial F_i}{\partial q}\Gamma - \nabla_b F_i \cdot B\right) G_i\left(b_i - \beta_i(q,b)\right) \\ &\quad + F_i(q,b)\left(B_i - \Gamma\frac{\partial \beta_i}{\partial q} - \nabla_b \beta_i \cdot B\right) G_i'\left(b_i - \beta_i(q,b)\right) \qquad (8.83) \\ B_i(x,0) &= b_{i,0}'(x), \quad i = 1,\ldots,n.\end{aligned}$$

Once the function $E(x,t)$ has been found, equations (8.81) can be integrated with the appropriate initial and boundary conditions.

(v) Calculate the new guess $q^*(x,t)$ by first defining

$$\hat{q}(x,t;\chi(t)) = \chi(t) + \int_0^1 \Gamma(q,\varepsilon,b)\,dx \qquad (8.84)$$

and determining $\chi(t)$ corresponding to q^* so that (8.84) is consistent with (8.71), i.e.,

$$\int_0^1 \frac{\hat{q}(x,t;\chi(t))}{K(b,m,\varepsilon)}\,dx = p_0(t). \qquad (8.85)$$

Existence and uniqueness of $\chi(t)$ satisfying equation (8.85) is established using the same argument as in Lemma 8.4. Thus the operator $\mathcal{F}q = q^*$, where $q^*(x,t) = \hat{q}(x,t;\chi(t))$, is well defined for any $q \in X_1$.

The existence of a unique fixed point $q^* = \mathcal{F}q$ in X_1 is proved using Banach's theorem, i.e., showing that $\mathcal{F}$ is a contraction in a suitably small time interval. Global existence follows from Schauder's fixed-point theorem. The main difficulty is to select the constant A_t so that it bounds the Lipschitz constants of both q and q^* with respect to t. The crucial point is to prove that the Lipschitz constant of b, m, and ε are independent of A_t.

It is important to remark that getting estimates of this kind allows us to avoid imposing other limitations that would certainly not be physical.

On the other hand, we must say that a condition that appears in a natural way in the proof is the following:

$$\begin{aligned}&F_0' \sum_{i=1}^n \delta_i \|b_{i,0}\| + F_0 \sum_{i=1}^n \delta_i \beta_0' + (\|g'\| + \|h'\|) \\ &\quad \times(\varepsilon_M - \varepsilon_m) + E_* \|g\| \le \left(1 + \frac{K_M}{K_m}\right)^{-1} \qquad (8.86)\end{aligned}$$

where $0 < \varepsilon_m < \varepsilon_M < 1$ are, respectively, lower and upper limits for both ε_* and ε^*, K_m and K_M lower and upper limits for K, the norm is the sup-norm and E_* is a suitable constant such that

$$-E_* \le \frac{\partial \varepsilon_*}{\partial q} \le 0.$$

Condition (8.86) does not seem purely technical; from a physical point of view, we may say that it expresses that the variation with q of the physical coefficients entering the model must be sufficiently slow. A possible explanation could be that violating such conditions could be in contrast with the requirement that saturation of the medium is maintained. In this aspect such a behavior seems related to the physical assumption underlying the volume balance equation (8.63). The final result can be stated as follows.

Theorem 8.3. *Under the assumptions listed in Section 8.4.1, problem (8.67) to (8.75) has one unique solution for all T, provided the derivatives with respect to q of the coefficients appearing in the model are sufficiently small.*

8.5 Part III: A Comprehensive Model (References: [22], [29])

Our aim is now to join together the various aspects of the problem analyzed separately in the previous sections. In other words, we want to combine the model presented in Part I, focused on the buildup of the compact layer by a single species of moving particles, with the model discussed in Part II, where several species are transported by the flow but they are allowed to leave the system.

In the model we are going to formulate, the removed components are both fine solid particles, which are transported convectively by the flow, and other substances, which may also diffuse in the liquid. Moreover, the porosity is affected by the removal process, but here we neglect the additional effects of flow-induced compression and elastic response of the medium described by equation (8.65). As a matter of fact, the elimination of deformability simplifies the exposition but is not a critical mathematical simplification. On the other hand, we will not introduce any approximation in the overall volume balance.

8.5.1 The Governing Equations

In addition to the concentrations b_i, m_i, $i = 1, \ldots, n$ defined in the same way as in Part II, we will use the following dimensionless quantities corresponding to the specific volumes of each species:

$$\begin{cases} \theta_i = b_i/\rho_i^{(b)}, & i = 1, \ldots, n \\ \eta_i = m_i/\rho_i^{(m)}, & i = 1, \ldots, n \\ \eta_w = m_w/\rho_w & \text{water} \end{cases} \tag{8.87}$$

where $\rho_i^{(\ell)}$, $\ell = b, m$ are the densities of each species.

We introduce the following distinction among the species:

- the indexes $i = 1, \ldots, k < n$ refer to fine solid particles, either when bound to the porous matrix (b_i) or when moving in the flow (m_i),
- the indexes $i = k+1, \ldots, n$ refer to substances in the porous matrix that once removed are dissolved in the fluid as solutes or droplets (b_i for the substances attached to the porous matrix and m_i for the dissolved substances).

In terms of the volumetric variables (8.87), the porosity is

$$\varepsilon = \eta^{(k)} + \eta_w \quad \text{porosity}, \qquad \eta^{(k)} = \sum_{i=k+1}^{n} \eta_i. \tag{8.88}$$

If we denote by V_{m_i} and V_w the molecular velocities of the species m_i and of the water, respectively, we find for the volumetric flux the following expression:

$$q = \eta_w V_w + \sum_{i=k+1}^{n} \eta_i V_{m_i}. \tag{8.89}$$

We also define the cumulative volume fractions

$$\eta_{(k)} = \sum_{i=1}^{k} \eta_i, \quad \theta_{(k)} = \sum_{i=1}^{k} \theta_i, \quad \theta^{(k)} = \sum_{i=k+1}^{n} \theta_i \tag{8.90}$$

and $\theta_0 = \theta_0(x)$ as the volume fraction (with respect to the unit volume of the total system) of the rigid porous skeleton. The part of unit volume complementary to (8.88) and occupied by solid components is partitioned as follows:

$$1 - \varepsilon = \eta_{(k)} + \theta_0 + \theta^{(k)} + \theta_{(k)}. \tag{8.91}$$

Before writing the complete mathematical model, we are going to model the two aspects that have been neglected in the previous model (part II), i.e., diffusion and formation of the compact layer with several species of particles. In order to write the balance equation for the diffusive species $i = k+1, \ldots, n$, we start from the usual balance (8.3) (written for m_i, b_i). However, the molecular velocities V_{m_i}, $i = k, \ldots, n$ are not purely convective as in (8.4), but they are related to the average velocity $V = q/\varepsilon$ in the following way (we refer to [29] for the detailed derivation of the formula):

$$m_i V_{m_i} = m_i V - \varepsilon D_i \frac{\partial}{\partial x}\left(\frac{m_i}{\varepsilon}\right), \quad i = k+1, \ldots, n. \tag{8.92}$$

Note that in (8.92) interdiffusion effects are neglected.

Concerning the migrating particles, we assume, as is natural, that they are no longer mobile in the compact layer. We call M_i, $i = 1, \ldots, k$, the concentration of the i-species in the compact layer $s(t) < x < 1$. The functions $M_i(x)$ are not known. The structure of the compact layer, corresponding to a sequence $M_1, \ldots M_k$, depends on the history of the process, because it depends on the incoming flux of particles.

This represents a nontrivial difference between the current situation and the case of a single species of particles (part I): in the latter model the concentration M is known a priori. Modeling the formation of the compact layer means to prescribe a constraint for the concentrations M_i, i.e., to prescribe a packing configuration:

$$f(M_1, \ldots, M_k) = 0 \tag{8.93}$$

A simple but reasonable way to prescribe the packing configuration (8.93) is the following, which refers to the specific volumes of the species:

$$\sum_{i=1}^{k} \frac{M_i}{\rho_i} = \Theta \tag{8.94}$$

where ρ_i is the density of the ith species and Θ is a known quantity. Equation (8.94) means that the layer is compact when the incoming particles occupy the maximum specific volume at their disposal, represented by Θ. A possible distribution of specific volumes at $t = 0$ is drawn in Figure 8.8.

At this point we define the two regions, which are outlined in Figure 8.9.

$$\begin{aligned} D_T &= \{(x,t) : 0 < x < s(t), 0 < t < T\} \\ R_T &= \{(x,t) : s(t) < x < 1, 0 < t < T\} \end{aligned} \tag{8.95}$$

We write the complete set of the governing equations, which will be commented on next (for more details we refer to ([22])):

$$\frac{\partial m_i}{\partial t} + \frac{\partial}{\partial x}\left(\alpha_i m_i \frac{q}{\varepsilon}\right) = -\frac{\partial b_i}{\partial t}, \quad i = 1, \ldots, k, \ (x,t) \in D_T \tag{8.96}$$

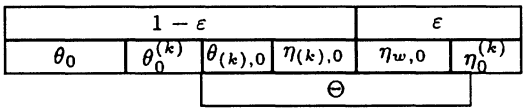

Figure 8.8 — The volume distributions at the initial time $t = 0$; the porosity ε is partitioned as in (8.87), while the complementary volume $1 - \varepsilon$ as in (8.91). The lower strip shows a possible value for the critical specific volume Θ (defined by (8.94)), which must be between $\theta_{(k),0} + \eta_{(k),0}$ and $\theta_{(k),0} + \eta_{(k),0} + \varepsilon$ (cfr. (8.120)).

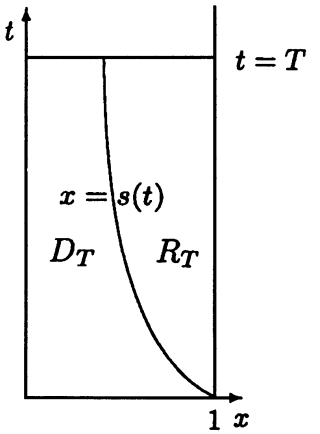

Figure 8.9 — The regions D_T (active region) and R_T (compact layer).

$$\frac{\partial m_i}{\partial t} + \frac{\partial}{\partial x}\left(-D_i\varepsilon\frac{\partial}{\partial x}\frac{m_i}{\varepsilon}\right) + \frac{\partial}{\partial x}\left(m_i\frac{q}{\varepsilon}\right) = -\frac{\partial b_i}{\partial t} \qquad i = k+1,\dots,n, \quad (x,t) \in D_T \cup R_T \tag{8.97}$$

$$q = -K(b,m,\varepsilon)\frac{\partial p}{\partial x}, \quad (x,t) \in D_T \cup R_T \tag{8.98}$$

$$\frac{\partial b_i}{\partial t} = -F_i(q,b)G_i[b_i - \beta_i(q,b)]^+, \quad i = 1,\dots,k, \quad (x,t) \in D_T \tag{8.99}$$

$$\frac{\partial b_i}{\partial t} = -H_i(q,b), \quad i = k+1,\dots,n, \quad (x,t) \in D_T \cup R_T \tag{8.100}$$

$$\frac{\partial \varepsilon}{\partial t} + \frac{\partial q}{\partial x} = -\frac{\partial}{\partial t}\theta^{(k)}, \quad (x,t) \in D_T \cup R_T \tag{8.101}$$

$$\frac{\partial q}{\partial x} + \frac{\partial}{\partial x}\sum_{i=1}^{k}\left(\alpha_i\eta_i\frac{q}{\varepsilon}\right) = 0, \quad (x,t) \in D_T \cup R_T. \tag{8.102}$$

The initial and boundary conditions are the following:

$$m_i(x,0) = m_{i,0}(x), \quad i = 1,\dots,n, \quad x \in [0,1] \tag{8.103}$$

$$\varepsilon(x,0) = \varepsilon_0(x), \quad x \in [0,1] \tag{8.104}$$

$$b_i(x,0) = b_{i,0}(x), \quad i = 1,\dots,n, \quad x \in [0,1] \tag{8.105}$$

$$m_i(0,t) = 0, \quad i = 1,\dots,k, \quad 0 \le t \le T \tag{8.106}$$

$$D_i\varepsilon(0,t)\frac{\partial m_i}{\partial x}(0,t) = \frac{q(0,t)m_i(0,t)}{\varepsilon(0,t)}, \quad i = k+1,\dots,n, \quad 0 < t < T \tag{8.107}$$

$$[[p]] = 0, \quad x = s(t), \tag{8.108}$$

$$\left[\left[\frac{m_i}{\varepsilon}\right]\right] = 0, \quad x = s(t), \quad i = k+1, \ldots, n \tag{8.109}$$

$$\left[\left[D_i \varepsilon \frac{\partial}{\partial x} \frac{m_i}{\varepsilon}\right]\right] = 0, \quad x = s(t), \quad i = k+1, \ldots, n \tag{8.110}$$

$$\left(\Theta - (\eta_{(k)} + \theta_{(k)})\right) \dot{s} = -\frac{q}{\varepsilon} \sum_{i=1}^{k} \alpha_i \eta_i, \quad x = s(t), \ 0 \le t \le T \tag{8.111}$$

$$\frac{\partial}{\partial x} \frac{m_i}{\varepsilon}(1,t) = 0, \quad i = k+1, \ldots, n \tag{8.112}$$

$$p(0,t) = p_0(t) > 0, \quad p(1,t) = 0, \quad 0 \le t \le T \tag{8.113}$$

$$s(0) = 1. \tag{8.114}$$

The unknown quantities for system (8.96) to (8.114) are the concentrations $b_i(x,t)$, $m_i(x,t)$, $i = 1, \ldots, n$ (or the specific volumes θ_i, η_i, $i = 1, \ldots, n$, see (8.87)), the liquid flux $q(x,t)$, the porosity $\varepsilon(x,t)$, the liquid pressure $p(x,t)$ and the free boundary $s(t)$. The balance (8.97) is written according to (8.92)). Note that the removal process (species $i = 1, \ldots, k$) occurs only in the region D_T, while the extraction process (species $i = k+1, \ldots, n$) may also take place in the compact layer R_T.

Equations (8.100) regulate the extraction of soluble substances from the porous matrix. Contrary to the fine particles, we assume that there is not a threshold concentration that interrupts the process.

The global conservation laws (8.101) and (8.102), introduced and discussed in [29] under the hypothesis $\rho_i^{(b)} = \rho_i^{(m)} = \rho_i$ (which will be assumed from now on), $i = 1, \ldots, n$, are found by rearranging the balance equations (8.96) and (8.97). Equation (8.101) describes the rate of change of porosity. Note that the quantities corresponding to the fine particles $i = 1, \ldots, k$ are not present in this evolutive equation, because they are computed in the complementary volume $1 - \varepsilon$, both if they are bound to the porous medium and if they are transported by the flow. The formula (8.102) is the conservation of the total volume of all the moving components (water and species η_i, $i = 1, \ldots, n$).

The initial and boundary conditions (8.103) to (8.106), (8.108), (8.113), and (8.114) need no comment. Eq. (8.107) corresponds to assuming that the velocity V_i, $i = k+1, \ldots, n$ vanishes for $x = 0$, while (8.109) means that the concentrations of the i-species, $i = k+1, \ldots, n$ in the flowing liquid are continuous across the boundary $x = s(t)$. The boundary condition (8.110), expressing the continuity of the diffusive flux at the interface, is a consequence of (8.8) (written for the species $i = k+1, \ldots, n$). The latter equation, together with (8.94) and written for the species $i = 1, \ldots, k$ also

gives the free boundary condition (8.111). Finally, by condition (8.112) we assume that the effect of diffusion is negligible at the outflow surface $x = 1$.

Remark 8.1. *The function $\theta_0(x)$, which gives the volume fraction of the porous skeleton (cfr. (8.91)), can be calculated by means of (8.103) to (8.105):*

$$\theta_0(x) = 1 - (\varepsilon_0(x) + \eta_{(k),0}(x) + \theta_{(k),0}(x) + \eta_0^{(k)}(x)). \tag{8.115}$$

Obviously, the initial data on the right-hand side of (8.115) are physically consistent only if $0 < \theta_0(x) < 1$.

Remark 8.2. *The water volume fraction η_w and the water velocity V_w can be computed a posteriori by means of (8.88) and (8.89), once problem (8.96) to (8.114) has been solved.*

Remark 8.3. *From (8.8) written for $i = k+1, \ldots, n$ the following condition at $x = s(t)$ can be obtained (cfr. (8.11) and the comment that follows it):*

$$[[\varepsilon]]\, \dot{s}(t) = [[q]]\,. \tag{8.116}$$

8.5.2 List of Assumptions

We assume that the given functions $K(b, m, \varepsilon)$, $F_i(q, b)$, $G_i(\eta)$, $\beta_i(q, b)$, $i = 1, \ldots, k$, $H_i(q, b)$, $i = k+1, \ldots, n$, $\varepsilon_0(x)$, $m_{i,0}(x)$, $b_{i,0}(x)$, $i = 1, \ldots, n$, and $p_0(t)$ are nonnegative C^1-functions of their respective arguments and each first derivative is Lipschitz continuous. Moreover, we will assume that there exist positive constants K_m, K_M, p_0^m, p_0^M, and m_0 such that:

$$0 < K_m \leq K(b, m, \varepsilon) \leq K_M \quad \forall\, b, m, \varepsilon \tag{8.117}$$

$$0 < p_0^m \leq p_0(t) \leq p_0^M, \quad t \geq 0. \tag{8.118}$$

The initial distribution of the various species must satisfy

$$m_{i,0}(x) \not\equiv 0, \quad b_{i,0}(x) \not\equiv 0, \quad x \in [0, 1] \tag{8.119}$$

$$\eta_{(k),0}(x) + \theta_{(k),0}(x) < \Theta < 1 - (\theta_0(x) + \theta_0^{(k)}(x)), \quad x \in [0, 1]. \tag{8.120}$$

Condition (8.120) means that the initial concentration of particles is below the packing configuration in any point of the medium. On the other hand, the critical specific volume Θ cannot exceed the space at disposal at the initial time.

We remark that combining (8.120) with (8.91) and recalling (8.115) we get the following constraint for the initial porosity:

$$1 - \left(\Theta + \theta_0(x) + \theta_0^{(k)}(x)\right) < \varepsilon_0(x) < 1 - \theta_0(x), \quad x \in [0, 1]. \tag{8.121}$$

Setting

$$\varepsilon_0^m = \min_{x\in[0,1]} \left(1 - (\Theta + \theta_0(x) + \theta_0^{(k)}(x))\right), \quad \varepsilon_0^M = \max_{x\in[0,1]} (1 - \theta_0(x)) \tag{8.122}$$

(note that $0 < \varepsilon_0^m < \varepsilon_0^M < 1$), we deduce from (8.121) and (8.122):

$$0 < \varepsilon_0^m < \varepsilon_0(x) < \varepsilon_0^M < 1, \quad x \in [0,1]. \tag{8.123}$$

8.5.3 The Fixed-Point Procedure for Local Existence and Uniqueness

The proof of existence and uniqueness for problem (8.96) to (8.114) consists of two steps. First, the result is shown locally with respect to time. Then, by showing that the local solution fulfills some special properties, we can extend the result with no limitation in time by an iterative procedure.

The proof is based on a fixed-point argument. In the same spirit of the procedure we illustrated in Part II, we observe that if a pair (q, s) is known to solve the problem, we can calculate all the remaining quantities as follows:

- Calculate $b_i(x,t)$, $i = 1, \ldots, n$, from (8.96).
- Solve the ordinary differential equation (8.101), (8.104) with respect to $\varepsilon(x,t)$.
- Find $m_i(x,t)$, $i = 1, \ldots, k$ from the hyperbolic problems in R_T (8.96), (8.103) ($i = 1, \ldots, k$), (8.106), find $m_i(x,t)$, $i = k+1, \ldots, n$ from the parabolic problems of diffraction type in $R_T \cup D_T$ (8.97), (8.103) ($i = k+1, \ldots, n$), (8.107), (8.109), (8.110), and (8.112).
- Calculate $p(x,t)$ from (8.98) and (8.113).

At this point, we use (8.102) and (8.111) to find the new guesses $\tilde{q}$ and $\tilde{s}$, respectively. Formally, we define the closed convex set of functions

$$\mathcal{E}_T(u_1, u_2, A_y, A_t, M_y, M_t, s_0, A_s, M_s) = \left\{(u(y,t), s(t)) \mid u \in C^{1,1}(\bar{B}_T)\right. \tag{8.124}$$

$$u(y,0) = q_0(y), \quad 0 \le y \le 1, 0 < u_1 \le u(y,t) \le u_2$$

$$\left|\frac{\partial u}{\partial y}(y,t)\right| \le A_y, \quad \left|\frac{\partial u}{\partial t}(y,t)\right| \le A_t, \quad (y,t) \in \bar{B}_T$$

$$\left|\frac{\partial}{\partial y}u(y_1,t) - \frac{\partial}{\partial y}u(y_2,t)\right| \le M_y\,|y_1 - y_2|, \quad \forall\, y_1, y_2 \in [0,1]$$

$$\left|\frac{\partial}{\partial t}u(y_1,t) - \frac{\partial}{\partial t}u(y_2,t)\right| \le M_t\,|y_1 - y_2|, \quad \forall\, y_1, y_2 \in [0,1]$$

$$s \in C^1[0,T], s(0) = 1, \quad 0 < s_0 \leq s(t) \leq 1$$

$$-A_s \leq \dot{s}(t) \leq 0, \quad 0 \leq t \leq 1$$

$$|\dot{s}(t_1) - \dot{s}(t_2)| \leq M_s |t_1 - t_2| \quad \forall\, t_1, t_2 \in [0,T]\}.$$

Taking a pair $(u,s) \in \mathcal{E}$, we set $q(x,t) = u(x/s(t),t)$, $(x,t) \in \bar{D}(T)$, and we define the map $\mathcal{F}(u,s) = (\tilde{u},\tilde{s})$ with

$$\tilde{u}(y,t) = f(t)\frac{1}{1+l(s(t)y,t)}, \quad (y,t) \in B_T$$

$$\tilde{s}(t) = 1 - \int_0^t \frac{l(s(\tau),\tau)q(s(\tau),\tau)}{\Theta - \left(\eta_{(k)}(s(\tau),\tau) + \theta_{(k)}(s(\tau),\tau)\right)}d\tau, \quad t \in [0,T]$$

where $l = \eta_{(k)}/\varepsilon$ and

$$f(t) = q(0,t) = \frac{p_0(t)}{\displaystyle\int_0^{s(t)} \frac{1}{1+l(\xi,t)}\frac{1}{K(\xi,t)}d\xi + \frac{1-s(t)}{K_0}}. \tag{8.125}$$

Then define $\tilde{q}(x,t) = \tilde{u}(x/\tilde{s}(t),t)$ in $\{(x,t) : x \in [0,\tilde{s}(t)],\, t \in [0,T]\}$.

If $(\bar{u},\bar{s})$ is a fixed point of $\mathcal{F}$ in $\mathcal{E}_T$, then $\bar{q} = \bar{u}(x/\bar{s},t)$ and $\bar{s}$ and the corresponding calculated functions $(\bar{b},\bar{m},\bar{\varepsilon},\bar{p})$ fulfill system (8.96) to (8.114). We do not reproduce here the proof of existence and uniqueness; we refer to [23] for all details. We just mention the fact that in the current case the initial flux $q_0(x)$ can also be computed: by integrating (8.98) and setting $l_0 = \frac{\eta_{(k),0}}{\varepsilon_0}$, we can find

$$q_0(x) = \frac{p_0(0)}{\displaystyle\int_0^1 \frac{1}{1+l_0(\xi)}\frac{1}{K(b_0(\xi),m_0(\xi),\varepsilon_0(\xi))}d\xi}\frac{1}{1+l_0(x)}. \tag{8.126}$$

We also remark that the partial differential equation problems for $m_i(x,t)$ require, once again, the spatial derivative of ε. In order to avoid such difficulty, we use (8.102) to replace $\partial\varepsilon/\partial x$ with the following expression

$$\frac{\varepsilon}{q}\left(\frac{\partial q}{\partial x} - \frac{q}{\varepsilon + \eta_{(k)}}(\zeta_0 + \sum_{i=1}^{k}\zeta_i)\right)$$

where ζ_i, $i = 1,\ldots,n$ play the role of $\partial\theta_i/\partial x$ and solve appropriate ordinary differential equations, which can be found in the same way as (8.83). We are going now to state the main result.

We first define (cfr. (8.99)) $\Phi_i(q,b) = F_i(q,b)G_i(q,b)$ $i = 1,\ldots,k$ and

$$\hat{\Phi}_i = \frac{\Phi_i}{\rho_i}(q,\rho_1\theta_1,\ldots,\rho_n\theta_n), \quad \hat{\Phi} = \sum_{i=1}^{k}\Phi_i.$$

Moreover, we introduce the following quantities:

$$\beta = \frac{\|\hat{\Phi}\| K_M p_0^M}{\varepsilon_0^m}, \quad \epsilon_2 = \varepsilon_0^M + \varepsilon_0^m + \|\theta_0^{(k)}\| \tag{8.127}$$

where the norm is the sup-norm. We also take C_1 as a constant such that

$$\left(\frac{\|\eta_{(k),0}\|}{\varepsilon_0^m} + \beta\right)(1-\beta)^{-1} < C_1 < \frac{\|\theta_{(k),0}\|}{\epsilon_2}.$$

In order to simplify the mathematical presentation of the proof, it can be assumed that the dependence of K on m_i occurs through q (in other words, $K = K(q, b, \varepsilon)$). Even if we are going to make such an assumption, it must be said that it plays a very marginal role in the proof of the main result, which is stated soon.

Theorem 8.4. *System (8.96) to (8.114) has exactly one solution for any $t \leq 0$ provided that:*

(*i*) $\beta < 1$, $\frac{\epsilon_2/\varepsilon_0^m}{1-\beta}\|\eta_{(k),0}\| + \|\theta_{(k),0}\| + \epsilon_2 \frac{1}{1-\beta} < \Theta$,

(*ii*) $p_0^M (1 + C_1)^2 \left|\frac{\partial K}{\partial q}\right| < 1$, *and*

(*iii*) *the Lipschitz constants with respect to x of the given functions ε_0, $\eta_{(k),0}$, $\eta_0^{(k)}$, ε_0', $\eta_{(k),0}'$, the Lipschitz constants $L_{\hat{S}_i}^q$, $L_{\hat{S}_i}^\theta$, $i = 1, \ldots, n$ of the removal functions are sufficiently small.*

As we said earlier, the first step in proving existence and uniqueness for (8.96) to (8.114) consists of showing that the result is true in a suitable interval $(0, T)$. In order to extend the proof globally in time, it is crucial to show that the local solution has the following properties:

(1) the interface $s(t)$ is bounded by the quantity $s_{\min}$, which depends only on the initial distribution of the fine particles:

$$s_{\min} = 1 - \frac{\bar{m}_0}{\Theta}, \quad \bar{m}_0 = \int_0^1 (\eta_{(k),0} + \theta_{(k),0})\, dx$$

(2) the total specific volume of the fine particles is below the critical value Θ in any point of the region D_T:

$$\eta_{(k)} + \theta_{(k)} < \Theta, \quad (x, t) \in D_T$$

(3) the porosity calculated at the time $t = T$ is bounded by the same quantities appearing in (8.122):

$$\varepsilon_0^m < \varepsilon(x, T) < \varepsilon_0^M, \quad x \in [0, s(T)].$$

We now revert to Theorem 8.4 to comment briefly on the assumptions stated there. Condition (*i*) is especially important: It is more restrictive

than the following one (cfr. (8.120))

$$\|\eta_{(k),0}\| + \|\theta_{(k),0}\| < \Theta. \tag{8.128}$$

In the model examined in Part I, condition (8.128) is sufficient to guarantee that the concentration of particles is below the critical value at any point of the region where the removal process occurs. In the current case, in which we allow for nonuniform initial distribution of particles and space-dependent volumetric flux, (8.128) is no longer sufficient. It is not difficult to exhibit examples of processes in which (8.128) is valid at the initial time but violated at some point in D_T. This kind of problem is indeed more complex; it is necessary to introduce a second free boundary for the developing new compact layer. It is worth noticing that condition (i) in Theorem 8.4 involves not only the initial distribution of particles but also the removal rate through the norm of $\hat{\Phi}$.

Conditions (ii) and (iii) require that the variation of the given functions with respect to their arguments is sufficiently slow. This is in the same spirit as the corresponding conclusions of part II, despite the different choice of the evolutive equation for the porosity.

We conclude with some qualitative properties of the solution. We have to say that in the current case the complexity of the problem does not allow us to develop as deep a qualitative analysis as the one performed in Part I. An immediate property coming from the study of the characteristic curves of (8.96) is showed in Figure 8.10. Referring to the global solution, we omit the index T in (8.95) and call (cfr. also (8.99))

$$\mathcal{S} = \{(x,t) \in D \mid b_i(x,t) \leq \beta_i(q,b),\ i = 1,\dots,k\} \quad \mathcal{R} = D/\mathcal{S}$$

It is easy to see that:

- if a characteristic curve of (8.96) Γ is such that $\Gamma \bigcap \mathcal{R} \neq \emptyset$ (curves Γ_1 and Γ_2 in Figure 8.10), then $\dot{s}(\tau) \neq 0$, where τ is the time when Γ intersect the boundary s.
- if Γ belongs entirely to $\mathcal{S}$ (curve Γ_3 in Figure 8.10), then $\dot{s}(\tau) = 0$.

Calling $\mathcal{S}_1 = \{\Gamma \subset \mathcal{S} | \Gamma \cup \mathcal{R} = \emptyset\}$ (in Figure 8.10 $\mathcal{S}_1$ is the region bounded by the t-axis, the curve $\hat{\beta}$, and $x = s(t)$), we have

$$\eta_{(k)} = 0, \quad \theta_{(k)} \text{ constant}, \quad \frac{\partial q}{\partial x}(x,t) = 0, \quad \dot{s}(t) = 0 \quad (x,t) \in \mathcal{S}_1$$

and

$$q_c(t) = q\left(1 + \frac{\eta_{(k)}}{\varepsilon}\right)|_{x=s} \quad (x,t) \in \mathcal{S}_1. \tag{8.129}$$

The (constant) value of s is obtained by solving the equation (cfr. (8.125))

$$q_c(t)\left(\frac{1-s}{K_0} + \int_0^s \frac{1}{K(\xi,t)} d\xi\right) = p_0(t).$$

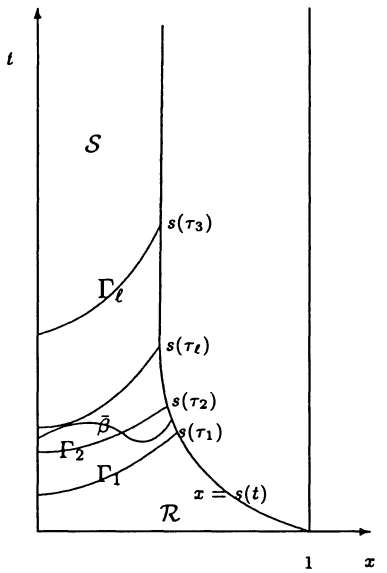

Figure 8.10 — The characteristic curves Γ_1 and Γ_2 are totally or partially contained in $\mathcal{R}$, hence $\dot{s}(\tau_1)$ and $\dot{s}(\tau_2)$ are negative; Γ_3 is contained in $\mathcal{S}$, hence $\dot{s}(\tau_3) = 0$. The curve $\bar{\beta}$ separates $\mathcal{S}$ from $\mathcal{R}$, while the curve Γ_ℓ is the lower boundary of the region $\mathcal{S}_1$. For $t \geq \tau_\ell$ we have $\dot{s}(t) = 0$.

We notice that, if $(x,t) \in \mathcal{S}_1$, then $K(x,t) = K(b(x,t), m(x,t), \varepsilon(x,t))$ changes with respect to t only if ε varies. From (8.101) we get

$$\frac{\partial K}{\partial t} = -\frac{\partial K}{\partial \varepsilon}\frac{\partial \theta^{(k)}}{\partial t}, \quad (x,t) \in \mathcal{S}_1.$$

We conclude that

- if $\partial K/\partial \varepsilon \geq 0$, then the water flux $q_c(t)$ increases if $p_0(t)$ increases and the removal process may restart ($\dot{s} < 0$) (this occurrence is actually not predictable by the model discussed in part I, cfr. Section 8.3.2).
- if $\partial K/\partial \varepsilon \leq 0$ and $p_0(t)$ does not increase, then $q_c(t)$ is a nonincreasing function and the removal process cannot occur again.

In particular, in the simpler case $K = K(b,m)$, we have that $q_c(t)$ increases (hence a second removal process can occur) if and only if $p_0(t)$ increases. Such a property is consistent with the results obtained in Part I, where p_0 is constant.

8.6 Open Questions and Related Problems

- As we saw in Parts II and III, the initial conditions are actually nonuniform, but the complexity of the corresponding problems do not allow us to perform a detailed qualitative analysis as in the current case. Thus, the asymptotic analysis with nonuniform initial distributions and more general functions $R(m, b)$ in the simpler context of single species of particles and constant porosity is a nontrivial generalization of the problem.
- We have confined our attention to cases in which the removed components of the porous medium go into the flow and there is no adsorption on the solid matrix. However, it also makes sense to consider a more general model of mass exchange (e.g., sorption-desorption processes), taking into account the possible influence of the reaction products. Interesting references about flows accompanied by chemical reactions are [8], [9], [10], [11], [24], [25], [26], and [30].
- The analysis performed so far refers to a simpler situation in which the temperature of the system is constant. It could be very interesting to consider the influence of a coupled thermal field, which entails the presence of heat diffusion and heat convection and the dependence of all the coefficients on the temperature. Such problems are very complex. They are found, for example, in processes for the manufacturing of composite materials (see chapter 9 by A. Farina and L. Preziosi).
- The hydraulic circuit external to the system can be quite complicated, including hydraulic resistances in series. Also the effect of the possible presence of gas bubbles in the supplying circuit is an important and difficult question to be analyzed.

References

1. Baldini, G., Filtrazione non lineare di un fluido attraverso un mezzo poroso deformabile, Thesis, University of Florence, Italy, 1992.
2. Baldini, G., and Petracco, M., Models for water percolation during the preparation of espresso coffee, *7th ECMI Conference*, edited by A. Fasano and M. Primicerio, Teubner, Stuttgart, 131–8 (1994).
3. Bandini, S., Illy, E., Simone, C., and Suggi Liverani, and F., A computational model based on the reaction-diffusion machine to simulate

transportation phenomena: The case of coffee percolation, in *Cellular Automata: Research towards Industry, Proc. ACRI'98*, edited by S. Bandini, R. Serra, and F. Suggi Liverani, Springer Verlag (1998).

4. Bear, J., *Dynamics of Fluids in Porous Media*, Elsevier (1972).
5. Bertaccini, D., Simulation of a filtration in a deformable porous medium. A numerical approach, *Nonlinear Analysis, Theory & Applications*, **30**, 1, 663–8 (1997) (Proc. 2nd World Congress of Nonlinear Analysis).
6. Borsani, C., Cattaneo, G., De Mattei, V., Jocher, U., and Zampini, B., 2D and 3D lattice gas technique for fluid-dynamics simulation, in S. Bandini, R. Serra, and F. Suggi Liverani, *Cellular Automata: Research Towards Industry*, Proc. ACRI'98, edited by Springer-Verlag (1998).
7. Bullo, T., and Illy, E., Considérations sur le procédé d'extraction, *Café, Cacao*, **7**, 4, 395–9 (1963).
8. Chadam, J., Chen, X., Comparini, E., and Ricci, R., Travelling wave solutions of a reaction-infiltration problem and a related free boundary problem, *European J. Appl. Math.*, **5**, 255–66 (1994).
9. Chadam, J., Chen, X., Gianni, E., and Ricci, R., A reaction infiltration problem: Existence, uniqueness and regularity of solutions in two space dimensions, *Math. Models Methods and Appl. Sci.*, **5**, 599–618 (1995).
10. Chadam, J., Hoff, D., Merino, E., Ortoleva, P., and Sem, A., Reactive infiltration instabilities, *IMA J. Appl. Math.*, **36**, 207–20 (1987).
11. Chadam, J., Peirle, A., and Sem, A., Weakly nonlinear stability of reaction-infiltration interfaces, *SIAM J. Appl. Math.*, **48**, 1362–78 (1988).
12. Comparini, E., and Mannucci, P., Penetration of a wetting front in a porous medium interacting with the flow, *Nonlinear Differential Equations and Applications*, **4**, 425–38 (1997).
13. Comparini, E., and Ughi, M., On the existence of shock propagation in a flow through deformable porous media. Preprint of the Mathematics Department of the University of Florence, 8, 1999. Submitted to Interfaces and Free Boundaries.
14. Comparini, E., and Ughi, M., Shock propagation in a one-dimensional flow through deformable porous media. Preprint of the Mathematics Department of the University of Florence, 7, 1999. Submitted to Interfaces and Free Boundaries.
15. Fasano, A., The penetration of a wetting front through a porous medium accompanied by the dissolution of a substance, in *International Congress on Math Modelling of Flow in Porous Media*, edited by A. Bourgeat et al., World Scientific, 183–95 (1995).

16. Fasano, A., Some nonstandard one-dimensional filtration problems, *The Bulletin of the Faculty of Education*, **44**, Chiba University (1996).

17. Fasano, A., and Mikelic, A., On the filtration through porous media with partially soluble permeable grains, *to appear.* in NoDEA.

18. Fasano, A., Mikelic, A., and Primicerio, M., Homogenization of flows through porous media with permeable grains, *Adv. Math. Sci. Appl.*, **8**, 1–31 (1998).

19. Fasano, A., and Primicerio, M., Flows through saturated mass exchanging porous media under high pressure gradients, *Proc. of Calculus of Variations, Applications and Computations*, edited by C. Bandle et al., Pitman Res. Notes Math. Series, **326** (1994).

20. Fasano, A., and Primicerio, M., Mathematical models for filtration through porous media interacting with the flow, in *Nonlinear Mathematical Problems in Industry, I*, M. Kawarada, N. Kenmochi, and N. Yanagihara, *Math. Sci. & Appl.*, **1**, 61–85, edited by Gakkotosho, Tokyo.

21. Fasano, A., Primicerio, M., and Watts, A., On a filtration problem with flow-induced displacement of fine particles, in *Boundary Control and Boundary Variation*, edited by J. P. Zolesio, M. Dekker, New York (1994), 205–32.

22. Fasano, A., and Talamucci, F., A comprehensive mathematical model for a multi-species flow through ground coffee, to appear in *SIAM J. Math. Anal.*

23. Fasano, A., and Tani, P., Penetration of a wetting front in a porous medium with time dependent hydraulic parameters, in *Nonlinear Problems in Applied Mathematics*, edited by K. Cooke et al., SIAM (1995).

24. Gianni, R., and Ricci, R., Existence and uniqueness for a reaction-diffusion problem in infiltration, *Ann. Mat. Pura Appl.*, **168**, 373–94 (1995).

25. Knabner, P., Van Duijn, C., and Nengst, S., An analysis of crystal dissolution fronts in flows through porous media. Part I: Compatible boundary conditions, *Advances in Water Resources*, **18**, 3, 171–85 (1995).

26. Pawell, A., and Krannich K-D, Dissolution effects in transport in porous media, arising in transport in porous media, *SIAM J. Appl. Math.*, **56**, 1, 89–118 (1996).

27. Petracco, M., Espresso coffee brewing dynamics: Development of mathematical and computational models, *15éme Colloque Scient. Internat. sur le Café,* Associat. Scientif. Internat. du Café, Paris (1993).

28. Talamucci, F., Analysis of coupled heat-mass transport in freezing saturated soils, *Surveys on Mathematics for Industry*, **7**, *Springer-Verlag*, 93–139, (1997).

29. Talamucci, F., Flow through a porous medium with mass removal and diffusion, *Nonlinear Differential Equations and Applications*, **5**, 427–44 (1998).

30. Van Duijn, C., and Knabner, P., Solute transport in porous media with equilibrium and non-equilibrium multiplicity adsorption in travelling waves, *J. Reine Angew. Math.*, 1–49 (1991).

9

Infiltration Processes in Composite Materials Manufacturing: Modeling and Qualitative Results

ANGIOLO FARINA

Politecnico di Torino
Dipartimento di Ingegneria Aeronautica e Spaziale
Torino, Italy

AND
LUIGI PREZIOSI

Politecnico di Torino
Dipartimento di Matematica
Torino, Italy

ABSTRACT. This chapter deals with those composite materials manufacturing processes, e.g., resin transfer molding and structural resin injection molding, consisting in the injection of a liquid into a porous medium made of reinforcing elements. In these processes the infiltration is coupled with phenomena affecting both the rheological properties of the liquid (thermal variation and curing) and the mechanical properties of the solid (deformations). We illustrate the general model and the analytical results obtained so far.

9.1 Introduction

Many composite materials are manufactured using some industrial processes, usually named resin transfer molding, structural resin injection

A. Fasano (ed.), *Complex Flows in Industrial Processes*

molding, or squeeze casting, which consist in injecting a polymeric, metallic, or ceramic melt into a porous preform of reinforcing elements. At the end, or during the production cycle, the liquid, which should uniformly fill the whole preform, solidifies, holding the reinforcing elements together and enabling the transfer of major stresses and loads to the solid preform.

It appears from the literature that the identification of the production cycle parameters to be used in practice is still more an art than a science (see, for example, [41], [52]), and it has to be developed every time on a trial-and-error basis.

From an industrial viewpoint it is important to have a model that allows us to foresee:

- the deformations of the solid preform;
- the stress evolution, in order to reveal in advance the possibility of damages in the reinforcing network, which may lead to material failure;
- the thermal state, in order to identify the regions undergoing premature solidification or curing;
- the position of the infiltration front, in order to establish the correct location of air vents and avoid the formation of dry spots; and
- the position of the preform border, in order to prevent race-tracking phenomena, i.e., the formation of an easier path for the infiltrating liquid that should fill the mold from the injection port to the air vents.

Modeling this process has drawn more and more attention. Most of the papers modeling injection molding processes assume that the solid preform is rigid ([5], [10], [11], [14], [15], [28], [29], [31], [35], [53], [54], [55]) and that the liquid matrix is Newtonian. This is a good approximation in some cases. In fact, the solid preform is compressed between the molds. A normal force acting on the molds and a friction force between the fiber mats and the mold face then develop, which hamper displacement and compression of the reinforcing elements during injection.

Many authors, however, observed deformation of the solid preform ([1], [44], [46], [48]) stimulating the formulations of models without the rigidity assumption, thus considering a flow in a deformable porous medium (see [20], [27], [49]).

This chapter is based on a model, presented in [18], aimed at simulating nonisothermal injection molding processes and reviews some analytical results related to it. In detail, the chapter studies a nonisothermal flow of a resin undergoing an exothermic crosslinking chemical reaction (usually referred to in the literature as *curing cycle*) through a deformable porous preform.

The problem presents the formation of three time-dependent domains; the first occupied by the liquid only, the second by the solid preform wet by the infiltrating resin, and the third consisting of the uninfiltrated region. It is assumed that sharp fronts divide the three domains.

The mathematical problem originated by the model is a free boundary problem. The general problem, i.e., the one obtained considering the whole coupled nonisothermal flow/deformation model, is extremely complicated, being constituted by a set of parabolic and hyperbolic nonlinear equations defined in two time-varying interfaced domains. At the moment the only results available concern two problems obtained from the general model performing some simplifications, namely:

1. one-dimensional nonisothermal infiltration in a rigid porous preform with resin polymerization ([7], [8]) and
2. one-dimensional isothermal infiltration in a deformable porous preform ([9]).

This chapter develops as follows. Section 9.2 focuses on the modeling part, illustrating a general 3-D nonisothermal model describing the injection molding process. Section 9.3 is devoted to the analysis of the 1-D nonisothermal problem in a rigid preform. Section 9.4 deals with the mathematical problem obtained considering the 1-D isothermal infiltration in a deformable porous medium. Finally, Section 9.5 will address some of the questions about modeling and theoretical investigation on the structure of the mathematical problems, which are still open and deserve to be thoroughly explored.

9.2 The Mathematical Model

Consider a deformable porous medium that at $t = 0$ starts being infiltrated. Referring to Figure 9.1, one can identify two time-varying domains $\mathcal{D}^w$ and

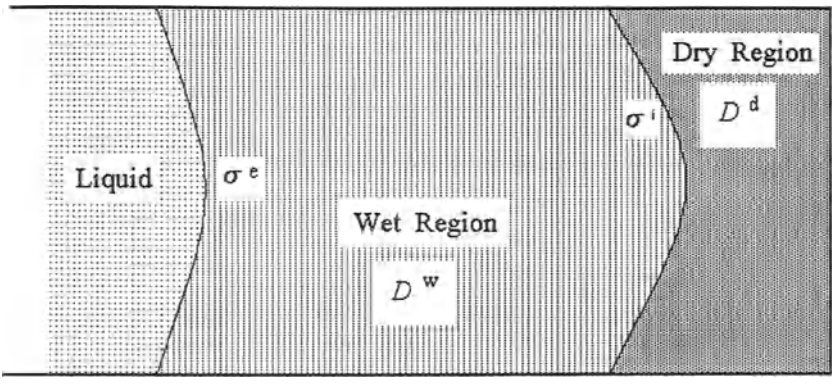

Figure 9.1 — A schematic representation of the infiltration process.

$\mathcal{D}^d$ corresponding, respectively, to the part of the solid preform wet by the infiltrating resin and the one not yet reached by the liquid.

If capillary phenomena can be neglected, as in most of the production processes, $\mathcal{D}^w$ and $\mathcal{D}^d$ are divided by a sharp interface σ^i that represents the infiltration front.

The mathematical model consists in the evolution equations for the state variables in both the wet and dry regions and in those for the interfaces σ^i and σ^e.

9.2.1 Wet Region

The dependent variables describing the state of the system are:

- ϕ volume fraction occupied by the solid constituent. Assuming saturation the volume fraction occupied by the liquid is $1 - \phi$;
- $\vec{v}_s$, $\vec{v}_l$ velocities of solid and liquid constituents;
- P pore liquid pressure;
- u temperature of the mixture. We are going to assume that solid and liquid constituents are locally in thermal equilibrium; and
- δ degree of cure of the resin. It is defined as the ratio between the amount of heat released by the exothermic polymerization reaction and the total heat of reaction. So δ is a dimensionless parameter ranging between 0 and 1.

Working in Eulerian formalism, the equations that can be written (see [39] and references therein for further details) are:

- Mass conservation of solid and liquid constituents

$$\frac{\partial \phi}{\partial t} + \nabla \cdot (\phi \vec{v}_s) = 0 \tag{9.1}$$

$$-\frac{\partial \phi}{\partial t} + \nabla \cdot [(1 - \phi)\, \vec{v}_l] = 0 \tag{9.2}$$

  where we have assumed that the densities of the solid ρ_s and liquid ρ_l are constant. This means that thermal expansion phenomena that may occur in nonisothermal processes are neglected. In some cases this cannot be done because the difference in thermal expansion coefficients may generate stresses in the composite during the solidification process, which may also generate microcracks in the reinforcing network.

- Stress equilibrium equation for the mixture as a whole

$$\nabla P - \nabla \cdot \mathbf{T} = 0 \tag{9.3}$$

  where $\mathbf{T}$ is called excess stress. We remark that in writing (9.3) we have implicitly neglected the body forces and inertial terms. Both are

usually very small. In particular, in previous papers ([2], [3], [40]) that considered inertia, it was noticed that the dimensionless form of the equations presents in front of the inertial term a coefficient that is usually negligible. Actually, it is known that inertia may play an important role only during the very initial stage of infiltration.

- Darcy's law

$$(1-\phi)\left(\vec{v}_l - \vec{v}_s\right) = -\frac{\mathbf{K}\left(\mathbf{F}_s\right)}{\mu}\nabla P \tag{9.4}$$

where $\mathbf{K}$ is the permeability tensor that depends on the deformation gradient $\mathbf{F}_s$ of the solid constituent and μ is the viscosity of the resin. Because we are considering nonisothermal processes with resin cure, the viscosity μ depends on both the temperature u and the degree of cure δ

$$\mu = \mu\left(u, \delta\right). \tag{9.5}$$

- Degree of cure of the resin

$$\frac{\partial \delta}{\partial t} + \vec{v}_l \cdot \nabla \delta = f\left(u, \delta\right) \tag{9.6}$$

where f is an experimentally determined function describing the reaction.

- Energy equation for the mixture

$$\begin{aligned}\rho_m c_m \left(\frac{\partial u}{\partial t} + \vec{v}_m \cdot \nabla u\right) = {} & \nabla \cdot \left(\mathbf{\Lambda}_m \nabla u\right) + \frac{1}{\mu}\mathbf{K}\nabla P \cdot \nabla P \\ & + (1-\phi) H_c f\left(u, \delta\right) \\ & - \frac{\rho_s \rho_l \phi (1-\phi)}{\rho_m}\left(c_l - c_s\right)\left(\vec{v}_l - \vec{v}_s\right) \cdot \nabla u\end{aligned} \tag{9.7}$$

where $\rho_m = \phi\rho_s + (1-\phi)\rho_l$ is the mixture density; c_m is the specific heat of the mixture modeled as

$$c_m = \frac{\rho_s \phi c_s + \rho_l (1-\phi) c_l}{\rho_m} \tag{9.8}$$

where c_s and c_l are the specific heats of the solid and liquid; $\vec{v}_m$ is the velocity of the mixture

$$\vec{v}_m = \frac{\rho_s \phi \vec{v}_s + \rho_l (1-\phi)\vec{v}_l}{\rho_m} \tag{9.9}$$

$\mathbf{\Lambda}_m$ is the thermal conductivity tensor of the mixture as a whole; $\mu^{-1}\mathbf{K}\nabla P \cdot \nabla P$ is the heat produced by the internal friction between solid and liquid; $(1-\phi) H_c f\left(u, \delta\right)$ represents the heat supplied by the

exothermic curing reaction of the resin (H_c is the total heat of reaction); and the last term represents the heat diffusion due to the relative motion.

We have to remark that these equations are based on a certain number of physical assumptions that must be recalled. We have neglected, as mentioned, all the inertial terms and body forces. Moreover, considering Darcy's law we have implicitly assumed that the liquid is Newtonian and that the Reynolds number characterizing the flow through the pores is much less than 1 (see [37] for a critical discussion of the hypotheses underlying Darcy's law).

Equation (9.7) is obtained assuming an elastic constitutive equation for the porous solid and no thermal deformations of the solid and liquid. We refer to [12], [13], [42] for the rigorous procedure to obtain the energy equation in the most general case.

Obviously these assumptions limit the applicability of the model. This, however, can still describe in a correct way a fairly large class of industrial processes.

9.2.2 Dry Region

We can proceed in a way similar to the one outlined earlier. However, in the dry region, due to the fact that air density and viscosity are very small, some simplifications can be done. First, because the air is easily expelled from the preform one can assume that its pressure is everywhere equal to the atmospheric pressure. Moreover the gas contribution to the global stress may be neglected. Finally, the average velocity is equal, in practice, to the velocity of the solid constituent, the composite density is $\rho_m \approx \phi\rho_s$, and, of course, there is no chemical reaction because no resin is present in the dry region.

Summarizing all these assumptions, the state variables in the dry region reduce to:

- ϕ solid volume fraction,
- $\vec{v}_s$ solid velocity, and
- u temperature.

The fundamental equations are, respectively, mass, momentum, and thermal energy balance

$$\frac{\partial \phi}{\partial t} + \nabla \cdot (\phi \vec{v}_s) = 0 \tag{9.10}$$

$$\nabla \cdot \mathbf{T} = 0 \tag{9.11}$$

$$\rho_s \phi c_s \left(\frac{\partial u}{\partial t} + \vec{v}_s \cdot \nabla u \right) = \nabla \cdot (\mathbf{\Lambda}_s \nabla u) \tag{9.12}$$

where $\mathbf{\Lambda}_s$ is the thermal conductivity of the solid.

To complete the model we still have to specify the constitutive equation for the stress tensor $\mathbf{T}$. We assume that the wet and dry solids have the same constitutive equation, which is of elastic type, coherently with the assumptions at the basis of the energy equation (9.7).

9.2.3 Interface and Boundary Conditions

Referring to Figure 9.1, consider the interface σ^i between $\mathcal{D}^w$ and $\mathcal{D}^d$ as given by the surface $\psi_i(\vec{x}, t) = 0$. As σ^i is a material surface for the liquid, its evolution equation is

$$\frac{\partial \psi_i}{\partial t} + \vec{v}_l(\sigma^i) \cdot \nabla \psi_i = 0 \tag{9.13}$$

where $\vec{v}_l(\sigma^i)$ is the liquid velocity on σ^i.

Another boundary is the contact surface σ^e between the pure liquid and the wet solid. Let it be given by $\psi_e(\vec{x}, t) = 0$. As the resin, pushed by the pressure gradient, penetrates the porous solid through σ^e, this is a material surface for the solid, and therefore its evolution equation is

$$\frac{\partial \psi_e}{\partial t} + \vec{v}_s(\sigma^e) \cdot \nabla \psi_e = 0 \tag{9.14}$$

where $\vec{v}_s(\sigma^e)$ is the solid velocity on σ^e.

Following [32] and taking into account that inertial terms have been neglected, these jump conditions can be imposed

$$[\![\rho_m(\vec{v}_m - \vec{v}_\sigma)]\!] \cdot n_\sigma = 0 \tag{9.15}$$

$$[\![-P\mathbf{I} + \mathbf{T}]\!]\, \vec{n}_\sigma = 0 \tag{9.16}$$

$$[\![\rho_s \phi u c_s (\vec{v}_s - \vec{v}_\sigma) \cdot \vec{n}_\sigma + \rho_l (1-\phi) u c_l (\vec{v}_l - \vec{v}_\sigma) \cdot \vec{n}_\sigma]\!] = [\![\mathbf{\Lambda}_m \nabla u]\!] \cdot \vec{n}_\sigma \tag{9.17}$$

where $[\![\cdot]\!]$ denotes the jump across the surface σ and $\vec{v}_\sigma$ and $\vec{n}_\sigma$ are, respectively, the surface velocity and the outside normal. In addition, as usual, we assume

$$[\![u]\!] = 0. \tag{9.18}$$

As the surface σ^i is a material surface for the liquid, following [32] one has

$$[\![P]\!] = 0. \tag{9.19}$$

Using (9.19), equation (9.16) entails

$$[\![\mathbf{T}]\!]\, \vec{n}_{\sigma^i} = 0 \tag{9.20}$$

which, assuming the same constitutive equation of elastic type for wet and dry solids, implies, in 1-D problems, the continuity of ϕ across σ^i and, from (9.15), the continuity of $\vec{v}_s$. Moreover if the specific heat of the solid

is continuous across σ^i, then equation (9.17) rewrites as

$$\mathbf{\Lambda}_m \nabla u^- \cdot \vec{n}_{\sigma^i} = \mathbf{\Lambda}_s \nabla u^+ \cdot \vec{n}_{\sigma^i} \tag{9.21}$$

where u^+ and u^- are the temperatures on the dry and wet sides of σ^i, respectively.

Consider now the boundary condition on σ^e. If the superscript $-$ denotes the quantities evaluated in the pure liquid region, one has

$$\phi^- = 0, \qquad \vec{v}_l^- = \vec{v}_{\text{in}}$$

$$\mathbf{T}^- \vec{n}_{\sigma^e} = 0, \qquad P^- = P_o$$

where $\vec{v}_{\text{in}}$ is the inflow velocity of the resin and P_o the pressure driving the flow.

From (9.16) and (9.19) one gets the following conditions

$$P = P_o \tag{9.22}$$

$$\mathbf{T} \vec{n}_{\sigma^e} = 0. \tag{9.23}$$

Assuming that the thermal field in the pure liquid region is known, on σ^e the only condition to impose on the temperature is equation (9.18), which rewrites as

$$u = u_{\text{in}} \tag{9.24}$$

where u_{in} is the temperature of the infiltrating liquid.

The boundary condition to impose on the hyperbolic curing equation is

$$\delta(\sigma^e) = \delta_{\text{in}} \tag{9.25}$$

on that part of σ^e where the liquid enters the preform, i.e., where $(\vec{v}_l - \vec{v}_s) \cdot \vec{n}_{\sigma^e} < 0$, where $\vec{n}_{\sigma^e}$ is directed outside the preform.

9.3 Nonisothermal Injection in a Rigid Preform

This section focuses on the analytical results obtained for the 1-D nonisothermal injection in a rigid preform, i.e., $v_s = 0$ and the solid volume fraction ϕ is constant and uniform. From (9.2) such assumptions imply that

$$\frac{\partial v_l}{\partial x} = 0, \qquad \forall x \in \mathcal{D}^w,\ t > 0 \tag{9.26}$$

where $\mathcal{D}^w = [0,\ s_i(t)]$ is the wet region and $x = 0$, $x = s_i(t)$ are, respectively, the inflow surface and the penetration front. The liquid velocity in

$\mathcal{D}^w$ is uniformly equal to the velocity of the infiltration front

$$v_l(x,t) = \dot{s}_i(t), \qquad \forall x \in \mathcal{D}^w,\ t > 0. \tag{9.27}$$

Denoting by K the xx component of $\mathbf{K}$, the constitutive assumption $\mathbf{K} = \mathbf{K}(\mathbf{F}_s)$ means, in this case, that K is a function of ϕ, i.e.,

$$K = K(\phi) \tag{9.28}$$

which, in the rigid case, implies that K is constant in space and time.

Using equations (9.2) and (9.4) one can easily show that

$$\frac{\partial}{\partial x}\left[\frac{1}{R(u,\delta)}\frac{\partial P}{\partial x}\right] = 0, \qquad x \in \mathcal{D}^w \tag{9.29}$$

where

$$R(u,\delta) = \frac{\mu(u,\delta)}{K} \tag{9.30}$$

is defined hydraulic resistivity and depends on the temperature u and the degree of cure δ. We remark that in isothermal problems with no curing, by virtue of (9.29), P is a harmonic function.

Darcy's law (9.4) and equation (9.26) then state that in $\mathcal{D}^w$ the liquid velocity v_l is constantly equal to

$$v_l(t) = -\frac{1}{(1-\phi)R}\frac{\partial P}{\partial x}. \tag{9.31}$$

In particular, the evolution equation of the infiltration front is

$$(1-\phi)\dot{s}_i(t) = -\left(\frac{1}{R}\frac{\partial P}{\partial x}\right)_{x=s_i(t)}. \tag{9.32}$$

Integrating (9.32) over the wet domain $\mathcal{D}^w$ one gets

$$\dot{s}_i(t) = \frac{P_o}{1-\phi}\left\{\int_0^{s_i(t)} R(u,\delta)\,dx\right\}^{-1} \tag{9.33}$$

where conditions (9.19) and (9.22) have been used and the atmospheric pressure has been scaled to 0.

At the interface $x = s_i(t)$, conditions (9.18) and (9.21) rewrite as

$$u\left(s_i(t)^-, t\right) = u\left(s_i(t)^+, t\right) \tag{9.34}$$

$$\left(\lambda_m \frac{\partial u}{\partial x}\right)\Big|_{x=s_i(t)^-} = \left(\lambda_s \frac{\partial u}{\partial x}\right)\Big|_{x=s_i(t)^+} \tag{9.35}$$

where λ_m and λ_s are, respectively, the xx components of $\mathbf{\Lambda}_m$ and $\mathbf{\Lambda}_s$. The other boundary conditions on $x = 0$ and $x = L$ are (see equations (9.18)

and (9.24))

$$u(0,t) = u_{\text{in}}(t) \tag{9.36}$$

$$u(L,t) = u_L(t) \tag{9.37}$$

while the initial conditions are

$$u(x,0) = u_o(x) \tag{9.38}$$

$$s_i(0) = b \in (0,L). \tag{9.39}$$

9.3.1 Nonisothermal Infiltration without Curing

The nonisothermal problem without curing has been studied in [7]. In order to discuss the results, it is useful to introduce

$$c = \phi\rho_s c_s + \chi_w(1-\phi)c_l\rho_l \tag{9.40}$$

$$\lambda = \phi\lambda_s + \chi_w(1-\phi)\lambda_l \tag{9.41}$$

where χ_w is the characteristic function of the wet region and λ_l is the xx component of the liquid heat conduction tensor $\mathbf{\Lambda}_l$. The heat equations (9.7) and (9.12) can be summarized by

$$c\frac{\partial u}{\partial t} + (1-\phi)\dot{s}_i\rho_l c_l\chi_w\frac{\partial u}{\partial x} - \frac{\partial}{\partial x}\left(\lambda\frac{\partial u}{\partial x}\right) = 0 \tag{9.42}$$

to be solved in the wet region ($x \in \mathcal{D}^w = [0, s_i(t)]$, $t > 0$, $\chi_w = 1$) and in the dry region ($x \in \mathcal{D}^d = (s_i(t), L]$, $t > 0$, $\chi_w = 0$). We remark that in writing (9.42) the heat source due to the internal friction has been neglected.

Existence and uniqueness of the solution (in the classical sense) of the free boundary problem (9.42), (9.33) to (9.39) has been proved in [7] under suitable assumptions on the data (the case $b = 0$ is treated separately).

The demonstration technique uses a fixed-point argument based on the following steps:

1. Define the set

$$\mathcal{S} = \left\{ s_i \in C([0,T]) : s(0) = b,\ \|s_i\|_\gamma \le M \right\} \tag{9.43}$$

   where M and T are constants to be selected later, γ is chosen arbitrarily in $\left(\frac{1}{2}, 1\right)$, and $\|\cdot\|_\gamma$ is the corresponding Hölder norm.

2. For any $s_i \in \mathcal{S}$ the thermal problem (9.42), (9.34) to (9.39) is solved. The determination of the corresponding temperature field is reduced to the solution of a system of four integral equations of Volterra type with weakly singular kernels.

3. The function $u(x,t)$ just found is used to define the mapping $\mathcal{T} : s_i \longmapsto s_i^{\text{new}}$ in the following way

$$\dot{s}_i^{\text{new}} = \frac{P_o}{1-\phi} \left\{ \int_0^{s_i(t)} R(u(x,t))\, dx \right\}^{-1} \tag{9.44}$$

so that a fixed point of $\mathcal{T}$ corresponds to a solution of the original free boundary problem.

4. The constants T and M in the set (9.43) are chosen in such a way that $s_i^{\text{new}} \in \mathcal{S}$ and the continuity of the mapping $\mathcal{T}$ in the topology of $C([0,T])$ is proved. Schauder's theorem guarantees the existence of at least one fixed point.
5. A finer analysis in the $C^1([0,T])$ topology shows that $\mathcal{T}$ is in fact a contraction in a sufficiently small time interval and uniqueness follows.

9.3.2 Nonisothermal Flow with Curing

In the current case the infiltrating resin also undergoes a polymerization process (curing). The thermal coefficients of the resin will be, in general, different according to whether the resin is polymerized or not. Therefore in [8] it is assumed that

$$c_l = \delta c_l^p + (1-\delta)\, c_l^{np} \tag{9.45}$$

$$\lambda_l = \delta \lambda_l^p + (1-\delta)\, \lambda_l^{np} \tag{9.46}$$

where c_l^p, c_l^{np} represent, respectively, the specific heats of the polymerized and nonpolymerized resins and λ_l^p, λ_l^{np} the thermal conductivities of resin in the polymerized and nonpolymerized states. The coefficients c and λ have to be redefined in the following way

$$c = \phi \rho_s c_s + \chi_w (1-\phi) \rho_l \left[\delta c_l^p + (1-\delta)\, c_l^{np}\right] \tag{9.47}$$

$$\lambda = \phi \rho_s \lambda_s + \chi_w (1-\phi) \rho_l \left[\delta \lambda_l^p + (1-\delta)\, \lambda_l^{np}\right]. \tag{9.48}$$

We remark that the densities of the cured and uncured resins are equal. This implies that the volume changes accompanying polymerization have been neglected. Exploiting equation (9.27), one again has that the liquid velocity is $\dot{s}_i(t)$ in the whole wet preform and is given by (9.32) or (9.33). So the curing equation rewrites as

$$\frac{\partial \delta}{\partial t} + \dot{s}_i(t) \frac{\partial \delta}{\partial x} = f(u, \delta). \tag{9.49}$$

Billi in [8] works under the assumption that the curing degree of the injected resin is null

$$\delta(0,t) = 0. \tag{9.50}$$

Actually, if $s_i(0) = b > 0$, he considers

$$\delta(x,0) = 0, \qquad 0 < x < b. \tag{9.51}$$

Finally the energy equation modifies to

$$c\frac{\partial u}{\partial t} = \frac{\partial}{\partial x}\left(\lambda\frac{\partial u}{\partial x}\right) - (1-\phi)\dot{s}_i\rho_l\left[\delta c_l^p + (1-\delta)c_l^{np}\right]\chi_w\frac{\partial u}{\partial x}$$

$$+ (1-\phi)H_c f(u,\delta)\chi_w. \tag{9.52}$$

We point out that the derivatives that appear in (9.52) are meant in the distributional sense, because the fluid does not invade the whole porous matrix and then the function δ is discontinuous, jumping to zero when passing from the wet to the dry region.

A slightly simplified version of this problem has been considered in [8]: Zero temperature boundary data and the last term on the right-hand side of (9.52) replaced by a given function $h(x,t)$.

Denoting by $\mathcal{D} = (0,L)$ and $\mathcal{Q} = (0,L)\times(0,T)$, a weak formulation is introduced for equation (9.52). Considering a generic $\varphi \in L^2\left(0,T;H_o^1(\mathcal{D})\right)$, $\varphi(\cdot,T) = 0$, $\varphi_t \in L^2(\mathcal{Q})$ equation (9.52) is multiplied by φ and integrated over $\mathcal{Q}$. Taking into account condition (9.38), the result is

$$\int_{\mathcal{Q}} \left\{-cu\varphi_t + \lambda u_x\varphi_x - (1-\phi)\dot{s}_i\rho_l\left[\delta c_l^p + (1-\delta)c_l^{np}\right]\chi_w u\varphi_x\right\}dx\,dt$$

$$= \int_{\mathcal{Q}} h\varphi\,dx\,dt + \int_0^L u_o(x)(c\varphi)_{t=0}\,dx$$

$$+ \int_{\mathcal{Q}} \left\{c_t + (1-\phi)\dot{s}_i\rho_l\left[\chi_w\left(\delta c_l^p + (1-\delta)c_l^{np}\right)\right]_x\right\}u\varphi\,dx\,dt\,. \tag{9.53}$$

Let us focus on the last term on the right-hand side of (9.53). Recalling (9.45), taking into account (9.49) and the fact that $\chi_{wt} + \dot{s}_i\chi_{wx} = 0$, it can be easily proved that

$$c_t + (1-\phi)\dot{s}_i\rho_l\left[\chi_w\left(\delta c_l^p + (1-\delta)c_l^{np}\right)\right]_x = (1-\phi)\rho_l\chi_w\left(c_l^p - c_l^{np}\right)f(u,\delta)\,. \tag{9.54}$$

Summing up, the weak formulation for the thermal balance equation is

$$\int_{\mathcal{Q}} \left\{-cu\varphi_t + \lambda u_x \varphi_x - (1-\phi)\dot{s}_i \rho_l \left[\delta c_l^p + (1-\delta)\, c_l^{np}\right] \chi_w u \varphi_x\right\} dx\, dt$$

$$= \int_{\mathcal{Q}} (ru + h)\, \varphi\, dx\, dt + \int_0^L u_o(x)\, (c\varphi)_{t=0}\, dx \tag{9.55}$$

where $u \in L^2\left(0,T; H_o^1(\mathcal{D})\right)$ and the coefficient r is defined as

$$r = (1-\phi)\rho_l \chi_w \left(c_l^p - c_l^{np}\right) f(u,\delta)\,. \tag{9.56}$$

Again the following fixed-point argument is used:

1. A set of C^1 functions with $x = s_i(t)$ prescribed, and a set of Lipschitz continuous functions with $\delta(x,t)$ prescribed are selected.
2. The existence and uniqueness results known in the literature [30] are used to find the solution $u(x,t)$ of (9.55). Observing that u is continuous in x for almost all t and that $\lambda(\cdot,t)\, u_x(\cdot,t) \in H^1(\mathcal{D})$ for almost all t, one has that the conditions (9.34), (9.35) are valid in an almost classical sense.
3. Introducing a mollified sequence δ^v of δ, defined throughout $\mathcal{Q}$ one can consider the corresponding classical version of (9.55). Estimates of $\|u(\cdot,t)\|_{L^2(\mathcal{D})}$, $\|u_x\|_{L^2(\mathcal{Q})}$ independent of v are obtained by means of standard arguments. Much more difficult are the estimates on $\|u_x(\cdot,t)\|_{L^2(\mathcal{D})}$ and $\|u_t\|_{L^2(\mathcal{Q})}$, obtained in [8].
4. Using these estimates, it is possible to prove that if a sequence $\{s_n\}$ converges in $C^1([0,T])$ and a sequence $\{\delta_n\}$ of uniformly Lipschitz continuous functions converges uniformly in $\overline{\mathcal{Q}}$, then the corresponding sequence $\{u_n\}$ of solution of (9.55) converges uniformly in $\overline{\mathcal{Q}}$.
5. On the basis of the preceding results, it can be shown that the operator $\mathcal{F}: (\delta, s_i) \longmapsto (\delta^{\text{new}}, s_i^{\text{new}})$ defined by

$$\dot{s}_i^{\text{new}} = \frac{P_o}{1-\phi} \left\{ \int_0^{s_i(t)} R(u,\delta)\, dx \right\}^{-1}$$

$$\frac{\partial \delta^{\text{new}}}{\partial t} + \dot{s}_i^{\text{new}} \frac{\partial \delta^{\text{new}}}{\partial x} = f\left(u, \delta^{\text{new}}\right)$$

$$s_i^{\text{new}}(0) = b,$$

$$\delta^{\text{new}}(x,0) = 0, \qquad 0 \le x \le b$$

$$\delta^{\text{new}}(0,t) = 0, \qquad t > 0$$

has a fixed point.

It must be remarked that this procedure requires uniform estimates of $\|\delta_x^{\text{new}}\|_{L^\infty(Q)}$ and $\|\delta_t^{\text{new}}\|_{L^\infty(Q)}$, which are quite delicate.

9.4 Isothermal Injection in a Deformable Preform

In the preceding section we considered the complication arising in the injection problem owing to nonisothermal conditions and possible occurrence of curing. However, deformation of the porous matrix (as a result of the high injection pressure) may also be important. Starting from [49], in [9] the isothermal problem has been studied assuming that the porous medium is deformable with a nonlinear elastic behavior.

Let ϕ_r be the solid volume fraction in the nonstressed configuration and L the relative length. At $t = 0$ a constant and known pressure P_o is applied on one end of the solid, which immediately compresses, reducing its length to L_c and acquiring a solid volume fraction ϕ_c corresponding to a stress that balances the applied pressure. In [49] the evolution of the system in this short initial transient is not considered. In fact, during it, inertial terms play a dominant role (this effect is studied in detail in [3]). The initial configuration is then the one in which the solid is fully compressed under the applied load but still not infiltrated (the one denoted "reference configuration" in Figure 9.2).

Denoting by τ the xx component of $\mathbf{T}$ counted as positive in compression, equations (9.1) to (9.4) rewrite as

$$\frac{\partial \phi}{\partial t} + \frac{\partial}{\partial x}(\phi v_s) = 0 \tag{9.57}$$

$$\frac{\partial \phi}{\partial t} - \frac{\partial}{\partial x}((1-\phi)\, v_l) = 0 \tag{9.58}$$

$$\frac{\partial P}{\partial x} + \frac{\partial \tau}{\partial x} = 0 \tag{9.59}$$

$$v_l - v_s = -\frac{K(\phi)}{\mu(1-\phi)} \frac{\partial P}{\partial x} \tag{9.60}$$

where μ is constant and K is a nonlinear C^1 function of the solid volume fraction ϕ.

The elasticity assumption means that the stress tensor τ is a function of the deformation gradient of the solid which, in one dimension, is given by

$$(\mathbf{F}_s)_{xx} = \frac{\partial x}{\partial \xi} = \frac{\phi_c}{\phi} \tag{9.61}$$

where (see Figure 9.2) ξ is the solid material coordinate, i.e., it labels

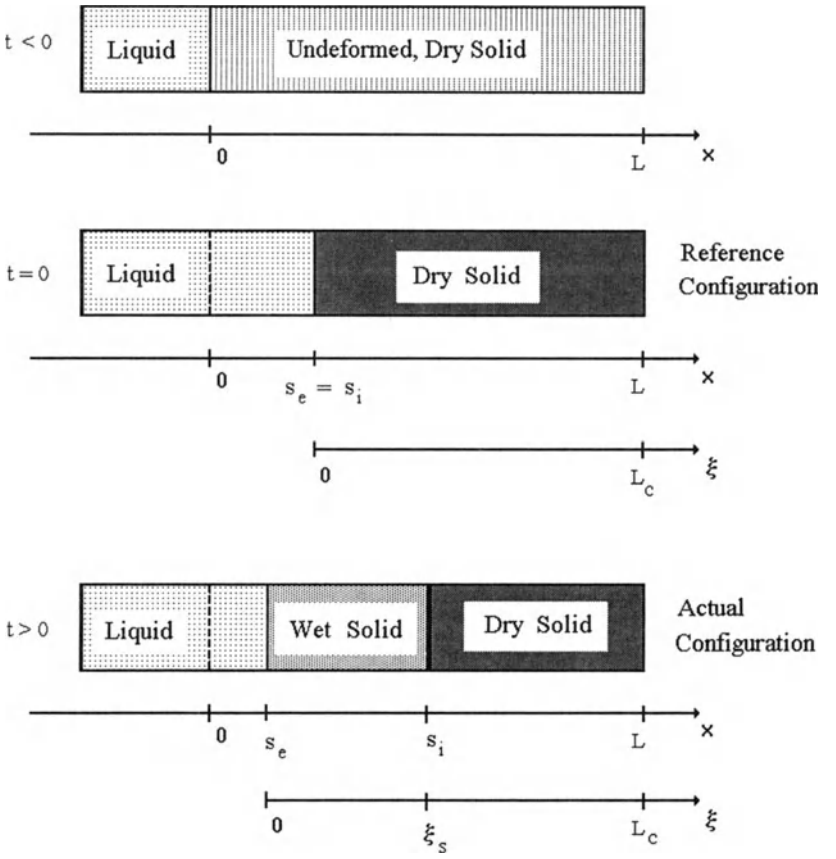

Figure 9.2 — A schematic representation of the 1-D infiltration process in a deformable porous solid.

the solid particle in the reference configuration. We assume, as already mentioned, that the wet and dry solids satisfy the same stress–strain relation that, according to the elasticity assumption, is

$$\tau = \tau(\phi) \tag{9.62}$$

where $\tau(\phi)$ is taken as a C^2 function. Under such hypotheses

$$\phi_c = \tau^{-1}(P_o) \tag{9.63}$$

where τ^{-1} is the inverse function of τ and P_o, as mentioned, is the applied pressure.

The time-varying subdomains, corresponding to the wet and dry solids, are (see Fig. 9.2)

$$\mathcal{D}^w = [s_e(t), s_i(t)] \tag{9.64}$$

$$\mathcal{D}^d = (s_i(t), L] \tag{9.65}$$

The boundary s_i is, in fact, the interface between the wet and dry parts and s_e is the border of the porous preform.

Summing (9.57) and (9.58) one can prove that the so-called composite velocity

$$v_c = \phi v_s + (1-\phi) v_l \tag{9.66}$$

is space-independent because

$$\frac{\partial v_c}{\partial x} = 0. \tag{9.67}$$

Combining in a suitable way (9.57) to (9.60) one obtains, in the wet region, the following equation

$$\frac{\partial \phi}{\partial t} = \frac{\partial}{\partial x}\left[\phi \frac{K(\phi)}{\mu} \Sigma(\phi) \frac{\partial \phi}{\partial x}\right] - v_c \frac{\partial \phi}{\partial x} \tag{9.68}$$

where

$$\Sigma(\phi) = \frac{d\tau(\phi)}{d\phi} > 0. \tag{9.69}$$

On the other hand, it can easily be proved that in the dry region the solid does not move and stays at a constant volume fraction ϕ_c.

Note that in equation (9.68), the coefficient v_c is still unknown. In order to complete the mathematical model, one has not only to find v_c, but also to specify the boundary conditions on s_e, s_i, and their evolution equations.

The boundary condition on s_e is deduced from (9.23) and corresponds to a stress–free condition

$$\phi(s_e(t), t) = \phi_r. \tag{9.70}$$

On the boundary s_i the continuity of stress and pressure, together with the assumption that wet and dry solids satisfy the same constitutive equation, imply

$$\phi(s_i(t), t) = \phi_c. \tag{9.71}$$

As the composite velocity is continuous across both material interfaces (see (9.15)) one has

$$v_c = [1 - \phi(s_i(t), t)]\, v_l(s_i(t), t) \equiv (1-\phi_c)\dot{s}_i(t) \tag{9.72}$$

which links v_c to $\dot{s}_i$.

As far as the evolution equations for the free boundaries s_i and s_e are concerned, using Darcy's law (9.60) and equations (9.59) and (9.69) one has the following Stefan-type condition for s_i

$$\dot{s}_i = \frac{K(\phi_c)}{(1-\phi_c)\mu}\Sigma(\phi_c)\left.\frac{\partial\phi}{\partial x}\right|_{x=s_i(t)}. \tag{9.73}$$

Evaluating v_c on s_e and joining Darcy's law with (9.72) and (9.73), one has the evolution equation for s_e

$$\dot{s}_e = \frac{K(\phi_c)}{\mu}\Sigma(\phi_c)\left.\frac{\partial\phi}{\partial x}\right|_{x=s_i(t)} - \frac{K(\phi_r)}{\mu}\Sigma(\phi_r)\left.\frac{\partial\phi}{\partial x}\right|_{x=s_e(t)}. \tag{9.74}$$

In conclusion, in the Eulerian formalism, the dynamics of the whole system is governed by a nonlinear free boundary problem defined in $\mathcal{D}^w$. In particular, the equations that define the problem are (9.68) with v_c given by (9.72), (9.70), (9.71), (9.73), and (9.74) with the initial condition $s_i(0) = s_e(0) = L - L_c$.

Let us make some comments on the structure of such a double free boundary problem.

Mathematically, the pair (9.71), (9.73) coincides with the well-known Stefan condition for the one-phase solidification problem. On the other hand, condition (9.74) involves the derivative $\frac{\partial\phi}{\partial x}$ evaluated at both boundaries. Another peculiarity is the presence of the term $v_c(t)$ in the governing differential equation.

The tools applied in [19] can provide an existence theorem. The quoted paper [9] is devoted to the determination of self-similar solutions.

The problem stated earlier is highly nonlinear and characterized by the presence of two free boundaries, which give rise to several mathematical difficulties. In order to reduce them, in [9] the material coordinate ξ fixed on the solid is introduced. In this framework the boundary s_e is fixed, so one has a nonlinear one-phase Stefan problem. In fact, using Lagrangian coordinates the wet domain becomes $\mathcal{D}^w = \{0 \le \xi \le \xi_s(t)\}$, where $\xi_s(t)$ denotes the solid particle just wet by the infiltration front, i.e., it locates the free boundary between the wet and dry domains. The image of the boundary s_e is simply $\xi = 0$ (see Figure 9.2).

Instead of ϕ, appearing in the Eulerian formulation, it is more convenient to consider as a dependent variable the so-called void ratio defined as

$$e = \frac{1-\phi}{\phi}. \tag{9.75}$$

Without loss of generality, it is also useful to consider τ and K as a function of e, i.e., $K = K(e)$ and $\tau = \tau(e)$ and to introduce the function $\tilde{\Sigma}(e)$

defined as

$$\tilde{\Sigma}(e) = \frac{d\tau(e)}{de}. \tag{9.76}$$

The free boundary problem rewrites then as

$$\begin{aligned}
&\frac{\partial e}{\partial t} = \frac{\partial}{\partial \xi}\left[F(e)\frac{\partial e}{\partial \xi}\right], \qquad 0 < \xi < \xi_s(t),\ t > 0 \\
&e(0,t) = e_r = \frac{1-\phi_r}{\phi_r}, \qquad t > 0 \\
&e(\xi_s(t),t) = e_c = \frac{1-\phi_c}{\phi_c}, \qquad t > 0 \\
&\dot{\xi}_s(t) = -\frac{F(e_c)}{e_c}\left.\frac{\partial e}{\partial \xi}\right|_{\xi=\xi_s(t)}, \qquad t > 0 \\
&\xi_s(0) = 0
\end{aligned} \tag{9.77}$$

where

$$F(e) = -\frac{(e_c+1)^2}{\mu(e+1)}K(e)\,\tilde{\Sigma}(e). \tag{9.78}$$

Defining

$$\zeta = \frac{\xi}{\xi_s(t)} \tag{9.79}$$

one looks for a solution of (9.77) in the form

$$e(\xi,t) = \theta(\zeta), \qquad 0 < \zeta < 1. \tag{9.80}$$

Because of $(9.77)_4$, ξ_s must satisfy

$$\xi_s\dot{\xi}_s = -\frac{F(e_c)}{e_c}\theta'(1) \tag{9.81}$$

so that the infiltration front in the Lagrangian reference has to evolve as $\sqrt{t}$ (note, however, that $\theta'(1)$ is still unknown). Going back to (9.77), one has the following boundary value problem for a nonlinear second order o.d.e.

$$\begin{aligned}
&\frac{F(e_c)}{e_c}\theta'(1)\zeta\theta' - [F(\theta)\theta']' = 0, \qquad 0 < \zeta < 1 \\
&\theta(0) = e_r \\
&\theta(1) = e_c.
\end{aligned} \tag{9.82}$$

Note that the differential equation contains the unknown boundary value $\theta'(1)$.

The existence and uniqueness theorem proved in [9] is based on a shooting technique. Setting $\theta'(1) = \alpha$ one can study the family of Cauchy problems

$$\begin{aligned} \frac{F(e_c)}{e_c}\alpha\zeta\theta' - [F(\theta)\theta']' &= 0 \\ \theta(1) &= e_c \\ \theta'(1) &= \alpha \end{aligned} \tag{9.83}$$

looking for the α such that $\theta(0) = e_r$. By integrating the differential equation between ζ and 1, one obtains

$$\begin{aligned} \theta' &= \frac{\alpha F(e_c)}{e_c F(\theta)}\left[\zeta\theta + \int_{\zeta}^{1} \theta(y)\,dy\right] \\ \theta'(1) &= e_c. \end{aligned} \tag{9.84}$$

Accordingly, the problem is equivalent to that of finding a unique $\alpha \leq 0$ such that the solution θ_α of (9.84) satisfies $\theta_\alpha(0) = e_r$. The demonstration is based on the following steps:

1. Chosen arbitrarily $\alpha < 0$, one shows that θ_α is strictly decreasing in $[0,1]$.
2. For any α, $\bar{\alpha}$ such that $\alpha < \bar{\alpha}$ one proves that $\theta_\alpha(\zeta) > \theta_{\bar{\alpha}}(\zeta)\ \forall\zeta \in [0,1)$.
3. Considering the application $\alpha \mapsto \theta_\alpha(0)$ a straightforward analysis shows that it is continuous and that $\theta_\alpha(0) \longrightarrow \infty$ when $\alpha \longrightarrow -\infty$.

By putting all these ingredients together, the result is that the application $\alpha \mapsto \theta_\alpha(0)$ is continuous, monotone, and unbounded when $\alpha \in (-\infty, 0]$. Therefore there exists a unique value of α such that $\theta_\alpha(0) = e_r$.

9.5 Open Problems

The studies mentioned in this chapter are motivated by the necessity, encountered in the technological literature, of developing mathematical models for injection molding processes and of obtaining qualitative results, which can help in identifying the process parameters and improving the processes themselves.

Even if some results have been obtained, they remain a first step toward a complete study of injection molding. Many questions are still open and many areas deserve to be explored. In particular, we will point out some possible developments that should be carried out on modeling aspects and on qualitative analysis.

9.5.1 Modeling

From the modeling point of view one of the phenomena that has been neglected but may play an important role in some cases is the resin flux between the mold walls and the preform, the so-called race-tracking problem ([16], [21]). In liquid composite molding, the preforms are placed in the mold cavity. The mold is then closed and the thermoseting resin is injected. Because it is difficult to precisely cut the fiber preform to the exact shape of the mold, sometimes a gap exists between the preform and mold edge. This gap, although small (1 or 2 mm), can create a preferential flow path. This may give rise to a nonuniform impregnation of the porous preform and even to dry spots. In some cases these preferential channels are opened by the flow itself, which displaces the preform ([22], [51]). In order to foresee such phenomena one has to build more detailed models, joining, say, Stokes equation in the fiber-free region with deformable porous media models. This problem is linked to the analysis of the correct boundary conditions when the impinging flow is not perpendicular to the border of the preform. It is known that in the rigid case and for flows parallel to the porous material Beavers-Joseph conditions [6] can be used. These conditions were modified by Saffman [47] and lately deduced, on the basis of homogenization theory, by Jäger and Mikelic [25] (see also section 3.5 of [23]). It is not known, however, how to proceed in the deformable case.

Another thorny problem, when we come to mixture theory, is the inability to prescribe boundary conditions for traction boundary value problems. One has to increase the number of boundary conditions. This can be done in more than one way: continuity of chemical potential, saturation condition, mechanical splitting of traction, etc. (see, for example, [32], [36], [42], [43], [50]). The point, which deserves to be explored, is the research of a unitary theory in order to avoid possible inconsistencies.

Particular attention should also be addressed to the constitutive equations of the solid preform, in conjunction with suitable experimental procedures to determine the mechanical behavior of the solids and their typical parameters (e.g., elastic constants, retardation time, and relaxation time). As a matter of fact, the whole modeling process suffers from the lack of precise measurements. Several researchers have found evidence of viscoelastic properties of the wet preforms with nonnegligible relaxation time [22], [27], [38], [49]. On the basis of such experimental observations and on the

fact that the solid and liquid constituents cannot deform independently but have to carry the load by joint deformation, the wet preform has been already modeled in [3] and [18] as a standard linear solid (the corresponding equation is a White–Metzner-type constitutive equation [26]). In the developed models, the velocity appearing in the convective derivative is the one related to the solid. This choice is based on heuristic arguments and the physical meaning of the boundary conditions required by the mathematical problem. However, the issue of which is the correct convective velocity to be used is still an open question in the literature, and it should be deeply analyzed.

In addition, one should take into account that the materials used are not isotropic but have characteristic directions, e.g., aligned fibers, so that a transversely isotropic or orthotropic constitutive equation would describe more accurately the behavior of the material.

As already mentioned in Section 9.2, the models presented here do not take into account thermal expansion and volume changes due to polymerization. These phenomena can have dramatic consequences. For example, in ceramic matrix composites the preform may be fragile and the thermal expansion can generate microcracks in the preform during cooling.

Another process for the production of composite materials that deserves to be studied is the so-called compression molding. In such a process a number of fibers are preimpregnated ("prepreg") with a certain quantity of liquid matrix (for example, epoxy resin that might be partially cured to facilitate handling), distributed in piles in a one-directional or multidirectional fashion and then placed in a possibly porous mold. The mixture of solid and liquid is then heated and compressed. The compression, operated by a piston, increases the solid volume fraction and produces a flow in a deformable porous media squeezing the exceeding liquid out of the pile ([24], [33], [45]). The whole process is rather complex because it has to be fast enough to reduce fabrication costs and control resin cure and, at the same time, accurate enough to avoid generating damages of the solid preform. In [17] a model for the 1-D isothermal process has been developed. It could be extremely interesting to improve such a model considering a more realistic 3-D geometry and including thermal effects.

9.5.2 Mathematical Analysis of the Existing Models

From the analytical point of view, one of the problems that should be investigated is the 1-D nonisothermal flow/deformation model. The study of the mathematical structure of such a model would complete the work concluding the theoretical analysis of the 1-D injection molding process. A first step in doing that could be a generalization of Billi's results, considering a constant in time but nonuniform in space solid volume fraction

and nonhomogeneous initial and boundary conditions. Another hypothesis that should be dropped is the one on the uncured injected resin, as in some practical cases the resin penetrating the preform is already partially cured, i.e., $\delta(s_e(t), t) > 0$. It would also be important to check what the minimal hypotheses need to be imposed on the heat capacity and thermal conductivity as the actual relations can be much more complex than those already used in [34].

A very interesting problem is also the study of the 1-D isothermal model when different constitutive equations for the wet and dry solids are used. As a matter of fact, when dealing with deformations, it has been found that stress–strain relations in the wet and dry domains are different ([2], [18], [27]). We are confident that results similar to the one obtained in [9] can be proved in this more general case. One could also analyze the correct formulation of the problem with Voigt-Kelvin constitutive equation for the wet solid. Such a problem is, in fact, highly nonlinear and presents nonstandard boundary conditions on the infiltration front.

The effects of the inertial terms have been studied, performing a sharp scaling, in [2], [3], and [40]. It has been shown, as mentioned earlier, that inertial terms play a dominant role only in the first instants of infiltration. From an analytical point of view it would be very interesting to study this initial transient using singular perturbation methods. Such an analysis can also have a fairly technological application allowing us to describe what happens during the initial stages of the process.

The general 3-D isothermal flow/deformation problem is completely open. Even if some 3-D simulations are available [4], to our knowledge there are no qualitative results on it. This, in fact, is a 3-D free boundary problem that presents two coupled equations: the stress equilibrium equation and the evolution equation for the pressure field in the liquid.

Finally, the mathematical problems generated by the 1-D compression molding model are open. They are essentially nonlinear parabolic problems with nonlinear boundary conditions. Actually, if one considers the pressure-driven dynamic model, one gets a free boundary problem of Stefan type.

This short list of possible future developments of the research is not exhaustive, not only for obvious reasons of conciseness, but also because these studies are more at the beginning than at the conclusion. This area is developing fast and is an incredible source of interesting mathematical problems.

Acknowledgments

The authors are grateful to the Italian Ministry for the University and Scientific Research (M.U.R.S.T.) and to the National Research Council (C.N.R. Contract 96.03858.ct01 on Multicomponent Flows) for funding this research.

References

1. Al-Hamdan, A., Rudd, C.D., and Long, A.C., Dynamic core movements during liquid moulding of sandwich structures, *Composites A*, **29A**, 273–82 (1998).
2. Ambrosi, D., and Preziosi, L., Modelling matrix injection through elastic porous preforms, *Composites A*, **29A**, 5–18 (1998).
3. Ambrosi D., and Preziosi L., Modelling injection moulding processes with deformable porous preform, *SIAM J. Appl. Math.*, in press.
4. Antonelli, D., and Farina, A., Injection moulding: Mathematical modelling and numerical simulations, *Composites A*, in press.
5. Baichen, L., Bickerton, S., and Advani, S.G., Modelling and simulation of resin transfer moulding (RTM)—Gate control, venting and dry spot prediction, *Composites A*, **27A**, 135–41 (1996).
6. Beavers, G.S., and Joseph, D.D., Boundary conditions at a naturally permeable wall, *J. Fluid Mech.*, **30**, 197–207 (1967).
7. Billi, L., Incompressible flows through porous media with temperature variable parameters, *Nonlinear Analysis, Theory, Math and Appl.*, **31**, 363–383 (1998).
8. Billi, L., Non-isothermal flows in porous media with curing, *EJAM*, **8**, 623–637.
9. Billi, L., and Farina, A., Unidirectional infiltration in deformable porous media: Mathematical modelling and self-similar solution, *Quart. Appl. Math.*, in press.
10. Blest, D.C., Duffy, B.R., McKee, S., and Marshall, P., A model of the fluid dynamics of resin-film infusion, *Strathclyde Mathematics Research Reports*, N. 3 (1995).
11. Blest, D.C., Duffy, B.R., McKee, S., and Zulkifle, A.K., Curing simulation of thermoset composites, *Strathclyde Mathematics Research Reports*, N. 37 (1998).
12. Bowen, R.M., Incompressible porous media models by use of the theory of mixtures, *Int. J. Engng. Sci.*, **18**, 1129–48 (1980).
13. Bowen, R.M., Theory of mixtures, in *Continuum Physics*, **3**, edited by A.C. Eringen, Academic Press (1976).
14. Bruschke, M.V., and Advani, S.G., A finite element control volume approach to mould filling in anisotropic porous media, *Polymer Compos.*, **11**, 398–405 (1990).
15. Bruschke, M.V., and Advani, S.G., A numerical approach to model non-isothermal viscous flow through fibrous media with free surfaces, *Int. J. Num. Meth. Fluids*, **19**, 575–603 (1994).

16. Calhoun, D.R., Yalvaç, S., Wetters, D.G., Wu, C.H., Wang, T.J., Tsai, J.S., and Lee, L.J., Mold filling analysis in resin transfer molding, *Polymer Compos.*, **17**, 251–64 (1996).

17. Farina, A., Cocito, P., and Boretto, G., Flow in deformable porous media: Modelling and simulations of the compression moulding process, *Mathl. Comput. Modelling*, **26**, 1–15 (1997).

18. Farina, A., and Preziosi, L., Non–isothermal injection moulding with resin cure and preform deformability, *Composites A*, submitted.

19. Fasano, A., and Primicerio, M., Free boundary problems for nonlinear parabolic equations, *J. Math. Anal. Appl.*, **72**, 247–73 (1979).

20. Gonzalez–Romero, V.M., and Macosko, C.W., Process parameters estimation for structural reaction injection moulding, *Polym. Engng. Sci.*, **30**, 142–6 (1990).

21. Hammami, A., Gauvin, R., and Trochu, F., Modelling the edge effect in liquid composites molding, *Composites A*, **29A**, 603–9 (1998).

22. Han, K., Lee, L.J., and Liu, M.J., Fiber mat deformation in liquid composite moulding. II: Modelling, *Polymer Compos.*, **14**, 151–60 (1993).

23. Hornung, U., *Homogenization and Porous Media*, Springer (1996).

24. Isayev, A.I., *Injection and Compression Moulding Fundamentals*, Marcel Dekker (1987).

25. Jäger, W., and Mikelic, A., On the boundary conditions at the contact interface between a porous medium and a free fluid, *Annali della Scuola Normale Superiore di Pisa*, Serie IV, **23**, 403–65 (1996).

26. Joseph, D.D., *Fluid Dynamics of Viscoelastic Liquids*, Springer–Verlag (1990).

27. Kim, Y.R., McCarthy, S.P., and Fanucci, J.P., Compressibility and relaxation of fiber reinforcements during composite processing, *Polymer Compos.*, **12**, 13–9 (1991).

28. Lacoste, E., Aboulfatah, M., Danis, M., and Girot, F., Numerical simulation of the infiltration of fibrous preforms by pure metal, *Metall. Trans.*, **24A**, 2667–78 (1993).

29. Lacoste, E., Danis, M., Girot, F., and Quennisset, J.M., Numerical simulation of the injection moulding of thin parts by liquid metal infiltration of fibrous preform, *Mater. Sci. Eng. A*, **135**, 45–9 (1991).

30. Ladyzenskaja, O.A., Solonnikov, V.A., and Ural'ceva, N.N., *Linear and Quasilinear Equations of Parabolic Type*, AMS Translations of Mathematical Monographs 23 (1968).

31. Lin, M., Hahn, T., and Huh, H., A finite element simulation of resin transfer molding based on partial nodal saturation and implicit time integration, *Composites A*, **29A**, 541–50 (1998).

32. Liu, I.S., On chemical potential and incompressible porous media, *J. Mech.*, **19**, 327–42 (1980).

33. Mallik, P.K., *Fiber–Reinforced Composites: Materials Manufacturing and Design*, Marcel Dekker (1988).

34. Markov, K., and Preziosi L., eds., *Heterogeneous Solids: Micromechanics, Modelling Methods and Simulations*, Birkhäuser (1999).

35. Mortensen, A., Masur, L.J., Cornie, J.A., and Flemings, M.C., Infiltration of fibrous preforms by a pure metal: Part I. Theory, *Metall. Trans.*, **20A,** 2535–47 (1989).

36. Müller, I., Rational thermodynamics of mixtures of fluids, in *Thermodynamic and Constitutive Equations*, Lecture Notes in Physics 228, edited by G. Grioli, Springer–Verlag (1985).

37. Munaf, D., Wineman, S., Rajagopal, K.R., and Lee, D.W., A boundary value problem in ground water motion analysis—Comparison of the prediction based on Darcy's law and the continuum theory of mixtures, *Mat. Models Methods Appl. Sci.*, **3**, 231–48 (1993).

38. Parker, K.H., Metha, R.V., and Caro, C.G., Steady flow in porous, elastic deformable materials, *Trans. ASME E: J. Appl. Mech.*, **54**, 794–800 (1987).

39. Preziosi, L., The theory of deformable porous media and its applications to composite materials manufacturing, *Surv. Math. Ind.*, **6**, 167–214 (1996).

40. Preziosi, L., Joseph, D.D., and Beavers, G.S., Infiltration in initially dry, deformable porous media, *Int. J. Multiphase Flows*, **22**, 1205–22 (1996).

41. Puslow, D., and Child, R., Autoclave moulding of carbon–fiber reinforcing epoxies, *Composites*, **17**, 127–36 (1986).

42. Rajagopal, K.R., and Tao, L., *Mechanics of Mixtures*, World Scientific (1995).

43. Rajagopal, K.R., Wineman, A.S., and Gandhi, M.V., On boundary conditions for a certain class of problems in mixture theory, *Int. J. Eng. Sci.*, **24**, 1453–63 (1986).

44. Rudd, C.D., and Kendall, K.N., Towards a manufacturing technology for high-volume production of components, *Proc. Inst. Mech. Eng.*, **206**, 77–91 (1992).

45. Rudd, C.D., Long, A.C., Kendall, K.N., and Mangin, C.G.E., *Liquid moulding Technologies*, Woodhead Publishing Limited (1997).

46. Rudd, C.D., Owen, M.J., and Middleton, V., Effects of process variables on cycle time during resin transfer moulding for high volume manufacture, *Mater. Sci. Tech.*, **6**, 656–65 (1990).

47. Saffman, P.G., On the boundary condition at the interface of a porous medium, *Studies in Appl. Math.*, **1**, 93–101 (1971).

48. Saunders, R.A., Lekakou, C., and Bader, M.G., Compression of fiber plain woven cloths in the processing of polymer composites, *Composites A*, **29A**, 443–54 (1998).

49. Sommer, J.L., and Mortensen, A., Forced unidirectional infiltration in deformable porous media, *J. Fluid Mech.*, **311**, 193–215 (1996).

50. Tao, L., and Rajagopal, K.R., On boundary conditions in mixture theory, in Recent Advances in Elasticity and Viscoelasticity, edited by K.R. Rajagopal, World Scientific (1994).

51. Trevino, L., Rupel, K., Young, W.B., Liu, M.J., and Lee, L.J., Analysis of resin injection moulding in moulds with preplaced fiber mats. I: Permeability and compressibility measurements, *Polymer Compos.*, **12**, 20–9 (1991).

52. Upadhyay, R.K., and Liang, E.W., Consolidation of advanced composites having volatile generation, *Polymer Compos.*, **12**, 417–29 (1991).

53. Yoo, Y.E., and Lee, W. I., Numerical simulation of resin transfer mold filling process using the boundary element method, *Polymer Compos.*, **17**, 368–74 (1996).

54. Young, W.B., Three–dimensional non–isothermal mold filling simulations in resin transfer moulding, *Polymer Compos.*, **15**, 118–27 (1994).

55. Young, W.B., Han, K., Fong, L.H., Lee, L.J., and Liu, M.J., Flow simulation in molds with preplaced fiber mats, *Polymer Compos.*, **12**, 391–403 (1991).

10

Porous Media with Hydrophile Granules

ANTONIO FASANO

Università di Firenze
Dipartimento di Matematica "U. Dini"
Firenze, Italy

ABSTRACT. A diaper is a porous medium with water-absorbing grains. The flow of a liquid in the presence of such absorption is studied taking Darcy's law as the basic equation for the liquid motion. The swelling of the granules, which obeys a given kinetic law, produces a progressive reduction of porosity. The mass balance leads to a nonlinear partial differential equation (parabolic in the unsaturated region and elliptic in the saturated region) with history-dependent coefficients. Here we present a careful analysis of the boundary conditions, which can be selected in various ways, according to the specific physical situations, on both the injection surface and the penetration front. We illustrate in some detail the one-dimensional case for unsaturated and saturated flows, and we point out the main open problems.

10.1 Introduction

The present study originates from a research performed at the University of Kaiserslautern [9] in cooperation with a German company.

The physical system (a baby's diaper) is a porous medium (made of cellulose fibers) whose pores contain granules that can absorb water up to 60 to 70 times their original volume. Absorption, of course, slows down the

A. Fasano (ed.), *Complex Flows in Industrial Processes*

penetration process, but the consequent reduction of porosity must not be too severe or the system becomes unable to accept liquid at the required rate (gel-blocking). As we shall see, in our approach such a condition will appear in a natural way.

The basic assumption in the model proposed in [9] was that the leading transport mechanism in the porous medium is diffusion. After a brief summary of that model we will point out the advantage of using the classical laws of filtration through porous media and we will shift to the model that is the real subject of this chapter.

Denoting by u, v the water concentrations in the porous medium and in the granules, respectively, the governing equations according to [9] are

$$\frac{\partial u}{\partial t} = \frac{1}{\theta(x)} \nabla \cdot (\theta(x)\, d(u) \nabla u) - A(u, v), \quad x \in Q \subset \mathbf{R}^3,\ 0 < t < T \tag{10.1}$$

$$\frac{\partial v}{\partial t} = A(u, v) \tag{10.2}$$

where the diffusivity $d(u)$ is taken as

$$d(u) = a e^{bu} \tag{10.3}$$

where a and b are positive constants. The function A represents the absorption rate

$$A(u, v) = \gamma(u v_\infty - v u_\infty) \tag{10.4}$$

with $\gamma > 0$, and u_∞, v_∞ denoting the maximum concentrations.

The role of the strictly positive function $\theta(x)$ is to describe a kind of microstructure for interstitial diffusion.

The boundary data are

$$\frac{\partial u}{\partial n} = 0 \tag{10.5}$$

on part of the boundary and

$$\theta(x)\, d(u) \frac{\partial u}{\partial n} = k(t)(u_\infty - u) \tag{10.6}$$

on the complementary part (supposed to be a convex domain). Here $k(t)$ is a step function.

Existence and uniqueness of a classical solution of (10.1) to (10.6) with prescribed initial data $u_0(x), v_0(x)$ have been proved in [8], assuming $\theta \in C^1$, $v_0 \in C^1$, $u_0 \in H^{2+\alpha}$ in $\overline{Q}$.

The fact that equation (10.1) never degenerates implies that even if $u_0 \equiv 0$, water will be present everywhere in Q after the injection time (i.e., the time at which k becomes positive), because linear absorption is not strong enough to generate propagation fronts.

If, on the contrary, we want to describe the evolution of a wetting front, it is better to use the most natural law for the flows through porous media, i.e., Darcy's law.

Starting from this viewpoint, a completely different mathematical model has been formulated in [4] as a free boundary problem.

In the next section we will illustrate the general multidimensional model based on Darcy's law. The only mathematical results available [3] are about the first stage of the one-dimensional version and will be dealt with and extended in Section 10.3.

Although largely based on the material of [3] and [4], this chapter contains some new contributions, performing a much deeper analysis of the model and presenting more general cases of the one-dimensional problem.

However, the main scope of the chapter is not to refer to the partial results obtained so far, but to point out that this is indeed an extremely rich research field with a number of open problems.

10.2 The General Multidimensional Model

10.2.1 The Governing Differential Equations

According to Darcy's law, the volumetric velocity of the flowing liquid is

$$\mathbf{q} = -k(S, \phi)(\nabla p - \mathbf{g}) \tag{10.7}$$

where $\mathbf{g}$ is the gravity acceleration, k is the hydraulic conductivity of the system, depending on the saturation S and the porosity ϕ.

The medium is saturated ($S = 1$) when the pressure exceeds the saturation pressure p_S, while for $p < p_S$ it is related to p due to capillarity effects:

$$S = S(p), \quad p \leq p_S \tag{10.8}$$

with $S(p_S) = 1, S'(p) > 0$ for $p < p_S$.

In [4] gravity was neglected. Another generalization we introduce here is to allow the hydrophile granules to be nonuniformly distributed in the system. Because we consider the system as a continuum, we can define a concentration of granules $\rho(x)$ so that if $V_g(x,t)$ is the volume of each of the granules in a volume element centered at x, the volume fraction occupied by the granules at x will be

$$V(x,t) = \rho(x)V_g(x,t). \tag{10.9}$$

An important feature of the system is that the granules are free to swell in the pores, so that they do not impinge the neighboring grains nor deform the porous matrix.

The increase of V occurs at the expense of porosity, because

$$\phi(x,t) + V(x,t) = \phi_0(x) + V_{\min}(x) \tag{10.10}$$

$\phi_0, V_{\min}$ being the initial data for ϕ and V. The right-hand side represents the porosity of the medium with no V swollen grains and $V_{\min} = \rho(x)V_g^{\min}$.

Denoting by $V_g^{\max}$ the maximum volume attainable by the granules (of course we are supposing just one family of identical granules) and putting $V_{\max}(x) = \rho(x)V_g^{\max}$, the (irreversible) absorption kinetics can be described by the equation

$$\frac{\partial V}{\partial t} = f(V_{\max}(x) - V)(S - S_0)_+ \tag{10.11}$$

where f is a C^1 function such that $f' \geq 0$, $f(0) = 0$, $f(\xi) > 0$ for $\xi > 0$. In (10.11) we have introduced the residual moisture content $S_0 > 0$ at atmospheric pressure and $(S - S_0)_+$ denotes the positive part. We suppose that the medium is initially dry (or the moisture content is in any case negligible) and that once it is wet it cannot release water to the granules if saturation is not larger than S_0. The liquid mass balance equation is

$$\frac{\partial(S\phi)}{\partial t} + \operatorname{div} \mathbf{q} = -\frac{\partial \mathrm{V}}{\partial \mathrm{t}} \tag{10.12}$$

which because of (10.7) and (10.10) becomes

$$\phi\frac{\partial S}{\partial t} + (S-1)\frac{\partial \phi}{\partial t} - \operatorname{div}(\mathrm{k}(\mathrm{S},\phi)\nabla \mathrm{p}) - \mathrm{g}\frac{\partial \mathrm{k}(\mathrm{S},\phi)}{\partial \mathrm{x}_3} = 0 \tag{10.13}$$

where x_3 is the upward vertical coordinate.

In the saturated region equation (10.13) reduces to

$$\operatorname{div}(\mathrm{k}(1,\phi)\nabla \mathrm{p}) + \mathrm{g}\frac{\partial \mathrm{k}(1,\phi)}{\partial \mathrm{x}_3} = 0 \tag{10.14}$$

as long as there are active granules. Granules may or may not reach the maximum size $V_g^{\max}$ in a finite time (depending on the structure of the function f). In a region where the granules have been saturated, k becomes constant and (10.14) simplifies to the standard equation for incompressible saturated flows

$$\Delta p = 0. \tag{10.15}$$

In the unsaturated region equation (10.13) is a parabolic partial differential equation for the pressure (remember (10.8)). The boundary conditions require a careful analysis.

10.2.2 Initial Conditions

Our porous medium occupies a bounded domain $\Omega \subset \mathbf{R}^3$, which we may suppose initially dry at the atmospheric pressure

$$S = 0, \quad p = p_{\text{atm}} \leq p_0 \quad \text{in } \Omega \text{ for } t = 0. \tag{10.16}$$

Remark 10.1. *Of course we mean that $t = 0$ is the time at which injection starts. The two conditions (10.16) are not compatible with the relationship (10.8) between S and p established by capillarity, because the medium has not been wet previously. In the not-penetrated material the ideal initial condition $S = 0$, $V_g = V_g^{\min}$ may be slightly altered by the exposure to air moisture, with corresponding nontrivial modifications of the free boundary problem we are going to deal with.*

10.2.3 Conditions on the Outer Boundary

As in [9] we must say that $\partial\Omega$ is the union of two regular surfaces Γ_1, Γ_2 with Γ_2 impermeable (to prevent outflow)

$$\mathbf{q} \cdot \mathbf{n} = 0 \quad \text{on } \Gamma_2 \quad \text{for } t > 0. \tag{10.17}$$

Clearly (10.17) comes into play only when the wetting front has reached Γ_2.

Injection occurs through the surface Γ_1. A typical condition is

$$-\mathbf{q} \cdot \mathbf{n} = \chi(\Gamma_0) q_0(t) \quad \text{on } \Gamma_1 \quad \text{on } t > 0 \tag{10.18}$$

($\mathbf{n}$ is the outer normal unit vector) where $\chi(\Gamma_0)$ is the characteristic function of a simply connected convex smooth subset of Γ_1 and $q_0(t)$ is the volume injection rate per unit surface through the injection surface Γ_0.

However, it may not be possible in practice to impose the flux condition (10.18) if the required injection rate over the "natural" injection area Γ_0 is too large (in the typical case $\operatorname{diam}\Gamma_0 \ll \operatorname{diam}\Gamma_1$).

A more correct boundary condition should contain some constraint. At this point the choice of the boundary condition becomes quite delicate.

10.2.3.1 Discharge Constrained Inflow

The real information we have at the boundary is the cumulative volume injection rate $Q_c(t)$. A simplified way of introducing a constraint is via the inequality

$$-\mathbf{q} \cdot \mathbf{n} \leq q_{\max} \quad \text{on } \Gamma_1 \tag{10.19}$$

where $q_{\max} > 0$ is a prescribed upper bound. Thus we can define $q_0(t) = \frac{Q_c(t)}{\operatorname{meas}\Gamma_0}$ if $q_0(t) \leq q_{\max}$, while in the opposite case we modify (10.18) as follows

$$-\mathbf{q} \cdot \mathbf{n} = \chi(\Gamma(t)) q_{\max} \tag{10.20}$$

where $\chi(\Gamma(t))$ is the characteristic function of a new set $\Gamma(t)$ such that $\Gamma_1 \supset \Gamma(t) \supset \Gamma_0$ satisfying the requirement

$$\text{meas}\,\Gamma(t) = \frac{Q_c(t)}{q_{\max}}. \tag{10.21}$$

Of course there is arbitrariness in the definitions of $\Gamma(t)$. For example, it can be constructed by imposing that all points of $\partial\Gamma(t)$ have the same distance from Γ_0 (in this way $\Gamma(t)$ will also be convex).

10.2.3.2 Pressure Constrained Inflow

It is well known that, particularly in the early stage of penetration, we can have a large pressure gradient at inflow surface even if injection pressure is relatively small. For this reason, the constraint (10.19) may be artificial and it seems more appropriate to introduce a constraint on pressure. The latter approach is, however, much more complicated. First, the constraint is applied to an unknown quantity

$$p \le p_{\max} \quad \text{on } \Gamma_1, \quad p_{\max} > p_S \tag{10.22}$$

and it can be checked a posteriori. As long as (10.22) is fulfilled, the boundary condition to be used is (10.18).

When the constraint comes into play the condition to be imposed contains the boundary of the "coincidence set" $\Gamma_p(t) = \{p = p_{\max}\}$, which is not necessarily included in Γ_0.

After the onset of $\Gamma_p(t)$ the set Γ_0 becomes insufficient for the required total discharge $Q_c(t)$, and again we must introduce the larger inflow region $\Gamma(t)$, which is no longer defined simply as (10.21). A correct boundary condition would be

$$-\mathbf{q}\cdot\mathbf{n} = \chi(\Gamma(t)\setminus\Gamma_p(t))q_0(t), \quad q_0(t) = \frac{Q_c(t)}{\text{meas}\,\Gamma_0}. \tag{10.23}$$

Again, we can require that the points of $\partial\Gamma(t)$ have the same distance from Γ_0, but this time the definition of $\text{meas}\,\Gamma(t)$ is implicit

$$\text{meas}\,\{\Gamma(t)\setminus\Gamma_p(t)\}q_0(t) + Q_p(t) = Q_c(t) \tag{10.24}$$

where $Q_p(t)$ is the (unknown) volumetric flux through the coincidence set $\Gamma_p(t)$; here, of course, we have the condition

$$p = p_{\max}.$$

Again the inclusion $\Gamma(t) \subset \Gamma_1$ implies a bound on $Q_c(t)$.

Remark 10.2. *In all conditions (10.17) to (10.20), (10.23)* $\mathbf{q}$ *is given by (10.7) and therefore it contains the unknown $S(p)$ as well as ϕ, which is actually a function of S and the unknown wetting front (see Section 10.3).*

Therefore the boundary conditions are in any case nonlocal and history-dependent.

Remark 10.3. *The no flux condition in the complement of the inflow region of Γ_1 is taken for simplicity. The wetting front will certainly expand over Γ_1 making the pressure raise because of capillarity. However, such a condition may become unsuitable if the saturation front expands beyond the inflow region, and it certainly does if pressure exceeds the constraint $p_{\max}$. In that case the model should allow for a seepage free boundary. However, outflow situations should be avoided and we will not deal with such a possibility.*

In the same spirit we say that the form of the constrained inflow conditions we have proposed are in fact a shortcut to avoid the study of the impact of the liquid over the surface (which can generate complex situations depending on the volume input rate and the medium permeability). However, in the specific case of diapers it is very reasonable to assume that basically no tangential motion takes place over the injection surface and that the conditions suggested are close to reality.

10.2.4 The Interior Free Boundaries

Besides the one or two free boundaries associated with the constrained flow conditions, the problem has two main moving unknown boundaries:

(i) the wetting front $\Gamma_w(t)$, and

(ii) the saturation front $\Gamma_S(t)$.

Both boundaries are absent for $t = 0$.

10.2.4.1 The Wetting Front

The interface between the wet and dry regions is a material surface and therefore it moves according to Darcy's law. We may conjecture different scenarios for the advancing mechanism of the front.

It is reasonable to assume that while the wetting front proceeds, the value of the saturation is at least S_0, i.e., the minimum moisture content of the wet medium. If it is precisely S_0 the conditions on $\Gamma_w(t)$ are

$$p|_{\Gamma_w} = p_0 \tag{10.25}$$

(p_0 is a reference pressure)

$$\phi_0 S_0 v_n = -k(S_0, \phi_0)\frac{\partial p}{\partial n} \tag{10.26}$$

where n is the outer normal to $\Gamma(t)$ and v_n is the normal component of the front speed. In (10.26) ϕ_0 is obviously evaluated on Γ_w. However, we can also suppose that on Γ_w S can be larger than S_0 if the penetration process is fast enough. The phase change analog to (10.25), (10.26) is represented

by the Stefan conditions, if instead we replace p_0 by a function $p_w(v_n)$ we have conditions similar to the so-called kinetic undercooling:

$$p = p_w(v_n) \geq p_0 \tag{10.27}$$

$$\phi_0 S_w(v_n) v_n = -k(S_w(v_n), \phi_0) \frac{\partial p}{\partial n} \tag{10.28}$$

where $S_w(v_n)$ is a nondecreasing function with values between S_0 and 1 and $p_w(v_n)$ is such that $S(p_w(v_n)) = S_w$.

If $S_w(v_n)$ becomes equal to 1, then the unsaturated region disappears (locally). The limit case is to eliminate the capillarity effect completely (a reasonable approximation for fast penetration). We will deal with this case in the one-dimensional case (Section 10.4).

Remark 10.4. *If initially the medium is not perfectly dry and there is some moisture S_d, the change to be introduced in (10.26) consists in replacing the saturation multiplying v_n by the saturation jump across $\Gamma_w(t)$.*

In doing so we suppose that the time scale of the wetting process is much shorter than the evolution time of S in the not-penetrated region. Also we keep $\phi = \phi_0$ because we assume that $S_d \leq S_0$.

10.2.4.2 The Saturation Front Γ_S

Unlike Γ_w, the saturation front is not a material surface, but is simply the level set defined by the equality

$$p = p_S \quad \text{on both sides of } \Gamma_S. \tag{10.29}$$

The second condition to be imposed on Γ_S is the continuity of volumetric velocity. Because both S and ϕ are continuous across Γ_S, the latter condition amounts to

$$\left[\frac{\partial p}{\partial n}\right]_{\Gamma_S} = 0 \tag{10.30}$$

where $[\ ]_{\Gamma_S}$ denotes the jump.

10.2.5 Summary of the Initial and Boundary Conditions

As we have seen, we have a problem with multiple free boundaries resulting from the combination of the following alternatives.

Initial Conditions. For $t = 0$, we may have:

(i1) the perfectly dry medium, or

(i2) the partially moisturized medium.

External Boundary Conditions (Γ_1). On the pervious part of the external boundary, we may have:

(eb1) the unconstrained inflow condition (no additional free boundaries),

(eb2) the discharge-constrained inflow (contains one additional free boundary $\partial\Gamma(t)$), or

(eb3) the pressure-constrained inflow (contains two additional free boundaries $\partial\Gamma_p(t)$, $\partial\Gamma(t)$).

Free Boundary Conditions (Γ_w). On the wetting front Γ_w, we may have the options:

($\Gamma_w S$) the Stefan-like conditions with two options—($\Gamma_w S0$) the saturation on Γ_w coincides with the threshold saturation for absorption S_0 or ($\Gamma_w S1$) the saturation for penetration is $S_1 \neq S_0$, or ($\Gamma_w U$) the kinetic undercooling analog.

Instead we have no alternatives for external boundary conditions (Γ_2):

(eb0) no flux through Γ_2

Free Boundary Conditions (Γ_S).

(Γ_S) conditions (10.29) and (10.30) on the saturation front.

The easiest combination is, of course, (i1), (eb1), ($\Gamma_w S0$), but even in that case the problem is open due to the complexity of the differential system (10.8) to (10.13), which we are going to analyze in the next section.

Remark 10.5. *Distinguishing between the saturation threshold for absorption and the one for penetration in the dry region is not a trivial change, particularly if it implies that Γ_w is no longer the set where absorption starts.*

Remark 10.6. *Although the device is not conceived for such an extreme use, we may envision the situation in which saturation zones are formed near the impervious boundary Γ_2. In other words, the saturated region may be disconnected.*

10.3 Statement of the General Problem

We want to find a more compact form of equations (10.13) and (10.14), emphasizing the fact that the coefficients are functionals of p and the wetting front. This can be done by integrating equation (10.11) and using (10.10). In the following, we refer explicitly to the option ($\Gamma_w S0$) for the conditions on Γ_w.

Let us define

$$\Phi(V,x) = \int_{V_0(x)}^{V} \frac{dy}{f(V_{\max}(x) - y)}, \quad V_0(x) \le V < V_{\max}(x) \tag{10.31}$$

and for any $x \in \Omega$

$$\theta(x) = \sup\{t \mid S(x,t) < S_0\}. \tag{10.32}$$

Clearly $\theta(x)$ is the time at which the wetting front Γ_w reaches the point x, thus triggering the absorption process.

The integration of (10.11) leads to

$$\Phi(V,x) = \Theta(S,\theta,t) \tag{10.33}$$

with

$$\Theta(S,\theta,t) = \int_{\theta(x)}^{t} [S(x,\tau) - S_0]\, d\tau, \quad \forall\, t > \theta(x). \tag{10.34}$$

Because Φ is invertible with respect to V, setting $\psi = \Phi^{-1}$ we have

$$V(x,t) = \psi(\Theta,x) \tag{10.35}$$

and from (10.10)

$$\phi(x,t) = \phi_0(x) + V_0(x) - \psi(\Theta). \tag{10.36}$$

It is now clear that

$$\frac{\partial \phi}{\partial t} = -\frac{\partial \psi}{\partial \Theta}(S(x,t) - S_0) \le 0, \quad \forall\, t > \theta(x) \tag{10.37}$$

where we have used $\frac{\partial \psi}{\partial \Theta} \ge 0$ and $S \ge S_0$ in the wet region. Moreover,

$$\frac{\partial \phi}{\partial x_i} = -\frac{\partial \psi}{\partial \Theta} \int_{\theta(x)}^{t} \frac{\partial S}{\partial x_i}\, d\tau - \frac{\partial \psi}{\partial x_i} + \frac{\partial}{\partial x_i}(\phi_0 + V_0) \tag{10.38}$$

(if, e.g., the function $\theta(x)$ is differentiable).

Equations (10.36), (10.37), and (10.38) must be used in (10.13) (together with $S = S(p)$) and in (10.14) in order to obtain the final partial differential equations to be solved in the wet region.

At this point the classical formulation of the problem can be stated as finding the continuously differentiable free boundaries $\Gamma_w(t)$, $\Gamma_S(t)$, the pressure $p(x,t)$ with the obvious regularity requirement, satisfying (10.13) in the unsaturated region, (10.14) in the saturated region (with the replacements shown earlier), and one of the possible sets of initial and boundary

conditions illustrated in the previous section (which may involve additional free boundaries).

Some of the basic assumptions that must be satisfied and that will be kept in the sequel are

(H1) $\phi_0 \in C^1(\overline{\Omega})$, $0 < \phi_m \le \phi_0(x) \le \phi_M < 1$;

(H2) $V_0 \in C^1(\overline{\Omega})$, $0 < V_m^{(0)} \le V_0(x) \le V_M^{(0)}$, $\phi_M + V_M^{(0)} < 1$;

(H3) $V_{\max} \in C^1(\overline{\Omega})$, $0 < V_m \le V_{\max}(x) \le V_M$, $V_M^{(0)} < V_m$, $\phi_m + V_m^{(0)} - V_M \equiv \phi_{\min} > 0$;

(H4) $k \in C^3([0,1] \times [0,1])$, $0 < k_m \le k(S,\phi) \le k_M$, $\frac{\partial k}{\partial \phi} > 0$; and

(H5) $S \in C^3([p_0, p_S])$, $S'(p) > 0$ in (p_0, p_S).

Remark 10.7. *Assumptions (H1) to (H3) ensure that $\phi \ge \phi_{\min} > 0$, so that (10.13) is parabolic (possibly degenerate).*

10.4 The One-Dimensional Problem with No Capillarity

The absence of capillarity eliminates the unsaturated region. The wetting front and the saturation front coincide. Saturation is either 0 or 1. In this situation our problem is a generalization of the well-known Green–Ampt model [7].

Setting $p_0 = 0$, we have to solve equation (10.14), where for simplicity we neglect gravity, i.e.,

$$\frac{\partial}{\partial x}\left[k(1,\phi)\frac{\partial p}{\partial x}\right] = 0, \quad 0 < x < s(t),\ t > 0 \tag{10.39}$$

with the boundary condition

$$-k(1,\phi)\frac{\partial p}{\partial x} = q_0(t) > 0 \quad \text{for } x = 0,\ t > 0. \tag{10.40}$$

The curve $x = s(t)$ is the penetration front, where we impose

$$p(s(t), t) = 0. \tag{10.41}$$

An immediate consequence of (10.39) is that (10.40) holds not only for $x = 0$ but also for any $x \in [0, s(t)]$. Moreover the equation

$$\phi_0(s)\dot{s}(t) = q_0(t) \tag{10.42}$$

together with the initial condition $s(0) = 0$ defines the penetration front in the form

$$s(t) = E^{-1}(L(t)) \tag{10.43}$$

where E^{-1} is the inverse function of

$$E(s) = \int_0^s \phi_0(\sigma)\, d\sigma \tag{10.44}$$

and

$$L(t) = \int_0^t q_0(\tau)\, d\tau. \tag{10.45}$$

Not only $s(t)$ is known, but also $\phi(x,t)$, because putting $S = 1$ in (10.34), we get from (10.36)

$$\phi(x,t) = \phi_0(x) + V_0(x) - \psi[(t - \theta(x))(1 - S_0), x] \tag{10.46}$$

where $\theta(x)$ is the inverse function of $s(t)$.

Thus $k(1,\phi)$ becomes a known function $K(x,t,\theta(x))$, and we can finally obtain the expression of pressure

$$p(x,t) = \int_x^{s(t)} \frac{q_0(t)}{K(\xi,t,\theta(\xi))}\, d\xi. \tag{10.47}$$

The problem is completely solved unless some constraint is imposed.

The assumptions on the data are very mild. If we accept (10.43) and (10.47) as a solution in a weak sense all we need is $q_0 > 0$ bounded, ϕ_0, V_0 continuous, and k bounded, continuous, and strictly positive.

Of course for 1-D problems the constraint on discharge can be imposed only directly on $q_0(t)$. More interesting is the pressure constrained inflow condition on $p(0,t) \le p_{\max}$, which comes into play if the inequality

$$q_0(t) \int_0^{s(t)} \frac{1}{K(\xi,t,\theta(\xi))}\, d\xi \le p_{\max} \tag{10.48}$$

is violated out of some finite interval $[0,t^*]$.

Beyond t^* we have the switch from the boundary condition (10.40) to

$$p = p_{\max}, \quad t > t^*. \tag{10.49}$$

The volumetric velocity $q(t)$ is now unknown and the pair of equations

$$-k(1,\phi)\frac{\partial p}{\partial x} = q(t) \tag{10.50}$$

$$\phi_0(s)\dot{s}(t) = q(t) \tag{10.51}$$

leads to the following integro-differential equation

$$p_{\max} = \phi(s)\dot{s}(t) \int_0^{s(t)} \frac{1}{K(\xi, t, \theta(\xi))}\, d\xi, \qquad s(t^*+) = s(t^*-) \equiv s^* \quad (10.52)$$

which involves $s(t)$ and its inverse $\theta(\xi)$.

Let us sketch the proof of the following theorem.

Theorem 10.1. *Under assumptions (H1) to (H4) of Section 10.3 and the assumptions made on the absorption kinetics (10.11), there exists a unique solution of (10.52),* $\forall\ t > 0$.

Proof. Taken $T > t^*$, define the set

$$\Sigma = \{\sigma \in C([t^*, T]) \mid \sigma(t^*) = s^*, \quad A_1 \le \frac{\sigma(t') - \sigma(t'')}{t' - t''} \le A_2\} \quad (10.53)$$

with $A_1(T), A_2(T)$ uniquely determined by the system

$$A_1 = \frac{p_{\max}}{\phi_M} \frac{k_m}{s^* + A_2[T - t^*]}, \qquad A_2 = \frac{p_{\max}}{\phi_m} \frac{k_M}{s^* + A_1[T - t^*]} \quad (10.54)$$

It is easy to see that the mapping $\widetilde{\sigma} = \mathcal{M}\sigma$ such that

$$\frac{d\widetilde{\sigma}}{dt} = \frac{p_{\max}}{\phi_0(\sigma)} \left(\int_0^{\sigma(t)} \frac{1}{K(\xi, t, \theta(\xi))}\, d\xi \right)^{-1}, \quad \widetilde{\sigma}(t^*) = s^* \quad (10.55)$$

where $\theta = \sigma^{-1}$ satisfies the property $\mathcal{M}(\Sigma) \subset \Sigma$.

The proof of the theorem consists in showing that $\mathcal{M}$ is continuous in the selected topology and contractive if $T - t^*$ is sufficiently small (note that Σ is closed, convex, and compact in the same topology).

The main step in this analysis is evaluation of the integral

$$\int_0^{\sigma_{\min}(t)} |\theta_1(\xi) - \theta_2(\xi)|\, d\xi \quad (10.56)$$

with $\sigma_{\min}(t) = \min(\sigma_1(t), \sigma_2(t))$, $\theta_1 = \sigma_1^{-1}$, $\theta_2 = \sigma_2^{-1}$, for any pair $\sigma_1, \sigma_2 \in \Sigma$.

It is easy to realize that (10.56) is dominated by

$$\int_{t^*}^{t} |\sigma_1(\tau) - \sigma_2(\tau)|\, d\tau. \quad (10.57)$$

The other terms in the estimate of $|\widetilde{\sigma}_1 - \widetilde{\sigma}_2|$ are standard. □

Theorem 10.1 provides the solution of the constrained problem as long as inequality (10.48) is not valid. If such a situation is reversed beyond some

interval $[t^*, t^{**}]$, then we have to introduce the flux condition (10.40), and so on.

Remark 10.8. *In the one-dimensional version, the impervious boundary Γ_2 is a plane situated a given distance from the inflow surface. In the case we have considered, when the wetting front reaches Γ_2 the solution is terminated.*

10.5 The One-Dimensional Problem with Capillarity

Here we will deal only with the first stage of penetration, i.e., before the appearance of the saturated region, and with no constraints on the inflow condition. So far the only known result is an existence theorem, confined to the options (i1), (eb1), and ($\Gamma_w S0$) of Section 10.2.

In addition to (H1) to (H5), we need the following simplifying assumptions

$$S'(p) > 0 \quad \text{in } [0, p_S], \qquad \frac{S''}{S'^2}(S - S_0) \leq 1 \quad \text{in } [0, p_S] \tag{10.58}$$

where $p = 0$ is the reference value on the free boundary, and

$$\frac{\partial k}{\partial S} = 0. \tag{10.59}$$

More conditions will be added later to deal with the case $S'' \neq 0$. Particularly the latter condition is a strong limitation from the physical point of view (see, e.g., page 143 in [2]). It has been removed in a very recent paper [6].

Besides the linear case $S(p) = S_0 + (1 - S_0)\frac{p}{p_S}$, a less trivial choice of $S(p)$ satisfying (10.58) is

$$S(p) = \frac{\gamma - S_0}{\gamma - 1} - \frac{\gamma}{\gamma - 1}(1 - S_0) \exp\left(- \frac{p}{p_S} \log \gamma \right), \quad \forall\, \gamma \in (1, 2].$$

To avoid formal complications we replace (H1) to (H3) by the simpler conditions $\phi_0 = \text{constant}$, $V_0 = \text{constant}$, $\rho = \text{constant}$, and

$$\phi_m = \phi_0 + V_0 - V_{\max} > 0. \tag{10.60}$$

Concerning the dependence of k on ϕ we impose

$$\frac{\phi}{k} k'(\phi) > 2, \quad \phi_m \leq \phi \leq \phi_0. \tag{10.61}$$

Specific examples in the literature agree with (10.61). For example, the Fair

and Hatch formula (see page 134 in [1]) gives the following dependence

$$k = \frac{\phi^3}{(1-\phi)^2} \tag{10.62}$$

for which the left handside of (10.61) is larger than 3.

One more condition is about the absorption kinetics (10.11). Besides the assumptions already made on the function f, we impose the following condition on the function Φ defined in Section 10.3:

$$\frac{1}{\phi_m}\psi'^2 + \psi'' \leq 0. \tag{10.63}$$

This inequality is equivalent to $\frac{\Phi''}{\Phi'} \leq \frac{1}{\phi_m}$. It arises in a very natural way during the course of the existence proof. It is not difficult to discover its physical meaning, choosing a power absorption law, i.e., setting

$$f(\xi) = \lambda\xi^n, \quad n > 0, \ \lambda > 0 \tag{10.64}$$

which gives

$$\psi(\Theta) = V_{\max} - [(V_{\max} - V_0)^{1-n} - \lambda(1-n)\Theta]^{1/(1-n)} \tag{10.65}$$

for $n \neq 1$, and

$$\psi(\Theta) = V_{\max} - (V_{\max} - V_0)e^{-\lambda\Theta} \tag{10.66}$$

for $n = 1$, so that (10.63) takes the form

$$\frac{V_{\max} - V}{\phi_n} \leq n$$

(note on the other hand that $\frac{\Phi''}{\Phi'} = \frac{n}{V_{\max}-V}$), which requires

$$\frac{V_{\max} - V_0}{\phi_m} = \frac{\phi_0 - \phi_m}{\phi_m} \leq n \tag{10.67}$$

and finally

$$\phi_m \geq \frac{\phi_0}{n+1}. \tag{10.68}$$

In other words, (10.63) expresses the physical requirement that once the granules have reached their maximum admissible volume, the corresponding reduction of porosity must not be too large (also it links ϕ_m to the order i.e., the speed, of the reaction). As we said in the introduction, this condition is necessary to prevent the gel-blocking effect. Once more, we neglect gravity for simplicity and impose no constraints on the inflow rate.

Thus the problem reduces to finding the pair (s,p) satisfying

$$\phi S'(p)\frac{\partial p}{\partial t} + (1-S)\psi'(\Theta)(S(p)-S_0) - \frac{\partial}{\partial x}\left(k(\phi)\frac{\partial p}{\partial x}\right) = 0$$

$$0 < x < s(t),\ 0 < t < t_S \tag{10.69}$$

$$-k(\phi)\frac{\partial p}{\partial x} = q_0(t), \qquad x = 0,\ 0 < t < t_S \tag{10.70}$$

$$s(0) = 0 \tag{10.71}$$

$$p(s(t),t) = 0 \tag{10.72}$$

$$\dot{s}(t) = -\frac{k(\phi_0)}{\phi_0 s_0}\frac{\partial p}{\partial x}\bigg|_{x=s(t)}, \qquad 0 < t < t_S \tag{10.73}$$

where t_S is the time at which the saturation front appears, ϕ is given by (10.36), and Θ is given by (10.34).

Theorem 10.2. *Under the assumptions listed earlier and if $q_0(t)$ is continuously differentiable and strictly positive for $t \geq 0$, problem (10.69) to (10.73) has at least one classical solution, provided that if $S'' \neq 0$, the additional conditions (10.93) and (10.95) are satisfied. If $S'' \neq 0$, the result is local in time.*

The proof is rather complex; we just summarize it here.

Our aim is not just to reproduce the results of [3] (derived in the simpler case $S' =$ constant), but to present some generalization and comment on the peculiar characteristics of this class of problems.

The general scheme is as follows:

(i) Choose a boundary $x = s(t)$ in the set

$$\Sigma = \{s \in C([0,T]) \mid s(0) = 0,\ s(t) > 0 \text{ for } t > 0$$

$$0 \leq \frac{s(t') - s(t'')}{t' - t''} \leq A,\ 0 \leq t' < t'' \leq T\} \tag{10.74}$$

with $A > 0$ to be defined ($T > 0$ is for the moment generic) and look for a solution $p(x,t)$ of the problem (10.69), (10.70), (10.72), (10.34), and (10.36).

(ii) Show that the solution so obtained can be used to define a new boundary $x = \sigma(t)$ such that

$$\dot{\sigma}(t) = -\frac{k_0}{s_0\phi_0}\frac{\partial p}{\partial x}\bigg|_{x=s(t)}, \quad \sigma(0) = 0,\ k_0 = k(\phi_0). \tag{10.75}$$

(iii) Show that the mapping $\mathcal{M}s = \sigma$ has at least one fixed point in σ for a suitable selection of the Lipschitz constant A.

Because the functions in Σ are not strictly increasing, we have to extend the validity of (10.34) and (10.36) to the case of nondecreasing boundaries.

If $s(t)$ is constant over an interval $[t_1, t_2]$ (and $s(t) < s(t_0)$ for $t < t_1$, $s(t) > s(t_2)$ for $t > t_2$), then $S = S_0 \Rightarrow \Theta = 0 \Rightarrow \phi = \phi_0$ along that part of the boundary. Trivially $\frac{\partial \phi}{\partial t} = 0$, while

$$\left.\frac{\partial \phi}{\partial x}\right|_{x=s(t_1)} = -\psi'(0)S'(0) \int_{t_1}^{t_2} \left.\frac{\partial p}{\partial x}\right|_{x=s(t_1)} d\tau$$

where $\psi'(0)$ is nothing but $f(V_{\max} - V_0)$.

The advantage of dealing with nondecreasing boundaries is that we do not have to estimate a positive lower bound for $-k\frac{\partial p}{\partial x}$, which would not be as easy as in the saturated flow.

We omit all the details of the steps (i) and (ii), which contain two difficulties: the fact that the coefficients in (10.60) are functionals and the degeneracy of the domain for $t = 0$. The problem is facilitated by assumption (10.58), which guarantees the uniform parabolicity of (10.60). The existence and uniqueness proof of such auxiliary problem is sketched in [3].

It is more interesting to outline the most relevant points in (iii), because they are peculiar to the specific problem we are considering. Let us list the key results.

(I) Bounds on p:

$$0 < p(x,t) < p_S \quad \text{in } \{0 < x < s(t),\ 0 < t < t_S\} = D \tag{10.76}$$

In order to obtain positivity we have to write equation (10.60) more appropriately with the positive part $(S - S_0)_+$ replacing $(S - S_0)$. Indeed, the corresponding term expresses $(S-1)\frac{\partial \phi}{\partial t}$, and clearly $\frac{\partial \phi}{\partial t} = 0$ in the negativity set of p (where S is under threshold for absorption). Therefore p satisfies a homogeneous parabolic equation in its negativity set.

Because the negative minimum must be taken inside (if it exists), because of the boundary conditions, then the strong maximum principle would extend the negativity set up to the boundary, producing a contradiction.

The inequality $p < p_S$ is an immediate consequence of the maximum principle.

(II) The volumetric velocity is positive in D. We set

$$-q = w = k(\phi)\frac{\partial p}{\partial x} \tag{10.77}$$

and differentiate (10.60) with respect to x. Using the known expressions for $\frac{\partial \phi}{\partial x}$ and $\frac{\partial \phi}{\partial t}$ and observing that

$$\frac{\partial^2 p}{\partial x \partial t} = \frac{1}{k}\left[\frac{\partial w}{\partial t} + \frac{k'}{k} w \psi'(\Theta) \int_{\theta(x)}^{t} S'(p) \frac{\partial p}{\partial x}\, d\tau\right]$$

we obtain the following parabolic partial differential equation for w:

$$\frac{\phi S'}{k}\frac{\partial w}{\partial t} + \left(\frac{S''}{S'}\frac{1}{k} w - \frac{1}{\phi}\psi'(\Theta)\Xi\right)\frac{\partial w}{\partial x} - \frac{\partial^2 w}{\partial x^2} + \frac{1}{k}\psi'(\Theta) S' \left\{\left(\frac{\phi k'}{k} - 1\right)\right.$$

$$\left. \times (S - S_0) + (1 - S)\left(1 - (S - S_0)\frac{S''}{S'^2}\right)\right\} w$$

$$= -(1 - S)(S - S_0)\Xi\left(\frac{1}{\phi}\psi'^2 + \psi''\right) \tag{10.78}$$

where

$$\Xi = \int_{\theta(x)}^{t} \frac{w(x,\tau)}{k(\phi(x,\tau))} S'(p(x,\tau))\, d\tau. \tag{10.79}$$

Because $\psi' > 0$, conditions (10.58) and (10.61) ensure that the coefficient of w is positive. Moreover, condition (10.63) implies that the source term in (10.78) has the same sign as Ξ.

The boundary conditions are such that $w(0,t) < 0$, $w(s(t),t) \leq 0$ because of (I), and $w < 0$ in some neighborhood of the origin.

Now we show that $w < 0$ through the following steps:

(α) Let the positivity set of w be nonempty and have a positive distance from the parabolic boundary of D. This means that there is a first positive time $\bar{t}$ at which w vanishes at some point $\bar{x}$ and $(\bar{x}, \bar{t})$ is an inner point. Furthermore $w(x,t) < 0$ for $t < \bar{t}$. Hence $\Xi < 0$ at least up to $t = \bar{t}$ and the maximum principle leads to a contradiction.

(β) The positivity set of w is nonempty and its boundary has points in common with the curve $x = s(t)$. Then we introduce a family of solutions $w^\delta(x,t)$ of (10.78) with the only change that on $x = s(t)$ we impose $w^\delta(s(t),t) = \min\{w(s(t),t), -\delta\}$, where $\delta > 0$. It is possible to show that for any δ sufficiently small w^δ exists and $w^\delta \to w$ uniformly as $\delta \to 0$. The argument under (α) applies for w^δ, so that $w^\delta < 0$ in D. Passing to the limit we obtain $w \leq 0$. Because $w < 0$ near the origin, we conclude that $\Xi < 0$, which implies the strict inequality $w < 0$.

Remark 10.9. *A consequence of (II) is* $\frac{\partial \phi}{\partial x} > 0$ *in the wet region (recall 10.38).*

(III) A bound on pressure gradient on $x = s(t)$. This is, of course, a basic estimate. It can be obtained by comparing $p(x,t)$ with a linear barrier. For any $t_0 > 0$ set

$$z(x,t) = p(x,t) - \Lambda(t_0)[s(t_0) - x] \tag{10.80}$$

where $\Lambda(t_0) = \frac{1}{k_m} \sup_{0<t<t_0} q_0(t)$.

Clearly we have $z(s(t),t) < 0$, $k\frac{\partial z}{\partial x}\Big|_{x=0} \geq 0$ for $t < t_0$. The equation satisfied by z in $D \cap \{t < t_0\}$ is

$$\phi S' \frac{\partial z}{\partial t} - \frac{\partial}{\partial x}\left(k(\phi)\frac{\partial z}{\partial x}\right) = -(1-S)\psi'(\Theta)(S-S_0) - k'\Lambda(t_0)\frac{\partial \phi}{\partial x}. \tag{10.81}$$

Therefore, recalling Remark 10.9, we conclude that the right-hand side is negative, whence it is easy to get the desired estimate

$$0 \geq \frac{\partial p}{\partial x}\bigg|_{x=s(t)} \geq -\frac{1}{k_m} \sup_{0<\tau<t} q_0(\tau). \tag{10.82}$$

Remark 10.10. *Inequality (10.82) allows us to select* $A = \frac{k_M}{k_m} \| q_0 \|$ *in (10.74).*

(IV) Bound on the volumetric velocity. Preliminarly we note that setting

$$\| w \|_t = \sup w(x,\tau) \quad \text{for } 0 < x < s(\tau),\ 0 < \tau < t$$

the right-hand side of (10.78) is larger than $-\frac{M}{k_m} N \int_0^t \| w \|_\tau \, d\tau$, where

$$M = \sup_{0<p<p_S} S'(p), \qquad N = \sup_{0<\Theta<T} \left| \frac{1}{\phi_n}\psi'^2(\Theta) + \psi''(\Theta) \right|.$$

Now divide both sides of (10.78) by $\frac{\phi S'}{k}$ and write the resulting equation in the form

$$\mathcal{L}w = -\left(\frac{\phi S'}{k}\right)^{-1}(1-S)(S-S_0)\Xi\left(\frac{1}{\phi}\psi'^2 + \psi''\right) \tag{10.83}$$

where the parabolic operator $\mathcal{L}$ has an obvious definition. At this point it is easy to see that $w \geq W$, where W solves the equation

$$\mathcal{L}W = -\frac{1}{\phi_n}\frac{k_M}{k_m}\frac{M}{m}N \int_0^t \| w \|_\tau \, d\tau \equiv -Q \int_0^t \| w \|_\tau \, d\tau \tag{10.84}$$

with $m = \inf_{0<p<p_S} S'(p) > 0$ (because of (10.58)), with data

$$W(0,t) = -\| q_0 \|_T, \quad W(s(t),t) = -\frac{k_M}{k_m}\| q_0 \|_T.$$

Note that implicitly we have supposed $T \leq t_S$, where t_S (the saturation time) still has to be estimated. Moreover, the maximum principle yields the inequality

$$\| W \|_t \leq \frac{k_M}{k_m}\| q_0 \|_T + Q \int_0^t \| w \|_\tau \, d\tau \tag{10.85}$$

and eventually

$$\| w \|_t \leq \frac{k_M}{k_m}\| q_0 \|_T + Q \int_0^t \| w \|_\tau \, d\tau \tag{10.86}$$

so that

$$0 > w \geq -\frac{k_m}{k_m}\| q_0 \|_T e^{QT}. \tag{10.87}$$

Remark 10.11. *All the preceding estimates could also be obtained if* $\frac{\partial k}{\partial S}>0$.

(V) Bounds on $\frac{\partial p}{\partial t}$ *and* $\frac{\partial^2 p}{\partial x^2}$. These are the most delicate estimates. We have to distinguish two cases:

(a) $S''(p) = 0$, and

(b) $S''(p) \neq 0$.

Let us derive the equation for $\frac{\partial p}{\partial t}$ in the general case by differentiating (10.69) with respect to time:

$$\begin{aligned}
&\phi S' \frac{\partial^2 p}{\partial t^2} - \frac{\partial}{\partial x}\left(k \frac{\partial}{\partial x}\frac{\partial p}{\partial t}\right) \\
&\qquad + \psi' S' \left\{(1-S) + \left(\phi \frac{k'}{k} - 2\right)(S - S_0)\right\}\frac{\partial p}{\partial t} + \phi S'' \left(\frac{\partial p}{\partial t}\right)^2 \\
&= -(1-S)(S-S_0)^2\psi'' + \frac{\partial p}{\partial x}(S-S_0)\Xi\left\{k''\psi'^2 + k'\psi'' + \frac{k'}{k}\psi'^2\right\} \\
&\qquad - k'\psi' S' \left(\frac{\partial p}{\partial x}\right)^2.
\end{aligned} \tag{10.88}$$

What we know on the boundary is

$$-k(\phi(0,t))\frac{\partial}{\partial x}\frac{\partial p}{\partial t}\bigg|_{x=0} = \dot{q}_0(t) + \frac{k'}{k} q_0(t) \frac{\partial \phi}{\partial t}\bigg|_{x=0} \tag{10.89}$$

$$\left.\frac{\partial p}{\partial t}\right|_{x=s(t)} = -\dot{s}(t)\left.\frac{\partial p}{\partial x}\right|_{x=s(t)}. \tag{10.90}$$

Here $\dot{s}$ is just L^∞, but we can adopt a smoothing procedure to get the final result, taking $\dot{s}(0) = \frac{1}{\phi_0} q_0(0)$, so that

$$\frac{\partial p}{\partial t}(0,0) = \frac{q_0^2(0)}{k(\phi_0)\phi_0}. \tag{10.91}$$

At this point we see that in case (a), assumption (10.61) is enough to obtain the estimate of $\| \frac{\partial p}{\partial t} \|_T$ in terms of already-known quantities.

Passing to case (b), we note that as long as

$$(1-S) + \left(\phi\frac{k'}{k} - 2\right)(S - S_0) + \frac{\phi S''}{\psi' S'}\frac{\partial p}{\partial t} > 0 \tag{10.92}$$

we are allowed to apply the maximum principle.

Now we strenghten condition (10.61), assuming, e.g.,

$$\phi\frac{k'}{k} \geq 3 \tag{10.93}$$

(still satisfied by the physical case (10.62)), so that instead of (10.92) it is enough to require

$$1 - S_0 + \frac{\phi S''}{\psi' S'}\frac{\partial p}{\partial t} > 0. \tag{10.94}$$

Now we impose the additional condition

$$\frac{\phi_M}{\inf \psi'} \sup \frac{S''}{S'}\frac{q_0^2(0)}{k(\phi_0)\phi_0} > -(1 - S_0) \tag{10.95}$$

which satisfies (10.94) near the origin, thanks to (10.91).

The possibility of applying the maximum principle to (10.88) near the origin enables us to estimate the time T for which (10.94) is valid just in terms of a general bound on the source term, which is already available.

Remark 10.12. *In (10.95) we tacitly assume that $\psi' > 0$ (always true if the grain swelling is not completed, and in any case can be obtained by reducing T in a known way). However, such limitations are not needed if $S'' \geq 0$. The same argument applies to the ratio $\frac{S''}{S'}$ (we stop before p reaches p_S).*

The conclusion is the following.

In case (a), $\| \frac{\partial p}{\partial t} \|_T$ is estimated in terms of known quantities for any $T < t_S$. In case (b), the analogous estimate is obtained under the additional requirements (10.93) and (10.95) for T less than a known constant.

Remark 10.13. *These estimates allow us to obtain a lower bound for t_S. In addition, once $\| \frac{\partial p}{\partial t} \|_T$ has been estimated, the same is true for $\| \frac{\partial^2 p}{\partial x^2} \|_T$.*

(VI) Continuity of the mapping $\mathcal{M}$. Integrating (10.69) written in its original form

$$\frac{\partial}{\partial t}[(1-S)\phi] + \frac{\partial}{\partial x}\left(k(\phi)\frac{\partial p}{\partial x}\right) = 0 \tag{10.96}$$

over $0 < x < s(t),\ 0 < \tau < t$, we get

$$\phi_0 S_0(\sigma(t) - s(t)) = \int_0^t q_0(\tau)\,d\tau + \int_0^{s(t)} (\phi(x,t) - \phi_0)\,dx - \int_0^{s(t)} \phi(x,t)S(x,t)\,dx. \tag{10.97}$$

Remark 10.14. *Note that if $\sigma = s$, i.e., if σ is a fixed point of $\mathcal{M}$, (10.97) gives the mass balance*

$$\int_0^{s(t)} \phi(x,t)S(x,t)\,dx = \int_0^t q_0(\tau)\,d\tau + \int_0^{s(t)} (\phi(x,t) - \phi_0)\,dx \tag{10.98}$$

expressing the fact that the amount of liquid in the medium at time t equals the amount of liquid injected minus the cumulative reduction of pore volume (which is the liquid absorbed).

Taking a pair s_1, s_2 in Σ, by means of (10.97), we can compare σ_1, σ_2:

$$\begin{aligned}\sigma_1(t) - \sigma_2(t) = s_1(t) - s_2(t) &+ \frac{1}{\phi_0 S_0}\int_0^{\alpha(t)} (\phi_1(x,t) - \phi_2(x,t))\,dx \\ &- \frac{1}{\phi_0 S_0}\int_0^{\alpha(t)} (\phi_1(x,t)S_1(x,t) - \phi_2(x,t)S_2(x,t))\,dx \\ &- \frac{1}{S_0}(s_1(t) - s_2(t)) - \frac{(-1)^j}{S_0\phi_0}\int_{\alpha(t)}^{\beta(t)} \phi_j(x,t)\,dx \\ &+ \frac{(-1)^j}{S_0\phi_0}\int_{\alpha(t)}^{\beta(t)} \phi_j(x,t)S_j(x,t)\,dx\end{aligned} \tag{10.99}$$

where $\alpha(t) = \min(s_1(t), s_2(t))$, $\beta(t) = \max(s_1(t), s_2(t))$, $j = i$ if $\beta = s_i$, and the other symbols are obvious.

The critical point of the proof is now to find an estimate for $S_1 - S_2$, i.e., $S(p_1) - S(p_2)$ in terms of $s_1 - s_2$. However, this objective is surprisingly difficult. Let us explain why.

Putting

$$u = p_1 - p_2 \tag{10.100}$$

the equation for u is

$$\begin{aligned}
&\phi_2 S'(p_2)\frac{\partial u}{\partial t} - \frac{\partial}{\partial x}\left(k_2\frac{\partial u}{\partial x}\right) \\
&\quad + \{(\phi_1 - \phi_2)S'(p_1) + \phi_2[S'(p_1) - S'(p_2)]\}\frac{\partial p_1}{\partial t} \\
&\quad + (S_1 - S_2)\{(1 - S_2)\psi'(\Theta_2) - (S_1 - S_0)\psi'(\Theta_1)\} \\
&\quad + (1 - S_2)(S_1 - S_0)[\psi'(\Theta_1) - \psi'(\Theta_2)] - \frac{\partial}{\partial x}\left[(k_1 - k_2)\frac{\partial p_1}{\partial x}\right] = 0.
\end{aligned} \tag{10.101}$$

We will soon come to the estimate of $\Theta_1 - \Theta_2$. The term in (10.101) that really makes it difficult to obtain an estimate of the sup-norm of $|u|$ is the one containing $\frac{\partial}{\partial x}(k_1 - k_2)$, which leads to the analysis of

$$\begin{aligned}
\frac{\partial}{\partial x}(\phi_1 - \phi_2) = &-[\psi'(\Theta_1) - \psi'(\Theta_2)] \int_{\theta_1(x)}^{t} S'(p_1)\frac{\partial p_1}{\partial x}\, d\tau \\
&- \psi'(\Theta_2)\left[\int_{\eta(x)}^{t} \frac{\partial}{\partial x}(S_1 - S_2)\, d\tau - (-1)^j \int_{\xi(x)}^{\eta(x)} S'(p_j)\frac{\partial p_j}{\partial x}\, d\tau\right]
\end{aligned} \tag{10.102}$$

where $\xi(x) = \min(\theta_1(x), \theta_2(x))$, $\eta(x) = \max(\theta_1(x), \theta_2(x))$ and j is the same as in (10.99). The delicate term appearing in (10.102) is $\int_{\eta(x)}^{t} S'(\overline{p})\frac{\partial u}{\partial x}\, d\tau$ where $\overline{p}(x,t)$ is between p_1 and p_2.

Integrating (10.96) over the rectangle $(0,x) \times (\eta(x), t)$ and subtracting the result for the two solutions, we can obtain the expressions of $\int_{\eta(x)}^{t} k_i\frac{\partial u}{\partial x}\, d\tau$, $i = 1, 2$. Because we cannot control the sign of $\frac{\partial u}{\partial x}$, the corresponding estimates are of no use in (10.102), except for the artificial case $S' =$ constant, $k =$ constant (note, however, that $k =$ constant violates (10.61)).

This is an important obstacle in the search for an estimate of u that is strong enough to infer uniqueness.

Because of this difficulty, we look for a weaker estimate, namely,

$$\int_0^{\alpha(t)} u^2(x,t)\,dx \le C \int_0^t \| s_1 - s_2 \|_\tau \, d\tau \tag{10.103}$$

with $C > 0$ a known constant.

Multiplying (10.101) by u and integrating over $0 < x < \alpha(t)$, $0 < \tau < t$ we obtain

$$\begin{aligned}
&\frac{1}{2}\int_0^{\alpha(t)} \phi_2 S'(p_2) u^2(x,t)\,dx + \int_0^t d\tau \int_0^{\alpha(\tau)} dx\, k_2 \left(\frac{\partial u}{\partial x}\right)^2 \\
&= \frac{1}{2}\int_0^t \phi_2 S'(p_2) u^2(\alpha(\tau),\tau)\dot{\alpha}(\tau)\,d\tau + \int_0^t u(\alpha(\tau),\tau)\left[k_1 \frac{\partial p_1}{\partial x} - k_2 \frac{\partial p_2}{\partial x}\right]_{x=\alpha(\tau)} d\tau \\
&\quad + \int_0^t d\tau \int_0^{\alpha(\tau)} dx\, u^2(x,\tau)\left\{\frac{1}{2}\left[\frac{\partial \phi_2}{\partial t} S'(p_2) + \phi_2 S''(p_2)\frac{\partial p_2}{\partial t}\right]\right. \\
&\quad \left. - S'(\overline{p})[(1-S_2)\psi'(\Theta_2) - (S_1 - S_0)\psi'(\Theta_1) - \phi_2 S''(\overline{p})\frac{\partial p_2}{\partial t}\right\} \\
&\quad + \int_0^t d\tau \int_0^{\alpha(\tau)} dx\, u(x,\tau)\left\{[\psi(\Theta_1) - \psi(\Theta_2)]\left[S'(p_1)\frac{\partial p_1}{\partial t} - (1-S_2)(S_1 - S_0)\right]\right. \\
&\quad - \int_0^t d\tau \int_0^{\alpha(\tau)} dx\,(k_1 - k_2)\frac{\partial u}{\partial x}\frac{\partial p_1}{\partial x}.
\end{aligned} \tag{10.104}$$

In this way we have eliminated precisely the critical term containing the expression (10.102). What remains to be estimated in (10.104) is the difference

$$\Theta_1 - \Theta_2 = \int_{\eta(x)}^t S'(\overline{p}) u\, d\xi - (-1)^j \int_{\xi(x)}^{\eta(x)} S_j(x,\tau)\,d\tau. \tag{10.105}$$

The way of using (10.104) is to construct an inequality of Gronwall type for the quantity $\int_0^{\alpha(t)} \sup_{0<\tau<t} u^2(x,\tau)\,dx$.

For example, we have to write

$$|\Theta_1(x,\tau) - \Theta_2(x,\tau)| \le \{M \sup_{0<\tau'<\tau} |u(x,\tau')| + 1\}(\eta(x) - \xi(x)). \tag{10.106}$$

Observing that $\int_0^{\alpha(t)} (\eta(x) - \xi(x))\,dx \le \int_0^t |s_1(\tau) - s_2(\tau)|\,d\tau$ and using all the estimates, we finally obtain (10.103).

At this point we return to (10.99), and we see that we can write

$$|\sigma_1(t) - \sigma_2(t)| \leq c_1 |s_1(t) - s_2(t)| + c_2 \int_0^t |s_1(\tau) - s_2(\tau)|\, d\tau$$

$$+ c_3 \int_0^{\alpha(t)} |u(x,t)|\, dx \leq c_4 \| s_1 - s_2 \|_t^{1/2} \qquad (10.107)$$

which proves the continuity of the mapping $\mathcal{M}$ and, eventually, the existence of at least one fixed point.

Remark 10.15. *The question of uniqueness has been solved in a paper still in preparation [5], which uses a different technique.*

Remark 10.16. *Also open is the problem of the unsaturated flow in a finite layer, whose second boundary is impermeable, as well as the problem in which saturated and nonsaturated regions coexist.*

10.6 Conclusions

We have presented a model for incompressible flows through porous media with hydrophile granules. Such a model leads to the formulation of several different free boundary problems, depending on how one selects the initial data, the boundary conditions (which may introduce additional free boundaries), and the conditions on the wetting front.

We have discussed in more detail the one-dimensional problem, which, except for the extreme case of no capillarity (Section 10.4), is solved only very partially.

Acknowledgment

I wish to thank Professor H. Neunzert for introducing me to the problem.

References

1. Bear, J., *Dynamics of Fluids in Porous Media*, America Elsevier, New York (1972).

2. Bear, J., and Verruijt, A., *Modelling Groundwater Flow and Pollution*, Reidel, Dordrecht, New York (1987).
3. Fasano, A., A one-dimensional flow problem in porous media with hydrophile grains. *Math. Meth. Appl. Sci.,* **22**, (1999) 605–617.
4. Fasano, A., Some two-scale processes involving parabolic equations, *Proc. Int. Conf. on Free Boundary Problems* (Creta, 1997), edited by I. Athanasopoulos, G. Makzakis and J.F. Rodriguez, CRC Press.
5. Fasano, A., and Solonnikov, V., An existence and uniqueness theorem for a flow problem through absorbing porous media, to appear.
6. Gianni, R., and Mannucci, P., The propagation of a wetting front through an absorbing porous material with saturation dependent permeability, to appear.
7. Green, W.H., and Ampt, G.A., Studies on soil physics. The flow of air and water through soils. *J. Agric. Sci.,* **4**, 1–24 (1911).
8. Mannucci, P., Study of the mathematical model for adsorption and diffusion in ultra-napkins, *Le Matematiche,* **50**, 3–14 (1995).
9. Weickert, J., A mathematical model for diffusion and exchange phenomena in ultra napkins, *Math. Meth. Appl. Sci.,* **16**, 759–77 (1993).

Index